HISTONE-TARGETED NUCLEIC ACID DELIVERY FOR TISSUE REGENERATIVE APPLICATIONS

by

Erik V. Munsell

A dissertation submitted to the Faculty of the University of Delaware in partial fulfillment of the requirements for the degree of Doctor of Philosophy in Chemical Engineering

Fall 2017

© 2017 Erik V. Munsell
All Rights Reserved

HISTONE-TARGETED NUCLEIC ACID DELIVERY FOR

TISSUE REGENERATIVE APPLICATIONS

by

Erik V. Munsell

Approved: _____

Eric M. Furst, Ph.D.
Chair of the Department of Chemical & Biomolecular Engineering

Approved: _____

Babatunde A. Ogunnaike, Ph.D.
Dean of the College of Engineering

Approved: _____

Ann L. Ardis, Ph.D.
Senior Vice Provost for Graduate and Professional Education

I certify that I have read this dissertation and that in my opinion it meets the academic and professional standard required by the University as a dissertation for the degree of Doctor of Philosophy.

Signed: _____

Millicent O. Sullivan, Ph.D.
Professor in charge of dissertation

I certify that I have read this dissertation and that in my opinion it meets the academic and professional standard required by the University as a dissertation for the degree of Doctor of Philosophy.

Signed: _____

Theresa A. Freeman, Ph.D.
Member of dissertation committee

I certify that I have read this dissertation and that in my opinion it meets the academic and professional standard required by the University as a dissertation for the degree of Doctor of Philosophy.

Signed: _____

April M. Kloxin, Ph.D.
Member of dissertation committee

I certify that I have read this dissertation and that in my opinion it meets the academic and professional standard required by the University as a dissertation for the degree of Doctor of Philosophy.

Signed: _____

Christopher J. Kloxin, Ph.D.
Member of dissertation committee

ACKNOWLEDGMENTS

There are a number of people, both past and present, who have been instrumental in helping me achieve this milestone in my professional career.

First and foremost, I'd like to thank my advisor, Dr. Millicent O. Sullivan. You have taught me so much about science, research, writing, and communication. I wouldn't be where I am today if it wasn't for your strong mentorship and guidance. I thank you for teaching me how to approach and solve scientific problems and for challenging me to think critically about my work. You have always motivated me to do the best I possibly could, and supported me whenever it was needed. I would especially like to thank you for teaching me how to effectively communicate my research and ideas to a diverse range of audiences. Your ability to organize thoughts, hypotheses, and results into a reasoned and compelling story never ceases to amaze me. It is a priceless skill to have, and I'm grateful to have been able to learn it from you during these past five years.

I'd also like to thank my committee members, Dr. Theresa A. Freeman, Dr. April M. Kloxin, and Dr. Christopher J. Kloxin, for their support during my time in graduate school. My conversations with you have provided me with valuable insights into my work throughout my career as graduate student. I also appreciate your time and your willingness to offer insight into my research and challenge my ideas. Your suggestions have helped me grow as a researcher and approach problems in new and interesting ways.

A huge thank you goes out to all the graduate students, past and present, that I have had the pleasure of getting to know these past five years. I am deeply indebted to all members of the Sullivan Group, who have always been there for me through the good times and the bad. Your friendship and thoughtful discussions are what got me through day, and kept me coming back. Your constructive feedback and questions have made me the scientist I am today. I would especially like to thank Dr. Abbygail Foster, Dr. Matthew Green, Dr. Nikki Ross, and Dr. Morgan Urello for taking me under their wing when I was a bright-eyed (possibly obnoxious) first year and showing me the ropes (and what grad school is really like). A big thanks also to Dr. Chad Greco, my partner in crime these past five years. You have been there since day 1, and always open to hearing my thoughts on research and life. I also thank Dr. Bing Fang for working close with me the past three years, and providing invaluable insight into my dissertation work. Without your help, this would not have been possible. I'd also like to thank Lacey Perdue, my talented undergraduate, who worked with me for the majority of my graduate career. Training and mentoring you has truly been the highlight of my time as a graduate student, and believe it or not, you have taught me so much. I wish you the best of luck in graduate school, and look forward to seeing what you accomplish.

A specific group of graduate students that I'd also like acknowledge are the incoming class of 2012. You have all made my choice to go to graduate school worthwhile. My CBI buddies: Dr. Nikodimos Gabreselassie and Chris Long, the first people I met when coming to UD. Dr. Ellinor Carlson, my homework buddy and (along with Dr. Torren Carlson) climbing buddy. Dr. Andrew Tibbits (Dr. Tibbs), Dr. Michelle Calabrese, Dr. Stefanie Berges, Dr. Molly Koehle, Dr. Edward Schreiner,

Kay Siu, Megan Smithmyer, Dr. Paul Mwasame, Gulsum Meric, Geun Ho Gu, Dr. Marcel Nunez, Juan Lucio-Vega, Alex Mironenko (and Olga Mironenko), Rebecca Chen, Kaleigh Reno, Dr. Ryan Patet, Dr. Cameron Shelton, Dr. Jennifer Mantle, Dr. Melissa Gordon, and Dr. Matthew Armstrong (my fellow RPI engineer): thank you all for your support and for keeping me sane.

There are a number of other scientists and staff members at the University of Delaware who helped made this dissertation possible. I thank Dr. Jeffrey Caplan and Michael Moore at the BioImaging Center for all of their help and knowledge in confocal and super resolution microscopy. Your insights played a pivotal role in designing and executing experiments during my first years of research. Big thanks go to Karen Black and Gary Lance for helping track down random chemicals or materials whenever I needed them for experiments. I'd also like to thank Kathie Young and Rechilda (Chil) Alba for always being there to help me with my many administrative questions over the years. You two have definitely made life and graduation much more manageable.

Outside of graduate school, I have been honored and fortunate to receive unconditional love and support from friends across the globe. Thank you to Nicholas Mozdzierz and Jakob Jeserpersen for spending time during breaks and vacation to get me back on my feet when I most needed it. Shout-out to the Rat Pack: Henry Barcohana, Jeremy Wambugu, Jordan Frias, and Elena Vasquez, representing the 401. I cannot possibly mention everyone by name without adding another hundred pages to this dissertation. But you know who you are. Whenever I need to feel at home, you have all always been there.

I'd especially like to thank Dr. Adriana Rojas, the love of my life and my best friend. One of the hardest things I have ever had to do is make the conscious decision to leave your side for five years while we attended graduate school on opposite sides of the country. You've been with me through the best of times and the worst of times. We've laughed, we've cried, we've shared new experiences, we've tried new things, we've been around the world, we've solved hard problems, we've done so many things and there's still so much to do. You've made me the scientist/friend/man that I am today, and I can't wait to spend the rest of my life with you.

Most importantly, I'd like to acknowledge my family. You have always inspired me to pursue my passions and overcome any challenges I may face. Thanks to Marc Tiberiis, my cousin but really my brother. We grew up together, and I honestly can't believe we made it this far. Thank you Auntie 'Chelle and Uncle Marc, for raising me and always keeping me laughing, no matter how hard times may get. Thank you Grammy and Papa for supporting me in everything I do, and always pushing me to be the very best. Finally, Mom and Dad, you are the ones that have made all of this possible. I could never have done it without you two in my corner, and I thank you from the bottom of heart for everything you have done for me. I dedicate this dissertation to you both.

TABLE OF CONTENTS

LIST OF TABLES

LIST OF FIGURES

ABSTRACT

Nucleic acid delivery has garnered significant attention as an innovative therapeutic approach for treating a wide variety of diseases. However, the design of non-viral delivery systems that negotiate efficient intracellular trafficking and nuclear entry represents a significant challenge. Overcoming these hurdles requires a combination of well-controlled materials approaches with techniques to understand and direct cellular delivery. Recent investigations have highlighted the roles histone tail sequences play in directing nuclear delivery and retention, as well as activating DNA transcription. We established the ability to recapitulate these natural histone tail activities within non-viral gene nanocarriers, driving gene transfer/expression by enabling effective navigation to the nucleus via retrograde vesicular trafficking. A unique finding of this histone-targeted approach was that nanocarriers gained enhanced access to the nucleus during mitosis.

The work described in this dissertation builds off of these fundamental insights to facilitate the translation of this histone-targeted delivery approach toward regenerative medicine applications. During native tissue repair, actively proliferating mesenchymal stem cells (MSCs) respond to a complex series of growth factor signals that direct their differentiation. Accordingly, the investigations in this work focused on utilizing the histone-targeted nanocarriers to enhance osteogenic growth factor gene transfer in dividing MSCs leading to augmented MSC chondrogenic differentiation, an essential first step in skeletal tissue repair. Concurrently, additional studies focused on optimizing the histone-targeted nanocarrier design strategy to

enable improved plasmid DNA (pDNA) binding stability and tunable harnessing of native cellular processing pathways for enhanced gene transfer.

Overall, the work presented herein demonstrated substantial increases in growth factor expression following histone-targeted gene transfer. This enhanced expression enabled more robust levels of chondrogenesis in MSCs than treatments with equivalent amounts of recombinant growth factor protein. Additionally, nanocarrier design optimization provided effective pDNA condensation and controllable interactions with native histone effectors. Importantly, these optimized nanocarriers conferred stable nanoplex formation and maintained transfection efficiency under physiologically relevant conditions. Taken together, these advances may help drive the clinical translation of histone-targeted nucleic acid delivery strategies for the regeneration of damaged tissue following traumatic injury.

Chapter 1

INTRODUCTION AND MOTIVATIONS

1.1 Therapeutic Potential of Nucleic Acid Delivery

Nucleic acid delivery, or gene therapy, represents a powerful therapeutic approach for treating a multitude of inherited and acquired diseases, including neurological, cardiovascular, and many types of cancer.[1, 2] The process works through the introduction of nucleic acids, either deoxyribonucleic acid (DNA) or ribonucleic acid (RNA), to cells in order to elicit a therapeutic effect.[3] The ability to successfully deliver nucleic acids allows scientists to treat a disease at the genetic level, gaining control over transcript and protein expression. Possessing the ability to regulate gene and protein expression has also enabled scientists to study gene function, identify gene products, and manipulate cellular responses, thus furthering our fundamental understanding of cell/tissue biology and disease progression.[4]

The number of product approvals in recent years[5] has firmly established the therapeutic potential of nucleic acid delivery, particularly in the field of regenerative medicine.[6] In the recent decades, thousands of gene therapy clinical trials have been initiated, with several progressing to the final stages of clinical development.[7] In 2012, Glybera became the first gene therapy approved in Europe to treat lipoprotein lipase deficiency.[8] More recently, in August 2017 Kymriah became the first FDA-approved gene therapy in the United States, targeting acute lymphoblastic leukemia.[9] With the additional advent of CRISPR/Cas9 and other innovative gene editing tools, gene therapy now stands poised to revolutionize disease treatment worldwide.

1.2 Delivery Vehicles

The effectiveness of gene therapy in human health applications relies heavily on the type of carrier used to deliver the nucleic acid payload. Naked DNA or RNA is highly susceptible to degradation when administered to the body.[10] In addition, the large size and negative charge of DNA and RNA significantly lowers their capacity for cellular uptake.[11] To overcome these hurdles, scientists have taken inspiration from nature, using modified viruses as delivery vehicles. Viral vectors encompass the vast majority of nucleic acid delivery vehicles being tested in the clinic today, given their innate ability to enter cells and facilitate gene transfer.[7, 12] However, the use of viral vectors engenders fundamental safety concerns regarding mutagenesis and immunogenesis.[13] In addition, viral vectors suffer from low loading capacities and are not readily amenable to industrial scale-up.[14]

To overcome these hurdles, researchers have begun developing non-viral based delivery approaches to deliver nucleic acids both safely and effectively.[4] These types of nucleic acid delivery vehicles can be broadly classified into four categories: peptides, polymers, lipids, and inorganic nanoparticles. Of these nanocarriers, both peptides and polymers have emerged in recent years as promising alternatives to viral vectors.[15]

1.2.1 Peptide- and Polymer-based Nanocarriers

Both peptide and polymeric materials possess properties that make them ideal candidates for non-viral gene therapy. Most notably, they possess scalable syntheses, excellent structural tailorability, and the ability to directly mimic cell-regulatory structures found in nature.[15] Typically, these materials contain cationic groups which function to electrostatically bind and condense the negatively charged nucleic acid,

self-assembling into a nanoscale complex (or polyplex). These polyplexes can protect the nucleic acid from degradation, and they help stimulate robust cellular uptake. These features have provided improved biocompatibility and bioavailability, as demonstrated by early phase clinical successes with RNA nanocarriers.[16, 17] Despite these promising results, both peptide- and polymer-based nanocarriers typically fall short of their viral counterparts in terms of delivery efficiency, and these issues must be overcome before these types of therapies become commercially available.[18]

1.3 Physiological Barriers to Intracellular Non-Viral Nucleic Acid Delivery

Non-viral nucleic acid nanocarriers typically enter cells via one of several endocytic uptake pathways.[19-22] These nanocarriers must navigate the intracellular milieu to orchestrate delivery to the intended therapeutic site of action within the cell (cytoplasm for RNA, nucleus for DNA). Directing these nanocarriers to their intended destination continues to be a major barrier to non-viral delivery efficacy,[23] as intracellular nanocarrier trafficking is not well understood. Additionally, nanocarriers encapsulating DNA have the added challenge of accessing the nucleus of cells, and nuclear delivery remains a preeminent challenge preventing clinical translation of many gene therapy applications.[15]

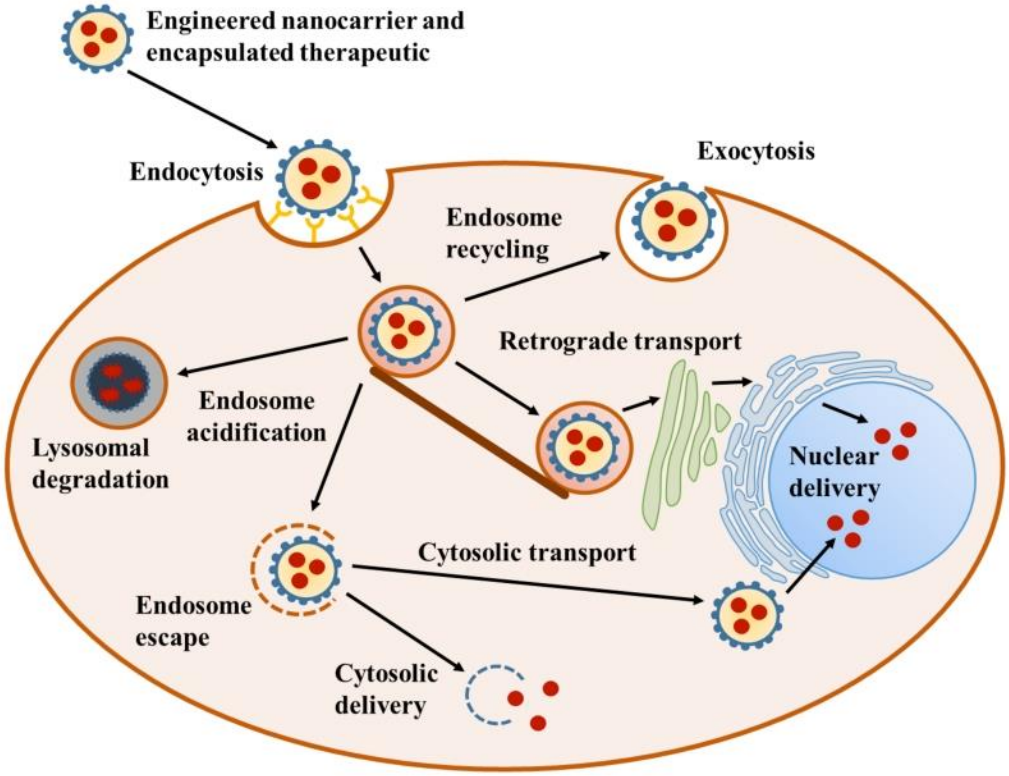

Figure 1.1: Intracellular trafficking of nucleic acid delivery nanocarriers following endocytosis. Figure reproduced with permission from EV Munsell, NL Ross, and MO Sullivan, Journey to the center of the cell: current nanocarrier design strategies targeting biopharmaceuticals to the cytoplasm and nucleus, *Curr Pharm Des*, 22 (2016) 1227-44.[15] Copyright 2016, Rights managed by Bentham Science Publishers.

1.3.1 Intracellular Trafficking and Endosome Escape

Following endocytic uptake, nanocarriers are internalized into vesicles known as endosomes via invagination of the plasma membrane (Figure 1.1). Endosomes are responsible for transporting cargoes to various destinations within the cell, and as part of this process, ultimately fuse with other compartments such as lysosomes, where their components are subsequently degraded by digestive enzymes.[24] Several studies have observed that the majority of internalized nanocarriers become entrapped within

endosomes,[25, 26] and many are believed to traffic to lysosomes. The result of these processes is that most nanocarriers along with their nucleic acids are degraded or recycled back to the plasma membrane before reaching their therapeutic target, which significantly impacts therapeutic efficacy.[19] Therefore, it is essential that non-viral gene nanocarriers be designed to avoid lysosomal degradation while effectively targeting the intended therapeutic destination.

To overcome lysosomal degradation and/or recycling, numerous groups have focused on designing nanocarriers with the capacity to induce endosome escape[3] following uptake (Figure 1.1). Design parameters often take inspiration from nature, such as viruses, bacteria, and other microorganisms, which have evolved efficient strategies to escape the endosome. Others have exploited the high buffering capacity of cationic nanocarriers to buffer endosome acidification by taking up protons.[27] This hypothesized process for endosome escape is known as the "proton sponge effect." The pumping of protons into the endosome is thought to be accompanied by an influx of chloride ions and water, causing osmotic swelling and eventual bursting of the endosome to release the entrapped nanocarrier into the cytosol.[28]

Although both native and artificial approaches to endosome escape have enhanced the delivery and effectiveness of nanocarriers containing RNA-based therapeutics,[15] nanocarriers delivering DNA have the added challenge of accessing the nuclear compartment. Due to the complexity of the intracellular space, nanocarriers cannot effectively diffuse in the cytoplasm,[29, 30] Thus, endosome escape is not always correlated with enhancements in nuclear delivery,[31, 32] and DNA-encapsulating non-viral nanocarriers often require active transport mechanisms to reach their intracellular target and achieve therapeutic efficacy.[33]

1.3.1.1 Cytoskeletal-Mediated Transport to the Therapeutic Site of Action

Cells have extensive microtubule (MT) networks that function to actively transport cellular components toward particular destinations in the cell, including the nucleus.[34] MTs are hollow cylinders which regulate the intracellular transport of vesicles, organelles, and chromosomes. They have also been implicated in the localization and nuclear import of proteins. The orientation of the MT network facilitates transport to the nucleus along MTs whose "minus" ends are located near the nucleus and "plus" ends located in the cell periphery. Another cytoskeletal component that can mediate transport of endocytic vesicles is actin. Actin is involved in many cellular functions such as maintenance of cell structure, cell motility, cytokinesis and movement of cargo,[35] These highly dynamic cellular components have different sizes and shapes and contribute to various aspects of cellular function.

Design strategies for DNA-encapsulating nanocarriers to harness these retrograde trafficking pathways following endocytic uptake take inspiration from mechanisms employed by pathogens as well as native proteins that are active in the nucleus.[36-38] Viruses have evolved diverse strategies to hijack the natural intracellular transportation network to ensure successful infection. Viruses rely on MTs[39] as well as actin filaments[40] to actively navigate the intracellular space and localize to the nuclear periphery.[41-43] Both viruses and native proteins often gain access to the nuclear compartment through the incorporation of nuclear localization sequences (NLSs). Inclusion of an NLS continues to be the most commonly studied approach for directing the transport and delivery of DNA-encapsulating nanocarriers to the nucleus[15] (Figure 1.1), avoiding premature endosome escape.

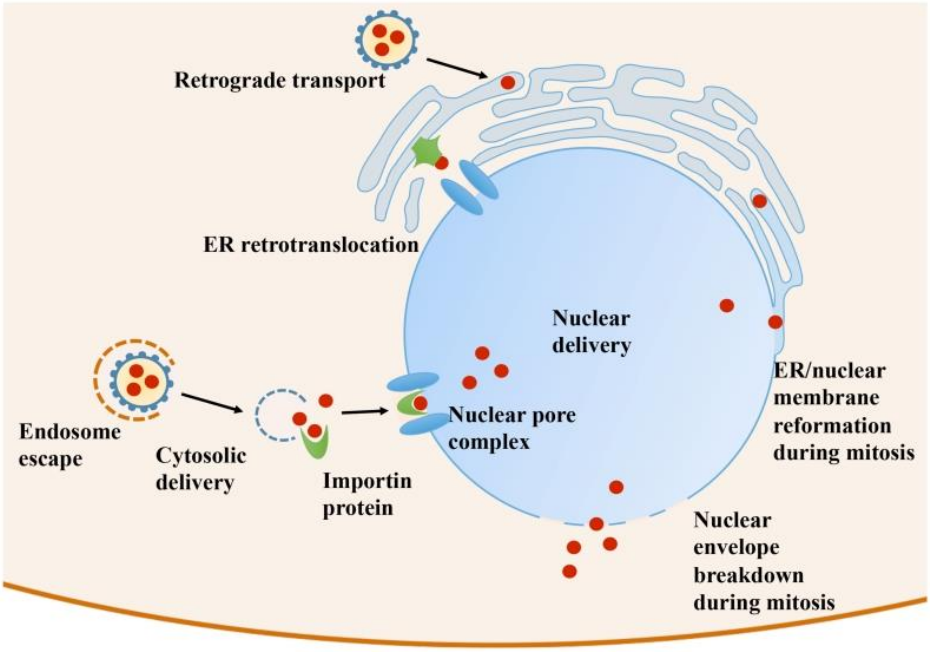

Figure 1.2: Nuclear entry of nanocarriers and their therapeutic cargos following intracellular trafficking. Figure reproduced with permission from EV Munsell, NL Ross, and MO Sullivan, Journey to the center of the cell: current nanocarrier design strategies targeting biopharmaceuticals to the cytoplasm and nucleus, *Curr Pharm Des*, 22 (2016) 1227-44.[15] Copyright 2016, Rights managed by Bentham Science Publishers.

1.3.2 Nuclear Delivery

Despite the advances in engineered nanocarrier design to harness native cellular transport pathways, the ability to efficiently access the nuclear compartment represents one of the most significant cellular transport barriers precluding efficacy of gene medicines.[44] The nucleus is separated from the cytoplasm by the nuclear envelope, which consists of two chemically distinct membranes (inner and outer), separated by a perinuclear cisterna. Transport of molecules between the cytoplasm and nucleus occurs through the nuclear pore complex (NPC), which are multi-protein membrane transport structures that are widely distributed throughout the nuclear

envelope.[45] Unless mitosis is occurring, molecules must pass through these channels in order to access the nucleus. Small molecules up to 9 nm can freely diffuse through the NPC, whereas molecules up to 39 nm can only enter through active transport.[46] Active transport is governed by a signal-mediated process[47] involving an NLS.[48] NLS-mediated import involves recognition by an NLS chaperone (a heterodimeric complex consisting of the NLS-binding protein importin-α and the NPC-docking protein importin-β),[49] and the subsequent docking of the bound complex at the NPC. This is followed by translocation through the NPC and into the nucleus.

Strategies aimed at enhancing nanocarrier nuclear delivery (Figure 1.2) again take inspiration from viruses and native cellular proteins. Prior to nuclear entry, both native proteins and most types of viruses are known to use the Sec61 translocon to retrotranslocate from the luminal side of endomembrane vesicles to the cytoplasmic face.[50, 51] Sec61 also functions in the endoplasmic reticulum (ER) to retrotranslocate misfolded proteins marked for degradation, and is harnessed by toxins during the intoxication process.[52] From here viruses/proteins can take advantage of NLS-mediated import and pass directly through the NPC (for small proteins and viruses),[53] or in the case of large viruses (e.g. herpes virus), dock at the NPC and release their viral DNA into the nucleus.[53, 54] Unfortunately, the size of non-viral nucleic acid delivery vehicles exceeds the limits for NPC-based nuclear delivery. Therefore, many investigations have focused on using mitosis as a means to enhance nuclear delivery.

1.3.2.1 Nuclear Access During Mitosis

During mitosis the nucleus disassembles and the NPCs dissociate. Nuclear envelope proteins then diffuse throughout the ER membrane, as they are no longer tethered to the pore complexes, nuclear membrane, or chromatin.[36] In combination,

these events result in the breakdown of the membrane that separates the nucleus and cytoplasm, and nuclear proteins that were not bound to membranes are free to mix with the cytosol of the dividing cell.[34] At the end of mitosis, the nuclear envelope reassembles on the surface of chromatin, while NPCs begin to reassemble and actively re-import proteins that contain NLSs. Some studies have also shown that the ER membrane forms the source of the newly forming nuclear membrane,[55] which wraps around chromosomes until the nuclear envelope is reformed.

A handful of large viruses take advantage of this nuclear envelope disassembly during mitosis to gain access to the nucleus. Viruses like the retrovirus murine leukemia virus[56] and papillomavirus[57] presumably wait for the dispersion of the nuclear membrane that occurs during mitosis, and become included within the nucleus during nuclear membrane reformation in the daughter cells. Multiple reports also indicate that mitosis plays a significant role in enhance the delivery of plasmid DNA (pDNA) as well as the nuclear delivery of DNA-encapsulating nanocarriers, with 30- to more than 500-fold higher transfection efficiencies reported when cells are exposed to delivery vehicles during S or G2 phase as compared with G1 phase.[58-60] These results suggest that nanocarrier access to the nucleus is likely facilitated by the temporary breakdown of the nuclear membrane. Unfortunately, efficient design strategies to exploit this effect remain significantly limited.

1.4 Improving Nanocarrier Trafficking and Nuclear Delivery with Histones

Targeting nucleic acid nanocarriers to the nucleus and achieving effective nuclear delivery continues to be a significant challenge. Improvements in therapeutic efficacy require increased understanding of how nanocarriers interact with cellular machinery, and how controlled materials design approaches can be used to harness

those interactions for enhanced transport and nuclear delivery. However, recent investigations have illuminated exciting progress in key areas. For example, nature's mechanisms for binding and retaining chromosomal DNA in the nucleus, as well as the mechanisms it uses to activate transcription have stimulated interest in histone proteins.[61-64] Histones are the major structural components of chromatin, and function to bind and condense DNA into a first-order packaging structure known as a nucleosome (Figure 1.3A). Each nucleosome is comprised of 146 base pairs of DNA wrapped around the surface of a histone octamer. The octamer is composed of homodimers of four core histone proteins, H2A, H2B, H3, and H4. The DNA wraps around the cationic core of the octamer, while the unstructured N-terminal tail sequences of the eight histone proteins extend outward (Figure 1.3B). These tail sequences act as a target for numerous cellular enzymes which post-translationally modify specific amino acids to alter histone activity.[65]

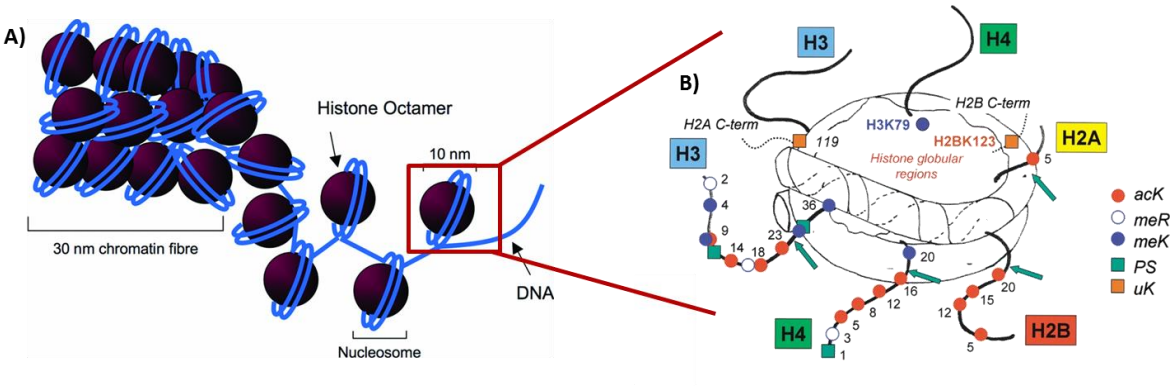

Figure 1.3: Schematic of (A) chromatin packaging in the nucleus of a eukaryotic cell and (B) nucleosome architecture. Figures adapted with permission from KM Wagstaff and DA Jans, Nucleocytoplasmic transport of DNA: enhancing non-viral gene transfer, *Biochem J* 406 (2007) 185-202[66] and BM Turner, Cellular memory and the histone code, *Cell* 111(3) (2002) 285-91.[67] (A) Copyright 2007, Rights managed by Biochemical Society (B) Copyright 2002, Rights managed by Cell Press.

Within the nucleus, the N-terminal tail sequence of the histone H3 protein has been shown to play an important role in activating chromosomal DNA for transcription through its interactions with histone acetyltransferase complexes.[65, 68-71] Recent studies have also implicated the H3 tail as an essential feature for nuclear import. Following translation, the H3 protein is transported from the cytoplasm to the nucleus via a receptor-mediated and energy-dependent process. The clustered basic amino acids present in the H3 tail serve as a potent NLS,[72] capable of interacting directly with importin proteins[73, 74] to translocate the H3 protein through the NPC. During mitosis, the H3 tail NLS is essential to ensuring nuclear localization of the H3 protein during nuclear envelope reformation in the daughter cells.[75] Finally, recent studies have identified the existence of vesicular trafficking machinery that is capable of interacting with and binding the H3 tail during active retrograde transport.[76, 77]

The unique properties of the H3 tail: its function as an NLS; its association with nuclear import proteins during mitosis; and its interactions with transcriptional activation machinery, make it an ideal candidate for addressing the challenges in nanocarrier intracellular transport and nuclear access described above. In addition, the H3 tail may provide unique fundamental insight into how nucleic acid nanocarriers interact with the native cellular environment en route to the nucleus.

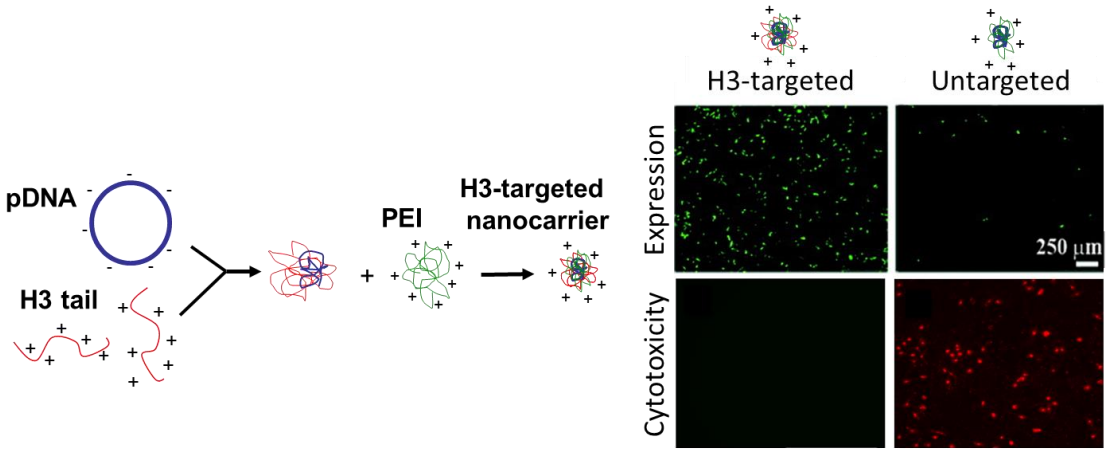

Figure 1.4: H3-targeted nanocarriers, formed via electrostatic interactions with pDNA and further condensation with PEI, yield significantly higher transfection efficiencies and cellular viabilities when compared to untargeted nanocarriers. Figures adapted with permission from MJ Reilly, JD Larsen, and MO Sullivan, Histone H3 tail peptides and poly(ethylenimine) have synergistic effects for gene delivery *Mol Pharm*, 9 (2012) 1031-40.[78] Copyright 2012, Rights managed by the American Chemical Society.

1.5 Novel H3-Targeted Nanocarriers for Improved Intracellular Transport and Nuclear Delivery

To address the inefficiencies of DNA-encapsulating nanocarriers, our group examined the effects that incorporating the N-terminal H3 tail sequence would have

on the interaction between non-viral nanocarriers with biological systems. It was hypothesized that inclusion of the H3 tail NLS would function to direct intracellular transport along vesicular retrograde trafficking pathways, avoiding endosome escape, and harnessing native nuclear import/localization machinery to achieve nuclear delivery/retention during mitosis. Formulation and characterization of these H3-targeted nanocarriers were conducted by Dr. John D. Larsen[68] and Dr. Meghan J. Reilly.[78] As shown in Figure 1.4, the H3 tail sequence was incorporated into non-viral nanocarriers via electrostatic complexation with pDNA. The initial polyplex was further condensed using the cationic polymer polyethylenimine (PEI) to form the final H3-targeted nanocarrier. Notably, when used to deliver pDNA encoding for the green fluorescent protein (GFP), H3-targeted nanocarriers achieved significantly higher transfection efficiencies than untargeted nanocarriers (containing PEI only) formulated at the same overall charge ratio. In addition, the cytotoxicity of the PEI polymer was significantly reduced upon inclusion of the H3 NLS. These promising results prompted investigations into the cellular trafficking and nuclear import characteristics of the H3-targeted nanocarriers. The increased gene transfer efficacy of the H3-targeted nanocarriers was likely due to an increased utilization of native intracellular transport pathways as well as H3 NLS-mediated nuclear portioning during mitosis. Detailed evaluation of nanocarrier trafficking and nuclear import was conducted by Dr. Nikki L. Ross (in collaboration with Erik V. Munsell for the endocytic trafficking and colocalization studies), and the resulting data was published in previous articles by the group.[79, 80] The subsequent sections provide an overview of the critical findings from these investigations, including: 1) H3-targeted nanocarriers avoid endosome escape and harness vesicular retrograde trafficking pathways to the perinuclear space;

2) these altered trafficking routes are in part regulated by histone effectors; and 3) H3-targeted nanocarriers associate with nuclear import proteins during mitosis to achieve enhanced nuclear delivery following post-mitotic reformation of the nuclear envelope.

1.5.1 H3-Targeted Nanocarriers Harness Vesicular Retrograde Trafficking Pathways en Route to the Nucleus

The text and figures in section 1.5.1 are adapted and reprinted from Ross, N.L.; Munsell, E.V.; Sabanayagam, C.; and Sullivan, M.O., Histone-targeted polyplexes avoid endosomal escape and enter the nucleus during postmitotic redistribution of ER membranes. *Mol. Ther. Nucleic Acids.* 2015, 4, e226.[79] Copyright 2015, Permitted for non-commercial reprint under the Creative Commons Attribution reserved by The American Society of Gene and Cell Therapy and Elsevier's open access policy.

This section details key findings observed in the trafficking behavior and pre- and postmitotic distributions of H3-targeted nanocarriers. Specific transfer pathways associated with retrograde transport versus endosome escape were dissected using pulse-chase transfections and detailed imaging approaches to analyze the rate, sequence, and extent of nanocarrier colocalization with GFP-fused Rab GTPases, key regulators of cellular transport.[81]

1.5.1.1 H3-Targeted Nanocarriers Traffic Through Rab GTPase-linked Vesicular Pathways

Chinese Hamster Ovary (CHO) K1 cells were pretransfected with constructs encoding Rab-GFP fusion proteins to enable live visualization of nanocarrier colocalization dynamics.[82] To determine the extent and kinetics of H3-targeted nanocarrier trafficking through endolysosomal pathways, traditionally associated with proton sponge theories, versus retrograde pathways that traffic to the Golgi and/or ER,

a pulse-chase transfection approach was used to expose cells to AlexaFluor555-labeled H3 nanocarriers and quantified nanocarrier colocalization with various Rab-GFPs as a function of time by using the Manders' correlation coefficient (M_r) (Figure 1.5). Overall, Rab staining was punctate, with organelle-specific distributions consistent with literature (Figure 1.5a-e). The nanocarriers colocalized significantly with multiple Rab-linked endomembrane compartments, indicating active transport via various pathways including endolysosomal, recycling, and retrograde trafficking routes (Figure 1.5f).

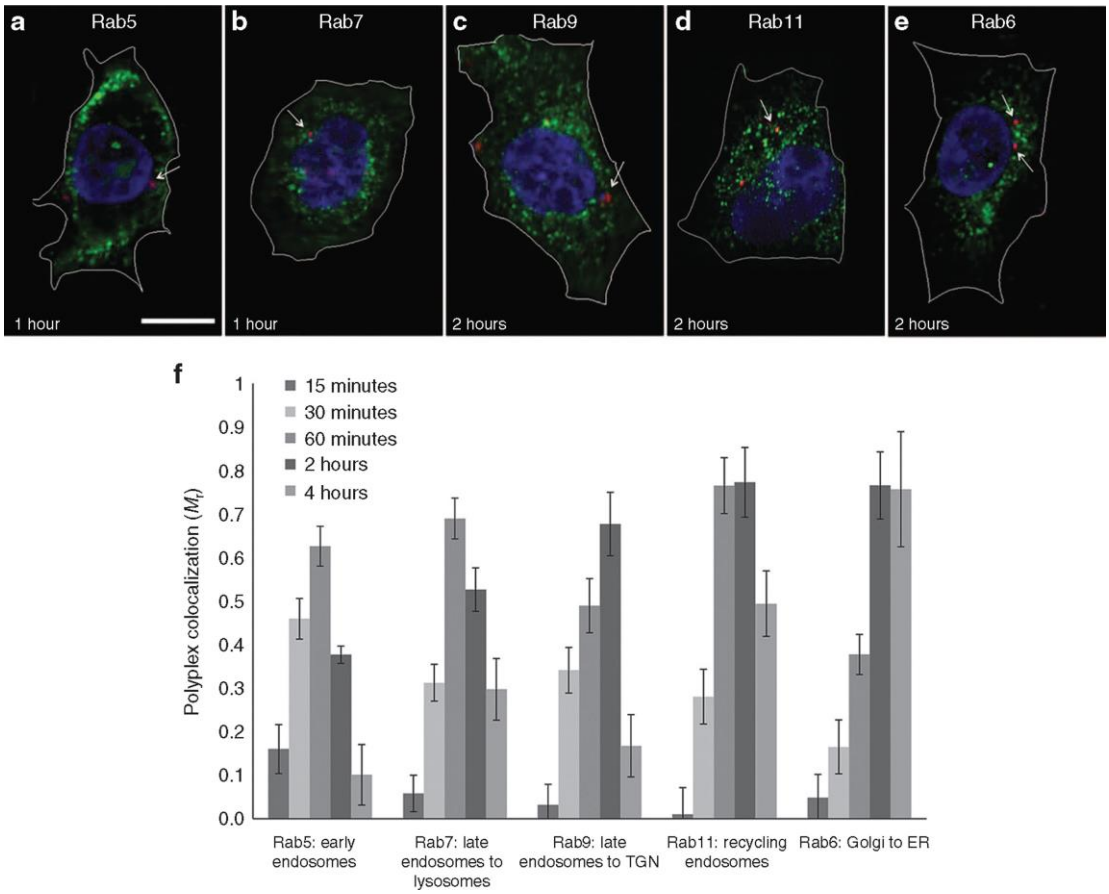

Figure 1.5: Colocalization of fluorescently labeled pDNA nanocarriers (red) with Rab-GFPs (green) in CHO cells. (a–e) Representative confocal microscopy z-slice images of cells with nuclei stained with DAPI (blue) following a pulse transfection with the H3-targeted nanocarriers. The scale bar (shown in a) = 10 μm. Cell images after (a, b) 1 hour or (c–e) 2 hours. (a) Rab5; (b) Rab7; (c) Rab9; (d) Rab11; and (e) Rab6. (f) Quantification of colocalization between nanocarriers and Rab-GFPs at different times post-transfection. Each data point represents the mean ± SE for a minimum of 100 nanocarriers from ~10 images.

Rab5 mediates endocytosis and early endosome fusion and is considered to be the first Rab GTPase encountered during both clathrin-mediated and caveolar endocytosis.[83] An initial increase in colocalization of H3-targeted nanocarriers with

Rab5 and a subsequent decrease at 1-hour posttransfection was observed. This brief transient occupancy indicated that nanocarriers were rapidly transferred from Rab5-labeled compartments to other endocytic vesicles. The high overall levels of colocalization with Rab5 demonstrated that a significant fraction of nanocarriers was endocytosed by clathrin-linked or caveolar vesicles, consistent with previous studies.[84]

Rab5 cargo can transition to Rab7-late endosomal compartments, Rab9-trans Golgi network (TGN) vesicles, and Rab11-recycling vesicles. Rab7 is essential for the maturation of late endosomes and fusion with the lysosomes;[85] therefore, this protein was utilized as a type of lysosomal marker. Meanwhile, Rab9 mediates transport between late endosomes and the TGN and also functions as the general organizer of late endosome subdomains.[86] Nanocarrier colocalization with Rab7 was slower than that observed for Rab5, consistent with literature documenting nanostructure transfer kinetics between Rab5- and Rab7-labeled structures. Because Rab7 vesicles transfer some cargo to recycling vesicles instead of lysosomes,[87] nanocarrier colocalization with Rab11 was also examined, which is associated with endocytic recycling downstream of clathrin-mediated endocytosis.[88] A portion of the H3-targeted nanocarriers colocalized with Rab11 with a slightly later colocalization maximum than Rab7, suggesting that some nanocarriers were indeed transported back to the plasma membrane via late endosomes. Meanwhile, the onset of nanocarrier colocalization with Rab9 also was delayed as compared with Rab5. The levels of colocalization with Rab9 remained steady until ~2 hours post-transfection, at which point the levels sharply decreased. The increase in colocalization with this marker, coincident with a decline in colocalization with Rab5, suggested that some nanocarriers were sequentially trafficked from early endosomes to TGN-sorting compartments.

To determine the mechanism of retrograde trafficking, nanocarrier colocalization with Rab6 was examined, which regulates native transport pathways from the Golgi to the ER[89] and is co-opted by pathogens including Shiga toxin B (STB) and herpes simplex virus 1.[90] Colocalization between nanocarriers and Rab6 peaked at 2 hours and then plateaued, suggesting accumulation within Golgi/ER vesicles.

1.5.1.2 H3-Targeting Enhances Nanocarrier Transport Through Rab5- and Rab6-linked Caveolar Pathways

Previous work in the group demonstrated that enhanced caveolar uptake was a key effect of adding H3-targeting peptides to PEI nanocarriers, and that those nanocarriers that were internalized within caveolae ultimately reached the nucleus and were responsible for transfection.[84] Accordingly, the extent to which H3-mediated changes in the initial endocytic event determined subsequent nanocarrier trafficking was investigated. Rab-GFP-expressing cells were transfected with H3-targeted or untargeted PEI nanocarriers in the presence of established endocytic inhibitors,[91] including chlorpromazine to disrupt clathrin-coated pit formation, filipin complex III to disrupt caveolar structure/function, or genistein to disrupt the phosphorylation of caveolin.

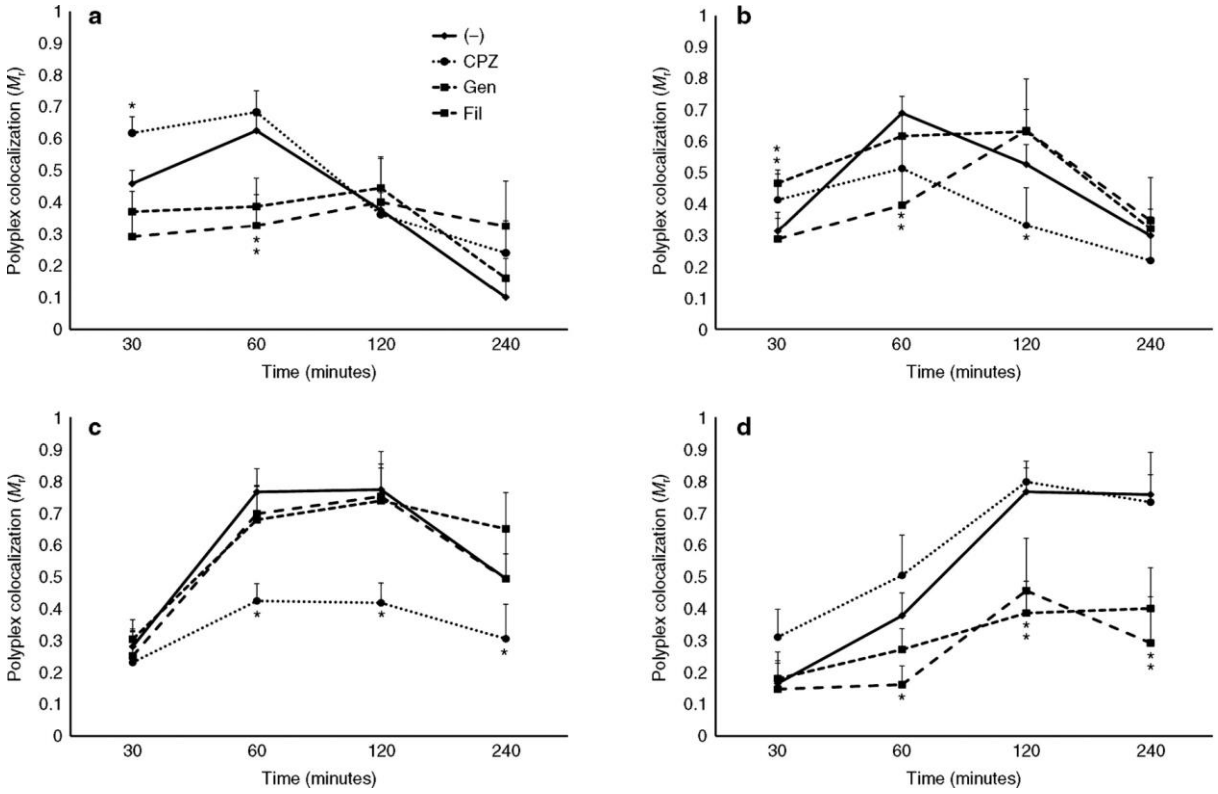

Figure 1.6: The effect of endocytic inhibitors on H3-targeted nanocarrier colocalization. (a) Rab5; (b) Rab7; (c) Rab11; and (d) Rab6. Each sample control (−) represents colocalization values from samples in which no inhibitors were added. Each data point represents the mean ± SE in M_r values obtained by analyzing a minimum of 100 nanocarriers from ~10 images. * Indicates a statistically significant difference relative to the respective nanocarrier control ($p < 0.05$).

Both clathrin and caveolar vesicles are known to traffic native proteins as well as various synthetic nanostructures through early endosomes. As shown in Figure 1.6a, clathrin inhibition minimally impacted H3-targeted nanocarrier colocalization with Rab5, whereas caveolar inhibition reduced trafficking to early endosomes during the first hour post-transfection when nanocarrier transit through early endosomes was maximal (Figure 1.5f). These data suggested that a large fraction of H3-targeted

nanocarriers trafficked through pathways exhibiting multiple similarities to those of STB, SV40 virus, and cholera toxin,[92, 93] which use caveolae/lipid rafts to travel from early endosomes directly into the Golgi and ER.[94] In contrast, clathrin cargo transfer from early endosomes to late endosomes, and ultimately, to lysosomes, the TGN, or recycling vesicles.[86] Hence, the effect of endocytic inhibition on nanocarrier localization within these downstream structures was examined. A slight decrease in H3-targeted nanocarrier colocalization with the late endosome marker Rab7 in the presence of chlorpromazine (Figure 1.6b) was observed, indicating that a fraction of H3-targeted nanocarriers were trafficking via typical clathrin-linked endolysosomal processing routes.[95]

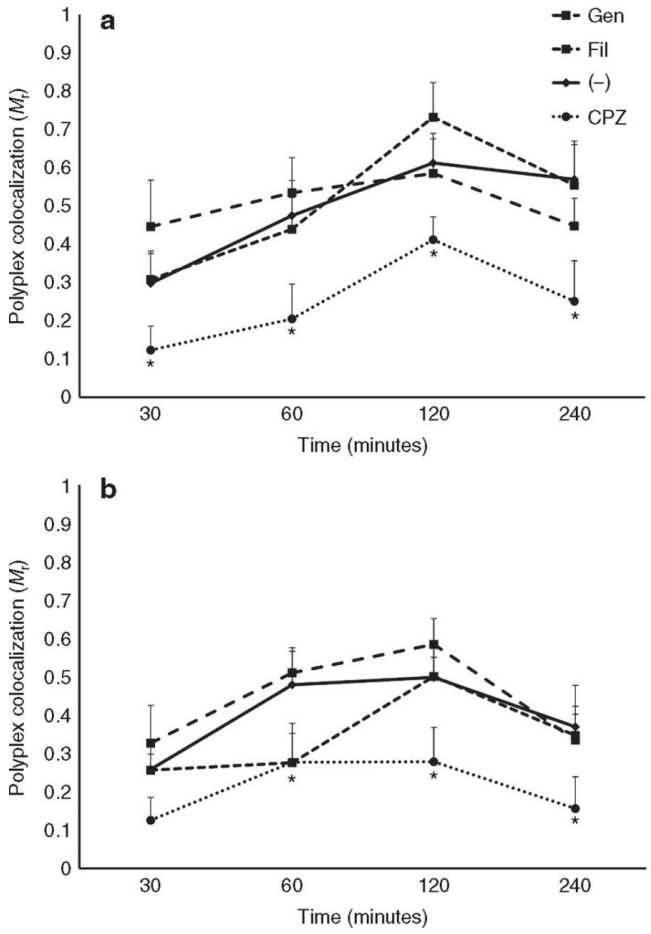

Figure 1.7: The effect of endocytic inhibitors on untargeted PEI nanocarrier colocalization. (a) Rab7; (b) Rab11. The respective sample control (−) was from a sample where no inhibitors were added. Each data point represents the mean ± SE for a minimum of 100 nanocarriers, ~10 images analyzed per replicate. * Indicates a statistically significant difference relative to the respective nanocarrier control ($p < 0.05$).

The colocalization of untargeted nanocarriers with Rab7 decreased more substantially in the presence of chlorpromazine (Figure 1.7a), suggesting that untargeted nanocarriers have an increased utilization of this pathway. The caveolae-associated inhibitors genistein and filipin complex III did not significantly change the levels of colocalization between both the targeted or untargeted nanocarriers and Rab7

(Figures 1.6b and 1.7a). These results agree with a previous study performed by Reilly et al., in which the role of lysosomal vesicles in H3-targeted nanocarrier trafficking was explored by exposing cells to lysosomotropic agents during transfection. The buffering agent chloroquine augmented the transfection efficiency for the PEI nanocarriers, suggesting that a significant fraction of the PEI nanocarriers trafficked through acidifying endosomes to lysosomes, and that chloroquine-mediated buffering was beneficial for the vesicular escape and transfection by these nanocarriers. In contrast, chloroquine decreased in the transfection efficiencies of the H3-targeted nanocarriers (~20% less than untreated controls) suggesting that the H3-targeted nanocarriers did not traffic to lysosomes, as buffering was not able to augment gene expression through vesicular escape.

To further probe nanocarrier transit through downstream compartments associated with clathrin or caveolar trafficking, endocytic inhibition studies were also used to examine the effects on colocalization with the TGN marker Rab9 and the recycling vesicle marker Rab11. None of the inhibitors significantly impacted colocalization with Rab9 (data not shown). These results indicated that nanocarriers did not reach the TGN through established clathrin-initiated routes. In contrast, H3-targeted nanocarrier colocalization with Rab11 was substantially reduced by endocytic inhibitors associated with clathrin but not by caveolar inhibitors (Figure 1.6c), and similar effects were observed with untargeted PEI nanocarriers (Figure 1.7b). These data demonstrated that nanocarrier recycling occurred subsequent to clathrin-mediated uptake through a process independent of H3 targeting.

Caveolae have been reported to directly route many cargoes from the plasma membrane or early endosomes to the Golgi and/or ER,[94] and Rab6 regulates the

downstream retrograde transport between early and late Golgi compartments and the ER. Hence, examination of whether nanocarriers colocalized with Rab6 downstream of caveolar uptake was conducted. In the presence of genistein or filipin complex III, there was a substantial decrease in H3-targeted nanocarrier/Rab6 colocalization, as shown in Figure 1.6d, suggesting that caveolar nanocarriers predominantly localized to perinuclear Rab6 structures. The effect was a function of H3 targeting, as untargeted PEI nanocarriers had minimal colocalization with Rab6 ($M_r < 0.1$). Chlorpromazine had no effect on nanocarrier-Rab6 colocalization (Figure 1.6d).

1.5.1.3 H3-Targeting Increases Nanocarrier Colocalization with Perinuclear mDPY-30

Recent studies have highlighted the roles of histone-processing enzymes in regulating cargo trafficking through the Golgi/ER following endocytic uptake.[76, 77] Thus, the H3-mediated changes in nanocarrier trafficking were thought to be caused not only by the established alterations in endocytic processing, but also by interactions with mammalian DPY-30 (mDPY-30), a key subunit of H3K4 methyltransferase (MT) complexes.[96] mDPY-30 localizes to both the nucleus and Golgi/ER endomembrane network, and its expression in these two regions was previously demonstrated in various mammalian cell lines including those derived from mouse, primate, and human.[76] Hence, pulse-chase transfections and immunostaining were utilized to quantify nanocarrier colocalization with mDPY-30 within the perinuclear membranes in NIH/3T3 murine fibroblasts (Figure 1.8). A fraction of the perinuclear H3-targeted nanocarriers colocalized with mDPY-30, with maximal colocalization at 2 hours post-transfection (Figure 1.8c), consistent with the kinetics of enhanced H3-targeted nanocarrier colocalization with Rab9 (Figure 1.5c). H3-targeted nanocarriers

colocalized with mDPY-30 at a significantly higher level than untargeted PEI nanocarriers at 2–3 hours post-transfection (Figure 1.8c), suggesting that H3 targeting increased utilization of H3K4 MT-regulated trafficking pathways.

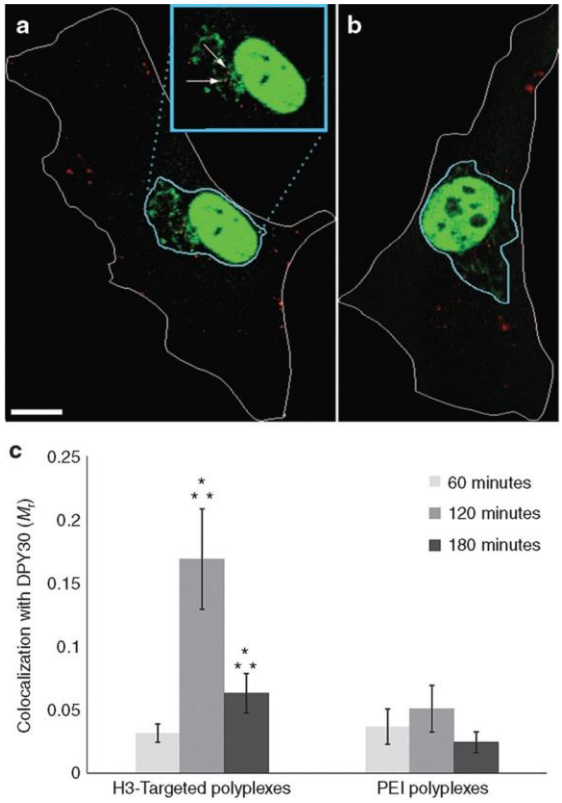

Figure 1.8: Colocalization of fluorescently labeled nanocarriers (red) with DPY30 (green). (a, b) Representative confocal microscopy images of cells with the perinuclear regions outlined in blue. Images were taken 2 hours after pulse-transfection with (a) H3-targeted or (b) untargeted nanocarriers. Scale bar (shown in a) = 10 μm. Inset in a: Colocalization of H3-targeted nanocarriers with DPY30 within the perinuclear region of the cell; arrows indicate colocalized nanocarriers. (c) Quantification of colocalization with DPY30 from confocal microscopy images at different times post-transfection. Each data point represents the mean ± SE for a total of 30 cells, a minimum of 40 nanocarriers analyzed. * Indicates statistically significant difference from PEI nanocarriers at the same time point ($p < 0.05$). ** Indicates statistically significant difference from the previous time point for the given nanocarrier ($p < 0.05$).

Approximately 18% of perinuclear H3-targeted nanocarriers colocalized transiently with mDPY-30 in the TGN; these nanocarriers were most likely shuttled within caveolae to the TGN via early endosomes, as previous studies showed that enhanced caveolar uptake was correlated with increased transfer through Golgi-associated compartments.[84] Glycosphingolipids exhibit similar transfer patterns involving caveolar uptake followed by Rab9-dependent microtubule-mediated transport to the TGN within human skin fibroblasts.[82] However, the current study showed only a minor effect of caveolae-associated inhibitors on nanocarrier colocalization with Rab9, even though colocalization with Rab9 occurred at a high level overall. These findings may indicate that nanocarrier trafficking through the TGN is highly transient, consistent with the role of the Golgi apparatus in cellular sorting.

To ensure that the altered colocalization of the H3-targeted nanocarriers with H3K4 MTs was sequence-specific, cellular transfection experiments with nanocarriers that were assembled identically, but with a scrambled H3 sequence (sH3 nanocarriers), were also performed. Fluorescence microscopy and flow cytometry analyses of GFP expression showed that only a small fraction (~10%) of cells expressed GFP when transfected with the sH3 nanocarriers (data not shown). Additionally, pulse-chase transfections with sH3 nanocarriers displayed negligible cellular uptake. Therefore, the observed effects with the H3-targeted nanocarriers were sequence-specific, and impacted nanocarriers interactions with the plasma membrane to alter endocytic trafficking.

1.5.1.4 H3-Targeted Nanocarriers Colocalize with Rab6-labeled Vesicles Until Mitosis

While H3-targeted nanocarrier colocalization with most Rab-linked structures was transient following pulse transfection (Figure 1.5), colocalization with Rab6 plateaued at 2 hours post-transfection. Because Rab6-linked cargo such as STB and other toxins ultimately translocate from the lumen of the ER to the cytosol during infection,[97] investigations into whether Rab6 colocalization ultimately decreased coincident with an increase in the cytosolic fraction of nanocarriers were conducted. Accordingly, using synchronized CHO-K1 cells, Rab6 colocalization with H3-targeted nanocarriers at extended time points was examined. Rab6 staining, as well as that of the nanocarriers, remained punctate and perinuclear until mitosis (Figure 1.9a–h). During mitosis, Rab6 staining became more disperse while H3-targeted nanocarrier staining remained largely punctate and gradually partitioned into the nucleus. The observed H3-targeted nanocarrier colocalization with Rab6 persisted at a high and unchanging level until division, at which time it rapidly decreased (Figure 1.9i). Untargeted PEI nanocarriers exhibited little accumulation in Rab6-labeled membranes, indicating that routing through Rab6-linked vesicles was mediated by the H3 sequence.

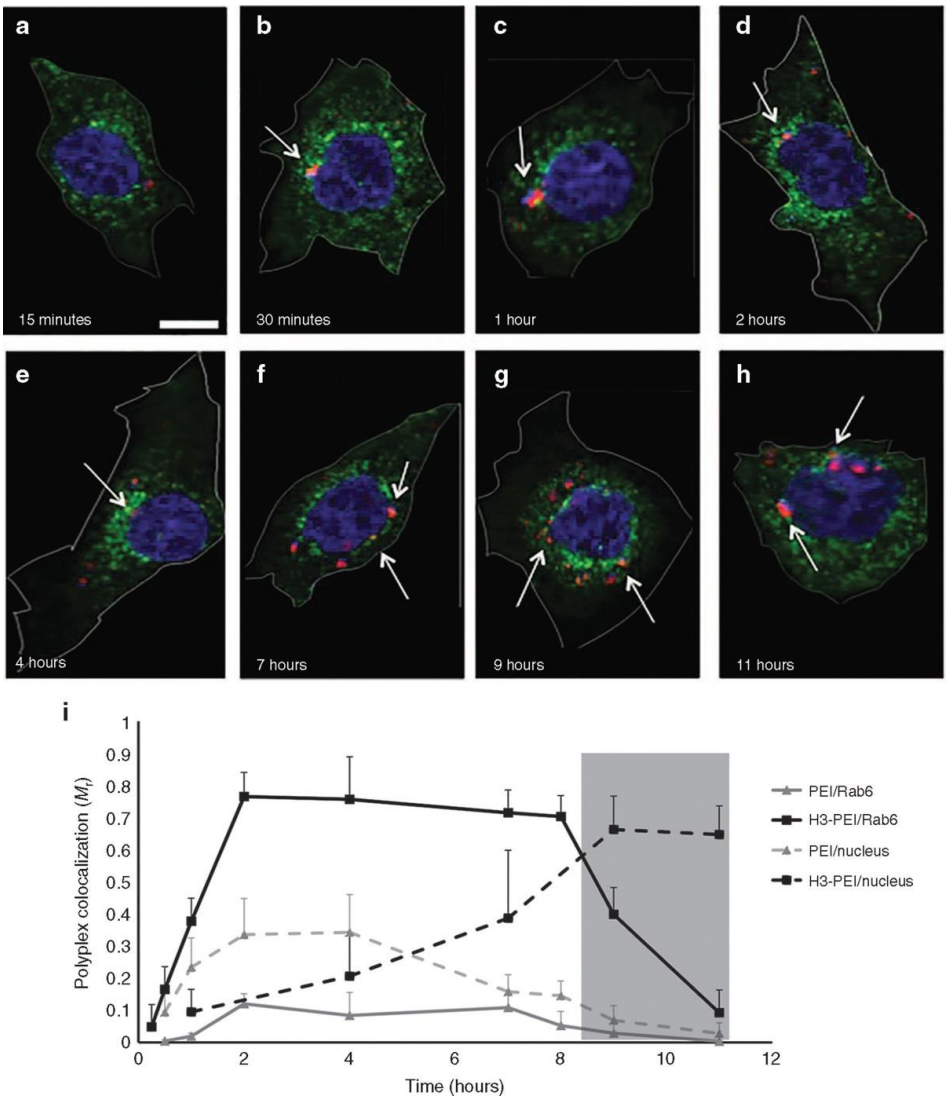

Figure 1.9: Colocalization of fluorescently labeled nanocarriers with Rab6 at eight different time points following transfection. (a-h) Representative confocal microscopy images of cells expressing Rab6-GFP (green) with the nuclei stained with DAPI (blue) following a pulse transfection with H3-targeted nanocarriers (red); arrows indicate regions of colocalization between nanocarriers and Rab6. The scale bar (shown in a) = 10 μm. The cell borders were outlined in white. (i) Quantification of colocalization from confocal microscopy images. Colocalization between H3-targeted nanocarriers and PEI nanocarriers with either Rab6 or the nucleus. Each data point represents the mean ± SE for a minimum of 100 nanocarriers, ~10 images analyzed per replicate. Gray box indicates cellular mitosis.

The striking decrease in H3-targeted nanocarrier colocalization with Rab6 during mitosis was likely due to the nanocarriers entering the nucleus; hence, nanocarrier colocalization with the nuclear stain DAPI (4′,6-diamidino-2-phenylindole) was quantified over similarly extended time frames (Figure 1.9i). As compared with Rab6, an opposite effect in nanocarrier colocalization occurred within the nucleus, with only moderate increases in nuclear colocalization prior to mitosis and significant increases coincident with mitosis. These results suggested that pre-mitotic accumulation in Rab6-linked compartments was necessary for H3-targeted transfection, whereas Rab6 localization and cellular division were unnecessary for nuclear colocalization by untargeted PEI nanocarriers.

1.5.2 Nuclear Entry and Retention of H3-targeted Nanocarriers During Mitosis

The text and figures in section 1.5.2 are adapted and reprinted with permission from Ross, N.L.; and Sullivan, M.O.; Importin-4 regulates gene delivery by enhancing nuclear retention and chromatin deposition by polyplexes. *Mol. Pharm.* 2015, 12, 4488-97.[80] Copyright 2015, Rights reserved by the American Chemical Society.

This section details key findings observed in the mechanisms of nuclear access for H3-targeted nanocarriers during mitosis, specifically, probing the role for the histone importin proteins in regulating the nuclear transport and retention of these nanocarriers. H3-targeted nanocarriers were shown to require importin-4 for postmitotic nuclear retention in CHO cells, and regulation and potential interactions with importin-4 occurred before mitosis. Silencing of importin-4 affected postmitotic nuclear retention as well as transfection efficiency by reducing nanocarrier codeposition with chromatin inside the nucleus.

1.5.2.1 H3-Targeted Nanocarriers Colocalize with Importin-4

The H3 NLS is an essential component of the H3 protein, required for nuclear accumulation following assembly in the cytoplasm.[98] The H3 NLS directly associates with importin-4 and importin-5 for translocation into the nucleus.[74] The H3 NLS also associates with importins-4 and -5 during post-mitotic redistribution, when it is deposited onto chromatin. Importin proteins and other histone chaperones shield histones from nonspecific interactions until they are assembled into chromatin.[99] Therefore, the possibility that importins might be involved in mediating postmitotic nuclear accumulation by H3-targeted nanocarriers was investigated. To enable analysis of nanocarrier transport kinetics, CHO cells were pulse transfected with nanocarriers containing plasmids labeled with AlexaFluor 555-peptide nucleic acids (PNA555),[100] and at various times following transfection, the cells were immunocytochemically (ICC) stained with antibodies targeting importin-4 and importin-5. Evidence of coordinated transport and a potential interaction between the H3-targeted nanocarriers and importin-4 was discovered, as determined by strong (42%) colocalization at 12 h post-transfection (Figure 1.10). Colocalization increased until reaching a maximum at 12 h, with a slight decrease at 24 h. These experiments were also performed with untargeted PEI nanocarriers and sH3 nanocarriers. Both the untargeted nanocarriers and the sH3 nanocarriers displayed substantially lower levels of colocalization with importin-4 as compared with the H3-targeted nanocarriers. These results suggest that importin-4 may play a key role in nuclear delivery of H3-targeted nanocarriers, via defined interactions with the H3 NLS.

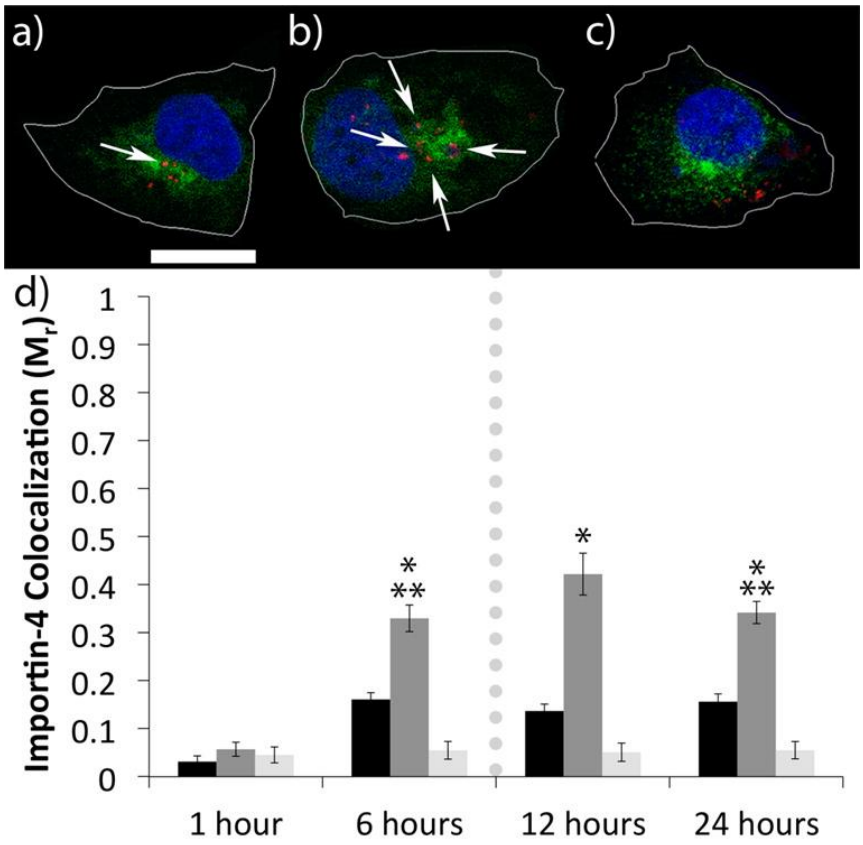

Figure 1.10: (a–c) Representative confocal microscopy images of cells expressing importin-4 (green) with the nuclei stained with DAPI (blue) 6 h after a pulse-transfection with PEI nanocarriers (a), H3-targeted nanocarriers (b), or sH3 nanocarriers (c). Nanocarriers are in red; arrows indicate regions of colocalization between nanocarriers and importin-4. The scale bar (shown in a) = 10 μm. The cell borders were outlined in white. (d) Manders coefficients quantifying colocalization between nanocarriers and importin-4 from confocal microscopy images taken at different times post-transfection. Colocalization with untargeted PEI nanocarriers (black), H3-targeted nanocarriers (dark gray), and sH3 nanocarriers (light gray) was analyzed at various times post-transfection. Each data point represents the mean ± SE with a minimum of 80 nanocarriers analyzed. The dotted line indicates mitosis. * Indicates a statistically significant difference from PEI nanocarriers at the same time point ($p < 0.05$). ** Indicates a statistically significant difference from the previous time point for the given nanocarrier ($p < 0.05$).

1.5.2.2 Importin-4 Knockdown Affects Transfection and Nuclear Delivery

The high levels of colocalization between the H3-targeted nanocarriers and importin-4 in both the nuclear periphery and the nucleus strongly suggested that importin-4 might mediate nuclear delivery and affect transfection efficiency. To further scrutinize this possibility, CHO cells were pre-transfected with siRNAs targeting importin-4 and the reductions in transfection efficiency subsequently quantified with the H3-targeted nanocarriers, PEI nanocarriers, or sH3 nanocarriers by using flow cytometry. A scrambled siRNA was used to control for nonspecific effects of siRNA transfection. Microscopy experiments and Western blots were performed to confirm knockdown,[80] and these experiments showed a 60% reduction in importin-4 expression following siRNA treatment as well as decreased levels of fluorescence in samples where ICC staining was used to detect importin-4. As compared to the scrambled control, siRNA-induced importin-4 silencing produced an approximately 80% reduction in transfection efficiency, confirming a likely role for importin-4 in H3-targeted nanocarrier trafficking and delivery, consistent with imaging experiments (Figure 1.11). In contrast, there was no statistically significant difference between the transfection efficiency after importin-4 knockdown and the transfection efficiency following scrambled siRNA treatment when either PEI nanocarriers or sH3 nanocarriers were used for transfection, indicating that these nanocarriers were not significantly transported by importin-4.

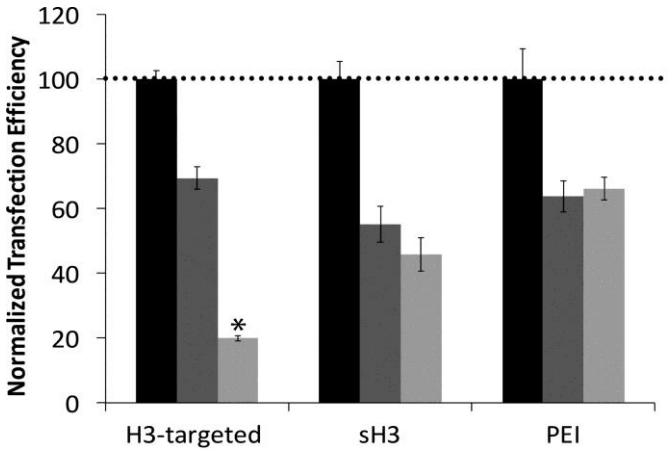

Figure 1.11: Summary of flow cytometry analyses of CHO cell transfection following siRNA-mediated importin-4 knockdown. Transfection efficiencies of the indicated nanocarriers were assessed 24 h post-transfection. Transfection with no treatment control (black), scrambled siRNA (dark gray), or importin-4 siRNA (light gray). Each data point represents the mean ± standard deviation for a total of at least four separately prepared samples. * Indicates a statistically significant difference from the scrambled siRNA treatment control ($p < 0.05$).

1.5.2.3 Post-Mitotic Nanocarrier Interaction with Chromatin and Importin-4 Knockdown

Because importin-4 plays an instrumental role in post-mitotic re-deposition of the H3 protein in chromatin, importin-4 might also function to deposit the H3-targeted nanocarriers on chromatin in a similar manner, leading to improved nuclear retention. Accordingly, the extent to which these nanocarriers bound to DAPI-stained chromatin post-mitosis, and whether this effect required importin-4, was determined using a combination of super resolution microscopy and structured illumination microscopy (Figure 1.12) as previously described in the literature.[101] 65% of the H3-targeted nanocarriers interacted with chromatin following mitosis. This interaction was further explored by performing the same experiments after siRNA-mediated silencing of importin-4. There was an approximately 75% decrease in chromatin binding by the

H3-targeted nanocarriers when importin-4 was inhibited (Figure 1.12c), consistent with confocal microscopy analyses at 12 h post-transfection.[80] From super resolution images, it was also evident that the majority of the nanocarriers did not even enter the nucleus when importin-4 was reduced, and that the nanocarriers were instead trapped around the nuclear periphery. Those nanocarriers that did enter the nucleus did not interact with chromatin to a measurable extent when importin-4 was inhibited (Figure 1.12b). Therefore, these data corroborate the finding that importin-4 was necessary for the H3-targeted nanocarriers to enter the nucleus, and the data also indicated that importin-4 drives interactions with chromatin to affect nuclear retention.

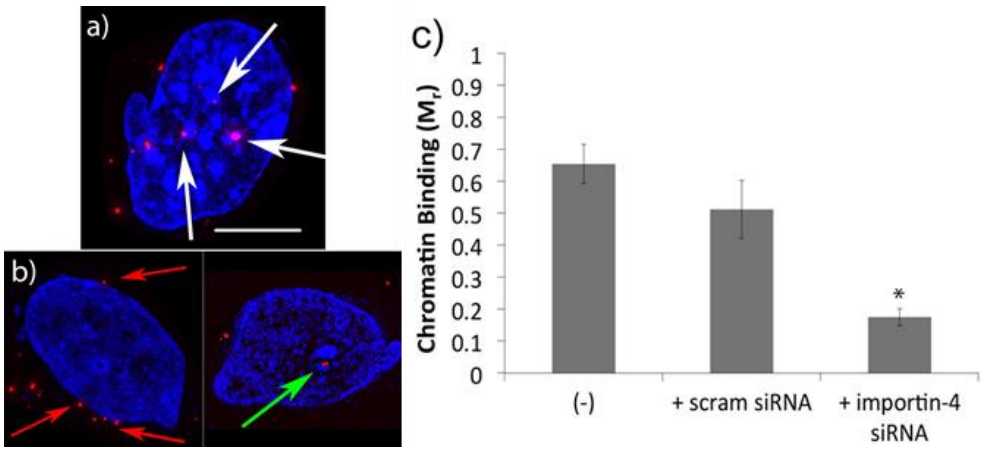

Figure 1.12: Representative images of chromatin (blue) binding by the H3-targeted nanocarriers (red) when cells were treated with scrambled importin-4 siRNA (a), or with importin-4 siRNA (b). The scale bar (shown in panel a) = 5 μm. White arrows indicate chromatin binding, green arrows represent the lack of chromatin binding by nuclear nanocarriers when importin-4 was inhibited, and red arrows indicate those nanocarriers that remained largely in the nuclear periphery with importin-4 inhibition. (c) Quantification of chromatin binding using Manders' coefficient at 12 h post-transfection. Ten images containing 8–10 cells per image were analyzed for each sample.

1.5.3 Summary of H3-Targeted Nanocarrier Intracellular Trafficking and Nuclear Delivery

Our group determined that H3 targeting peptides enhance the utilization of caveolar endocytic routes and improve transfection by transferring nanocarriers through retrograde vesicular compartments that localize to the ER and nucleus, similar to the trafficking behavior of several types of native proteins[102] and pathogens.[79] These studies showed that the transport behavior of the H3-targeted nanocarriers was conferred in part by interactions with native histone H3 effectors, such as H3K4 MT subunits involved in regulating vesicular transport between late endosomes and the Golgi[79] (Figure 1.13). These findings motivated analyses to determine whether other H3 effectors, such as the H3 importins, might be involved in shuttling H3-targeted nanocarriers into the nucleus during mitosis. These investigations revealed that H3-targeted nanocarriers subsequently enter the nucleus during post-mitotic redistribution of ER membranes, utilizing the natural import machinery of histone protein chaperones[80] (Figure 1.13). These importins drive nanocarrier interactions with chromatin to enhance nuclear retention post-mitosis. In contrast to H3-targeted nanocarriers, untargeted nanocarriers (PEI and sH3) were trafficked through a different pathway toward the nucleus, exhibiting significantly decreased localization with H3K4 MT subunits and importin-4. These fundamentally different results strongly indicate that cellular interactions are occurring sequence-specifically with the H3-targeted nanocarriers during intracellular trafficking and nuclear import.

Collectively, these findings demonstrate the need for a fundamentally different approach to non-viral nucleic acid nanocarrier design, one that promotes efficient utilization of native intracellular trafficking and nuclear import pathways to guide delivery and expression, thereby enhancing therapeutic efficacy. Additionally, the

finding that mitosis plays an essential role in enhancing both nuclear delivery and retention, highlights the utility H3-targeting to potentially reduce the amount of DNA dosing required in gene therapy applications involving actively dividing cells.

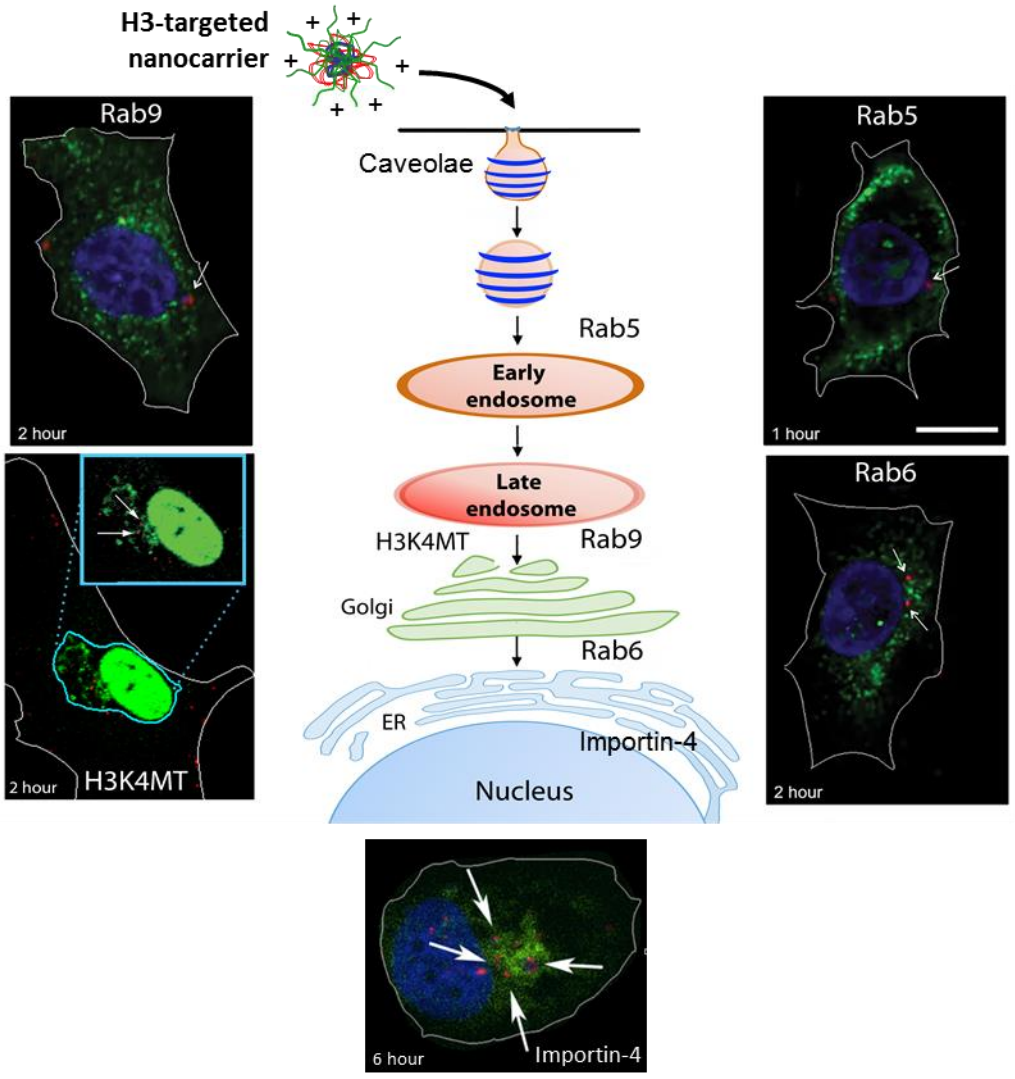

Figure 1.13: Uptake, trafficking, and nuclear import mechanisms for H3-targeted nanocarriers. Key regulators include Rab5, Rab9/H3K4 MTs, Rab6, importin-4, and ER membrane-mediated nuclear entry during mitosis.

1.6 H3-Targeting for Regenerative Medicine Applications: Fracture Healing/Bone Regeneration

A specific application that would greatly benefit from H3-targeted gene transfer is in the field of bone regeneration following traumatic injury, which affect approximately six million people annually in the United States alone.[103-105] Surgically invasive orthopedic grafting procedures are the current gold standard for treating these types of ailments.[105] However, limitations in grafting approaches[106] and the absence of effective methods to manage large segmental bone defects[107] emphasize the need for alternative treatment strategies. A variety of osteogenic growth factors have been investigated for their bone regenerative capacity. Among these, bone morphogenetic proteins (BMPs) have shown great promise in stimulating natural bone growth in animal models;[106, 108] BMP-2 and BMP-7 already FDA-approved for treating severe orthopedic defects. However, numerous issues with recombinant growth factors including poor stability, suboptimal delivery vehicles, and the need for repeated dosing at high concentrations have highlighted gene therapy as a compelling alternative treatment strategy.[106, 107, 109] Gene manipulations offer a proven capacity for controlled *in situ* production of stable nascent growth factors at their native concentrations, capable of initiating bone repair cascades.[106, 109]

Figure 1.14 details the key steps involved in the initial stages of fracture healing, where effective application of gene transfer strategies could potentially augment bone repair. Following a traumatic bone injury, the inflammatory process begins and a hematoma forms around the fracture gap.[110] This is invaded by a wide variety of cell types including fibroblasts, macrophages, and most notably mesenchymal stem cells (MSCs). Following inflammation, MSCs begin to proliferate and differentiate in and around the fracture gap. Chondrogenic differentiation is active

within the fracture gap (Figure 1.14), where mature chondrocytes produce and secrete an intermediary cartilage matrix to replace the hematoma. This ultimately links the two ends of the fracture together by a soft callus.[111] Distal to the fracture gap capillary growth into the soft callus is active alongside osteogenic differentiation. Mature osteoblasts invade the soft callus, converting it to rigid calcified tissue.[110] In this manner the bone fragments are united once again by new bone. This process, known as endochondral ossification, continues until the initial woven bone is remodeled to fully mature lamellar bone.[112]

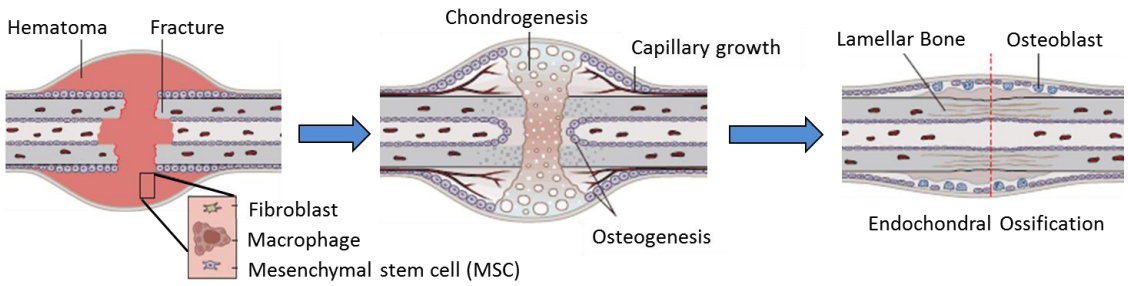

Figure 1.14: Schematic of the initial stages of bone healing subsequent to fracture formation. Figure adapted from: K Ito and SM Perren, The biology of fracture healing. https://www2.aofoundation.org/wps/portal /surgerymobile?contentUrl=/srg/popup/further_reading/PFxM2/12_33_biol_fx_heal.jsp&soloState=precomp&title=&. (Accessed Oct. 12, 2017), AO Foundation Publishing, Open Access.

Formation and calcification of the soft callus are regulated by a wide variety of growth factor signals, most notably BMPs, which direct the early-stage osteogenic and chondrogenic differentiation of proliferating MSCs within the fracture gap.[106] Utilizing a localized gene transfer approach to deliver BMP growth factor genes to proliferating MSCs within the fracture gap possesses enormous therapeutic potential

to increase bone formation, accelerate fracture repair, and improve the bone healing response. Additionally, the actively proliferating cells within the fracture gap represent ideal targets for H3-targeted gene transfer approaches to enhance the nuclear delivery, retention, and expression of native osteogenic BMPs, thereby reducing growth factor dosing, and enhancing MSC differentiation.

1.7 Controlling Cellular Interactions Using a Materials Design Approach

The elucidation of altered intracellular trafficking[79] and nuclear delivery properties[80] associated with H3-targeted nanocarriers have highlighted the importance of designing nucleic acid delivery vehicles that can interact favorably with the cellular environment in order to advance the field of non-viral gene therapy. By combining these fundamental insights into native histone biology with controlled materials design approaches, novel nucleic acid delivery systems may be created that provide improved control over nanocarrier interactions with the cellular environment to further enhance delivery and release at the therapeutic site of action. A successful material synthesis strategy will focus on improving the display of the H3 tail peptide within the final formulated nanocarrier, mimicking its native presentation within nucleosomes (Figure 1.3), in order to improve interactions with native histone effectors. Additionally, the design must be multifaceted and highly tunable, providing control over interactions with these histone effectors as well as controllable interactions with the DNA to be delivered.

1.7.1 Gold Nanoparticles as Scaffolds for Histone-Mimetic Gene Transfer

An ideal synthetic candidate that provides a robust foundation for the desired biomimetic and controllable display of the H3 NLS is the gold nanoparticle (AuNP).

AuNPs possess a number of properties that make them perfect candidates for delivery applications. The AuNPs themselves are inert, non-toxic, and highly biocompatible.[113] In addition, multiple synthetic routes have been established to easily fabricate AuNPs across a wide range of sizes (1-150 nm) with well controlled dispersity[114] and a high surface area-to-volume ratio for dense loading capacities.[115] Most importantly, the AuNP surface is highly tunable and amenable to different covalent and non-covalent modifications.[116, 117] This ability tailor the surface has made AuNPs effective scaffolds for displaying a wide range of targeting ligands and therapeutic materials for drug delivery applications.[118] An example of the multitude of surface structures commonly employed for drug delivery applications is shown in Figure 1.15.

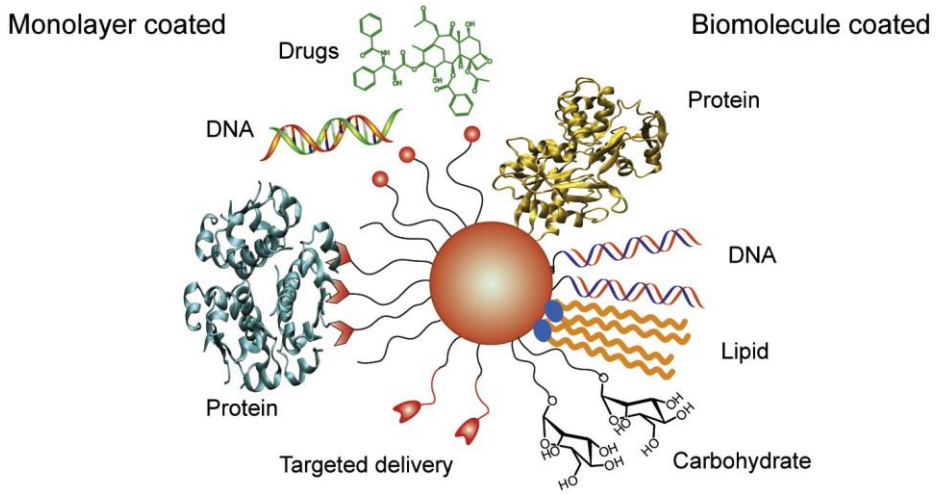

Figure 1.15: Schematic presentation of AuNP surface structures commonly employed in drug delivery applications. Figure adapted with permission from S Rana, A Bajaj, R Mout, and VM Rotello, Monolayer coated gold nanoparticles for delivery applications. *Adv. Drug Del Revs.* 64, 200-16 (2012).[118] Copyright 2011, Rights reserved by Elsevier B.V.

Surface-functionalized AuNPs have been used in a wide variety of nucleic acid delivery applications.[119] These modified AuNPs offer significantly enhanced stability in association with nucleic acids,[120-122] and can initiate cellular entry with unprecedented efficiency.[123-125] Preparing AuNPs as gene delivery nanocarriers typically involves surface functionalization with positively charged ligands, including amino acids, cationic peptides, or primary amine-containing molecules. This promotes efficient nucleic acid condensation and can effectively prevent enzymatic degradation.[122] Tuning the density of positively charged ligands on the surface can effectively tune interactions with the nucleic acid to be delivered, ultimately effecting overall transfection efficiency.[123] In a related fashion, for AuNPs functionalized with specific ligands for targeted delivery applications, the density of targeting ligand displayed on the surface directly correlates with the amount of AuNPs delivered to the therapeutic target.[126]

Well-established synthetic techniques to generate polycationic AuNPs coupled to H3 tail motifs can be utilized to create novel nanocarrier structures that effectively mimic the native presentation of histone sequences in the nucleosome (Figure 1.16). Dual display of these ligands will theoretically endow these nanocarriers with the capacity to stably bind as well as controllably deliver DNA through enhanced interactions with native histone effectors. In addition, the tailorability of the AuNP surface provides an ideal platform easily manipulating both surface charge and H3 tail display density, allowing DNA binding, cellular interactions, and intracellular transcription to be simultaneously optimized. Possessing the ability to recapitulate and control native interactions with histone effectors represents a unique and

significant advance in nanocarrier design, addressing the crucial barriers to effective non-viral DNA delivery described in the preceding sections.

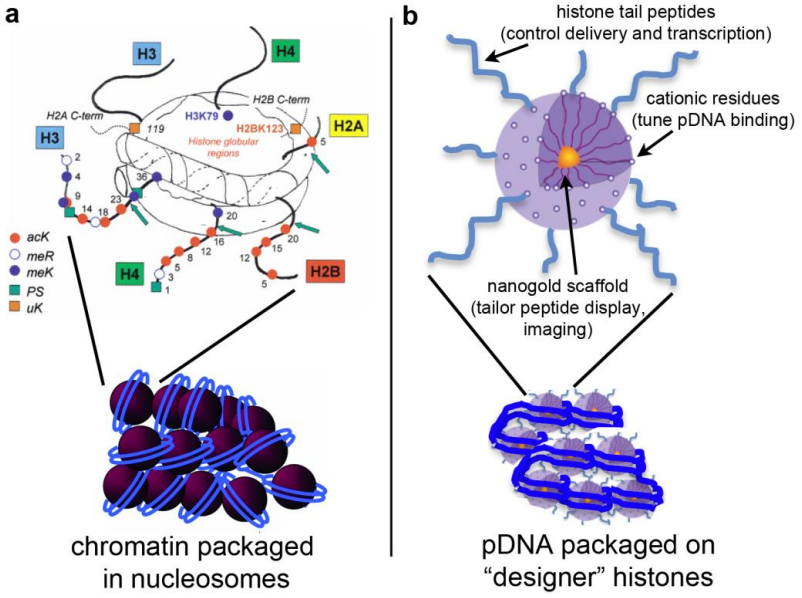

Figure 1.16: Schematic of (a) chromosomal DNA binding the histone octamer to form a nucleosome[66, 67] and (b) nanoscaffolds mimicking the native presentation of histone tail peptides within the histone octamer for improved/controllable DNA binding stability and improved/controllable interactions with native histone effectors. Image in (b) adapted and modified with permission from PS Ghosh, JK Kim, G Han, NS Forbes, and VM Rotello, Efficient gene delivery vectors by tuning the surface charge density of amino acid-functionalized gold nanoparticles, *ACS Nano*, 2(11) 2213-18 (2008).[120] Copyright 2008, Rights reserved by the American Chemical Society.

1.8 Dissertation Synopsis

The work described in this dissertation was aimed toward (1) understanding how histone-targeted gene transfer could be utilized in regenerative medicine applications and (2) designing a novel and ordered nanoscaffold delivery system that

can be utilized to control nanocarrier interactions with both the DNA to be delivered and histone effectors in order to more effectively harness native intracellular trafficking and nuclear import pathways to further improve DNA delivery. The finding that H3-targeted nanocarriers provides enhanced nuclear delivery and retention during mitosis highlights the role they may play in improving the delivery of growth factor genes to actively dividing cells present during native tissue regeneration. In addition, the fundamental insights gained from histone-targeted nanocarrier trafficking and nuclear import provide a strong foundation for designing a novel delivery system to effectively control these cellular interactions, thereby further improving gene transfer. Combined, the work in this dissertation represents a significant step forward in histone-based nucleic acid delivery design and application, providing a better understanding of how synthetic approaches and be utilized to advance the field of non-viral gene therapy overall and open additional pathways to clinical translation in regenerative medicine.

Chapter 2 provides an introduction to the synthetic techniques employed to generate both the AuNPs and peptide ligands utilized to create the novel biomimetic nanocarriers discussed in this dissertation (termed histone-mimetic nanoscaffolds). The characterization techniques utilized to examine the structure and functionalization of these histone-mimetic nanoscaffolds are also described in detail. Care was taken in the selection of synthesis and characterization techniques to ensure that the final histone-mimetic nanoscaffolds were generated in high efficiency, high purity, and low dispersity, suitable for drug delivery applications. Chapter 3 explores the utility of using H3-targeted gene transfer as a means to significantly reduce growth factor dosing for bone regenerative applications. H3-targeting was demonstrated *in vitro* to

augment stem cell chondrogenic differentiation more substantially than equivalent amounts of topically applied recombinant growth factor protein. Chapter 4 details how the synthetic and characterization concepts described in Chapter 2 were utilized to create a small library of tunable histone-mimetic nanoscaffolds, each functionalized with varying degrees of H3 tail ligand. Tuning the ligand surface display chemistry was shown to effectively tune interactions with native histone effectors, highlighting their potential in controlling cellular interactions for enhanced gene transfer. In particular, the histone-mimetic nanoscaffolds exhibited enhanced stability when bound to pDNA and were able to maintain maximum transfection efficiency in the presence of physiological amounts of heparin. Chapter 5 outlines how all of the insights gained from the previous chapters provide an opportunity of further translating histone-targeted gene transfer into animal models (*in vivo*) of tissue regeneration. Suggestions for future work focus on further refining the surface chemistry of the histone-mimetic nanoscaffolds to provide enhanced control over cellular interactions, nuclear delivery, and pDNA binding stability under physiological conditions. Furthermore, the idea of enhanced nuclear retention following H3-targeted gene transfer is explored as a means to potentially provide better control over the duration of growth factor localization and activity for regenerative medicine applications.

REFERENCES

1. Sheridan, C., Gene therapy finds its niche. Nature Biotechnology 2011, 29 (2), 121-128.

2. Ratko, T. A.; Cummings, J. P.; Blebea, J.; Matuszewski, K. A., Clinical gene therapy for nonmalignant disease. American Journal of Medicine 2003, 115 (7), 560-569.

3. Pack, D. W.; Hoffman, A. S.; Pun, S.; Stayton, P. S., Design and development of polymers for gene delivery. Nature Reviews Drug Discovery 2005, 4 (7), 581-593.

4. Burke, P. A.; Pun, S. H.; Reineke, T. M., Advancing Polymeric Delivery Systems Amidst a Nucleic Acid Therapy Renaissance. Acs Macro Letters 2013, 2 (10), 928-934.

5. Sridharan, K.; Gogtay, N. J., Therapeutic nucleic acids: current clinical status. British Journal of Clinical Pharmacology 2016, 82 (3), 659-672.

6. Ruiz, M. M.; Regueiro, J. R., New tools in regenerative medicine: Gene Therapy. In Stem Cell Transplantation, LopezLarrea, C.; LopezVazquez, A.; SuarezAlvarez, B., Eds. Springer-Verlag Berlin: Berlin, 2012; Vol. 741, pp 254-275.

7. Ginn, S. L.; Alexander, I. E.; Edelstein, M. L.; Abedi, M. R.; Wixon, J., Gene therapy clinical trials worldwide to 2012 an update. Journal of Gene Medicine 2013, 15 (2), 65-77.

8. Yla-Herttuala, S., Endgame: Glybera Finally Recommended for Approval as the First Gene Therapy Drug in the European Union. Molecular Therapy 2012, 20 (10), 1831-1832.

9. FDA News Release: FDA Approval Brings First Gene Therapy to the United States. *FDA News and Events.* 2017.

10. Yin, H.; Kanasty, R. L.; Eltoukhy, A. A.; Vegas, A. J.; Dorkin, J. R.; Anderson, D. G., Non-viral vectors for gene-based therapy. Nature Reviews Genetics 2014, 15 (8), 541-555.

11. Al-Dosari, M. S.; Gao, X., Nonviral Gene Delivery: Principle, Limitations, and Recent Progress. Aaps Journal 2009, 11 (4), 671-681.

12. Mingozzi, F.; High, K. A., Therapeutic in vivo gene transfer for genetic disease using AAV: progress and challenges. Nature Reviews Genetics 2011, 12 (5), 341-355.

13. Yi, Y.; Hahm, S. H.; Lee, K. H., Retroviral gene therapy: Safety issues and possible solutions. Current Gene Therapy 2005, 5 (1), 25-35.

14. Vannucci, L.; Lai, M.; Chiuppesi, F.; Ceccherini-Nelli, L.; Pistello, M., Viral vectors: a look back and ahead on gene transfer technology. New Microbiologica 2013, 36 (1), 1-22.

15. Munsell, E. V.; Ross, N. L.; Sullivan, M. O., Journey to the Center of the Cell: Current Nanocarrier Design Strategies Targeting Biopharmaceuticals to the Cytoplasm and Nucleus. Current Pharmaceutical Design 2016, 22 (9), 1227-1244.

16. Davis, M. E., The First Targeted Delivery of siRNA in Humans via a Self-Assembling, Cyclodextrin Polymer-Based Nanoparticle: From Concept to Clinic. Molecular Pharmaceutics 2009, 6 (3), 659-668.

17. Whitehead, K. A.; Langer, R.; Anderson, D. G., Knocking down barriers: advances in siRNA delivery. Nature Reviews Drug Discovery 2009, 8 (2), 129-138.

18. Jones, C. H.; Chen, C. K.; Ravikrishnan, A.; Rane, S.; Pfeifer, B. A., Overcoming Nonviral Gene Delivery Barriers: Perspective and Future. Molecular Pharmaceutics 2013, 10 (11), 4082-4098.

19. Khalil, I. A.; Kogure, K.; Akita, H.; Harashima, H., Uptake pathways and subsequent intracellular trafficking in nonviral gene delivery. Pharmacological Reviews 2006, 58 (1), 32-45.

20. Sahay, G.; Alakhova, D. Y.; Kabanov, A. V., Endocytosis of nanomedicines. Journal of Controlled Release 2010, 145 (3), 182-195.

21. Hillaireau, H.; Couvreur, P., Nanocarriers' entry into the cell: relevance to drug delivery. Cellular and Molecular Life Sciences 2009, 66 (17), 2873-2896.

22. Hansen, C. G.; Nichols, B. J., Molecular mechanisms of clathrin-independent endocytosis. Journal of Cell Science 2009, 122 (11), 1713-1721.

23. Nguyen, J.; Szoka, F. C., Nucleic Acid Delivery: The Missing Pieces of the Puzzle? Accounts of Chemical Research 2012, 45 (7), 1153-1162.

24. Mukherjee, S.; Ghosh, R. N.; Maxfield, F. R., Endocytosis. Physiological Reviews 1997, 77 (3), 759-803.

25. Gilleron, J.; Querbes, W.; Zeigerer, A.; Borodovsky, A.; Marsico, G.; Schubert, U.; Manygoats, K.; Seifert, S.; Andree, C.; Stoter, M.; Epstein-Barash, H.; Zhang, L. G.; Koteliansky, V.; Fitzgerald, K.; Fava, E.; Bickle, M.; Kalaidzidis, Y.; Akinc, A.; Maier, M.; Zerial, M., Image-based analysis of lipid nanoparticle-mediated siRNA delivery, intracellular trafficking and endosomal escape. Nature Biotechnology 2013, 31 (7), 638-U102.

26. Suh, J.; An, Y.; Tang, B. C.; Dempsey, C.; Huang, F. R.; Hanes, J., Real-time gene delivery vector tracking in the endo-lysosomal pathway of live cells. Microscopy Research and Technique 2012, 75 (5), 691-697.

27. Won, Y. Y.; Sharma, R.; Konieczny, S. F., Missing pieces in understanding the intracellular trafficking of polycation/DNA complexes. Journal of Controlled Release 2009, 139 (2), 88-93.

28. Behr, J. P., The proton sponge: A trick to enter cells the viruses did not exploit. Chimia 1997, 51 (1-2), 34-36.

29. Dauty, E.; Verkman, A. S., Actin cytoskeleton as the principal determinant of size-dependent DNA mobility in cytoplasm. Journal of Biological Chemistry 2005, 280 (9), 7823-7828.

30. Ondrej, V.; Lukasova, E.; Krejci, J.; Kozubek, S., Intranuclear trafficking of plasmid DNA is mediated by nuclear polymeric proteins lamins and actin. Acta Biochimica Polonica 2008, 55 (2), 307-315.

31. Kulkarni, R. P.; Mishra, S.; Fraser, S. E.; Davis, M. E., Single cell kinetics of intracellular, nonviral, nucleic acid delivery vehicle acidification and trafficking. Bioconjugate Chemistry 2005, 16 (4), 986-994.

32. Forrest, M. L.; Meister, G. E.; Koerber, J. T.; Pack, D. W., Partial acetylation of polyethylenimine enhances in vitro gene delivery. Pharmaceutical Research 2004, 21 (2), 365-371.

33. Lukacs, G. L.; Haggie, P.; Seksek, O.; Lechardeur, D.; Freedman, N.; Verkman, A. S., Size-dependent DNA mobility in cytoplasm and nucleus. Journal of Biological Chemistry 2000, 275 (3), 1625-1629.

34. Alberts, B., Molecular Biology of the Cell, Garland Science: New York. 2002.

35. Rogers, S. L.; Gelfand, V. I., Membrane trafficking, organelle transport, and the cytoskeleton. Current Opinion in Cell Biology 2000, 12 (1), 57-62.

36. Pouton, C. W.; Wagstaff, K. M.; Roth, D. M.; Moseley, G. W.; Jans, D. A., Targeted delivery to the nucleus. Advanced Drug Delivery Reviews 2007, 59 (8), 698-717.

37. Whittaker, G. R.; Kann, M.; Helenius, A., Viral entry into the nucleus. Annual Review of Cell and Developmental Biology 2000, 16, 627-651.

38. Whittaker, G. R., Virus nuclear import. Advanced Drug Delivery Reviews 2003, 55 (6), 733-747.

39. Dohner, K.; Nagel, C. H.; Sodeik, B., Viral stop-and-go along microtubules: taking a ride with dynein and kinesins. Trends in Microbiology 2005, 13 (7), 320-327.

40. Greber, U. F.; Way, M., A superhighway to virus infection. Cell 2006, 124 (4), 741-754.

41. Su, Y.; Qiao, W. T.; Guo, T. T.; Tan, J. A.; Li, Z.; Chen, Y.; Li, X.; Li, Y.; Zhou, J.; Chen, Q. M., Microtubule-dependent retrograde transport of bovine immunodeficiency virus. Cellular Microbiology 2010, 12 (8), 1098-1107.

42. Lehmann, M.; Milev, M. P.; Abrahamyan, L.; Yao, X. J.; Pante, N.; Mouland, A. J., Intracellular Transport of Human Immunodeficiency Virus Type 1 Genomic RNA and Viral Production Are Dependent on Dynein Motor Function and Late Endosome Positioning. Journal of Biological Chemistry 2009, 284 (21), 14572-14585.

43. Amorim, M. J.; Bruce, E. A.; Read, E. K. C.; Foeglein, A.; Mahen, R.; Stuart, A. D.; Digard, P., A Rab11-and Microtubule-Dependent Mechanism for Cytoplasmic Transport of Influenza A Virus Viral RNA. Journal of Virology 2011, 85 (9), 4143-4156.

44. Terry, L. J.; Shows, E. B.; Wente, S. R., Crossing the nuclear envelope: Hierarchical regulation of nucleocytoplasmic transport. Science 2007, 318 (5855), 1412-1416.

45. Grossman, E.; Medalia, O.; Zwerger, M., Functional architecture of the nuclear pore complex. Annu Rev Biophys 2012, 41, 557-84.

46. Pante, N.; Kann, M., Nuclear pore complex is able to transport macromolecules with diameters of about 39 nm. Mol Biol Cell 2002, 13 (2), 425-34.

47. De Robertis, E. M.; Longthorne, R. F.; Gurdon, J. B., Intracellular migration of nuclear proteins in Xenopus oocytes. Nature 1978, 272 (5650), 254-6.

48. Dingwall, C.; Sharnick, S. V.; Laskey, R. A., A polypeptide domain that specifies migration of nucleoplasmin into the nucleus. Cell 1982, 30 (2), 449-58.

49. Moroianu, J.; Blobel, G.; Radu, A., Previously identified protein of uncertain function is karyopherin alpha and together with karyopherin beta docks import substrate at nuclear pore complexes. Proc Natl Acad Sci U S A 1995, 92 (6), 2008-11.

50. Marsh, M.; Helenius, A., Virus entry: Open sesame. Cell 2006, 124 (4), 729-740.

51. Schmitz, A.; Herrgen, H.; Winkeler, A.; Herzog, V., Cholera toxin is exported from microsomes by the Sec61p complex. Journal of Cell Biology 2000, 148 (6), 1203-1212.

52. Sandvig, K.; van Deurs, B., Transport of protein toxins into cells: pathways used by ricin, cholera toxin and Shiga toxin. Febs Letters 2002, 529 (1), 49-53.

53. Newcomb, W. W.; Booy, F. P.; Brown, J. C., Uncoating the herpes simplex virus genome. Journal of Molecular Biology 2007, 370 (4), 633-642.

54. Ojala, P. M.; Sodeik, B.; Ebersold, M. W.; Kutay, U.; Helenius, A., Herpes simplex virus type 1 entry into host cells: Reconstitution of capsid binding and uncoating at the nuclear pore complex in vitro. Molecular and Cellular Biology 2000, 20 (13), 4922-4931.

55. Anderson, D. J.; Hetzer, M. W., Shaping the endoplasmic reticulum into the nuclear envelope. Journal of Cell Science 2008, 121 (2), 137-142.

56. Goff, S. P., Host factors exploited by retroviruses. Nature Reviews Microbiology 2007, 5 (4), 253-263.

57. Pyeon, D.; Pearce, S. M.; Lank, S. M.; Ahlquist, P.; Lambert, P. F., Establishment of Human Papillomavirus Infection Requires Cell Cycle Progression. Plos Pathogens 2009, 5 (2), 9.

58. Brunner, S.; Sauer, T.; Carotta, S.; Cotten, M.; Saltik, M.; Wagner, E., Cell cycle dependence of gene transfer by lipoplex polyplex and recombinant adenovirus. Gene Therapy 2000, 7 (5), 401-407.

59. Grosse, S.; Thevenot, G.; Monsigny, M.; Fajac, I., Which mechanism for nuclear import of plasmid DNA complexed with polyethylenimine derivatives? J Gene Med 2006, 8 (7), 845-51.

60. Larsen, J. D.; Ross, N. L.; Sullivan, M. O., Requirements for the nuclear entry of polyplexes and nanoparticles during mitosis. J Gene Med 2012, 14 (9-10), 580-9.

61. Wagstaff, K. M.; Glover, D. J.; Tremethick, D. J.; Jans, D. A., Histone-mediated transduction as an efficient means for gene delivery. Molecular Therapy 2007, 15 (4), 721-731.

62. Kamiya, H.; Goto, H.; Kanda, G.; Yamada, Y.; Harashima, H., Transgene expression efficiency from plasmid DNA delivered as a complex with histone H3. International Journal of Pharmaceutics 2010, 392 (1-2), 249-253.

63. Balicki, D.; Putnam, C. D.; Scaria, P. V.; Beutler, E., Structure and function correlation in histone H2A peptide-mediated gene transfer. Proceedings of the National Academy of Sciences of the United States of America 2002, 99 (11), 7467-7471.

64. Fritz, J. D.; Herweijer, H.; Zhang, G. F.; Wolff, J. A., Gene transfer into mammalian cells using histone-condensed plasmid DNA. Human Gene Therapy 1996, 7 (12), 1395-1404.

65. Strahl, B. D.; Allis, C. D., The language of covalent histone modifications. Nature 2000, 403 (6765), 41-45.

66. Wagstaff, K. M.; Jans, D. A., Nucleocytoplasmic transport of DNA: enhancing non-viral gene transfer. Biochemical Journal 2007, 406, 185-202.

67. Turner, B. M., Cellular memory and the histone code. Cell 2002, 111 (3), 285-291.

68. Larsen, J. D.; Reilly, M. J.; Sullivan, M. O., Using the Epigenetic Code To Promote the Unpackaging and Transcriptional Activation of DNA Polyplexes for Gene Delivery. Molecular Pharmaceutics 2012, 9 (5), 1041-1051.

69. Ruthenburg, A. J.; Allis, C. D.; Wysocka, J., Methylation of lysine 4 on histone H3: Intricacy of writing and reading a single epigenetic mark. Molecular Cell 2007, 25 (1), 15-30.

70. Saksouk, N.; Avvakumov, N.; Champagne, K. S.; Hung, T.; Doyon, Y.; Cayrou, C.; Paquet, E.; Ullah, M.; Landry, A. J.; Cote, V.; Yang, X. J.; Gozani, O.; Kutateladze, T. G.; Cote, J., HBO1 HAT Complexes Target Chromatin throughout Gene Coding Regions via Multiple PHD Finger Interactions with Histone H3 Tail. Molecular Cell 2009, 33 (2), 257-265.

71. Mizuguchi, G.; Tsukiyama, T.; Wisniewski, J.; Wu, C., Role of nucleosome remodeling factor NURF in transcriptional activation of chromatin. Molecular Cell 1997, 1 (1), 141-150.

72. Campos, E. I.; Fillingham, J.; Li, G. H.; Zheng, H. Y.; Voigt, P.; Kuo, W. H. W.; Seepany, H.; Gao, Z. H.; Day, L. A.; Greenblatt, J. F.; Reinberg, D., The program for processing newly synthesized histones H3.1 and H4. Nature Structural & Molecular Biology 2010, 17 (11), 1343-U201.

73. Jakel, S.; Mingot, J. M.; Schwarzmaier, P.; Hartmann, E.; Gorlich, D., Importins fulfil a dual function as nuclear import receptors and cytoplasmic chaperones for exposed basic domains. Embo Journal 2002, 21 (3), 377-386.

74. Alvarez, F.; Munoz, F.; Schilcher, P.; Imhof, A.; Almouzni, G.; Loyola, A., Sequential Establishment of Marks on Soluble Histones H3 and H4. Journal of Biological Chemistry 2011, 286 (20), 17714-17721.

75. Miyauchi, Y.; Michigami, T.; Sakaguchi, N.; Sekimoto, T.; Yoneda, Y.; Pike, J. W.; Yamagata, M.; Ozono, K., Importin 4 is responsible for ligand-independent nuclear translocation of vitamin D receptor. Journal of Biological Chemistry 2005, 280 (49), 40901-40908.

76. Xu, Z. J.; Gong, Q.; Xia, B.; Groves, B.; Zimmermann, M.; Mugler, C.; Mu, D. Z.; Matsumoto, B.; Seaman, M.; Ma, D., A role of histone H3 lysine 4 methyltransferase components in endosomal trafficking. Journal of Cell Biology 2009, 186 (3), 343-353.

77. Wu, C. C.; MacCoss, M. J.; Mardones, G.; Finnigan, C.; Mogelsvang, S.; Yates, J. R.; Howell, K. E., Organellar proteomics reveals Golgi arginine dimethylation. Molecular Biology of the Cell 2004, 15 (6), 2907-2919.

78. Reilly, M. J.; Larsen, J. D.; Sullivan, M. O., Histone H3 tail peptides and poly(ethylenimine) have synergistic effects for gene delivery. Mol Pharm 2012, 9 (5), 1031-40.

79. Ross, N. L.; Munsell, E. V.; Sabanayagam, C.; Sullivan, M. O., Histone-targeted Polyplexes Avoid Endosomal Escape and Enter the Nucleus During Postmitotic Redistribution of ER Membranes. Molecular Therapy-Nucleic Acids 2015, 4, 13.

80. Ross, N. L.; Sullivan, M. O., Importin-4 Regulates Gene Delivery by Enhancing Nuclear Retention and Chromatin Deposition by Polyplexes. Molecular Pharmaceutics 2015, 12 (12), 4488-4497.

81. Stenmark, H., Rab GTPases as coordinators of vesicle traffic. Nature Reviews Molecular Cell Biology 2009, 10 (8), 513-525.

82. Choudhury, A.; Dominguez, M.; Puri, V.; Sharma, D. K.; Narita, K.; Wheatley, C. L.; Marks, D. L.; Pagano, R. E., Rab proteins mediate Golgi transport of caveola-internalized glycosphingolipids and correct lipid trafficking in Niemann-Pick C cells. Journal of Clinical Investigation 2002, 109 (12), 1541-1550.

83. Rink, J.; Ghigo, E.; Kalaidzidis, Y.; Zerial, M., Rab conversion as a mechanism of progression from early to late endosomes. Cell 2005, 122 (5), 735-749.

84. Reilly, M. J.; Larsen, J. D.; Sullivan, M. O., Polyplexes Traffic through Caveolae to the Golgi and Endoplasmic Reticulum en Route to the Nucleus. Molecular Pharmaceutics 2012, 9 (5), 1280-1290.

85. Vanlandingham, P. A.; Ceresa, B. P., Rab7 Regulates Late Endocytic Trafficking Downstream of Multivesicular Body Biogenesis and Cargo Sequestration. Journal of Biological Chemistry 2009, 284 (18), 12110-12124.

86. Lombardi, D.; Soldati, T.; Riederer, M. A.; Goda, Y.; Zerial, M.; Pfeffer, S. R., Rab9 functions in transport between late endosomes and the trans golgi network. Embo Journal 1993, 12 (2), 677-682.

87. Buczynski, G.; Bush, J.; Zhang, L. Y.; RodriguezParis, J.; Cardelli, J., Evidence for a recycling role for Rab7 in regulating a late step in endocytosis and in retention of lysosomal enzymes in Dictyostelium discoideum. Molecular Biology of the Cell 1997, 8 (7), 1343-1360.

88. Ullrich, O.; Reinsch, S.; Urbe, S.; Zerial, M.; Parton, R. G., Rab11 regulates recycling through the pericentriolar recycling endosome. Journal of Cell Biology 1996, 135 (4), 913-924.

89. White, J.; Johannes, L.; Mallard, F.; Girod, A.; Grill, S.; Reinsch, S.; Keller, P.; Tzschaschel, B.; Echard, A.; Goud, B.; Stelzer, E. H. K., Rab6 coordinates a novel Golgi to ER retrograde transport pathway in live cells. Journal of Cell Biology 1999, 147 (4), 743-759.

90. Johns, H. L.; Gonzalez-Lopez, C.; Sayers, C. L.; Hollinshead, M.; Elliott, G., Rab6 Dependent Post-Golgi Trafficking of HSV1 Envelope Proteins to Sites of Virus Envelopment. Traffic 2014, 15 (2), 157-178.

91. Ilina, P.; Hyvonen, Z.; Saura, M.; Sandvig, K.; Yliperttula, M.; Ruponen, M., Genetic blockage of endocytic pathways reveals differences in the intracellular processing of non-viral gene delivery systems. Journal of Controlled Release 2012, 163 (3), 385-395.

92. Sandvig, K.; VanDeurs, B., Endocytosis, intracellular transport, and cytotoxic action of shiga toxin and ricin. Physiological Reviews 1996, 76 (4), 949-966.

93. Mallard, F.; Antony, C.; Tenza, D.; Salamero, J.; Goud, B.; Johannes, L., Direct pathway from early/recycling endosomes to the Golgi apparatus revealed through the study of Shiga toxin B-fragment transport. Journal of Cell Biology 1998, 143 (4), 973-990.

94. Pelkmans, L.; Kartenbeck, J.; Helenius, A., Caveolar endocytosis of simian virus 40 reveals a new two-step vesicular-transport pathway to the ER. Nature Cell Biology 2001, 3 (5), 473-483.

95. Vonderheit, A.; Helenius, A., Rab7 associates with early endosomes to mediate sorting and transport of semliki forest virus to late endosomes. Plos Biology 2005, 3 (7), 1225-1238.

96. Cho, Y. W.; Hong, T.; Hong, S.; Guo, H.; Yu, H.; Kim, D.; Guszczynski, T.; Dressler, G. R.; Copeland, T. D.; Kalkum, M.; Ge, K., PTIP associates with MLL3-and MLL4-containing histone H3 lysine 4 methyltransferase complex. Journal of Biological Chemistry 2007, 282 (28), 20395-20406.

97. Hazes, B.; Read, R. J., Accumulating evidence suggests that several AB-toxins subvert the endoplasmic reticulum-associated protein degradation pathway to enter target cells. Biochemistry 1997, 36 (37), 11051-11054.

98. Mosammaparast, N.; Guo, Y. R.; Shabanowitz, J.; Hunt, D. F.; Pemberton, L. F., Pathways mediating the nuclear import of histones H3 and H4 in yeast. Journal of Biological Chemistry 2002, 277 (1), 862-868.

99. Hamiche, A.; Shuaib, M., Chaperoning the histone H3 family. Biochimica Et Biophysica Acta-Gene Regulatory Mechanisms 2012, 1819 (3-4), 230-237.

100. Millili, P. G.; Yin, D. H.; Fan, H. L.; Naik, U. P.; Sullivan, M. O., Formulation of a Peptide Nucleic Acid Based Nucleic Acid Delivery Construct. Bioconjugate Chemistry 2010, 21 (3), 445-455.

101. Schermelleh, L.; Carlton, P. M.; Haase, S.; Shao, L.; Winoto, L.; Kner, P.; Burke, B.; Cardoso, M. C.; Agard, D. A.; Gustafsson, M. G. L.; Leonhardt, H.; Sedat, J. W., Subdiffraction multicolor imaging of the nuclear periphery with 3D structured illumination microscopy. Science 2008, 320 (5881), 1332-1336.

102. Wang, Y. N.; Wang, H. M.; Yamaguchi, H.; Lee, H. J.; Lee, H. H.; Hung, M. C., COPI-mediated retrograde trafficking from the Golgi to the ER regulates EGFR nuclear transport. Biochemical and Biophysical Research Communications 2010, 399 (4), 498-504.

103. Vo, T. N.; Kasper, F. K.; Mikos, A. G., Strategies for controlled delivery of growth factors and cells for bone regeneration. Advanced Drug Delivery Reviews 2012, 64 (12), 1292-1309.

104. Greenwald, A. S.; Boden, S. D.; Goldberg, V. M.; Khan, Y.; Laurencin, C. T.; Rosier, R. N.; Comm Biological, I., Bone-graft substitutes: Facts, fictions, and applications. Journal of Bone and Joint Surgery-American Volume 2001, 83A, 98-103.

105. Laurencin, C.; Khan, Y.; El-Amin, S. F., Bone graft substitutes. Expert Review of Medical Devices 2006, 3 (1), 49-57.

106. Phillips, J. E.; Gersbach, C. A.; Garcia, A. J., Virus-based gene therapy strategies for bone regeneration. Biomaterials 2007, 28 (2), 211-229.

107. Pelled, G.; Ben-Arav, A.; Hock, C.; Reynolds, D. G.; Yazici, C.; Zilberman, Y.; Gazit, Z.; Awad, H.; Gazit, D.; Schwarz, E. M., Direct Gene Therapy for Bone Regeneration: Gene Delivery, Animal Models, and Outcome Measures. Tissue Engineering Part B-Reviews 2010, 16 (1), 13-20.

108. Wozney, J. M., Overview of bone morphogenetic proteins. Spine 2002, 27 (16), S2-S8.

109. Evans, C. H., Gene delivery to bone. Advanced Drug Delivery Reviews 2012, 64 (12), 1331-1340.

110. Marsell, R.; Einhorn, T. A., The biology of fracture healing. Injury-International Journal of the Care of the Injured 2011, 42 (6), 551-555.

111. Einhorn, T. A., The cell and molecular biology of fracture healing. Clinical Orthopaedics and Related Research 1998, (355), S7-S21.

112. McKibbin, B., Biology of fracture healing in long bones. Journal of Bone and Joint Surgery-British Volume 1978, 60 (2), 150-162.

113. Connor, E. E.; Mwamuka, J.; Gole, A.; Murphy, C. J.; Wyatt, M. D., Gold nanoparticles are taken up by human cells but do not cause acute cytotoxicity. Small 2005, 1 (3), 325-327.

114. Daniel, M. C.; Astruc, D., Gold nanoparticles: Assembly, supramolecular chemistry, quantum-size-related properties, and applications toward biology, catalysis, and nanotechnology. Chemical Reviews 2004, 104 (1), 293-346.

115. Love, J. C.; Estroff, L. A.; Kriebel, J. K.; Nuzzo, R. G.; Whitesides, G. M., Self-assembled monolayers of thiolates on metals as a form of nanotechnology. Chemical Reviews 2005, 105 (4), 1103-1169.

116. Ghosh, P.; Han, G.; De, M.; Kim, C. K.; Rotello, V. M., Gold nanoparticles in delivery applications. Advanced Drug Delivery Reviews 2008, 60 (11), 1307-1315.

117. Kim, C. K.; Ghosh, P.; Rotello, V. M., Multimodal drug delivery using gold nanoparticles. Nanoscale 2009, 1 (1), 61-67.

118. Rana, S.; Bajaj, A.; Mout, R.; Rotello, V. M., Monolayer coated gold nanoparticles for delivery applications. Advanced Drug Delivery Reviews 2012, 64 (2), 200-216.

119. Loh, X. J.; Lee, T. C.; Dou, Q. Q.; Deen, G. R., Utilising inorganic nanocarriers for gene delivery. Biomaterials Science 2016, 4 (1), 70-86.

120. Ghosh, P. S.; Kim, C. K.; Han, G.; Forbes, N. S.; Rotello, V. M., Efficient Gene Delivery Vectors by Tuning the Surface Charge Density of Amino Acid-Functionalized Gold Nanoparticles. Acs Nano 2008, 2 (11), 2213-2218.

121. Sullivan, M. M. O.; Green, J. J.; Przybycien, T. M., Development of a novel gene delivery scaffold utilizing colloidal gold-polyethylenimine conjugates for DNA condensation. Gene Therapy 2003, 10 (22), 1882-1890.

122. Han, G.; Martin, C. T.; Rotello, V. M., Stability of gold nanoparticle-bound DNA toward biological, physical, and chemical agents. Chemical Biology & Drug Design 2006, 67 (1), 78-82.

123. Sandhu, K. K.; McIntosh, C. M.; Simard, J. M.; Smith, S. W.; Rotello, V. M., Gold nanoparticle-mediated Transfection of mammalian cells. Bioconjugate Chemistry 2002, 13 (1), 3-6.

124. Noh, S. M.; Kim, W. K.; Kim, S. J.; Kim, J. M.; Baek, K. H.; Oh, Y. K., Enhanced cellular delivery and transfection efficiency of plasmid DNA using positively charged biocompatible colloidal gold nanoparticles. Biochimica Et Biophysica Acta-General Subjects 2007, 1770 (5), 747-752.

125. Verma, A.; Uzun, O.; Hu, Y. H.; Hu, Y.; Han, H. S.; Watson, N.; Chen, S. L.; Irvine, D. J.; Stellacci, F., Surface-structure-regulated cell-membrane penetration by monolayer-protected nanoparticles. Nature Materials 2008, 7 (7), 588-595.

126. Bergen, J. M.; Von Recum, H. A.; Goodman, T. T.; Massey, A. P.; Pun, S. H., Gold nanoparticles as a versatile platform for optimizing physicochemical parameters for targeted drug delivery. Macromolecular Bioscience 2006, 6 (7), 506-516.

Chapter 2

SYNTHETIC STRATEGIES AND CHARACTERIZATION TECHNIQUES

This chapter describes the procedures for synthesizing colloidal gold nanoparticles (AuNPs) and peptides as well as the techniques utilized to characterize the resulting materials. The protocols described herein provide the required control over both nanoparticle and peptide composition to generate well-defined macromolecular assemblies that can be used in drug delivery applications. The concepts behind these techniques are presented in this chapter, while the results are discussed in the proceeding chapters.

2.1 Colloidal Gold Nanoparticle and Macromolecule Synthesis

In order to effectively develop and optimize macromolecular assemblies for drug delivery, the component materials must be synthesized with well-defined composition, low dispersity, and high purity. The following sections describe the synthetic approaches that were employed to meet these rigorous demands.

2.1.1 Two-Phase Brust-Schiffrin Gold Nanoparticle Synthesis

2.1.1.1 Introduction

The synthesis of colloidal gold has been documented since the 4th-century, as evidenced by the Lycurgus Cup,[1] a type of cage cup made during the late Roman Empire. Modern scientific evaluation of colloidal gold began with work of Michael Faraday in the 1850s,[2] who first recorded the light scattering properties of suspended

gold particles.[3] Today, AuNPs are produced by a wide variety of liquid chemical methods, typically by reduction of hydrogen tetrachloroaurate ($HAuCl_4$). Synthesis methods differ by the type of reducing agent used, reaction temperature, final particle dispersity, and whether the resulting AuNPs are soluble in the aqueous or the organic phase. Citrate reduction of $HAuCl_4$, pioneered by J. Turkevich and colleagues[4] in 1951 and refined by G. Frens[5] in the 1970s, is one of the most popular methods used to produce spherical, water-soluble AuNPs with relatively low dispersity and a core size ~20 nm in diameter. Core diameter is tuned by controlling the amount of sodium citrate reducing agent that is added to the reaction. The citrate ions also function to stabilize the AuNPs from aggregation.

More recently, Brust-Schiffrin reported a biphasic method for preparing monolayer-protected gold clusters.[6] This synthetic strategy has the advantage of producing much smaller (2-10 nm), more stable, and more mono-disperse particles with a 10-fold higher particle loading density. The enhanced stability of the resulting AuNPs is attributed to the alkanethiol monolayer that strongly binds to the gold surface.[7, 8] In addition, the core diameter is controlled by adding different amounts of alkanethiol,[7, 9-11] rather than varying the amount of reducing agent added to the reaction. The enhanced properties of these AuNPs have been studied extensively,[12-14] and utilized to generate a large variety of functionalized nanoparticles,[15] particularly for drug and gene delivery applications.[16]

The Brust-Schiffrin reaction is represented schematically in Figure 2.1. The method works by first transferring the chloroauric acid ($AuCl_4^-$) to the organic phase (typically toluene) using the phase transfer reagent tetraoctylammonium bromide (TOAB) via the following reaction:[6]

$$AuCl_4^- \ (aq) \ + \ (C_8H_{17})_4N^+ \ (org) \ \rightarrow \ (C_8H_{17})_4N^+AuCl_4^- \ (org) \qquad (1)$$

Following phase transfer, the stabilizing alkanethiol chain (RSH) is added to the organic phase where it is believed to reduce a portion of Au^{3+} ions to Au^{1+} in the form of $-(AuSR)_z-$ polymer.[14] Reduction of the remaining Au^{3+} ions to Au^0 occurs through addition of sodium borohydride (BH_4^-) as follows:

$$mAuCl_4^- \ (org) + nRSH \ (org) + 3me^- \ \rightarrow Au_x(SR)_y \ (org) + 4mCl^- \ (aq) \ (2)$$

where BH_4^- supplies the source of electrons and the reaction conditions determine the ratio of n/m (i.e. thiol:gold). The Au^{+1} ions are also reduced to Au^0 in a similar fashion.

Following this reduction of Au ions, nucleation of the Au atoms begins to occur, forming nanoparticles. Although nanoparticle synthesis is not completely understood, the formation is believed to follow a nucleation-growth-capping mechanism. Rapid addition of the BH_4^- reducing agent to a well-stirred reaction mixture is thought to play an important role to ensure homogenous nucleation and growth of the AuNPs, followed by capping with the RSH chain present in the reaction mixture. The rate of nanoparticle growth and RSH capping (passivation) is controlled by tuning the thiol:gold molar ratio in the reaction mixture (i.e. higher thiol:gold molar ratios results in smaller AuNPs).[7, 11]

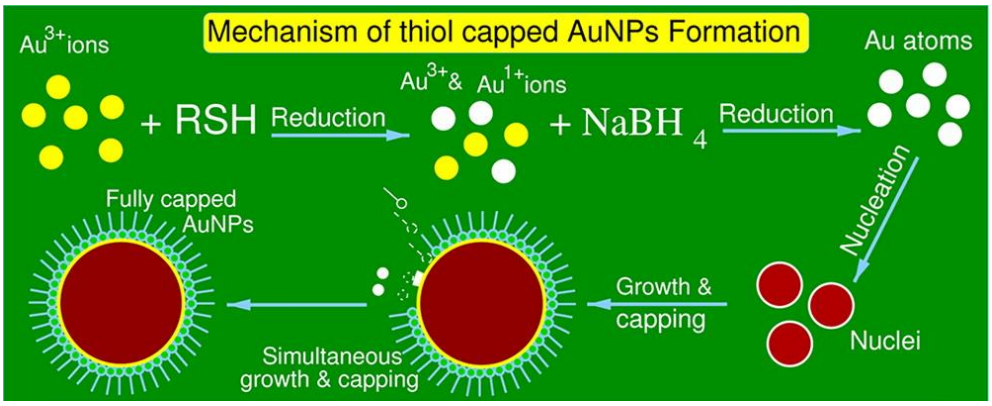

Figure 2.1: Schematic representation of the Brust-Schiffrin synthetic procedure followed by the nucleation-growth-capping mechanism to form monolayer-protected AuNPs. This figure was adapted with permission from SRK Perala and S Kumar, On the mechanism of metal nanoparticle synthesis in the Brust-Schiffrin method, *Langmuir* 29(31) (2013) 9863-73.[14] Copyright 2013, Rights managed by American Chemical Society.

The following sections describe the reagents, conditions, and protocols utilized to synthesize the AuNPs studied in Chapter 4 of this dissertation via the Brust-Schiffrin synthetic procedure.

2.1.1.2 Materials and Solvents

It is critical that all materials, reagents, and solvents used during nanoparticle formation be clean and of high purity to ensure a mono-disperse population of AuNPs. In addition, all glassware used in the synthesis should be vigorously washed and cleaned with *aqua regia*. High purity hydrogen tetrachloroaurate (III) hydrate ($HAuCl_4 \bullet 3H_2O$), TOAB, 1-pentanethiol, and sodium borohydride ($NaBH_4$) were all purchased from Sigma Aldrich. Solvents including toluene, Bio-Pure water, acetone, and ethanol were purchased from Fisher Scientific.

2.1.1.3 Synthesis[6, 17, 18]

One molar equivalent of $HAuCl_4$ was weighed using a Teflon coated spatula into a clean round bottomed flask and dissolved in Bio-Pure water (~150 mL/g of $HAuCl_4$). The solution was stirred for 5 minutes until complete dissolution. The solution should be clear yellow. Then, 1.5 molar equivalents of TOAB in toluene (~50 mL/g) were added to the gold solution and stirred vigorously for 15 minutes until the solution turned a cloudy dark orange color. While stirring, 2 molar equivalents of 1-pentanethiol were added dropwise over the course of 5 minutes. The solution was stirred until the color changed from dark orange to deep white and cloudy. Note that if the color change does not occur after 20 minutes, the process should be started again with new materials. A fresh solution of $NaBH_4$ (20 molar equivalents) in Bio-Pure water (~5 mL/g) was quickly added. The solution turned black within seconds (indicative of a mono-disperse product) and was stirred while covered for 5 hours. The aqueous phase was removed, and the majority of the AuNP-containing toluene phase was evaporated under reduced pressure.

Residual TOAB present in the organic phase after the initial AuNP formation is highly cytotoxic and must be removed before proceeding to downstream drug delivery applications. To remove the TOAB, the AuNPs were washed with ethanol and acetone. First, ethanol was added to the concentrated AuNPs and the solution stored at -20 ˚C for 2+ days allowing for full AuNP precipitation. The ethanol was carefully decanted, fresh ethanol added, and the solution stored again at -20 ˚C until full AuNP precipitation. This process was repeated at least 4 times, switching to acetone for the final 2 washes for faster precipitation. After the final wash, the AuNPs were collected in ~25 mL of ethanol, sonicated, and pelleted via centrifugation to remove any residual TOAB. The pellet was re-suspended in ethanol and washed via

centrifugation 2 more times. The collected pentanethiol-capped AuNPs were analyzed using electrospray ionization mass spectrometry (ESI MS) to ensure that all of the TOAB (m/z 466) had been removed, and transmission electron microscopy (TEM) was used to confirm small and mono-disperse average particle diameters before use in subsequent reactions.

2.1.2 Fmoc Solid Phase Peptide Synthesis (SPPS)

2.1.2.1 Introduction

In 1963, Dr. Robert Bruce Merrifield published his pioneering work in the *Journal of the American Chemical Society (JACS)* on the synthesis of a tetrapeptide using a solid-phase approach.[19] His seminal publication caused a paradigm shift within the peptide synthesis community, with over 500 papers published on solid phase peptide synthesis over the next 10 years.[20] Merrifield was awarded the Nobel Prize in Chemistry in 1984 for his invention, and his work remains the fifth most-cited article in *JACS's* history.

SPPS enables facile synthesis of peptides and small proteins through exquisite control of amino acid sequences. The technique allows for incorporation of unnatural amino acids, peptide/protein backbone modification, and facilitates the synthesis of peptide sequences containing D-amino acids. By conducting the synthesis on a solid support, excess reagents can be used to drive reactions to completion followed by simple washing to remove any unreacted materials.[20] The simplicity of the technique has also enabled the design of automation technologies, which are routinely used in industry to develop peptide therapeutics.[21]

Figure 2.2 outlines the concept of SPPS. The general principle revolves around repeated cycles of deprotection-wash-coupling-wash. Peptides are built on porous resin beads containing numerous functional linker units. The C-terminus of an N-protected amino acid is attached to the resin linker via its carboxyl group. Next, the protecting group is removed from the α-amino group, followed by a wash step, to reveal a new N-terminal amine on which to couple the second amino acid via amide bond formation. After coupling, the excess reagents are washed way from the resin and the process begins anew until the desired peptide sequence is synthesized. Once completed, the entire peptide can be removed from resin.

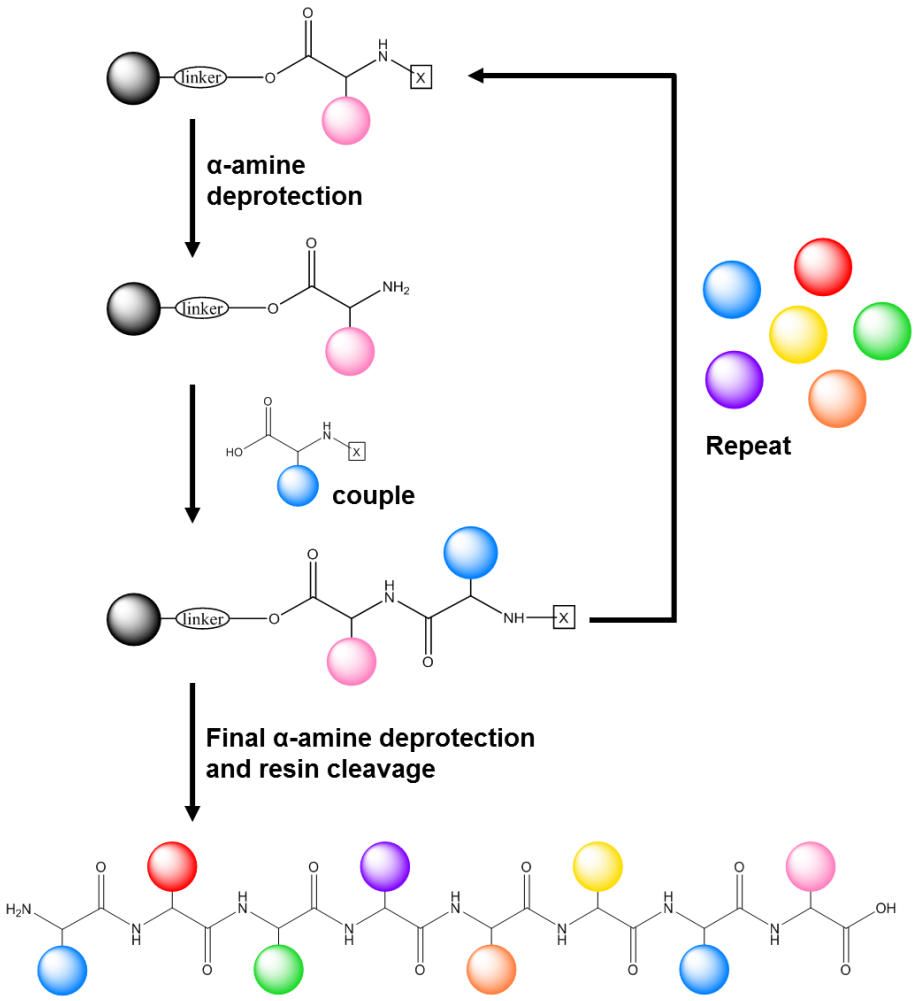

Figure 2.2: Schematic of Bruce Merrifield's solid-phase peptide synthesis (SPPS)

Although this technique is incredibly powerful, there are limitations that must be considered. Given the sequential addition of each amino acid to the growing peptide chain, the purity of the final peptide is significantly affected by coupling step efficiency. For example, if each coupling step were to have a 95% yield, the final yield of a 20 amino acid peptide chain would be <40% (assuming 100% yield in each deprotection step). Therefore it is extremely important to generate high yields during

each step of SPPS and to minimize side reactions. This is often accomplished using excess amounts of highly pure reagents.

In Merrifield's original SPPS publication, the α-amines were protected by tert-butoxycarbonyl (t-Boc) groups.[19] Although effective at generating well-defined peptides, Merrifield SPPS required side-chain protecting groups with different sensitivities to acidolysis, and required hydrofluoric acid to cleave the peptide from the resin. Today, the development of orthogonal deprotection chemistries that require mild conditions have made SPPS more accessible at the laboratory scale.[20] Most peptides are now synthesized using fluorenylmethyloxycarbonyl (Fmoc)-based deprotection. The Fmoc group protects the α-amine and is base-labile, while the side-chain protecting groups on each amino acid are typically acid labile. The peptide is also attached to the resin via an acid-labile linker. Using this strategy, the Fmoc groups can be sequentially removed prior to each coupling step, without affecting the integrity of the side-chain protecting groups. Both the final peptide product and side-chain protecting groups can be removed from the resin with a variety of acidic cleavage cocktails.[20]

The advent of Fmoc SPPS has initiated concerted efforts to design innovative side-chain protecting groups and resin linkers that afford additional levels of orthogonality to the synthetic strategy.[20] These types of modifications have enabled more complex syntheses capable of producing branched, cyclic, and partially/fully protected peptides in high yields. Branching has been shown to be particularly effective in creating new peptides and peptide-conjugates for therapeutic applications.[22, 23] Branching is typically accomplished by introducing lysine residues that do not contain an acid-labile side-chain (ε-amino) protecting group. Following

the assembly of a single sequence after Fmoc deprotection, selective removal of the orthogonal ε-amino group allows assembly of another sequence in a similar manner, creating a branched peptide. The ε-amine can also be used to covalently attach a wide variety of molecular conjugates to the peptide chain prior to cleavage from the resin.

The following sections detail the reagents and protocols used in the Fmoc SPPS reported throughout this dissertation.

2.1.2.2 Materials and Reagents

Fmoc-protected amino acids, 2-(1H-benzotriazole-1-yl)-1,1,3,3-tetramethyluronium hexafluorophosphate (HBTU), hydroxybenzotriazole (HOBt), and N,N'-diisopropylcarbodiimide (DIC) were purchased at high purity from NovaBiochem (EMD Biosciences). The side chain protecting groups of the amino used for Fmoc SPPS in this dissertation are shown in Table 2.1. Low-loading H-Rink Amide ChemMatrix resin was purchased from PCAS BioMatrix Inc. All other reagents and solvents were purchased at high purity from Sigma Aldrich.

Table 2.1: Side chain protecting groups used in SPPS

Amino acid (abbreviation)	**Side chain protecting group (abbreviation)**
Arginine (R)	2,2,4,6,7-pentamethyldihydrobenzofuran-5-sulfonyl (Pbf)
Glutamine (Q)	Triphenylmethyl (Trt)
Lysine (K)	Tert-butyl carbonyl (Boc) 1-(4,4-dimethyl-2,6-dioxacyclohexylidene)ethyl (Dde)
Serine (S)	t-butyl ether (tBu)
Threonine (T)	t-butyl ether (tBu)

All SPPS reagents were prepared before beginning each synthesis. Fmoc deprotection solution contained 20 vol% piperidine in dimethylformamide (DMF), and

amino acid dissolution solvent contained 0.4 M methylmorpholine (MMP) in DMF. Amino acids and HBTU used for coupling were weighed into a vial and sealed with a septum.

2.1.2.3 Synthesis

All peptides were synthesized at a 0.1 mmol scale using a Tribute Automated Peptide Synthesizer from Protein Technologies, Inc. First, resin was weighed into a reaction vessel, rinsed with DMF, and swelled in dichloromethane (DCM) for 10 minutes. The Fmoc protecting group of the amine-functionalized resin was then cleaved using standard deprotection conditions[20] (Figure 2.3).

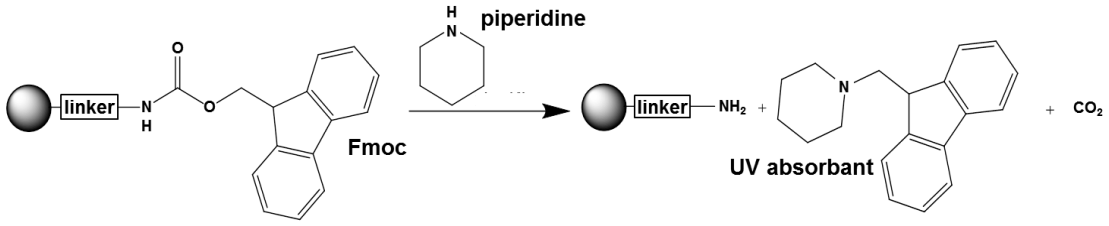

Figure 2.3: N-Fmoc removal reaction using piperidine.

The cleaved Fmoc group forms a molecular adduct with piperidine that absorbs ultraviolet (UV) light. Thus the progress of the deprotection reaction can be monitored by measuring this adduct's UV absorbance. The Tribute is equipped with a UV-monitoring and feedback control system to ensure effective Fmoc removal. Fmoc deprotection typically required 5 minutes incubation with piperidine, however the deprotection step was repeated until UV absorbance fell below a certain threshold value. Once removed, the resin was washed again with DMF.

Following resin deprotection, the first amino acid was coupled to the resin using standard HBTU/MMP coupling conditions. 6 molar equivalents of amino acid and HBTU were dissolved in 3 mL of 0.4 M MMP in DMF and allowed to dissolve for 2 minutes to activate the carboxylic acid group. The activated amino acid was then added to the resin and mixed for 2 h under nitrogen gas. The resin was again rinsed with DMF to remove excess reagents, and the process (deprotection-coupling) repeated until the desired sequence was complete. After final amino acid coupling, the N-terminal Fmoc protecting group was removed and the resin rinsed in DMF, swelled in DCM and dried for 10 minutes under nitrogen. The dried resin was stored at 4 ˚C.

In the case of peptides synthesized in Chapter 4, molecular conjugates were covalently attached at either the N- or C-terminal end of the peptide. For N-terminal conjugation following synthesis, the N-terminal Fmoc was removed and the resin washed with DMF. 5 molar equivalents of the molecular conjugate and 7 molar equivalents of HOBt/DIC were dissolved in 3 mL of DMF and stirred for 2 minutes to activate the carboxylic acid group on the conjugate. The activated conjugate was added to the resin and allowed to mix for 12 h, followed by washing with DMF to remove excess reagent, swelling in DCM, and drying under nitrogen.

To achieve C-terminal conjugation, a glycine residue and Dde-protected lysine residue were first coupled to the resin via the standard procedures described above. At this point a deprotection cocktail, fully orthogonal to Fmoc deprotection,[24] was prepared to selectively remove the Dde ε-amino protecting group. The deprotection mixture was prepared by dissolving 1.8 mmol of hydroxylamine hydrochloride ($NH_2OH \bullet HCl$) and 1.35 mmol of imidazole in 5 mL of N-methyl-2-pyrrolidone (NMP) via sonication until complete dissolution. The mixture was diluted with 1 mL

of DCM and mixed with the resin for 3 h to remove the Dde group. The resin was washed with DMF followed by covalent attachment of the molecular conjugate to the free ε-amine on the lysine residue as described above. Standard Fmoc deprotection and coupling procedures were then followed to synthesize the peptide chain.

Final peptides and peptide-conjugates were removed from resin using a trifluoroacetic acid (TFA)-based cocktail.[20] Acid-cleavage also functioned to deprotect all acid-labile side chain protecting groups. Triisopropylsilane (TIS), water, and 1,2-ethaneditihol (EDT) were utilized as scavengers to quench the resulting cations produced during the cleavage reaction.[20] Two different types of cleavage mixtures were used depending on the peptides synthesized. The first mixture contained 95/2.5/2.5 v/v TFA/TIS/water and the second mixture contained 94/2.5/2.5/1 v/v TFA/TIS/water/EDT. Cleavage was performed for 2 h while mixing, and the cleaved peptide separated from the resin beads via filtration. The peptide containing filtrate was concentrated under nitrogen and the peptide precipitated in cold diethyl ether. Precipitated peptides were recovered via centrifugation, dried, re-suspended in water, and lyophilized. Crude peptide products were purified and characterized using reverse phase high performance liquid chromatography (RP-HPLC) and mass spectrometry (MS) as described in subsequent sections.

2.1.3 Murray Place Exchange

2.1.3.1 Introduction

Proper surface functionalization is of fundamental importance when utilizing synthesized AuNPs for specific applications, particularly drug delivery applications.[25] Ligands present on the AuNP surface determine interactions with the environment,

which ultimately affect stability, targeting, and association with the cargo to be delivered.[26] Ligand exchange reactions are the primary tools employed to endow AuNPs with unique physio-chemical properties.[27] Exchange reactions can be used to promote phase transfer of the AuNPs, enhance their biocompatibility, and enable bioconjugation with a number of macromolecules (e.g. nucleic acids, proteins, polymers).[16]

Colloidal gold synthesized via the 2-phase Brust-Schiffrin reaction procedure described above yields monodisperse AuNPs stabilized by a protective alkanethiol monolayer. In order for these particles to be compatible with biological systems and relevant to drug delivery, their surfaces must be functionalized with ligands that facilitate transfer from organic to aqueous solutions. Numerous strategies have been proposed and studied to endow these alkanethiol-protected AuNPs with hydrophilic properties.[26] However, the most common and well-studied method is the place exchange reaction first pioneered by Murray and co-workers[28] in the 1990s.

Development of the Murray place exchange reaction represented a key step in unlocking alkanethiol-protected AuNP functionalization.[15] Properties of the surface ligands and the dynamics of their exchange are analogous to early work conducted by George Whitesides[29, 30] and Ralph Nuzzo[31] on the assembly and surface properties of 2D self-assembled monolayers (2D-SAMS). The foundation of the place exchange reaction lies in the strong binding affinity between thiol groups and the gold metal (~200 kJ/mol)[32] in a process known as "chemisorption." The place exchange reaction is generally thought to proceed by an associative S_N2-like mechanism.[33, 34] In the reaction, a new ligand (R'S) is incorporated into the monolayer by mixing its corresponding thiol (R'SH) with the alkanethiol-protected (RS) AuNPs in solution.[33]

Under ideal conditions, a 1:1 stoichiometric replacement of surface ligands for free ligands takes place, shown by the following reaction:[15]

$$x(R'SH) + (RS)_m Au \rightarrow x(RSH) + (R'S)_x(RS)_{m-x}Au \quad (3)$$

Where x and m are the numbers of new and original ligands respectively on the AuNP surface. The rate of reaction (3) and equilibrium stoichiometry (x) are controlled by the molar ratio of R'SH to RS ligands, their steric bulk, and the length of the R' versus R chains.[35] Finally, the displaced ligands remain in solution as thiols.[33]

The Murray place exchange reaction has become an invaluable tool for generating AuNPs with a wide variety of surface functionalities useful for drug delivery applications.[15, 16] Ligands containing longer alkane chains are typically utilized to drive the place exchange reaction forward, as the increased Van der Waals interactions between the longer chain groups further stabilizes the AuNPs. The forward reaction is further favored by mass action, increasing the R'SH to RS molar ratio to drive R'SH adsorption. By this method the hydrophobic ligands present on the surface of the AuNPs can be displaced by enough hydrophilic ligands to produce both water soluble and biocompatible AuNPs.

The following sections detail the materials and protocols utilized in the Murray place exchange reactions described in Chapter 4 to generate AuNPs displaying varying degrees of cationic ligands for nucleic acid delivery applications.

2.1.3.2 Materials and Reagents

Freshly prepared and fully characterized pentanethiol-coated AuNPs and peptide-conjugates as described in sections 2.1.1 and 2.1.2 respectively were used in all place exchange reactions. High purity DCM, methanol (MeOH), and Bio-Pure water were all purchased from Fisher Scientific. Snakeskin dialysis tubing (10 kDa)

and 10 kDa molecular weight cut-off (MWCO) centrifugal filters were purchased from Thermo Fisher Scientific. All glassware was vigorously washed with *aqua regia* prior to use. All other materials and reagents were purchased from Fisher Scientific.

2.1.3.3 Synthesis

The synthesis of the cationic AuNPs described in this dissertation proceeded via a 2-step Murray place exchange process (Figure 2.4).

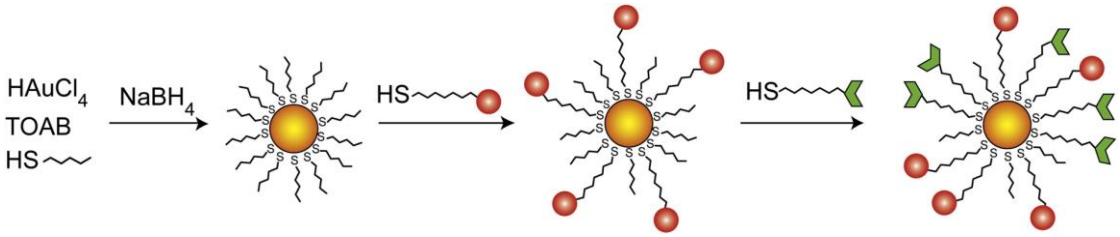

Figure 2.4: Schematic of the 2-step Murray place exchange reaction to generate multi-functionalized AuNPs following 2-phase Brust-Schiffrin synthesis. This figure was adapted with permission from S Rana, A Bajaj R Mout, & VM Rotello; Monolayer coated gold nanoparticles for delivery applications. *Adv. Drug Deliv. Revs.* 64(3) 200-16. 2012.[16] Copyright 2011, Rights managed by Elsevier B.V.

In the first Murray place exchange reaction, pentanethiol-coated AuNPs were suspended in DCM at 1 mg/mL and purged with nitrogen gas. In a separate container, at least 2 equivalents of the cationic peptide-conjugate was dissolved in a DCM/MeOH (60/40 v/v) mixture and purged with nitrogen gas. *Note: it is good practice to use as much DCM as possible when dissolving the ligands to ensure efficient place exchange.* Next, the two mixtures were combined in a round bottomed

flask, the air purged with nitrogen gas, and the flask sealed. The combined solution was stirred for 3 days at room temperature.

After 3 days, visible precipitates of place exchanged AuNPs were observed at the bottom of the flask. The solvents were concentrated on a rotary evaporator at 37 ˚C and the AuNPs re-suspended in a 20:1 v/v mixture of DCM:MeOH. The AuNPs were then pelleted via centrifugation and the washing process repeated 4 times with DCM:MeOH (20:1) to remove excess ligands. Following the final pelleting, the precipitate was dried under nitrogen and dissolved in a small amount of Bio-Pure water. The suspended AuNPs were then dialyzed against water in snakeskin dialysis tubing for 3 days to remove any remaining ligands. *Note: during dialysis, the bulk water solution should be changed every 2 hours, but can run overnight.*

Following dialysis, a small sample of AuNPs was taken and filtered via centrifugation (10 kDa MWCO). The filtrate was recovered and then analyzed for the presence of free ligands using MS. *Note: If ligands are found in the filtrate, continue dialysis for another 24 h and re-test for free ligands. Repeat until all excess ligands are removed.* The cationic AuNPs were harvested from the dialysis tubing, lyophilized, and stored at 4 ˚C under nitrogen gas until further use.

For the second Murray place exchange reaction, solutions of the cationic AuNPs from the first place exchange and peptide-conjugate ligands were prepared separately in Bio-Pure as described above. For this place exchange, different equivalents of the peptide-conjugate were mixed with the cationic AuNPs in order to generate mixed monolayer-protected AuNPs displaying varying amounts of the second peptide-conjugate. 1, 2, and 4 equivalents of peptide-conjugate were used in separate place exchange reactions to generate mixed-monolayer protected AuNPs of low-, mid-

and high-coverage, in accordance with ligand place exchange dynamics based on ratios of R'SH to RS.[33, 35]

The solutions were mixed for 3 days and the excess ligands removed by dialysis as described above. After confirming the absence of excess ligands by MS, the final AuNPs were lyophilized and stored under nitrogen at 4 ˚C.

The number of cationic ligands displayed on the surface of all the place-exchanged AuNPs was characterized using a combination of thermogravimetric analysis (TGA) and carbon-hydrogen-nitrogen-sulfur (CHNS) elemental analysis. Particle core size was determined with TEM.

2.2 Chemical Characterization

Strategies utilized to determine the molecular weight, purity, and composition of the synthesized AuNPs and macromolecules are described in the proceeding sections. Peptide-conjugates were characterized using a combination of RP-HPLC and MS. AuNPs were characterized using a combination of TEM, TGA, and CHNS elemental analysis.

2.2.1 Reverse Phase High Performance Liquid Chromatography (RP-HPLC)

2.2.1.1 Theory

Chromatography is a standard technique employed to assess the purity and distribution of synthetic macromolecules. Chromatography works by first dissolving the macromolecule (analyte) in a suitable solvent (mobile phase) and passing it over a porous surface (stationary phase). The differential partitioning of the molecules between the mobile and stationary phases are what drive separation. A wide variety of chromatographic techniques have been developed since its first implementation as a

separation process in the early 1900s.[36] Techniques differ based on different interactions between the macromolecules and stationary phase, and it is important to consider these interactions carefully in order to provide the best separation for a particular analyte.

In peptide synthesis, RP-HPLC is the standard chromatographic technique utilized to assess and control purity of the final product.[20] The chromatography column containing the stationary phase is hydrophobic, while the mobile phase is typically more hydrophilic. Pumps are used to pass the mobile phase containing the dissolved samples over the stationary phase in the column. Each component in the sample interacts with the stationary phase slightly different (i.e. higher hydrophobicity, stronger interaction) causing different flow rates, and ultimately separation as components flow out of the column. It is common to use a mixture of two or more solvents as the mobile phase when conducting HPLC, whose ratios will change with time creating a gradient of compositions within the mobile phase. Mobile phase gradients will typically start more hydrophilic and gradually increase in hydrophobicity (Figure 2.5). The more hydrophobic a particular component of the sample is, the longer it will take to elute off the column.

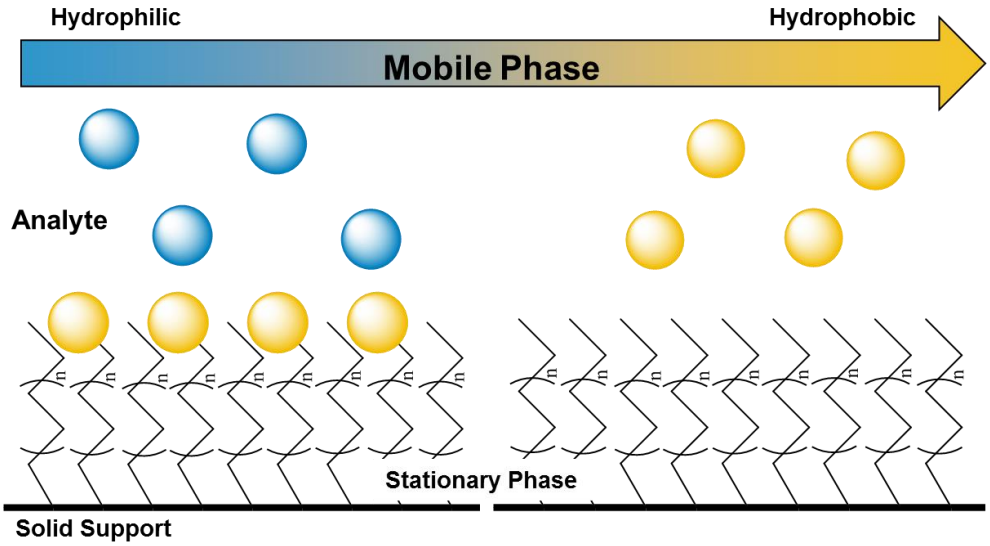

Figure 2.5: Schematic of RP-HPLC. Analyte enters the column in an initial hydrophilic mobile phase, causing hydrophobic components to associate with the stationary phase. As the mobile phase increases in hydrophobicity, hydrophobic components begin to elute off the column.

2.2.1.2 Application

In this dissertation, RP-HPLC was utilized to assess the purity of peptides and peptide-conjugates, and to separate these macromolecules from any unreacted intermediates, as well as any leftover side products formed during peptide cleavage/deprotection. Analyses were performed using a packed silica gel column decorated with octadecyl (C18) carbon chains, acting as the stationary phase. The mobile phase consisted of a linear gradient between 0.1 vol% TFA in water (solvent A) and 0.1 vol% TFA in acetonitrile (solvent B). TFA was added to each solvent in order to enhance analyte affinity to the mobile phase and control pH. Peptide and peptide-conjugate elution was monitored by ultraviolet visible spectroscopy (UV-Vis) absorbance at 210 nm, which corresponds to intrinsic absorbance of the peptide backbone. Crude products were assessed on a small-scale analytical C18 column

before purifying on a preparatory C18 column with a 10-fold higher loading capacity. Fractions of eluent were collected, taking care to isolate the purified peptide or peptide-conjugate.

Figure 2.6 depicts a standard solvent gradient and corresponding RP-HPLC peptide trace used in this dissertation. A linear gradient of AB solvent was run, starting from 7.5% B to 13% B over the course of 22 minutes at a flow rate of 5 mL/min. Following the gradient run, remaining analyte was flushed from the column with 95% B before returning to 7.5% B to equilibrate the column for the next run.

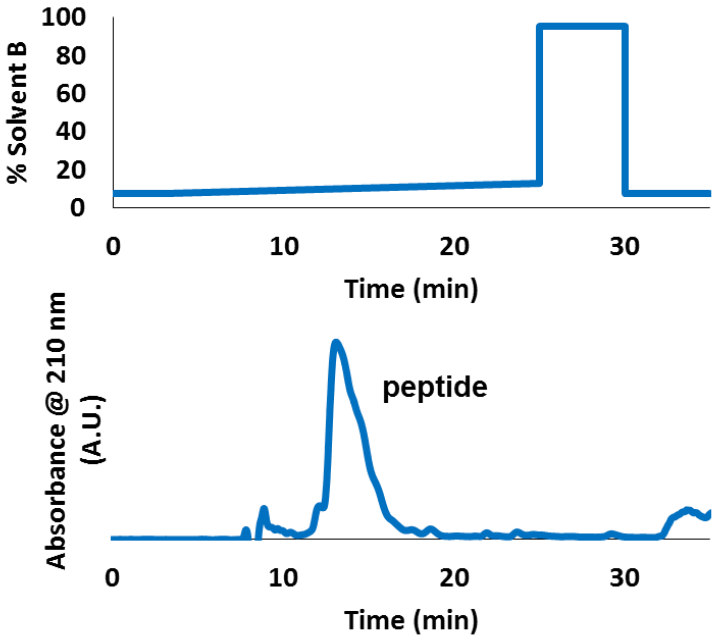

Figure 2.6: Representative RP-HPLC analysis for peptide characterization and purification. Solvent gradient used to effectively elute peptide from the column (above), where solvent B is 0.1 vol% TFA in acetonitrile. Elution chromatogram of the peptide from the column during run (bottom).

2.2.2 Matrix-Assisted Laser Desorption/Ionization Time-of-Flight Mass Spectrometry (MALDI-TOF MS)

2.2.2.1 Theory

MALDI-TOF MS is an essential analytical tool for characterizing both biomolecules (e.g. peptides, proteins, sugars) and large organic molecules (e.g. polymers, dendrimers).[37-39] MALDI is ideal for characterizing these large and often fragile macromolecules because it does not fragment the sample upon ionization. MALDI analysis proceeds via a three-step process. First, the sample (analyte) is mixed with a suitable chromophore-containing organic acid matrix in excess, followed by co-crystallization of the resulting mixture onto a target plate. Proper matrix selection is critical to ensure efficient crystallization and to obtain a high quality mass spectrum of the analyte.[40] The most common matrices utilized in protein and peptide characterization are shown in Table 2.2.

Table 2.2: Common Matrices for Peptide and Protein MALDI Analysis

Matrix	Size Range	Preparation
Alpha-cyano-4-hydroxycinnamic acid (α-CHCA)	Suitable for <10,000 Da	Dissolve matrix and analyte in 1:1 H_2O:ACN solution with 0.1 vol% TFA For proteins: 1-10 pmol/µl For peptides: 1 pmol/µl Mix 1 µl sample with 10 µl of matrix
3,5-dimethoxy-4-hydroxycinnamic acid (sinapinic acid, SA)	Suitable for >10,000 Da	

Following co-crystallization, a pulsed laser irradiates the matrix-analyte crystal (Figure 2.7), which triggers ablation and ionization of the sample. The matrix absorbs the majority of the laser pulse, and is thought to transfer a proton to the analyte.[40] The process is capable of creating singly or multiply charge analyte ions ($[M+H]^+$ or

$[M+H]^{n+}$ respectively) depending on laser intensity and the type of matrix. The ionized analytes are then accelerated by an electric potential down the TOF mass spectrometer where they are ultimately analyzed by the detector. Lighter ions hit the detector before heavier ions, which records intensity as a function of time yielding the final mass spectrum. Intensity results are recorded as a function of mass to charge (m/z) ratio.

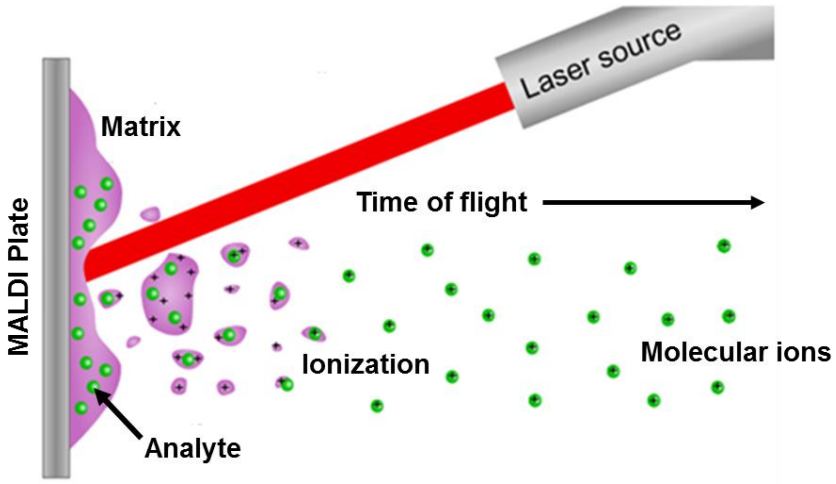

Figure 2.7: Schematic of MALDI process. This figure is adapted from WikiMedia Commons, https://commons.wikimedia.org/wiki/File:Maldi.svg. 2014.

2.2.2.2 Application

MALDI-TOF MS was utilized to assess the molecular weight of all peptides and peptide-conjugates described in this dissertation, and to confirm removal of all impurities. When conducting MALDI-TOF MS, the following should be noted: (1) it is essential to use highly pure solvents and reagents to ensure a high quality mass spectrum, (2) the plate used to spot the matrix-analyte must be completely dry before being inserted into the mass spectrometer, (3) during analysis peptides frequently

interact with other cations (often Na^+ or K^+) present in the system, resulting in higher MW adduct peaks in the resulting mass spectrum.

Peptides and peptide-conjugates were prepared as described in Table 2.2 and spotted on a ground steel MALDI target plate (Bruker, Germany). The sample was dried overnight at room temperature followed by analysis on a Bruker MALDI-TOF Microflex Series instrument. An example mass spectrum from peptide-conjugate analysis is shown in Figure 2.8.

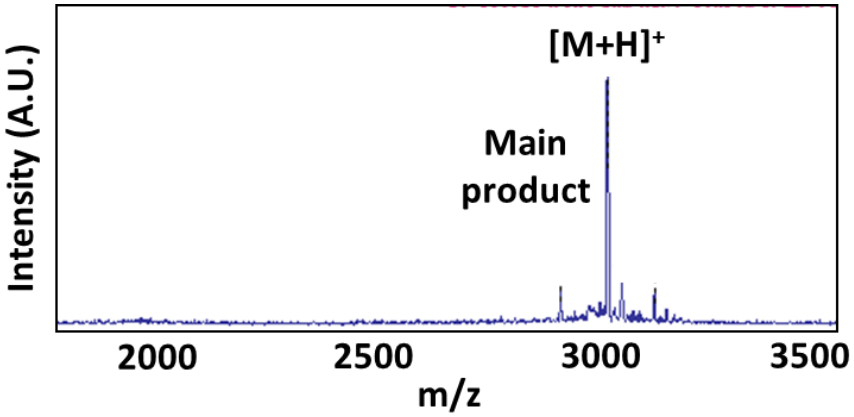

Figure 2.8: Representative MALDI-TOF mass spectrum from peptide-conjugate analysis following RP-HPLC purification.

2.2.3 Thermogravimetric Analysis (TGA)

2.2.3.1 Theory

TGA is an important thermal analysis strategy that measures the change in mass of a sample over time in response to changes in temperature. Such measurements provide important information regarding a sample's chemical (e.g. thermal decomposition) and physical (e.g. phase transitions) characteristics.[41] A

standard TGA instrument consists of a precision balance and sample holder located inside a furnace. The furnace is linked to a programmable temperature control, which generally increases temperature at a constant rate to produce a thermal reaction. Reactions can be performed under a variety of pressures depending on the application.[41]

The output from a TGA instrument is a plot of mass or percentage of initial mass as a function of time, referred to as the TGA curve. The change in temperature is often displayed on the same plot as a separate y-axis.

2.2.3.2 Application

In this dissertation, TGA was utilized to measure the total wt% of ligands present on the surface of the synthesized and place-exchanged AuNPs. As the AuNP samples are heated, the ligands attached to the surface combust, leaving behind the solid gold metal. The change in the overall weight of the sample as the ligands burn off the surface of the AuNPs is recorded.

In a typical TGA, 2-3 mg of AuNPs was loaded onto the sample tray of the instrument and purged with nitrogen gas. The AuNPs were then heated from 25-700 ˚C at a rate of 10 ˚C/min. When analyzing AuNPs covered by hydrophilic/cationic ligands, the temperature was held at 100 ˚C for 10 minutes in order to fully evaporate any atmospheric water that had associated with AuNPs. The wt% loss from water evaporation was omitted from the total wt% loss. A typical TGA curve from these evaluations is shown in Figure 2.9. Total ligand wt% loss, combined with peptide-conjugate MALDI-TOF MS and CHNS elemental analysis, was used to accurately determine the species and number of ligands present on the AuNP surface, as discussed in Chapter 4.

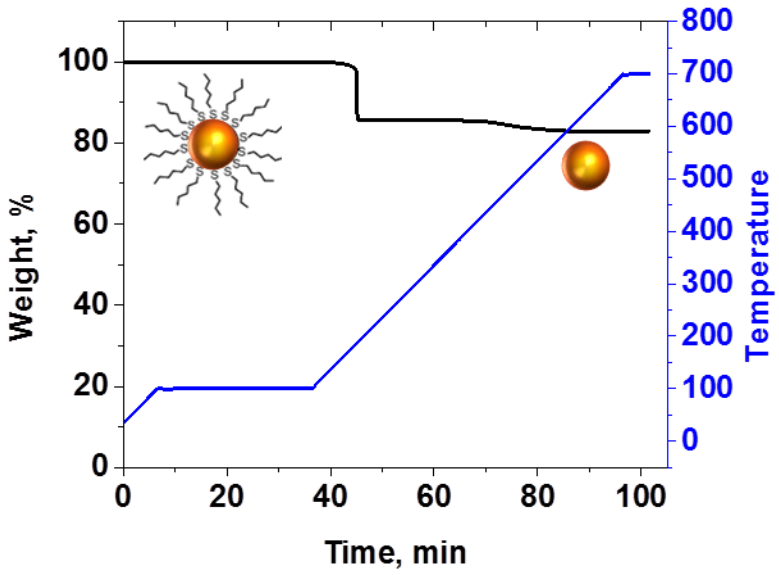

Figure 2.9: Representative TGA of pentanethiol-coated AuNPs. An overall wt% loss of ~18% was observed following heating from 25 °C to 700 °C.

2.2.4 Carbon-Hydrogen-Nitrogen-Sulfur (CHNS) Elemental Analysis

2.2.4.1 Theory

CHNS elemental analysis is a form of combustion analysis utilized to evaluate the elemental and sometimes isotopic mass fractions of carbon, hydrogen, nitrogen, and sulfur of a particular material. The technique was pioneered by Antoine Lavoisier's work on combustion theory in the late 1770s,[42] and improved upon by Fritz Pregl in the early 1900s,[43] who received the Nobel Prize for his contributions. Today, the technique works by burning a sample in excess oxygen and collecting the oxidized combustion products: carbon dioxide, water, nitric oxide, and sulfur dioxide in multiple traps (Figure 2.10). The masses of these products are then used to calculate the elemental composition of the sample.

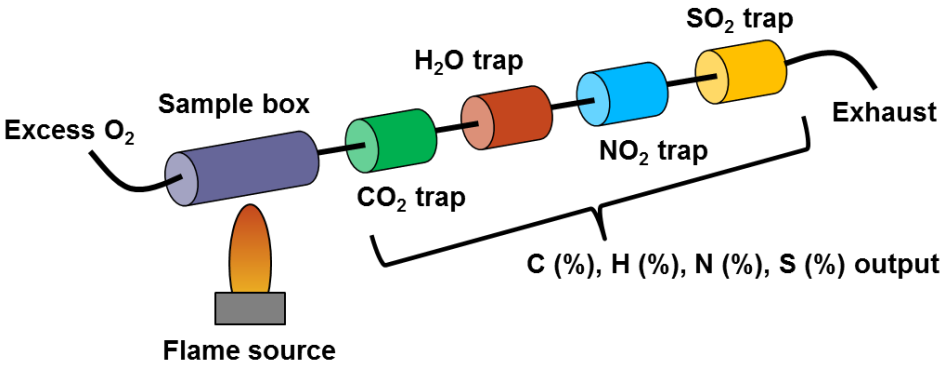

Figure 2.10: Schematic of CHNS elemental analysis.

CHNS analysis can be either quantitative or qualitative, depending on the intended application. For quantitative analyses, the output determines the ratio of elements within the unknown sample, and works to fit a chemical formula to the final results.

2.2.4.2 Application

CHNS elemental analysis was used as complimentary tool to evaluate the number/composition of ligands present on the surface of AuNPs discussed in Chapter 4 of this dissertation. All CHNS analyses were conducted by Intertek Pharmaceutical Services (Whitehouse, NJ).

For CHNS analysis, 5 mg of AuNPs were loaded into a furnace and rapidly burned in the presence of excess oxygen, immediately combusting all ligands present on the surface of the AuNPs. The combustion products were trapped and the elemental composition analyzed, represented as %C, %N, %H, and %S. These percentages, combined with TGA and peptide-conjugate MW analyses from MALDI-TOF MS were utilized to determine AuNP ligand composition.

2.2.5 Transmission Electron Microscopy (TEM)

2.2.5.1 Theory

TEM is the standard method of choice when it comes to characterizing both the size and dispersity of synthesized AuNPs. The high contrast potential of the gold atoms enables direct visualization on nanometer and even atomic length scales. Such high resolution provides unique insight not only into the size distribution of the synthesized AuNPs, but also the lattice-like architecture of the gold atoms within each individual nanoparticle.

TEM was first demonstrated in the early 1930s by Max Knoll and Ernst Ruska. The publication of the De Broglie hypothesis in 1927 made it theoretically possible to produce high resolution images at the atomic scale, given the fact that the wavelength of electrons was orders of magnitudes smaller than light. This was first achieved in 1933,[44, 45] when Knoll and Ruska acquired images of cotton fibers at much higher magnification than those available with light microscopes. Today, advances in optics, imaging, and electron formation have enabled high resolution imaging of both soft and hard materials.

TEM works by focusing a monochromatic electron beam onto a sample under high vacuum conditions, to prevent beam scattering by air or other contaminants.[46] The electron beam is refined using a complex series of lenses and apertures that ultimately control focus and magnification of the sample to be imaged. As the electrons pass through a sample, they are scattered by the atoms present in the sample. Thicker samples, or samples containing atoms of higher atomic number, will scatter more electrons.[46] The objective aperture, positioned below the sample's focal plane, blocks the scattered electrons, allowing only the direct beam to pass through[47] (Figure

2.11). Thus, a thicker/denser sample will produce a darker image. The high electron density of the gold atoms present in the AuNPs result in a much higher degree of electron beam scattering, producing high-contrast images with atomic-level resolution.

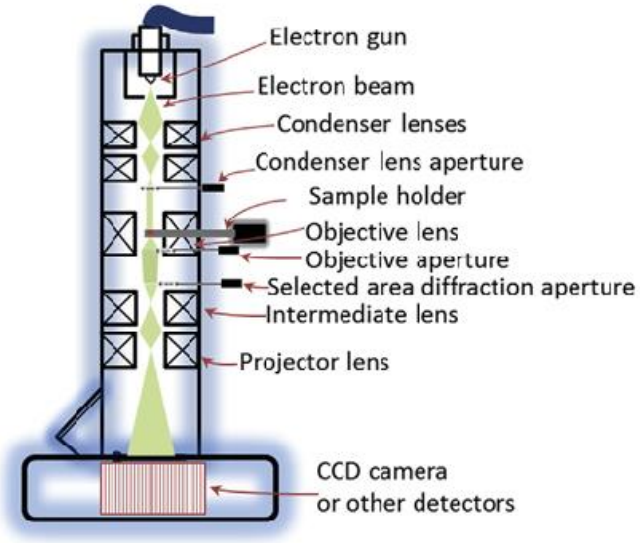

Figure 2.11: Schematic of key optical components in a standard TEM instrument. Figure was adapted with permission from Y Lin, JA McCarthy, KR Poeppelmeier, and LD Marks, Applications of electron microscopy in heterogeneous catalysis, *Cat Mats Def Structs.* 193-238, 2015.[48] Copyright 2015, Rights managed by Elsevier B.V.

2.2.5.2 Application

TEM was used primarily used to ensure that both small size and mono-dispersity were achieved following Brust-Schiffrin AuNP synthesis and Murray place exchange. These analyses are discussed throughout Chapter 4 of this dissertation. All TEM imaging was performed on a JEM-3010 ultrahigh resolution analytical electron microscope using bright-field imaging. *Note: given the high-vacuum operation*

conditions for TEM imaging, samples must be completely dried before loading into the TEM instrument.

In a typical analysis, dried AuNPs were dissolved in a small amount of solvent (water or toluene depending on ligand coverage) to a final concentration of 0.5 mg/mL. ~5 μL of the resulting solution was dropped onto carbon-coated copper grids and allowed to stand for ~1 minute. Excess solution was wicked away from the grid using clean filter paper. AuNPs in organic solutions were dried for 1 h at room temperature before imaging, while AuNPs in aqueous solutions were dried for at least 24 h before imaging. Figure 2.12 shows a representative TEM image of pentanethiol-coated AuNPs, synthesized via the Brust-Schiffrin reaction procedure described above. High magnification imaging (Figure 2.12b) of these AuNPs reveals the lattice-like arrangement of the gold atoms within each individual nanoparticle.

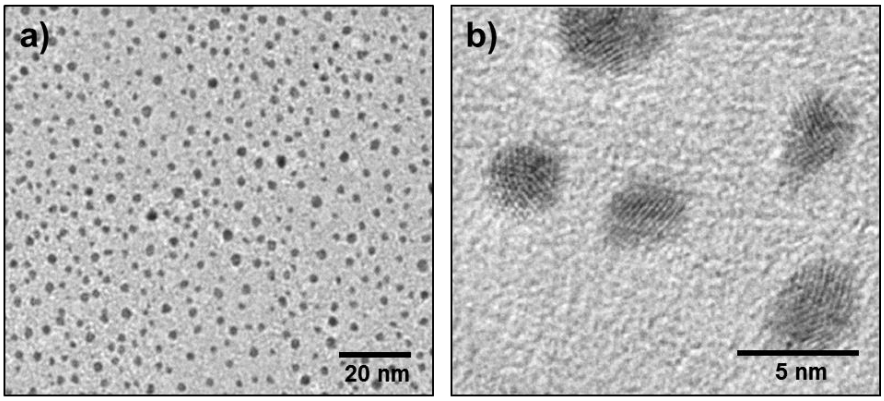

Figure 2.12: Representative images of pentanethiol-coated AuNPs taken at (a) low and (b) high magnification using bright-field TEM. AuNPs display an average core diameter size of 2.5 nm.

2.3 Summary

This chapter provided an overview of the synthesis techniques utilized in this dissertation to create well-defined AuNPs, peptides, and peptide-conjugates at high purities. These macromolecular materials were characterized using complementary techniques that verified their molecular composition and confirmed their high purity. Accurate analysis of the molecular composition and purity of these materials was crucial in determining their solution and biological properties as described in the remaining chapters of this dissertation. Most importantly, the synergistic use of these analyses provided the information required to effectively formulate nucleic acid delivery assemblies with these materials.

REFERENCES

1. Freestone, I.; Meeks, N.; Sax, M.; Higgitt, C., The Lycurgus Cup - A Roman nanotechnology. Gold Bulletin 2007, 40 (4), 270-277.

2. Reddy, V. R., Gold nanoparticles: Synthesis and applications. Synlett 2006, (11), 1791-1792.

3. Faraday, M., The Bakerian Lecture: experimental relations of gold (and other metals) to light. Philosophical Transactions: Royal Society London. 1857, (147), 145-181.

4. Turkevich, J.; Stevenson, P. C.; Hillier, J., A study of the nucleation and growth processes in the synthesis of colloidal gold. Discussions of the Faraday Society 1951, (11), 55-&.

5. Frens, G., Controlled nucleation for regulation of particle-size in monodisperse gold suspensions. Nature-Physical Science 1973, 241 (105), 20-22.

6. Brust, M.; Walker, M.; Bethell, D.; Schiffrin, D. J.; Whyman, R., Synthesis of thiol-derivitized gold nanoparticles in a 2-phase liquid-liquid system. Journal of the Chemical Society-Chemical Communications 1994, (7), 801-802.

7. Hostetler, M. J.; Wingate, J. E.; Zhong, C. J.; Harris, J. E.; Vachet, R. W.; Clark, M. R.; Londono, J. D.; Green, S. J.; Stokes, J. J.; Wignall, G. D.; Glish, G. L.; Porter, M. D.; Evans, N. D.; Murray, R. W., Alkanethiolate gold cluster molecules with core diameters from 1.5 to 5.2 nm: Core and monolayer properties as a function of core size. Langmuir 1998, 14 (1), 17-30.

8. Negishi, Y.; Takasugi, Y.; Sato, S.; Yao, H.; Kimura, K.; Tsukuda, T., Kinetic stabilization of growing gold clusters by passivation with thiolates. Journal of Physical Chemistry B 2006, 110 (25), 12218-12221.

9. Shon, Y. S.; Mazzitelli, C.; Murray, R. W., Unsymmetrical disulfides and thiol mixtures produce different mixed monolayer-protected gold clusters. Langmuir 2001, 17 (25), 7735-7741.

10. Shimmin, R. G.; Schoch, A. B.; Braun, P. V., Polymer size and concentration effects on the size of gold nanoparticles capped by polymeric thiols. Langmuir 2004, 20 (13), 5613-5620.

11. Leff, D. V.; Ohara, P. C.; Heath, J. R.; Gelbart, W. M., Thermodynamic control of gold nanocrystal size – experiment and theory. Journal of Physical Chemistry 1995, 99 (18), 7036-7041.

12. Chen, S. W.; Templeton, A. C.; Murray, R. W., Monolayer-protected cluster growth dynamics. Langmuir 2000, 16 (7), 3543-3548.

13. Goulet, P. J. G.; Lennox, R. B., New Insights into Brust-Schiffrin Metal Nanoparticle Synthesis. Journal of the American Chemical Society 2010, 132 (28), 9582-9584.

14. Perala, S. R. K.; Kumar, S., On the Mechanism of Metal Nanoparticle Synthesis in the Brust-Schiffrin Method. Langmuir 2013, 29 (31), 9863-9873.

15. Templeton, A. C.; Wuelfing, M. P.; Murray, R. W., Monolayer protected cluster molecules. Accounts of Chemical Research 2000, 33 (1), 27-36.

16. Rana, S.; Bajaj, A.; Mout, R.; Rotello, V. M., Monolayer coated gold nanoparticles for delivery applications. Advanced Drug Delivery Reviews 2012, 64 (2), 200-216.

17. Moyano, D. F.; Duncan, B.; Rotello, V. M., Preparation of 2 nm Gold Nanoparticles for In Vitro and In Vivo Applications. In Nanomaterial Interfaces in Biology: Methods and Protocols, Bergese, P.; HamadSchifferli, K., Eds. Humana Press Inc: Totowa, 2013; Vol. 1025, pp 3-8.

18. Waters, C. A.; Mills, A. J.; Johnson, K. A.; Schiffrin, D. J., Purification of dodecanethiol derivatised gold nanoparticles. Chemical Communications 2003, (4), 540-541.

19. Merrifield, R. B., Solid phase peptide synthesis: 1. Synthesis of a tetrapeptide. Journal of the American Chemical Society 1963, 85 (14), 2149-&.

20. Chan, W.C. and White, P.D. Fmoc Solid Phase Peptide Synthesis, Oxford University Press, 2000.

21. Kaspar, A. A.; Reichert, J. M., Future directions for peptide therapeutics development. Drug Discovery Today 2013, 18 (17-18), 807-817.

22. Pini, A.; Falciani, C.; Bracci, L., Branched Peptides as Therapeutics. Current Protein & Peptide Science 2008, 9 (5), 468-477.

23. Ahrens, V. M.; Bellmann-Sickert, K.; Beck-Sickinger, A. G., Peptides and peptide conjugates: therapeutics on the upward path. Future Medicinal Chemistry 2012, 4 (12), 1567-1586.

24. Diaz-Mochon, J. J.; Bialy, L.; Bradley, M., Full orthogonality between Dde and Fmoc: The direct synthesis of PNA-peptide conjugates. Organic Letters 2004, 6 (7), 1127-1129.

25. Giljohann, D. A.; Seferos, D. S.; Daniel, W. L.; Massich, M. D.; Patel, P. C.; Mirkin, C. A., Gold Nanoparticles for Biology and Medicine. Angewandte Chemie-International Edition 2010, 49 (19), 3280-3294.

26. Sperling, R. A.; Parak, W. J., Surface modification, functionalization and bioconjugation of colloidal inorganic nanoparticles. Philosophical Transactions of the Royal Society a-Mathematical Physical and Engineering Sciences 2010, 368 (1915), 1333-1383.

27. Sardar, R.; Funston, A. M.; Mulvaney, P.; Murray, R. W., Gold Nanoparticles: Past, Present, and Future. Langmuir 2009, 25 (24), 13840-13851.

28. Hostetler, M. J.; Green, S. J.; Stokes, J. J.; Murray, R. W., Monolayers in three dimensions: Synthesis and electrochemistry of omega-functionalized alkanethiolate-stabilized gold cluster compounds. Journal of the American Chemical Society 1996, 118 (17), 4212-4213.

29. Folkers, J. P.; Laibinis, P. E.; Whitesides, G. M., Self-assembled monolayers of alkanethiols on gold – comparisons of monolayers containing mixtures of short-chain and long-chain constituents with CH_3 and CH_2OH terminal groups. Langmuir 1992, 8 (5), 1330-1341.

30. Bain, C. D.; Whitesides, G. M., Formations of monolayers by the coadsorption of thiols on gold – variations in the length of the alkyl chain. Journal of the American Chemical Society 1989, 111 (18), 7164-7175.

31. Nuzzo, R. G.; Allara, D. L., Adsorption of biofunctional organic disulfides on gold surfaces. Journal of the American Chemical Society 1983, 105 (13), 4481-4483.

32. Love, J. C.; Estroff, L. A.; Kriebel, J. K.; Nuzzo, R. G.; Whitesides, G. M., Self-assembled monolayers of thiolates on metals as a form of nanotechnology. Chemical Reviews 2005, 105 (4), 1103-1169.

33. Hostetler, M. J.; Templeton, A. C.; Murray, R. W., Dynamics of place-exchange reactions on monolayer-protected gold cluster molecules. Langmuir 1999, 15 (11), 3782-3789.

34. Guo, R.; Song, Y.; Wang, G. L.; Murray, R. W., Does core size matter in the kinetics of ligand exchanges of monolayer-protected Au clusters? Journal of the American Chemical Society 2005, 127 (8), 2752-2757.

35. Ingram, R. S.; Hostetler, M. J.; Murray, R. W., Poly-hetero-omega-functionalized alkanethiolate-stabilized gold cluster compounds. Journal of the American Chemical Society 1997, 119 (39), 9175-9178.

36. Strain, H. H.; Sherma, J., Tswett, M., Adsorption analysis and chromatographic methods – applications to chemistry of chlorophylls. Journal of Chemical Education 1967, 44 (4), 238-&.

37. Hoteling, A. J.; Erb, W. J.; Tyson, R. J.; Owens, K. G., Exploring the importance of the relative solubility of matrix and analyte in MALDI sample preparation using HPLC. Analytical Chemistry 2004, 76 (17), 5157-5164.

38. Nielen, M. W. F., Maldi time-of-flight mass spectrometry of synthetic polymers. Mass Spectrometry Reviews 1999, 18 (5), 309-344.

39. Hillenkamp, F.; Karas, M.; Beavis, R. C.; Chait, B. T., Matrix-assisted laster desorption ionization mass-spectrometry of biopolymers. Analytical Chemistry 1991, 63 (24), A1193-A1202.

40. Gibson, D., Costello, C.E., Mass Spectrometry of Biomolecules, Separation Science and Technology: Volume 2, 2000, 299-327.

41. Coats, A. W.; Redfern, J. P., Thermogravimetric analysis. Analyst 1963, 88 (105), 906-&.

42. Lavoisier, A., Traite Elementaire de Chimie. 1st edition. Cuchet Libraire: Paris. 1789.

43. Karpenko-Jereb, L. V.; Shaposhnik, V. A., Fritz pregl, inventor of quantitative elemental microanalysis of organic compounds. Journal of Analytical Chemistry 2012, 67 (6), 600-602.

44. Knoll, M.; Ruska, E., The Electron Microscope. Zeitschrift Fur Physik 1932, 78 (5-6), 318-339.

45. Ruska, E., The development of the electron-microscope and of electron microscopy. Reviews of Modern Physics 1987, 59 (3), 627-638.

46. Williams, D.B. and Carter, C.B., Transmission Electron Microscopy. 2nd edition, Springer. 2009.

47. Smith, M. F.; Langmore, J. P., Quantitation of molecular densities by cryoelectron microscopy – determination of the radial density distribution of tobacco mosic-virus. Journal of Molecular Biology 1992, 226 (3), 763-774.

48. Lin, Y., McCarthy, J.A., Poeppelmeier, K.R., and Marks, L.D., Applications of electron microscopy in heterogeneous catalysis, Catalysis of Materials and Definite Structures. 2015, 193-238.

Chapter 3

HISTONE-TARGETED GROWTH FACTOR GENE TRANSFER ENHANCES MESENCHYMAL STEM CELL CHONDROGENESIS

As discussed in the Chapter 1, the design of DNA-encapsulating nanocarriers that achieve effective nuclear delivery represents a significant challenge. Histone-targeted nanocarriers were shown to address this challenge by gaining enhanced access to the nucleus during mitosis, highlighting the role these nanocarriers may play in tissue regenerative applications, where cell populations are actively dividing and differentiating. Accordingly, this chapter describes the techniques and analyses used to demonstrate how histone-targeted gene transfer approaches can be utilized to enhance osteogenic growth factor delivery and chondrogenic differentiation in actively proliferating mesenchymal stem cells (MSCs) during bone tissue regeneration. The text, tables, and figures in this chapter are adapted and reprinted with permission from Munsell, E.V.; Kurpad, D.S.; Freeman, T.A.; and Sullivan M.O., Histone-targeted gene transfer of Bone Morphogenetic Protein-2 enhances mesenchymal stem cell chondrogenic differentiation. Acta Biomaterialia, *under review* (2017).

3.1 Introduction

Several gene transfer strategies have demonstrated promise in preclinical studies to deliver bone morphogenetic proteins (BMPs) and other osteogenic growth factors for bone regenerative applications. For example, viral approaches to deliver growth factors have shown potential to improve the healing response and enhance bone formation.[1-4] Non-viral gene manipulations also have shown a capacity to

enhance MSC differentiation[5, 6] and/or promote bone formation *in vivo*,[7-9] and these synthetic carriers may offer potential benefits in terms of safety and controlled release as compared with their viral counterparts. Despite these accomplishments, existing approaches have on the whole lacked sufficient activity to progress through clinical translation.[10, 11] Specifically, while multiple proof-of-concept studies in rodent and murine models of bone regeneration have been successful, studies in larger animal models have yielded only moderate success.[12] In addition, there are prohibitively high costs associated with the detailed pharmacological and toxicological studies required for clinical translation. These prohibitive costs, coupled with the gap in nanocarrier effectiveness between small and large animal models, suggest a need for improved understanding of nanocarrier interactions with biological systems in order to design more effective gene transfer strategies for human application.

Knowledge of the enhanced mitotic behavior of MSCs during bone repair may offer insight into the design of nanocarrier delivery systems with improved efficacy. In particular, mitosis is known to play a key role in enhancing the transfection efficiency of non-viral nanocarriers,[13-15] suggesting that the change in MSC proliferative state could be harnessed to locally accelerate growth factor gene transfer in coordination with repair activities. In fact, recent reports have illuminated exciting progress in the design of nanocarrier structures that can effectively navigate the intracellular space and gain access to the nucleus during mitosis. For example, several studies have demonstrated that designing nanocarriers to target caveolar uptake often enhance gene transfer.[16, 17] Both L-arginine[18] and glycopolymer[19] functionalities have been reported to harness caveolar trafficking and enhance nanocarrier accumulation in the perinuclear region. In addition, the use of transcription factors,[20] chromatin

interacting proteins,[21] and nuclear localization sequences derived from SV40 large T-antigen[22, 23] have been shown to direct nanocarrier nuclear delivery in dividing cells by potentially engaging native nuclear import machinery.

Building off of the fundamental insights into how H3-targeted nanocarriers navigate the intracellular space (see section 1.5), we questioned whether their improved subcellular trafficking and post-mitotic nuclear import properties could enhance gene delivery and expression of the osteogenic growth factor BMP-2 in MSCs. We further hypothesized that the improved expression of nascent BMP-2 growth factor, correlated with the initiation of fracture healing by MSCs, would function to trigger more robust levels of MSC differentiation along cellular lineages essential to bone repair, not only when compared to untargeted non-viral nanocarriers, but also when compared to topical application of exogenous growth factors. Collectively, our data show that H3-targeted nanocarriers are well-tolerated by MSCs and can achieve enhanced osteogenic BMP-2 expression over untargeted nanocarriers. Accumulation of expressed BMP-2 in cell culture following a single H3-targeted transfection persisted over the course of 1 week, similar to the time period of the initial increase in BMP-2 expression during native skeletal repair.[24] H3-mediated BMP-2 expression ultimately triggered more robust levels of chondrogenic differentiation over the subsequent 1 to 2 weeks. Importantly, the levels of chondrogenesis achieved following H3-targeted gene transfer significantly exceeded the levels achieved following either MSC treatment with an equivalent amount of exogenous BMP-2 protein, or BMP-2 gene delivery using untargeted nanocarriers. Evaluation of the mechanisms by which H3-targeted gene delivery yielded such enhancements revealed that H3-targeting enabled more effective MSC condensation

and differentiation via the upregulation of transcription factors essential to driving chondrogenesis. These novel findings represent the first application of histone-targeted gene therapy for improved MSC delivery and differentiation for skeletal tissue repair, and demonstrate the importance of developing improved nanocarrier design strategies to target the nucleus for the advancement of gene therapy in bone defect management.

3.2 Materials and Methods

3.2.1 Materials

H3 tail peptides comprised of the mammalian N-terminal H3 residues 1-25 (ARTKQTARKSTGGKAPRKQLATKAA-$CONH_2$) were purchased from Anaspec (Fremont, CA) at ≥ 95% purity. The scrambled H3 (sH3) peptide sequence was designed to incorporate residues 1-25 of the N-terminal H3 tail in a randomized sequence (LSAARPRTAKGARQTKRQKAKGTAK-$CONH_2$). The peptide was synthesized and purified as previously described [39]. The peptide was synthesized by solid phase peptide synthesis with a Protein Technologies Inc. Tribute series peptide synthesizer (Tucson, AZ) and a rink amide ChemMatrix resin from PCAS-Biomatrix Inc. (Quebec, Canada). Purification was performed by reverse-phase high performance liquid chromatography (HPLC) on a UFLC 20 series instrument from Shimadzu Inc. (Columbia, MD) through a Viva C18 column from Restek (Lancaster, PA). The pCMV6-XL4 mammalian expression plasmid encoding BMP-2 was obtained from OriGene Technologies (Rockville, MD). The gWIZ mammalian expression plasmid encoding the green fluorescent protein (GFP) was obtained from Genlantis (San Diego, CA). Both plasmids were amplified in DH5α *Escherichia coli*

in Lysogeny Broth, and purified with a QIAGEN Plasmid Maxi Kit (QIAGEN, Valencia, CA) following the manufacturer's protocols. Recombinant human TGF beta 1 protein was obtained from Abcam (ab50036; Cambridge, MA). Recombinant BMP-2 protein was obtained from GenScript (Z02913; Piscataway, NJ). Primers were synthesized by Eurofins MWG Operon (Huntsville, Al). Primary antibodies used for Western blot included: rabbit anti-MMP13, Sox 9 (H-90) and VEGF and mouse anti-β-actin (Santa Cruz Biotechnology, Dallas, TX); rabbit anti-COL-X (Abcam, Cambridge, MA); and mouse anti-RUNX2 (Invitrogen); and goat anti-Col II(N-19) (R&D Systems, Minneapolis, MN). Horseradish peroxidase (HRP) conjugated secondary antibodies were purchased from Santa Cruz Biotechnology (Dallas, TX). Cell culture reagents were purchased from Fisher Scientific (Pittsburgh, PA). Branched polyethylenimine (PEI, 25 kDa) and all other reagents were purchased at analytical grade from Sigma (St. Louis, MO).

3.2.2 Nanocarrier Formation

H3-targeted PEI nanocarriers, untargeted PEI nanocarriers, and sH3 nanocarriers were formed in 20 mM 4-(2-hydroxyethyl)piperazine-1-ethanesulfonic acid (HEPES) at a pH of 6 as previously described.[25] For all experiments, nanocarriers were formed at an overall N:P ratio of 10. For the formation of H3-targeted (and sH3) PEI nanocarriers, the peptide was added first, and an N:P ratio of 6/4 was used, with N = 6 from H3 (or sH3) and N = 4 from PEI. This corresponds to ~90% (w/w) H3 (or sH3) and 10% PEI in the polycationic solution for pDNA complexation. Nanocarrier structure and amount of peptide within nanocarrier were analyzed in our prior work by gel electrophoresis, zeta-potential, and RP-HPLC.[25, 26]

3.2.3 Cell Culture and Transfection

Murine C3H10T1/2 mesenchymal stem cells were obtained from the American Type Culture Collection (ATCC; Manassas, VA). The cells were cultured according to ATCC protocols at 37°C and 5% CO_2 in modified Eagle's medium (MEM) supplemented with 10% fetal bovine serum and 1% penicillin-streptomycin. For transfection, cells were plated on collagen-I coated plates at 10,000 cells/cm^2 in complete growth medium. 24 hours later, cells were rinsed with phosphate-buffered saline (PBS) and incubated with nanocarriers for 2 hours in Opti-MEM. MSCs were transfected at a fixed dose of 1 μg pDNA/cm^2 well surface area. Cells were subsequently washed with PBS and fresh MEM was added to the cells until a specified time point.

3.2.4 Flow Cytometry and Transfection Efficiency

Cells were plated and transfected with nanocarriers containing the gWIZ-GFP expression plasmid as stated above. After 24 h, cells were imaged with a Leica 6000 fluorescence microscope (Wetzler, Germany). GFP expression was quantified on a FACS Caliber Flow Cytometer (San Jose, CA). For cytometry analyses, cells were collected after imaging and prepared for analysis by standard trypsin-mediated protocols. Briefly, cells were rinsed with PBS, incubated with trypsin, pelleted, suspended in 300 μl PBS, filtered through a 35 μm nylon mesh to remove aggregates, and stored at 4°C until analysis. Scatter plots were gated for quantification purposes, and a total of 10,000 cells were analyzed for each cell sample. Dead cells were excluded from analyses of transfection efficiency. To calculate the mean fluorescence intensity (MFI) of the transfected cell population, untransfected cells were gated for autofluorescence, and the MFI of the transfected cell population obtained. Scatter

plots were analyzed for both untransfected cells and cells transfected with identical nanocarriers containing a gWIZ-luciferase plasmid (Genlantis, San Diego, CA). This vector served as a non-GFP expressing control, accounting for any shifts in live cell autofluorescence due to polycationic presence.

3.2.5 Cell Viability and Live Surface Area Coverage

Live and dead cells were visualized by fluorescence microscopy as described above, following staining with Calcein-AM and propidium iodide. 24 h post transfection, cells were washed 2X with PBS and incubated in Opti-MEM containing 0.1 % (v/v) Calcein-AM and propidium iodide for 50 min at 37°C. The percent of viable cells was quantified by counting the number of live and dead cells using ImageJ analysis software.[27] Live cell surface area coverage was also quantified using ImageJ analysis software by counting the total number of live cells and scaling to the surface area of the well. Samples were analyzed relative to untransfected controls.

3.2.6 BMP-2 Expression Immunoassay

For analysis of BMP-2 expression following nanocarrier transfection, 10T1/2 MSCs were plated and transfected as described above with nanocarriers containing the BMP-2 expression plasmid. Every 24 h, 110 µL of the supernatant was collected, and the expression level of BMP-2 analyzed using a Quantikine BMP-2 ELISA Kit (R&D systems; Minneapolis, MN) according to the manufacturer's instructions.

3.2.7 Evaluation of Chondrogenic Differentiation: Alcian Blue Staining

Following transfection with BMP-2 pDNA containing nanocarriers, cells were maintained in serum free MEM media containing 0.2 mM ascorbic acid, 10^{-7} M dexamethasone, 10 ng/mL TGF-β1, and a 1:100 dilution of ITS+ Premix solution

(Corning; Corning, NY). Untransfected recombinant BMP-2 (rhBMP-2) protein control cultures were further supplemented with either 1 ng/mL or 100 ng/mL rhBMP-2. Media was half-refreshed every 3-4 days until the specified time point. Glycosaminoglycan (GAG) deposition following chondrogenic differentiation was evaluated via Alcian blue staining at days 7 and 14 post-transfection or treatment with rhBMP-2. A 1% Alcian blue solution (pH 2.5) was prepared in 3% acetic acid and filtered. Cells were washed 2X with room temperature PBS and fixed in 4% paraformaldehyde for 15 min. Cells were then rinsed 2X with ddH_2O and incubated with the Alcian blue solution in the dark for 45 min at room temperature. Cells were rinsed 3X with ddH_2O to neutralize acidity and imaged on a Zeiss LSM fluorescence microscope fitted with a AxioCam ERc 5s color camera (Jena, Germany).

3.2.8 Chondrogenic mRNA Expression Analysis

Gene expression levels of chondrogenic markers were evaluated on days 7 and 14 post-transfection using real-time quantitative polymerase chain reaction (RT-qPCR). Cells were maintained in the culture medium described above, and total RNA was isolated by TRIzol® Reagent (ThermoFisher Scientific; Waltham, MA) following the manufacturer's instructions. The iTaq™ Universal SYBR® Green One-Step Kit (Bio-Rad; Hercules, CA) and primers specific to Acan, COL IIA, MMP 13, and COL X (Figure A.1) were used to prepare samples in triplicate as stated in the manufacturer's protocol. Primers were designed using Primer-BLAST.[28] Both cDNA synthesis and qPCR were conducted on a Bio-Rad CFX96 instrument under the following conditions: 10 min at 50°C; 1 min at 95°C; and 40 cycles of 10 s at 95°C and 30 s at 60°C. Following amplification, a melt curve analysis was performed from 65 to 95°C at 0.5°C increment steps every 5 s to analyze the purity of the product

generated. The ΔΔCT method was used for fold-change analyses,[29] using Actin as the endogenous control. All test sample data were analyzed relative to untreated cell data.

3.2.9 Chondrogenic Protein Expression Analysis

Expression levels of chondrogenic extracellular matrix (ECM) and transcription factor proteins were evaluated on days 1, 2, 7, and 14 post-transfection by Western blot analyses as previously described.[30] In brief, cells were lysed in Mammalian Protein Extraction Reagent (MPER, Thermo Fisher, Waltham, MA), and protein concentrations were measured using a Bio-Rad Protein Assay (Bio-Rad Laboratories Inc.). Approximately 40 μg of protein were loaded onto each lane of a sodium dodecyl sulfate (SDS) polyacrylamide gel, and after electrophoresis the proteins were transferred to a polyvinylidene difluoride (PVDF) membrane. The membrane was blocked by incubation in Tris buffered saline (TBS) with 0.05% Tween 20 (Thermo Fisher, Waltham, MA) and 5% Membrane Blocking Agent (GE Healthcare, Buckinghamshire, UK) for 1 hour while shaking. The membranes were then incubated with their respective primary antibodies (1:500 dilution) in 2% ECL membrane blocking agent (RPN2125V-GE Healthcare UK limited) diluted in TBS with 0.05% Tween 20 overnight at 4°C. The primary antibody solution was removed and the blots were washed three times in TBS with 0.05% Tween 20. Subsequently, the appropriate horseradish peroxidase (HRP) conjugated secondary antibodies were applied to the blots, and these blots were incubated for 1 h at room temperature, washed intensively in TBS with 0.05% Tween 20, and reacted with ECL Advanced Detection Reagent (Amersham, Pittsburgh, PA) for 5 min at 25°C. Detection of the membranes was done using a FujiFilm Intelligent Darkbox (FujiFilm Co., Tokyo, JP).

The band intensity of each target protein was quantified using ImageJ analysis software.[27]

3.2.10 Statistical Analyses

Results for all plots are shown as the mean ± standard deviation of data obtained from at least 3 independent samples. Statistical analyses were performed using Student's *t*-test or one-way analysis of variance (ANOVA). A value of $p < 0.05$ was considered to be statistically significant.

3.3 Results

3.3.1 Histone-Targeted Transfection Efficiency and Cellular Viability

We first sought to assess the overall transfection efficiency of H3-targeted nanocarriers in MSCs by delivering a GFP reporter plasmid and analyzing expression with fluorescence microscopy and flow cytometry (Figure 3.1). Different H3-targeted nanocarrier formulations were tested in order to maximize transfection efficiency in MSCs (data not shown). The optimized H3-targeted nanocarriers transfected approximately 45% of MSCs in culture, as shown in Figure 3.1B. In contrast, both scrambled H3 (sH3) nanocarriers (nanocarriers made identically to H3-targeted nanocarriers but with a scrambled H3 sequence) and untargeted PEI nanocarriers yielded significantly lower transfection efficiencies, with only ~25% of cells transfected. Complementary to these results, the mean fluorescence intensities of the transfected cell populations were assessed. As shown in Figure 3.1C, cells transfected with H3-targeted nanocarriers displayed nearly 2-fold and 4-fold higher mean fluorescence levels than scrambled and untargeted nanocarriers, respectively. These

results suggest a more effective utilization of H3-targeted nanocarriers for transfection in MSCs as compared with either scrambled or untargeted PEI nanocarriers.

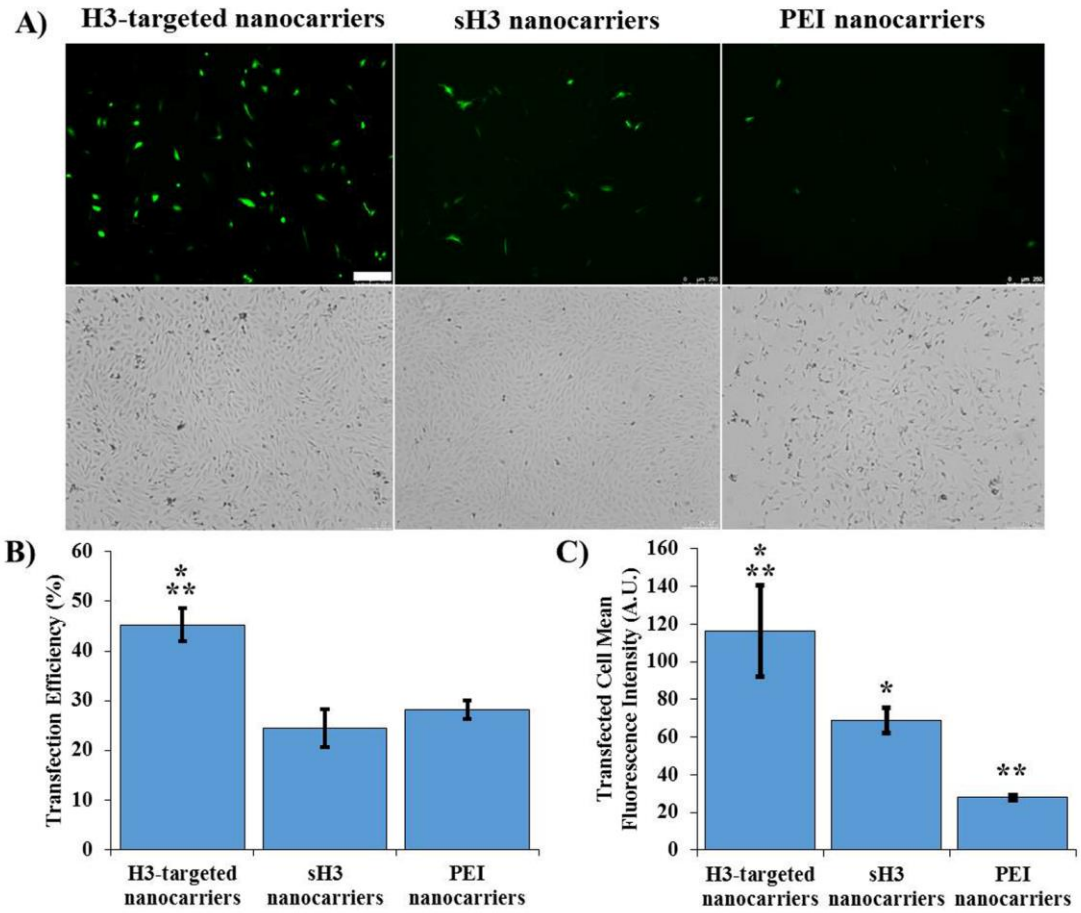

Figure 3.1: 10T1/2 MSC transfection efficiency. (A) Representative fluorescence microscopy images of GFP expression (top) and phase contrast microscopy images (bottom) of cells 24 h post-transfection with the indicated nanocarriers. (B) Quantification of transfection efficiency using flow cytometry. (C) Quantification of the transfected cell mean fluorescence intensity using flow cytometry. All results are shown as the mean ± standard deviation based on data collected from 3 independent experiments. * Indicates a significant difference from PEI nanocarriers ($p < 0.05$). ** Indicates a significant difference from sH3 nanocarriers. Scale bar = 250 μm.

Phase contrast images from our GFP transfection experiments (Figure 3.1A) also suggested significant differences in associated cytotoxicity between H3-targeted nanocarriers and untargeted PEI nanocarriers, with many fewer cells visible in PEI nanocarrier-treated cells 24 h after transfection. To quantify the potential reductions in cytotoxicity resulting from the nanocarrier treatments, cellular viability analyses were performed using live/dead staining with Calcein AM and propidium iodide. Fluorescent images indicated a significant reduction in cytotoxicity following transfections with H3-targeted and sH3 nanocarriers (Figure 3.2A), consistent with the literature.[25, 31] Quantification of the live/dead staining revealed a 25% loss in cellular viability following transfection with untargeted PEI nanocarriers (Figure 3.2B). To further demonstrate the cytotoxicity associated with PEI nanocarriers, the number of live MSCs present following transfection was also assessed. As shown in Figure 3.2B, transfection with PEI nanocarriers resulted in an 80% reduction in live cell surface coverage, relative to untransfected controls. In contrast, live cell surface coverage in MSCs transfected with H3-targeted or sH3 nanocarriers remained unaffected.

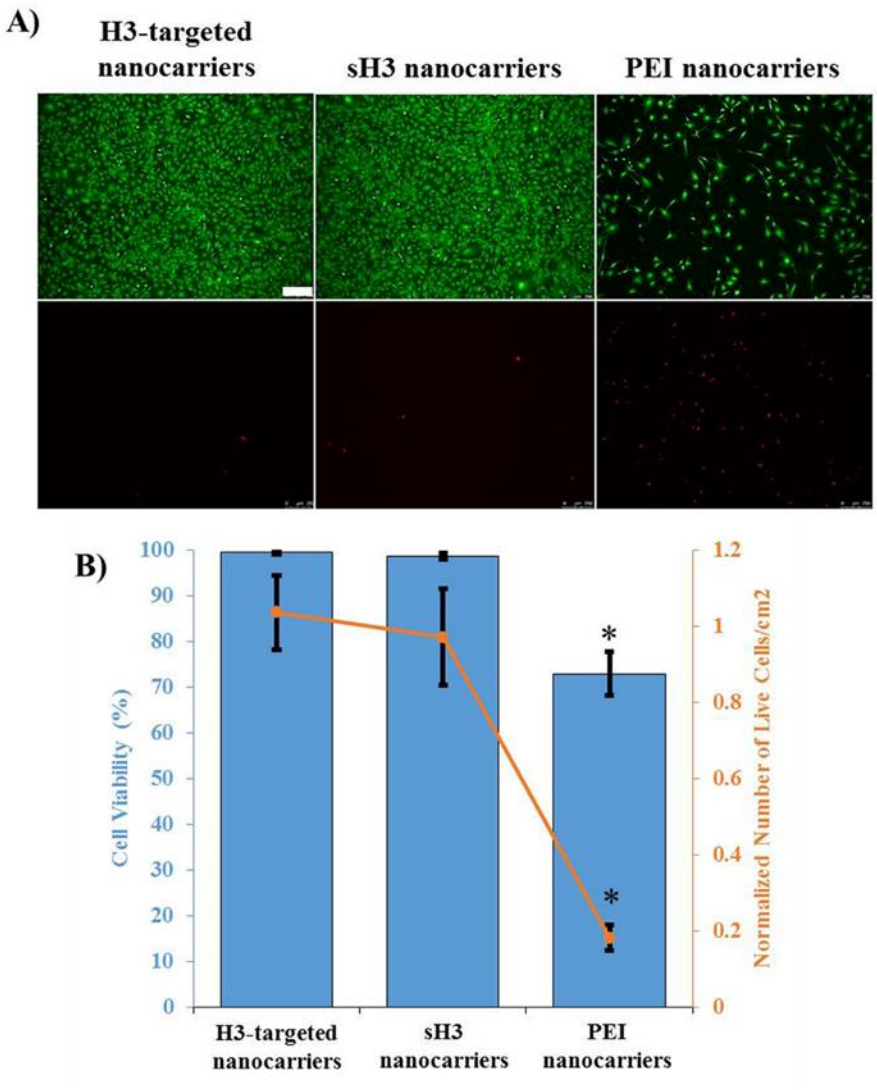

Figure 3.2: 10T1/2 MSC cellular viability and live cell surface coverage analyses 24 h post-transfection. (A) Representative fluorescence microscopy images of live cells stained with Calcein AM (green) and dead cells stained with propidium iodide (red) following transfection with the indicated nanocarriers. (B) Quantification of cellular viability (left axis, blue bars) and live cell surface coverage (right axis, orange line) from the fluorescence microscopy images in (A) calculated by ImageJ analysis. The number of live cells/cm^2 was normalized to the value in untransfected controls. All results are shown as the mean ± standard deviation of data collected from at least 5 images obtained from 3 independent experiments. * Indicates a significant difference from untransfected controls ($p < 0.05$). Scale bar = 250 μm.

3.3.2 BMP-2 Expression

Given the significant enhancements in transfection efficiency and biocompatibility achieved with H3-targeted nanocarriers in MSCs, H3-targeted delivery of DNA encoding the osteogenic growth factor BMP-2 was examined. Native BMP-2, in its mature form, is secreted into the extracellular space during the initial stages of fracture healing as MSCs enter the fracture site and begin to undergo chondrogenesis.[24, 32, 33] BMP-2 acts as potent inducer of both chondrogenesis and osteogenesis,[34] thus initiating the bone repair cascade. To measure mature BMP-2 expression in the cell culture supernatant, an enzyme-linked immunosorbent assay (ELISA) was employed following transfection with a BMP-2 reporter plasmid. As shown in Figure 3.3, BMP-2 was expressed in all transfected cell samples. In contrast, untransfected MSCs did not display any significant BMP-2 expression (data not shown). Maximum accumulation of BMP-2 in the cell culture supernatant was observed between day 3 and day 4 post-transfection following all nanocarrier treatments. Cells transfected with H3-targeted nanocarriers achieved a maximum accumulation of approximately 0.9 ng/mL of BMP-2, which decreased to approximately 0.5 ng/mL by day 6 post-transfection. In comparison, cells transfected with both sH3 and PEI nanocarriers displayed nearly ~4-fold lower levels of maximum secreted BMP-2 accumulation, and the levels of BMP-2 in these cell samples decreased to approximately 0.05 ng/mL by day 6 post-transfection. These results demonstrated the ability of the H3-targeted nanocarriers to not only improve growth factor expression over untargeted nanocarriers, but also maintain higher levels of protein in the extracellular space over an extended period of time that was commensurate with the time frame of maximal BMP-2 activity during native repair.

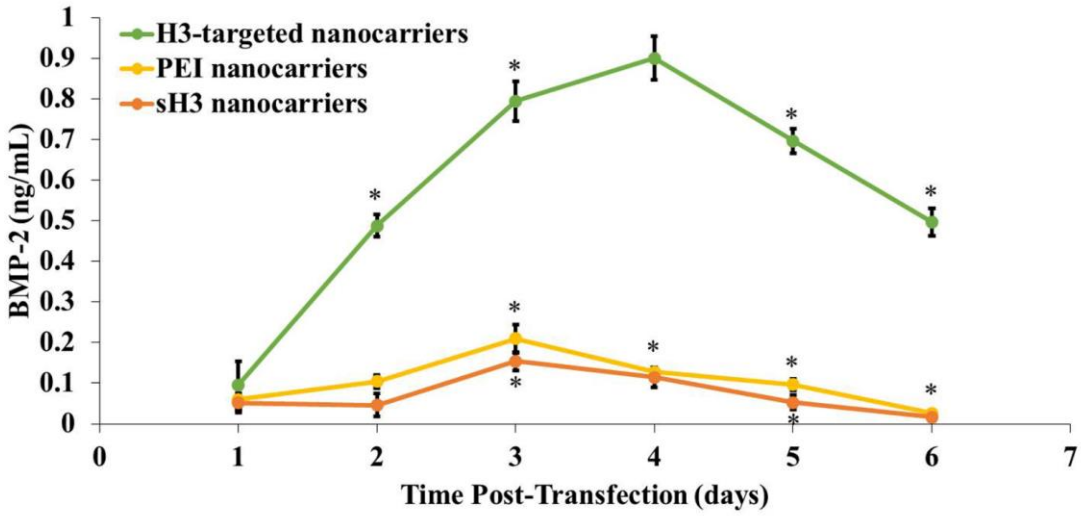

Figure 3.3: Amount of BMP-2 accumulation in the cell culture supernatant following a single transfection with the indicated nanocarriers. All results are shown as the mean ± standard deviation of data collected from 3 independent experiments. * Indicates a significant difference from the previous time point ($p < 0.05$).

3.3.3 Chondrogenic Differentiation Potential

After verifying the ability of H3-targeted nanocarriers to improve osteogenic growth factor expression over the course of 6 days, we next sought to determine whether this enhanced and prolonged expression could ultimately augment MSC differentiation and proliferation along chondrogenic cellular lineages. BMP-2 is a potent inducer of chondrogenic differentiation, and thus we hypothesized that its increased levels in the supernatant following H3-targeted transfection would result in more robust levels of chondrogenesis when compared to cells transfected with control nanocarriers (sH3 and PEI). In addition, we hypothesized that localized, cell-mediated production of BMP-2 by MSCs would induce higher levels of chondrogenesis than the levels in MSCs that received a dose of exogenously applied recombinant BMP-2 protein (rhBMP-2). For these comparative studies, we treated cells with a single dose

of rhBMP-2 at a concentration of 1 ng/mL, similar to the maximum concentration of BMP-2 that accumulated in the cell culture supernatant following H3-targeted transfection (Figure 3.3). Additionally, to evaluate the maximum activity that would result from a large supply of growth factor, we compared each of these treatments to the result in MSCs subjected to a sustained dose of rhBMP-2 at a concentration of 100 ng/mL. Such high and repeated doses of rhBMP-2 mimic the growth factor delivery regimens used in bone repair studies. These dosing schemes are also known to induce chondrogenic differentiation in MSCs,[35, 36] and thus were designed to serve as a positive control. A schematic depicting the BMP-2 gene and protein dosing timelines in MSCs is compared with a general timeline of MSC chondrogenic differentiation in Figure 3.4.

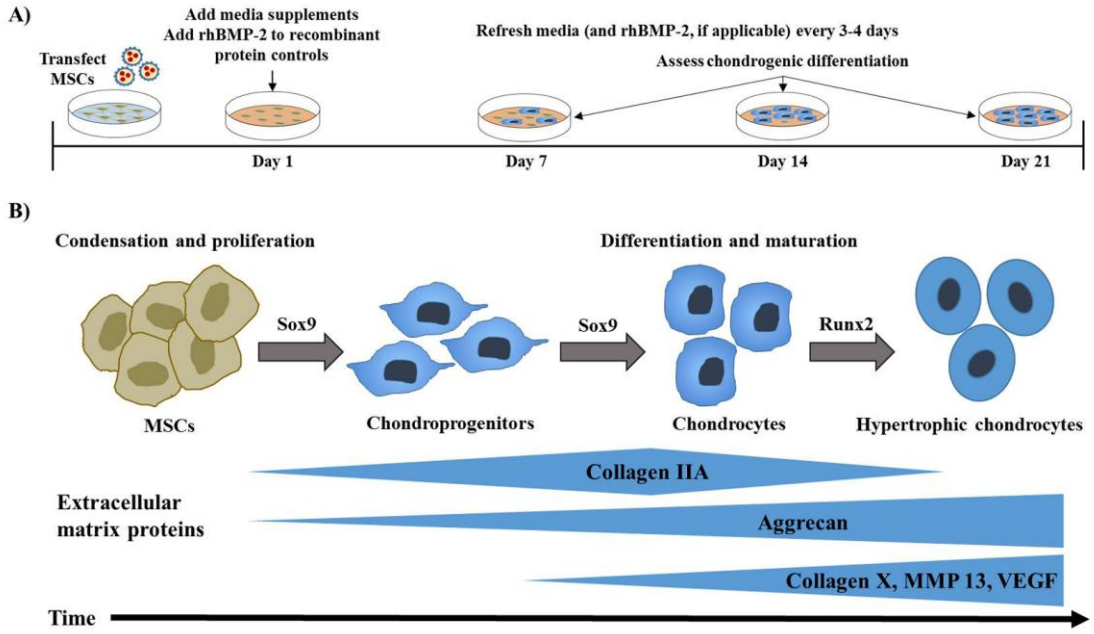

Figure 3.4: Schematic depictions of the experimental timeline versus the timeline for native chondrogenic differentiation. (A) Following a single transfection, MSCs were maintained in chondrogenic media until the specified time points for analysis. Untransfected cells (with or without rhBMP-2) were maintained in parallel. (B) Simplified timeline of MSC chondrogenesis and the major transcription factors and ECM proteins expressed. Thicker ramps correspond to higher expression levels.

3.3.4 Chondrogenic Extracellular Matrix Formation

To qualitatively confirm that active chondrogenesis was occurring in MSCs treated with the different BMP-2 gene or protein applications, extracellular proteoglycan deposition was analyzed. Proteoglycans such as aggrecan, decorin, and annexin are produced and secreted by actively proliferating chondrocytes,[37] and these proteoglycans help form the intermediate cartilage matrix necessary for mineralization and endochondral ossification to form mature bone.[38] Proteoglycans are heavily modified with glycosaminoglycans (GAGs), which are easily stained with cationic dyes. To that end, Alcian blue staining was used to identify intermediary cartilage

matrix formation on days 7, 14, and 21 post-treatment (Figure 3.5). GAG deposition is indicated if the area surrounding the cells is stained dark blue. For untreated MSCs, no extracellular staining was observed at any time point, and the only staining observable was punctate staining of chromatin within the nuclei of cells. Similarly, MSCs transfected with sH3 and PEI control nanocarriers, as well as MSCs treated with a single dose of rhBMP-2 (1 ng/mL), did not exhibit any significant levels of GAG deposition over the course of 3 weeks. In contrast, extracellular GAG deposition following H3-targeted nanocarrier transfection was observed by day 7, and this staining continued to increase over the 3 week time period, indicating the presence of mature and active chondrocytes. Interestingly, GAG deposition levels on days 7 and 14 following H3-targeted transfection were similar to the levels obtained following repeated treatments with 100 ng/mL rhBMP-2. By day 21, excessive cellular proliferation and nutrient depletion from continuous cell culture in the presence of excess rhBMP-2 prevented effective Alcian blue staining analysis. Overall, these results suggested that H3-targeted gene therapy could trigger more robust levels of chondrogenesis in MSCs when compared to either untargeted gene nanocarriers or MSCs treated with equivalent amounts of rhBMP-2. Notably, 100-fold excess rhBMP-2, as compared with the maximum BMP-2 expression levels in H3 transfected cells, was required to achieve similar GAG deposition.

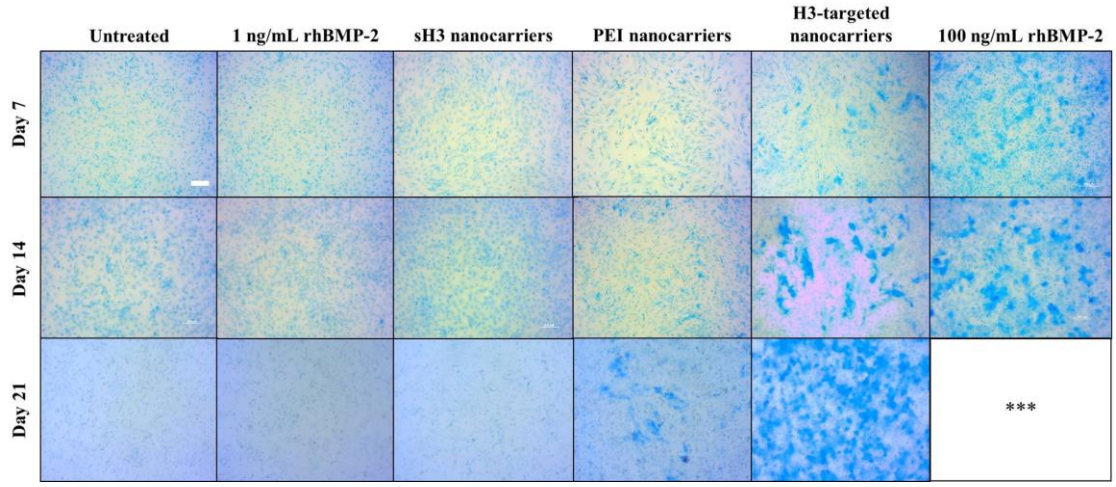

Figure 3.5: Representative light microscopy images of Alcian blue staining of 10T1/2 MSCs on days 7, 14, and 21 showing extracellular GAG deposition following transfection with the indicated nanocarriers, or treatment with the indicated doses of rhBMP-2. *** Sample could not be accurately analyzed due to significant over-proliferation and cell crowding. Scale bar = 200 μm.

3.3.5 Chondrogenic mRNA Expression

To further confirm the ability of H3-targeted gene transfer to augment chondrogenic differentiation in MSCs, we quantitatively monitored changes in both mRNA and protein expression of specific chondrogenic markers over the course of 2 weeks. We examined the expression of extracellular matrix (ECM) protein markers indicative of either early- or late-stage chondrogenesis (Figure 3.4). Early-stage markers included collage type IIA (COL IIA) and aggrecan (Acan), both of which form the major structural components of the intermediary cartilage matrix secreted by active chondrocytes.[37] Late-stage markers included collagen type X (COL X) and matrix-metalloproteinase 13 (MMP 13), both of which function to restructure the cartilage matrix in preparation for mineralization and osteoclast invasion, indicative of fully mature hypertrophic chondrocyte formation.[38] Acan also continues to be

expressed during hypertrophy.[37] The mRNA expression levels for each of these chondrogenic markers were analyzed on days 7 and 14 post-transfection/treatment (Figures 3.6 and 3.7) using the real-time quantitative reverse transcription polymerase chain reaction (RT-qPCR) with primers specific to COL IIA, Acan, MMP 13, and COL X (Figure A.1). mRNA expression in all treated samples was analyzed relative to the mRNA levels expressed by untreated MSCs. Day 7 RT-qPCR analysis of early-stage chondrogenic markers indicated an approximate 3-fold enhancement in COL IIA mRNA and a 50-fold enhancement in Acan mRNA (Figure 3.6) in MSCs transfected with H3-targeted nanocarriers. In contrast, MSCs transfected with untargeted control nanocarriers or MSCs treated with equivalent amounts of rhBMP-2 displayed no significant increases in COL IIA or Acan mRNA expression relative to untreated controls. Additionally, both COL IIA and Acan mRNA expression levels had increased by day 14 following H3-targeted transfection to approximately 5-fold and 500-fold the levels in untreated MSCs, respectively, while MSCs treated with untargeted nanocarriers and 1 ng/mL rhBMP-2 remained unchanged. Interestingly, by day 14 both COL IIA and Acan mRNA expression levels in cells treated with H3-targeted nanocarriers exceeded those levels in MSCs treated with 100-fold excess rhBMP-2.

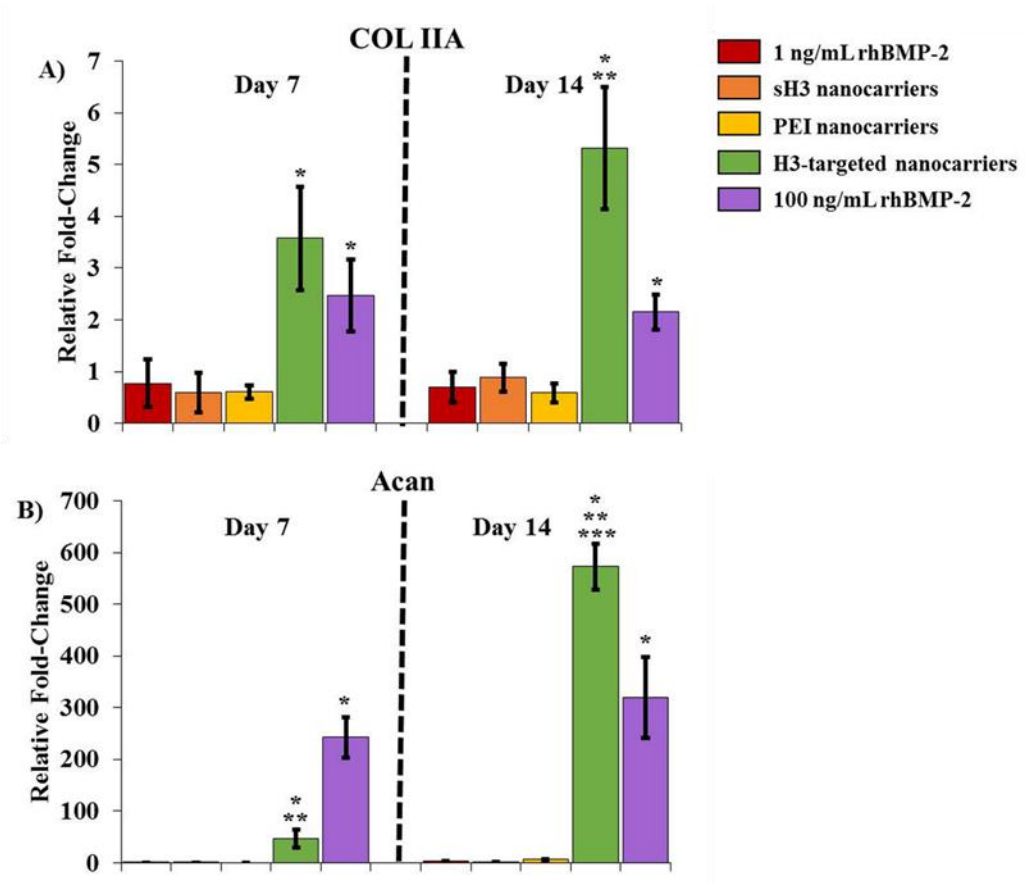

Figure 3.6: Cartilage-specific mRNA expression of collagen IIA (COL IIA) and aggrecan (Acan) on day 7 and 14 post-transfection/treatment. Each data point represents the mean ± standard deviation based upon data from 3 independent experiments. * Indicates a significant difference from 1 ng/mL rhBMP-2, sH3, and PEI nanocarriers ($p < 0.05$). ** Indicates a significant difference from 100 ng/mL rhBMP-2 ($p < 0.05$). *** Indicates a significant difference from previous time point ($p < 0.05$).

Similar trends in mRNA expression were observed when analyzing late-stage chondrogenic markers. By day 14, the mRNA expression levels of both MMP 13 and COL X (Figure 3.7) in MSCs transfected with H3-targeted nanocarriers had increased significantly, by approximately 20-fold and 200-fold, respectively, relative to the untreated controls. In comparison, mRNA expression levels from control samples

treated with 1 ng/mL rhBMP-2 or untargeted nanocarriers remained unchanged. Interestingly, by day 14, MSCs transfected with H3-targeted nanocarriers exhibited higher levels of COL X mRNA expression relative to MSCs treated with 100-fold excess rhBMP-2, but lower levels of MMP 13 mRNA expression. Expression of both MMP 13 mRNA and COL X mRNA was evident as early as day 7 post-transfection with H3-targeted nanocarriers or post-treatment with 100 ng/mL rhBMP-2. Taken together, these RT-qPCR analyses further corroborated the findings that H3-targeted gene transfer approaches could enable significant improvements in chondrogenic MSC differentiation relative to recombinant protein therapy.

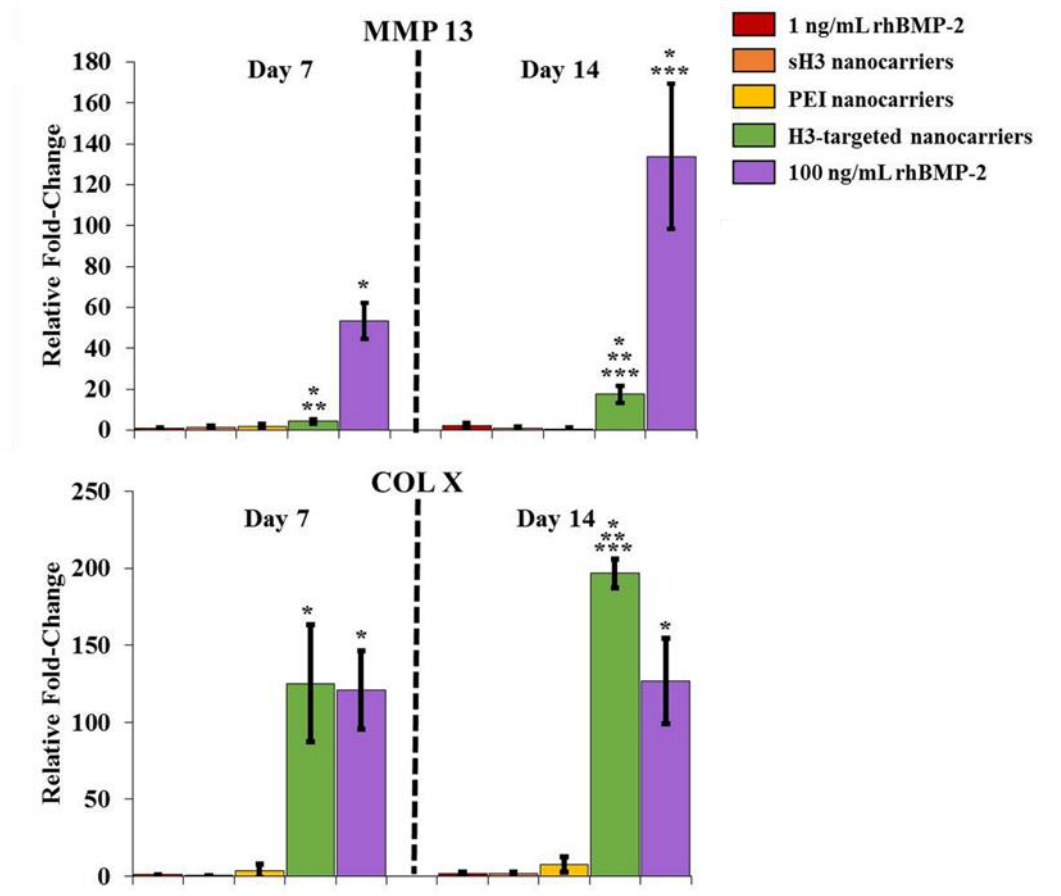

Figure 3.7: Cartilage-specific mRNA expression of matrix-metalloproteinase 13 (MMP 13) and collagen X (COL X) on day 7 and 14 post-transfection/treatment. Each data point represents the mean ± standard deviation based upon data from 3 independent experiments. * Indicates a significant difference from 1 ng/mL rhBMP-2, sH3, and PEI nanocarriers ($p < 0.05$). ** Indicates a significant difference from 100 ng/mL rhBMP-2 ($p < 0.05$). *** Indicates a significant difference from previous time point ($p < 0.05$).

3.3.6 Chondrogenic Protein Expression

After verifying that the H3-targeted nanocarriers were inducing increased mRNA expression levels of early- and late-stage chondrogenic markers, we next sought to analyze corresponding changes in protein expression using Western blotting

(Figures 3.8 and 3.9). The protein expression levels of COL IIA, MMP 13, and COL X were evaluated in MSCs at day 7 and 14 following BMP-2 transfection or treatment with rhBMP-2, and these levels were calculated relative to the expression levels in untreated MSCs. As shown in Figure 3.8, COL IIA protein expression was significantly enhanced (~1.8-fold increase) at day 7 following H3-targeted transfection, and these COL IIA protein levels were equivalent to the levels in MSCs treated with 100-fold excess rhBMP-2. By day 14, COL IIA protein expression had decreased back to its basal level, consistent with the timing of COL IIA expression during native progression through chondrogenesis (Figure 3.4). In contrast, MSCs treated with untargeted nanocarriers or equivalent amounts of rhBMP-2 did not exhibit any significant enhancements in COL IIA expression at either day 7 or day 14. Investigation of MMP 13 protein expression showed a significant increase in cells transfected with H3-targeted nanocarriers (Figure 3.9), from basal expression at day 7 to a 1.2-fold increase by day 14, equivalent to the expression level in MSCs treated with 100-fold excess rhBMP-2. Again, no significant enhancements in MMP 13 protein expression were observed in MSCs treated with untargeted nanocarriers or equivalent amounts of rhBMP-2. As expected, the protein expression patterns of COL X were similar to those of MMP 13 (Figure 3.9). By day 14, COL X exhibited an approximate 1.6-fold increase in expression following H3-targeted transfection or treatment with 100-fold excess rhBMP-2, relative to untreated MSCs. Interestingly, MSCs treated with a single dose of rhBMP-2, equivalent to the maximum accumulated BMP-2 following H3-targeted transfection, also exhibited a slight increase (1.2-fold) in COL X protein expression relative to untreated MSCs at day 14. However, this fold-increase in expression was significantly less than the increase induced by H3-

targeted transfection. Collectively, these data further confirm the ability of H3-targeted gene transfer to trigger robust chondrogenesis in MSCs, by enhancing chondrocyte proliferation from early to late hypertrophic stages in preparation for matrix mineralization and ossification. Most importantly, these enhancements are equivalent to those achieved through repeated dosing of MSCs with 100-fold excess rhBMP-2, suggesting the capacity for enabling substantial reductions in growth factor dosing using H3-targeted gene therapy for bone regenerative applications.

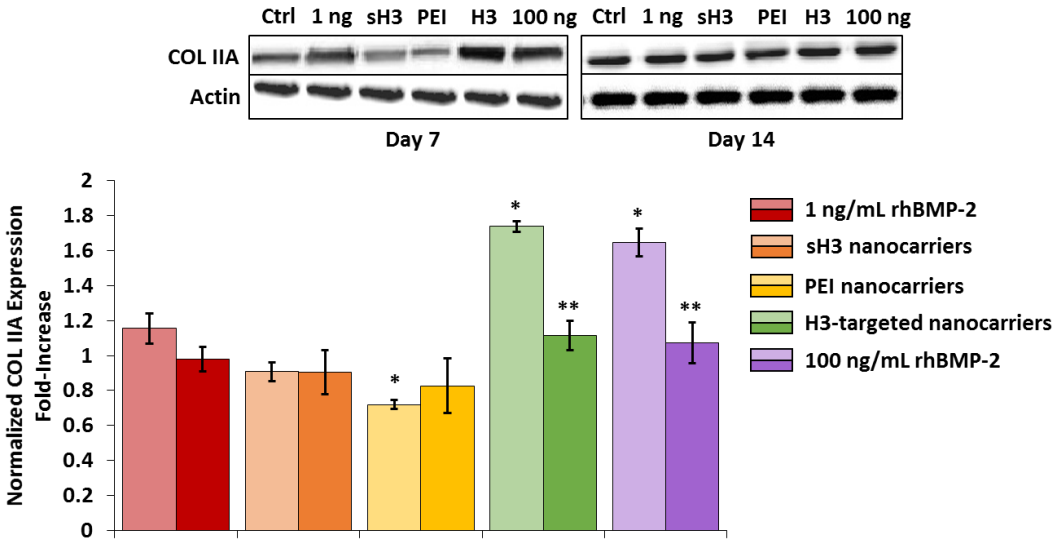

Figure 3.8: Cartilage-specific protein expression of collagen IIA (COL IIA) on day 7 (faded bars) and day 14 (solid bars) with representative Western blot images of the indicated proteins. All data represent the protein expression levels relative to the levels of the loading control β-actin, normalized to the native protein levels in untreated controls. All values in are shown as the mean ± standard deviation of data obtained from 3-5 separately prepared and analyzed samples. * Indicates a significant difference from the untreated control ($p < 0.05$). ** Indicates a significant difference from the previous time point ($p < 0.05$).

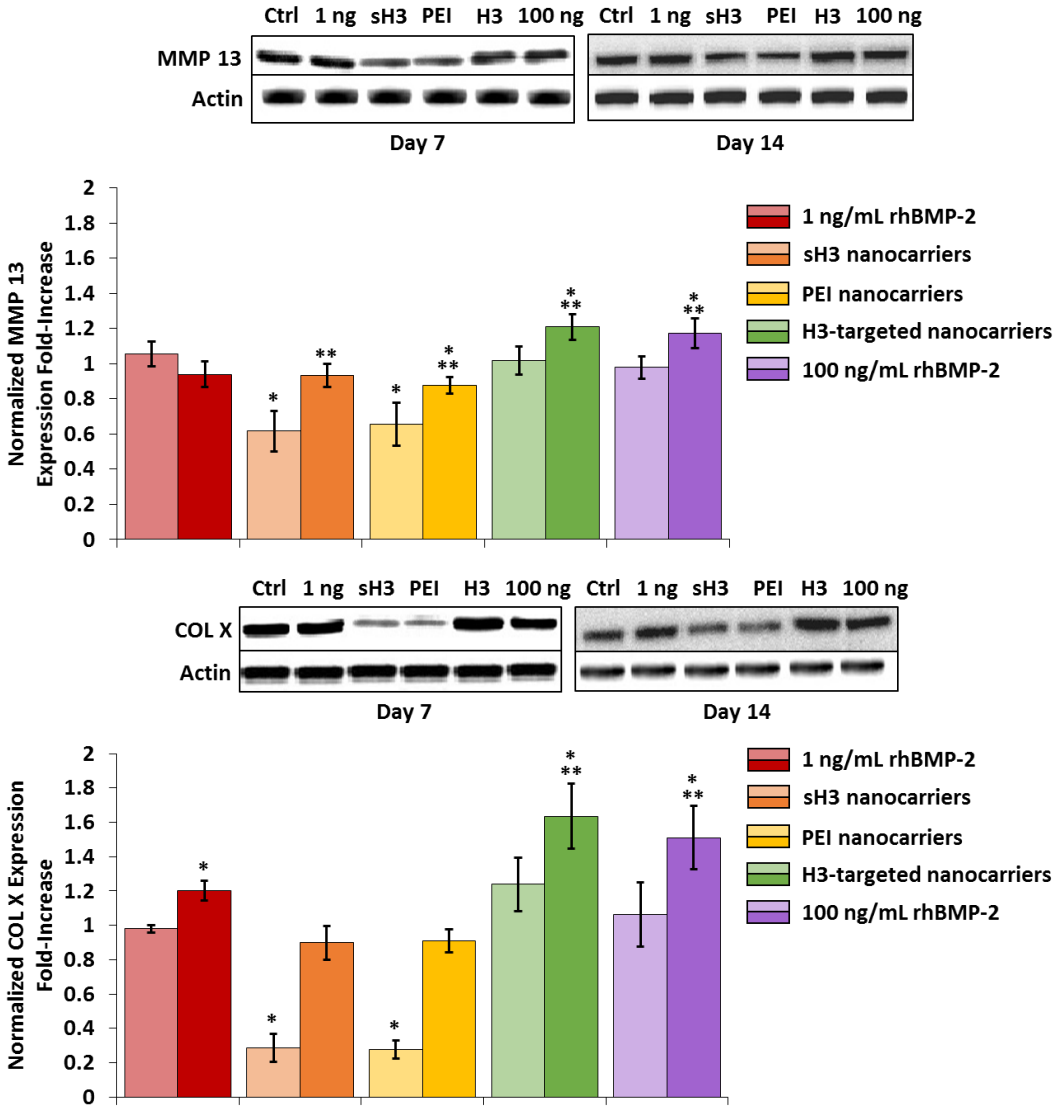

Figure 3.9: Cartilage-specific protein expression of matrix-metalloproteinase 13 (MMP 13) and collagen X (COL X) on day 7 (faded) and day 14 (solid) with representative Western blot images of the indicated proteins. All data represent the protein expression levels relative to the levels of the loading control β-actin, normalized to the native protein levels in untreated controls. All values are shown as the mean ± standard deviation of data obtained from 3-5 separately prepared and analyzed samples. * Indicates difference from the untreated control ($p < 0.05$). ** Indicates difference from the previous time point ($p < 0.05$).

3.3.7 Mechanisms Underlying H3-Targeted Chondrogenic Enhancement

The ability of H3-targeted gene transfer to improve chondrogenesis in MSCs as compared with either untargeted gene carriers or equivalent amounts of recombinant protein suggested that a more global change in cellular behavior was occurring in response to H3-targeted BMP-2 expression. We hypothesized that the enhanced MSC-mediated expression of growth factor would result in both improved MSC proliferation/condensation in preparation for differentiation, as well as increased activation of major regulatory factors driving chondrogenesis. To test this, we examined changes in the protein expression of the transcription factors Sox9 and Runt-related transcription factor 2 (Runx2) induced by either BMP-2 transfection or treatment with rhBMP-2 (Figure 3.10). Sox9 plays an essential role in activating MSC condensation prior to chondrogenesis,[39, 40] and continues to activate genes essential to driving the initial stages of chondrogenic differentiation. Runx2 plays an essential role in driving matrix mineralization and helps to promote chondrocyte hypertrophy.[38, 39] As shown in Figure 3.10A, an approximate 1.5-fold increase in Sox9 protein expression in MSCs was observed by day 7 in cells transfected with H3-targeted nanocarriers, relative to untreated MSCs. This increase in Sox9 expression was equivalent to Sox9 expression in MSCs that had been treated with 100-fold excess rhBMP-2. In fact, Sox9 transcription factor activation was observed as early as 48 h post-transfection with H3-targeted nanocarriers (Figure 3.11). In contrast, Sox9 expression remained unchanged in MSCs following transfection with untargeted nanocarriers or treatment with equivalent amounts of rhBMP-2. Similar protein expression trends were observed for Runx2 on day 14 in both H3-targeted transfected cells and 100 ng/mL rhBMP-2 treated cells (Figure 3.10B), which displayed approximately 1.5- and 1.4-fold increases, respectively, in Runx2 protein relative to

untreated MSCs. Collectively, these data suggest that growth factor expression following H3-targeted gene transfer functions to activate MSC cellular mechanisms that drive condensation and chondrogenesis more efficiently than either untargeted gene transfer or topically applied recombinant protein therapy.

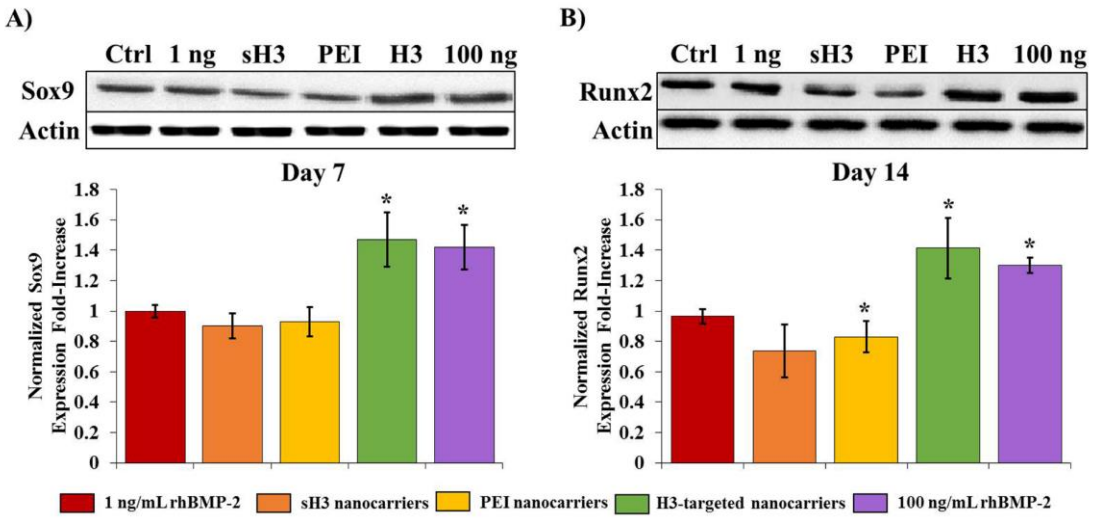

Figure 3.10: Representative Western blot analyses and quantification of A) Sox9 and B) Runx2 transcription factor protein expression levels at day 7 and day 14 respectively. All data represent the protein expression levels relative to the loading control β-actin, normalized to the native protein levels in untreated controls. All values are shown as the mean ± standard deviation of data obtained from 4 separately prepared and analyzed samples. * Indicates a significant difference from the untreated control ($p < 0.05$).

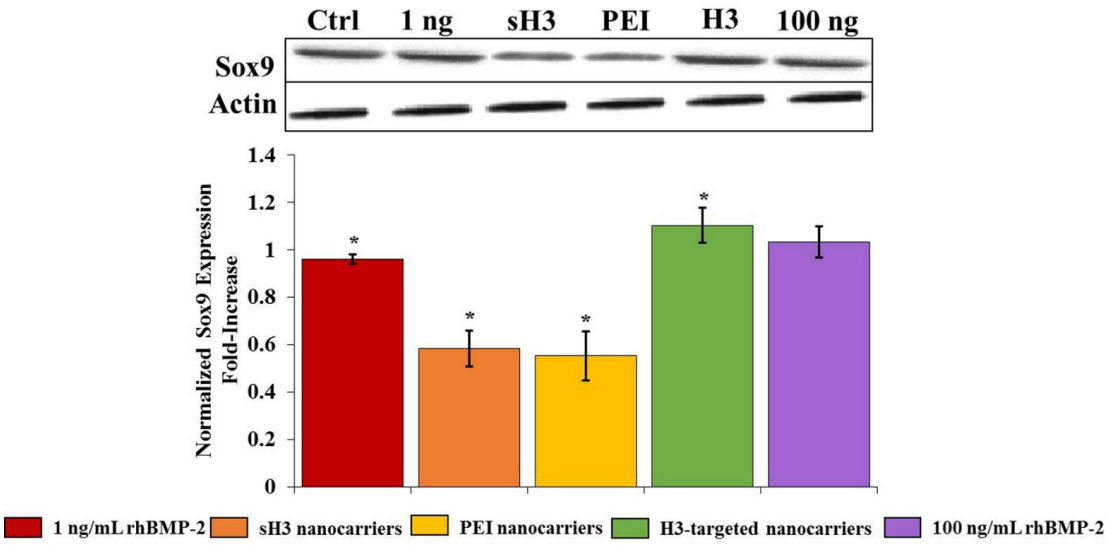

Figure 3.11: Representative Western blot analysis and quantification of transcription factor Sox9 protein expression on day 2 post-transfection with the indicated nanocarriers or post-treatment with rhBMP-2. All data represent the protein expression levels relative to the levels in the loading control β-actin, normalized to the native protein levels in untreated/untransfected controls. All values are shown as the mean ± standard deviation of data obtained from 5 separately prepared and analyzed samples. * Indicates a significant difference from the untreated/untransfected control ($p < 0.05$).

3.4 Discussion

Non-viral gene therapy possesses enormous potential to improve fracture healing, as the rapidly dividing cells within the fracture site are an ideal target for gene transfection with enhanced efficiency. Local, transient expression of key growth factors by these cells can stimulate the healing response to enable significant reductions in exogenous growth factor stimulation required to initiate bone repair cascades. Many non-viral gene nanocarriers have a critical limitation of low transfection efficiency. Accordingly, this study sought to address this challenge by utilizing a materials design approach aimed toward improved gene transfer, and

ultimately improved growth factor production, to accelerate MSC differentiation and thereby enable faster fracture healing. Our studies document the first examination of histone-targeted nanocarriers for bone regenerative applications and demonstrate their utility in triggering more robust levels of chondrogenic differentiation, an essential first step in the bone repair process, as compared with exogenously applied recombinant growth factor proteins. An unprecedented finding was that nearly 100-fold excess recombinant growth factor was required to produce similar levels of chondrogenic mRNA and protein expression, illustrating the importance of well-controlled non-viral nanocarrier design for the advancement of bone defect management.

In our previous investigations, we demonstrated that H3-targeting improves gene transfer by shuttling nanocarriers away from traditional endosome escape pathways to vesicular transport pathways that localize to the ER and drive nuclear delivery, similar to native pathogen trafficking.[41-43] This altered intracellular trafficking and improved nuclear delivery was conferred via nanocarrier interactions with H3 effectors involved in native retrograde transport[31] and nuclear import during mitosis.[44] Such findings motivated the analyses herein to determine whether this improved nuclear delivery and expression in actively dividing cells could be exploited to enhance osteogenic growth factor expression, coordinated with increases in MSC proliferation, leading to enhanced differentiation along cellular lineages essential to bone regeneration.

GFP transfection studies and cellular viability analyses demonstrated that H3-targeting could enable distinct improvements in gene transfer and reductions in cytotoxicity in MSCs compared with untargeted PEI nanocarriers. Closer examination

of cellular morphology post-transfection revealed the detrimental cytotoxic effects PEI nanocarriers exhibited in MSCs (Figure 3.1A). The phase contrast images show a significant reduction in total number of MSCs still adhered to the plate following transfection with PEI nanocarriers. This substantial loss in cell surface coverage due to the PEI polymer was reflected in Figure 3.2B, showing a near 5-fold reduction in the number of live cells post-transfection with PEI nanocarriers. These cell surface reductions also explain the discrepancy between the levels of transfection observed by fluorescence microscopy (Figure 3.1A) versus what was quantified with flow cytometry (Figure 3.1B). Since flow cytometry and fluorescence microscopy analyze different cell populations (live cells versus total cells, respectively), the level of transfection as observed by fluorescence microscopy appeared visually lower than that observed by flow cytometry.

Examination of osteogenic BMP-2 growth factor expression indicated a substantial increase in the levels of BMP-2 secreted into the extracellular space following transfection with H3-targeted nanocarriers. BMP-2 remained present in the cell culture supernatant for 6 days following a single transfection. This was a surprising result, given the fact that non-viral transfections are transient in nature. Many growth factors, including BMPs, are natively sequestered by components of the ECM, such as proteoglycans, elastins, and collagens, in order to regulate their activity.[45] BMP-2 itself is known to bind collagen,[46, 47] which has been used as a means to enhance therapeutic activity of rhBMP-2 via prolonged release.[48-50] Sustained and localized release from ECM scaffolds can greatly enhance the half-life of rhBMP-2 from ~7 min (following systemic administration) to several days.[49, 51] As these experiments were conducted on collagen type I coated culture plates, it is

possible that the collagen functioned to sequester the initially expressed BMP-2 to some extent, prolonging its release to the cell culture supernatant. In addition, our previous investigations using histone-targeted nanocarriers demonstrated that the H3 tail functioned to retain nanocarriers in the nucleus of cells post-mitosis.[15] This prolonged nuclear retention may have helped promote gradual gene expression over the course of several days. Together, these factors could have contributed to sustained BMP-2 expression over a period of 6 days.

The capacity for prolonged BMP-2 accumulation in the cell culture supernatant following H3-targeted transfection prompted us to examine the potential of the expressed BMP-2 to induce chondrogenic differentiation in MSCs. In particular, we sought to demonstrate the advantage of histone-targeted gene therapy by triggering increased chondrogenic differentiation following transfection than the levels achieved via a single equivalent dose of recombinant BMP-2 protein. Analyses of proteoglycan deposition (Figure 3.5), mRNA expression (Figures 3.6 and 3.7), and protein expression (Figures 3.8 and 3.9) of key chondrogenic markers illustrated a clear progression from early- to late-stage chondrogenesis (Figure 3.4), consistent with the literature,[37] following H3-targeted gene transfer. Furthermore, a 1.8-fold increase in vascular endothelial growth factor (VEGF) was observed by day 14 (Figure 3.12), indicating that the mature chondrocytes were beginning to prepare the intermediate cartilage matrix for vascular invasion and ossification by osteoclasts, an essential step for the replacement of cartilage by bone.[38, 52]

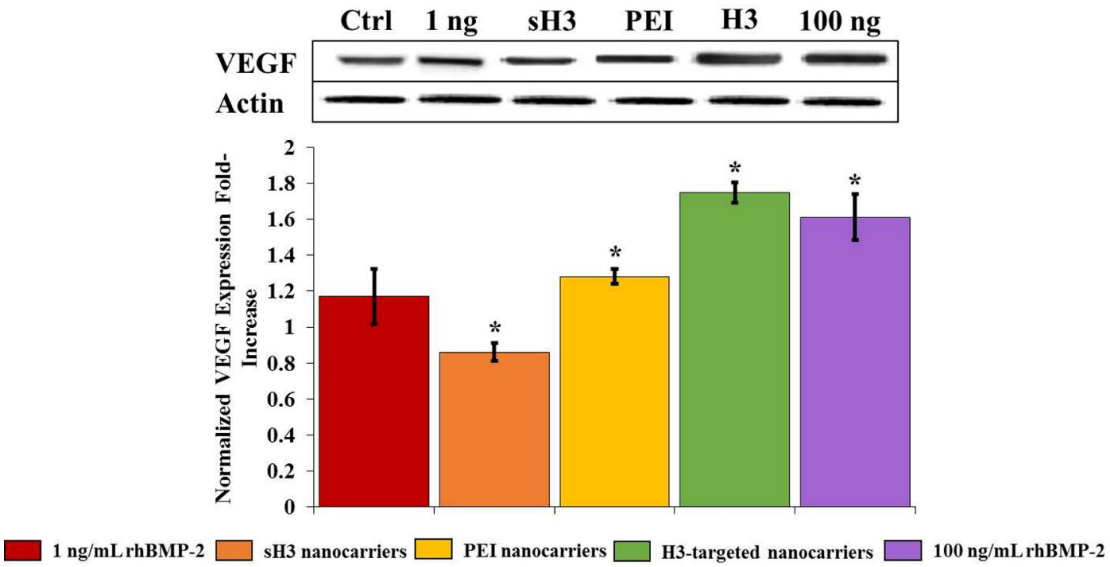

Figure 3.12: Representative Western blot analysis and quantification of vascular endothelial growth factor (VEGF) protein expression on day 14 post-treatment with rhBMP-2 or transfection with the indicated nanocarriers. All data represent the protein expression levels relative to the levels in the loading control β-actin, normalized to the native protein levels in untreated/transfected controls. All values are shown as the mean ± standard deviation of 3 separately prepared and analyzed samples. * Indicates a significant difference from the untreated/transfected control ($p < 0.05$).

In contrast, MSCs treated with a single equivalent dose of rhBMP-2 (1 ng/mL) displayed no indications of chondrogenic differentiation, with the exception of a slight enhancement in COL X protein expression on day 14 post-treatment. This considerable discrepancy between gene and protein therapy was partially explained by the absence of any transcription factor activation following rhBMP-2 treatment (Figures 3.10 and 3.11). Expression of Sox9 is essential to MSC progression through the early stages of chondrogenesis (Figure 3.4) and is responsible for the activation of both COL IIA and Acan genes in proliferating chondrocytes.[53] Similarly, Runx2 is an

important driver of terminal chondrogenic differentiation and has been shown to activate MMP 13 and COL X genes in hypertrophic chondrocytes.[38, 54] Without the coordinated expression of these transcription factors, chondrogenic differentiation is not possible. In addition, by delivering the BMP-2 plasmid, we expect that we were able to achieve more natural expression profiles of the fully mature BMP-2 protein, with native post-translational modifications (PTMs) and more similar BMP-2 induction kinetics. BMPs require PTMs to enable their biological stability and activity,[55] and hence the absence of appropriate PTMs in topical rhBMP-2 application may have contributed to the insignificant levels of chondrogenic differentiation achieved using equivalent rhBMP-2 doses in our investigations. Furthermore, it is likely that the increased cell-cell interactions established during the first few days of culture functioned to amplify both transcription factor and native BMP signaling, since MSC condensation and cellular communication are required for chondrogenic differentiation.[37] The gap junctions formed between MSCs are thought to play essential roles in triggering signal transduction pathways, and have been shown to operate in conjunction with growth factor mediated chondrogenesis *in vitro*.[56]

Due to the short systemic half-life of rhBMP-2,[57] sustained and localized delivery of excess recombinant growth factor is often required to initiate bone repair cascades in both *in vitro* and *in vivo* models of bone regeneration.[58] To simulate these approaches, we subjected MSCs to repeated doses of excess rhBMP-2 at concentrations known to initiate chondrogenic differentiation *in vitro* (100 ng/mL).[59, 60] The amount of rhBMP-2 used in these studies was over 100-fold greater than the maximum accumulation of nascent BMP-2 achieved following a single H3-targeted transfection (Figure 3.3). At these high repeated doses, MSCs in this study were

shown to successfully undergo chondrogenic differentiation. In comparing the experimental results from these repeated excess rhBMP-2 treatments to those achieved with a single H3-targeted gene transfection, it is interesting to note the similarities in overall expression levels of chondrogenic markers. Equivalent levels of ECM protein expression (Figure 3.8 and 3.9), transcription factor expression (Figures 3.10 and 3.11), and proteoglycan deposition (Figure 3.5) were observed on days 7 and 14 following repeated excess rhBMP-2 treatment and H3-targeted gene transfer, demonstrating the utility of H3-targeting to enable reductions in growth factor dosing.

It is interesting to note that the mRNA expression levels of COL IIA (Figure 3.6), Acan (Figure 3.6), and COL X (Figure 3.7) remained unchanged from day 7 to day 14 following excess rhBMP-2 treatment, despite the changes that were observed in protein expression of these same factors (Figures 3.8 and 3.9). Although there is not always a direct correlation between mRNA and protein expression levels, the unchanged mRNA expression may indicate a difference in cellular behavior in response to excess rhBMP-2 treatment. Studies of MSC chondrogenesis *in vitro* have shown that BMP treatment induces proliferation[37] and drives terminal chondrocyte hypertrophy[38, 61] in a dose dependent manner. Hypertrophic chondrocytes increase in cell volume, degrading the ECM around them, and ultimately undergo cell death in preparation for osteoclast invasion and mineralization.[38] Thus, overstimulation with excess rhBMP-2 likely enhanced the rate of cell death by increasing chondrogenic hypertrophy and promoting over-proliferation which led to cell crowding and depletion of necessary nutrients. These cell culturing effects became especially pronounced by day 21, at which point cellular overcrowding and cell death prohibited effective analysis of GAG deposition with Alcian blue following excess rhBMP-2

(100 ng/mL) treatment. In contrast, GAG deposition was significantly enhanced from day 14 to day 21 following H3-targeted nanocarrier treatment (Figure 3.5), indicating the presence of healthy chondrocytes that were actively secreting and forming a mature cartilage matrix. In the context of fracture healing and endochondral ossification, healthy cartilage matrix formation is critical to ensure mature bone integrity. This further demonstrates the utility of a histone-targeted gene-based approach to better enable natural progression through the complex signaling cascades of bone repair, and avoid any over-proliferation/cell death that may result from excess recombinant protein treatment.

In contrast to MSCs transfected with H3-targeted nanocarriers, untargeted PEI nanocarriers and sH3 nanocarriers did not trigger any significant levels of chondrogenic differentiation in MSCs. The cytotoxicity associated with the untargeted PEI nanocarriers likely played a key role in hindering chondrogenesis, as evidenced by the decreased fold-changes in protein expression of certain ECM and transcription factor proteins. Figure 3.5 shows evidence of GAG deposition following untargeted PEI nanocarrier transfection on days 14 and 21. In addition, PEI transfected cells also displayed a minor 1.3-fold increase in VEGF expression by day 14 (Figure 3.12). As these MSCs recovered from PEI transfection they likely began to proliferate in isolated "colonies" rather than in a continuous monolayer. Since MSC condensation plays an important role chondrogenesis, the close proximity of these MSCs likely triggered chondrogenic differentiation, resulting in low observed levels of GAG deposition and VEGF expression. Finally, the insignificant levels of chondrogenesis triggered by sH3 nanocarriers strongly indicate that transfection alone

cannot drive chondrogenic differentiation, but requires elevated expression of native BMP-2 growth factor protein.

3.5 Conclusions

In this study, we observed that H3-targeted gene therapy functions to enhance transfection efficiency and reduce cytotoxicity in MSCs. H3-targeting resulted in a 4-fold enhancement in expression of the osteogenic growth factor BMP-2 compared to untargeted gene nanocarriers, and H3-transfected cultures maintained significant accumulation of BMP-2 in the cell culture supernatant over the course of 6 days. As a result of this prolonged expression, H3-targeting improved chondrogenic differentiation potential in MSCs, an important first step in the fracture healing process, over untargeted nanocarriers. More importantly, both qualitative and quantitative analyses of chondrogenic mRNA and protein expression demonstrated that a single transfection with H3-targeted nanocarriers could trigger more robust levels of chondrogenic differentiation in MSCs when compared to MSCs treated with a single equivalent dose of exogenously applied BMP-2 protein. In fact, a 100-fold increase in rhBMP-2 dosage was required to trigger similar levels of chondrogenic gene and protein expression. Analysis of transcription factor expression indicated that H3-targeted gene transfer functions to activate the MSC cellular processes that drive proliferation and chondrogenesis more efficiently than topically applied recombinant protein. Collectively, these findings demonstrate the utility of using histone-targeted gene transfer to gain more effective control over growth factor expression and MSC differentiation, and ultimately contribute to the overall advancement of gene therapy in the context of bone defect management.

REFERENCES

1. Phillips, J. E.; Gersbach, C. A.; Garcia, A. J., Virus-based gene therapy strategies for bone regeneration. Biomaterials 2007, 28 (2), 211-229.

2. Lieberman, J. R.; Daluiski, A.; Stevenson, S.; Wu, L.; McAllister, P.; Lee, Y. P.; Kabo, J. M.; Finerman, G. A. M.; Berk, A. J.; Witte, O. N., The effect of regional gene therapy with bone morphogenetic protein-2-producing bone-marrow cells on the repair of segmental femoral defects in rats. Journal of Bone and Joint Surgery-American Volume 1999, 81A (7), 905-917.

3. Baltzer, A. W. A.; Lattermann, C.; Whalen, J. D.; Wooley, P.; Weiss, K.; Grimm, M.; Ghivizzani, S. C.; Robbins, P. D.; Evans, C. H., Genetic enhancement of fracture repair: healing of an experimental segmental defect by adenoviral transfer of the BMP-2 gene. Gene Therapy 2000, 7 (9), 734-739.

4. Rundle, C. H.; Miyakoshi, N.; Kasukawa, Y.; Chen, S. T.; Sheng, M. H. C.; Wergedal, J. E.; Lau, K. H. W.; Baylink, D. J., In vivo bone formation in fracture repair induced by direct retroviral-based gene therapy with bone morphogenetic protein-4. Bone 2003, 32 (6), 591-601.

5. Raisin, S.; Belamie, E.; Morille, M., Non-viral gene activated matrices for mesenchymal stem cells based tissue engineering of bone and cartilage. Biomaterials 2016, 104, 223-237.

6. Santos, J. L.; Pandita, D.; Rodrigues, J.; Pego, A. P.; Granja, P. L.; Tomas, H., Non-Viral Gene Delivery to Mesenchymal Stem Cells: Methods, Strategies and Application in Bone Tissue Engineering and Regeneration. Current Gene Therapy 2011, 11 (1), 46-57.

7. Huang, Y. C.; Simmons, C.; Kaigler, D.; Rice, K. G.; Mooney, D. J., Bone regeneration in a rat cranial defect with delivery of PEI-condensed plasmid DNA encoding for bone morphogenetic protein-4 (BMP-4). Gene Therapy 2005, 12 (5), 418-426.

8. Sheyn, D.; Kimelman-Bleich, N.; Pelled, G.; Zilberman, Y.; Gazit, D.; Gazit, Z., Ultrasound-based nonviral gene delivery induces bone formation in vivo. Gene Therapy 2008, 15 (4), 257-266.

9. Geiger, F.; Bertram, H.; Berger, I.; Lorenz, H.; Wall, O.; Eckhardt, C.; Simank, H. G.; Richter, W., Vascular endothelial growth factor gene-activated matrix (VEGF(165)-GAM) enhances osteogenesis and angiogenesis in large segmental bone defects. Journal of Bone and Mineral Research 2005, 20 (11), 2028-2035.

10. Evans, C. H., Gene delivery to bone. Advanced Drug Delivery Reviews 2012, 64 (12), 1331-1340.

11. Evans, C. H., Gene therapy for bone healing. Expert Reviews in Molecular Medicine 2010, 12, 17.

12. Bleich, N. K.; Kallai, I.; Lieberman, J. R.; Schwarz, E. M.; Pelled, G.; Gazit, D., Gene therapy approaches to regenerating bone. Advanced Drug Delivery Reviews 2012, 64 (12), 1320-1330.

13. Fasbender, A.; Zabner, J.; Zeiher, B. G.; Welsh, M. J., A low rate of cell proliferation and reduced DNA uptake limit cationic lipid-mediated gene transfer to primary cultures of ciliated human airway epithelia. Gene Therapy 1997, 4 (11), 1173-1180.

14. Brunner, S.; Sauer, T.; Carotta, S.; Cotten, M.; Saltik, M.; Wagner, E., Cell cycle dependence of gene transfer by lipoplex polyplex and recombinant adenovirus. Gene Therapy 2000, 7 (5), 401-407.

15. Larsen, J. D.; Ross, N. L.; Sullivan, M. O., Requirements for the nuclear entry of polyplexes and nanoparticles during mitosis. J Gene Med 2012, 14 (9-10), 580-9.

16. Gabrielson, N. P.; Pack, D. W., Efficient polyethylenimine-mediated gene delivery proceeds via a caveolar pathway in HeLa cells. Journal of Controlled Release 2009, 136 (1), 54-61.

17. McLendon, P. M.; Fichter, K. M.; Reineke, T. M., Poly(glycoamidoamine) Vehicles Promote pDNA Uptake through Multiple Routes and Efficient Gene Expression via Caveolae-Mediated Endocytosis. Molecular Pharmaceutics 2010, 7 (3), 738-750.

18. Li, H.; Luo, T.; Sheng, R. L.; Sun, J. J.; Wang, Z.; Cao, A., Endoplasmic reticulum localization of poly(omega-aminohexyl methacrylamide)s conjugated with (L-)-arginines in plasmid DNA delivery. Biomaterials 2013, 34 (32), 7923-7938.

19. Fichter, K. M.; Ingle, N. P.; McLendon, P. M.; Reineke, T. M., Polymeric Nucleic Acid Vehicles Exploit Active Interorganelle Trafficking Mechanisms. Acs Nano 2013, 7 (1), 347-364.

20. Badding, M. A.; Vaughan, E. E.; Dean, D. A., Transcription factor plasmid binding modulates microtubule interactions and intracellular trafficking during gene transfer. Gene Therapy 2012, 19 (3), 338-346.

21. Wagstaff, K. M.; Fan, J. Y.; De Jesus, M. A.; Tremethick, D. J.; Jans, D. A., Efficient gene delivery using reconstituted chromatin enhanced for nuclear targeting. Faseb Journal 2008, 22 (7), 2232-2242.

22. Ciolina, C.; Byk, G.; Blanche, F.; Thuillier, V.; Scherman, D.; Wils, P., Coupling of nuclear localization signals to plasmid DNA and specific interaction of the conjugates with importin alpha. Bioconjugate Chemistry 1999, 10 (1), 49-55.

23. Misra, R.; Sahoo, S. K., Intracellular trafficking of nuclear localization signal conjugated nanoparticles for cancer therapy. European Journal of Pharmaceutical Sciences 2010, 39 (1-3), 152-163.

24. Cho, T. J.; Gerstenfeld, L. C.; Einhorn, T. A., Differential temporal expression of members of the transforming growth factor beta superfamily during murine fracture healing. Journal of Bone and Mineral Research 2002, 17 (3), 513-520.

25. Reilly, M. J.; Larsen, J. D.; Sullivan, M. O., Histone H3 tail peptides and poly(ethylenimine) have synergistic effects for gene delivery. Mol Pharm 2012, 9 (5), 1031-40.

26. Larsen, J. D.; Reilly, M. J.; Sullivan, M. O., Using the Epigenetic Code To Promote the Unpackaging and Transcriptional Activation of DNA Polyplexes for Gene Delivery. Molecular Pharmaceutics 2012, 9 (5), 1041-1051.

27. Schneider, C. A.; Rasband, W. S.; Eliceiri, K. W., NIH Image to ImageJ: 25 years of image analysis. Nature Methods 2012, 9 (7), 671-675.

28. Ye, J.; Coulouris, G.; Zaretskaya, I.; Cutcutache, I.; Rozen, S.; Madden, T. L., Primer-BLAST: A tool to design target-specific primers for polymerase chain reaction. Bmc Bioinformatics 2012, 13, 11.

29. Schmittgen, T. D.; Livak, K. J., Analyzing real-time PCR data by the comparative C-T method. Nature Protocols 2008, 3 (6), 1101-1108.

30. Eaton, G. J.; Zhang, S.; Diallo, C.; Matsuzawa, A.; Ichijo, H.; Steinbeck, M. J.; Freeman, T. A., Inhibition of apoptosis signal-regulating kinase 1 enhances endochondral bone formation by increasing chondrocyte survival. Cell Death & Disease 2014, 5, 11.

31. Ross, N. L.; Munsell, E. V.; Sabanayagam, C.; Sullivan, M. O., Histone-targeted Polyplexes Avoid Endosomal Escape and Enter the Nucleus During Postmitotic Redistribution of ER Membranes. Molecular Therapy-Nucleic Acids 2015, 4, 13.

32. Tsuji, K.; Bandyopadhyay, A.; Harfe, B. D.; Cox, K.; Kakar, S.; Gerstenfeld, L.; Einhorn, T.; Tabin, C. J.; Rosen, V., BMP2 activity, although dispensable for bone formation, is required for the initiation of fracture healing. Nature Genetics 2006, 38 (12), 1424-1429.

33. Salazar, V. S.; Gamer, L. W.; Rosen, V., BMP signalling in skeletal development, disease and repair. Nature Reviews Endocrinology 2016, 12 (4), 203-221.

34. Chen, D.; Zhao, M.; Mundy, G. R., Bone morphogenetic proteins. Growth Factors 2004, 22 (4), 233-241.

35. Wang, E. A.; Rosen, V.; Dalessandro, J. S.; Bauduy, M.; Cordes, P.; Harada, T.; Israel, D. I.; Hewick, R. M.; Kerns, K. M.; Lapan, P.; Luxenberg, D. P.; McQuaid, D.; Moutsatsos, I. K.; Nove, J.; Wozney, J. M., Recombinant Human Bone Morphogenetic Protein Induces Bone-Formation. Proceedings of the National Academy of Sciences of the United States of America 1990, 87 (6), 2220-2224.

36. Wozney, J. M., Overview of bone morphogenetic proteins. Spine 2002, 27 (16), S2-S8.

37. Gadjanski, I.; Spiller, K.; Vunjak-Novakovic, G., Time-Dependent Processes in Stem Cell-Based Tissue Engineering of Articular Cartilage. Stem Cell Reviews and Reports 2012, 8 (3), 863-881.

38. Mackie, E. J.; Ahmed, Y. A.; Tatarczuch, L.; Chen, K. S.; Mirams, M., Endochondral ossification: How cartilage is converted into bone in the developing skeleton. International Journal of Biochemistry & Cell Biology 2008, 40 (1), 46-62.

39. Chen, H. Y.; Ghori-Javed, F. Y.; Rashid, H.; Adhami, M. D.; Serra, R.; Gutierrez, S. E.; Javed, A., Runx2 Regulates Endochondral Ossification Through Control of Chondrocyte Proliferation and Differentiation. Journal of Bone and Mineral Research 2014, 29 (12), 2653-2665.

40. Akiyama, H., Control of chondrogenesis by the transcription factor Sox9. Modern Rheumatology 2008, 18 (3), 213-219.

41. Sandvig, K.; VanDeurs, B., Endocytosis, intracellular transport, and cytotoxic action of shiga toxin and ricin. Physiological Reviews 1996, 76 (4), 949-966.

42. Mallard, F.; Antony, C.; Tenza, D.; Salamero, J.; Goud, B.; Johannes, L., Direct pathway from early/recycling endosomes to the Golgi apparatus revealed through the study of Shiga toxin B-fragment transport. Journal of Cell Biology 1998, 143 (4), 973-990.

43. Goff, S. P., Host factors exploited by retroviruses. Nature Reviews Microbiology 2007, 5 (4), 253-263.

44. Ross, N. L.; Sullivan, M. O., Importin-4 Regulates Gene Delivery by Enhancing Nuclear Retention and Chromatin Deposition by Polyplexes. Molecular Pharmaceutics 2015, 12 (12), 4488-4497.

45. Belair, D. G.; Le, N. N.; Murphy, W. L., Design of growth factor sequestering biomaterials. Chemical Communications 2014, 50 (99), 15651-15668.

46. Sieron, A. L.; Louneva, N.; Fertala, A., Site-specific interaction of bone morphogenetic protein 2 with procollagen II. Cytokine 2002, 18 (4), 214-221.

47. Friess, W.; Uludag, H.; Foskett, S.; Biron, R.; Sargeant, C., Characterization of absorbable collagen sponges as rhBMP-2 carriers. International Journal of Pharmaceutics 1999, 187 (1), 91-99.

48. Geiger, M.; Li, R. H.; Friess, W., Collagen sponges for bone regeneration with rhBMP-2. Advanced Drug Delivery Reviews 2003, 55 (12), 1613-1629.

49. Seeherman, H.; Wozney, J. M., Delivery of bone morphogenetic proteins for orthopedic tissue regeneration. Cytokine & Growth Factor Reviews 2005, 16 (3), 329-345.

50. Zhao, J. Y.; Shinkai, M.; Takezawa, T.; Ohba, S.; Chung, U.; Nagamune, T., Bone regeneration using collagen type I vitrigel with bone morphogenetic protein-2. Journal of Bioscience and Bioengineering 2009, 107 (3), 318-323.

51. El Bialy, I.; Jiskoot, W.; Nejadnik, M. R., Formulation, Delivery and Stability of Bone Morphogenetic Proteins for Effective Bone Regeneration. Pharmaceutical Research 2017, 34 (6), 1152-1170.

52. Goldring, M. B.; Tsuchimochi, K.; Ijiri, K., The control of chondrogenesis. Journal of Cellular Biochemistry 2006, 97 (1), 33-44.

53. Bell, D. M.; Leung, K. K. H.; Wheatley, S. C.; Ng, L. J.; Zhou, S.; Ling, K. W.; Sham, M. H.; Koopman, P.; Tam, P. P. L.; Cheah, K. S. E., SOX9 directly regulates the type-II collagen gene. Nature Genetics 1997, 16 (2), 174-178.

54. Komori, T., Runx2, a multifunctional transcription factor in skeletal development. Journal of Cellular Biochemistry 2002, 87 (1), 1-8.

55. Heng, S.; Paule, S.; Hardman, B.; Li, Y.; Singh, H.; Rainczuk, A.; Stephens, A. N.; Nie, G. Y., Posttranslational Activation of Bone Morphogenetic Protein 2 Is Mediated by Proprotein Convertase 6 during Decidualization for Pregnancy Establishment. Endocrinology 2010, 151 (8), 3909-3917.

56. Coleman, C. M.; Tuan, R. S., Functional role of growth/differentiation factor 5 in chondrogenesis of limb mesenchymal cells. Mechanisms of Development 2003, 120 (7), 823-836.

57. Wegman, F.; Geuze, R. E.; van der Helm, Y. J.; Oner, F. C.; Dhert, W. J. A.; Alblas, J., Gene delivery of bone morphogenetic protein-2 plasmid DNA promotes bone formation in a large animal model. Journal of Tissue Engineering and Regenerative Medicine 2014, 8 (10), 763-770.

58. Vo, T. N.; Kasper, F. K.; Mikos, A. G., Strategies for controlled delivery of growth factors and cells for bone regeneration. Advanced Drug Delivery Reviews 2012, 64 (12), 1292-1309.

59. Wang, E. A.; Israel, D. I.; Kelly, S.; Luxenberg, D. P., Bone Morphogenetic Protein-2 Causes Commitment and Differentiation in C3H10T1/2 and 3T3 Cells. Growth Factors 1993, 9 (1), 57-&.

60. Roy, R.; Kudryashov, V.; Doty, S. B.; Binderman, I.; Boskey, A. L., Differentiation and mineralization of murine mesenchymal C3H10T1/2 cells in micromass culture. Differentiation 2010, 79 (4-5), 211-217.

61. Caron, M. M. J.; Emans, P. J.; Cremers, A.; Surtel, D. A. M.; Coolsen, M. M. E.; van Rhijn, L. W.; Welting, T. J. M., Hypertrophic differentiation during chondrogenic differentiation of progenitor cells is stimulated by BMP-2 but suppressed by BMP-7. Osteoarthritis and Cartilage 2013, 21 (4), 604-613.

Chapter 4

HISTONE-MIMETIC GOLD NANOPARTICLES AS VERSATILE SCAFFOLDS FOR GENE TRANSFER AND CHROMATIN ANALYSIS

As described in Chapter 1, incorporation of the histone H3 tail nuclear localization sequence functioned to direct the nuclear delivery of DNA-encapsulating nanocarriers through specific interactions with intracellular trafficking and nuclear import proteins. However, the current nanocarrier design strategy lacks control over the display and the amount of peptide contained within the final nanocarrier. Developing a coordinated synthesis and assembly approach to improve and selectively tune peptide display may function to enhance gene transfer by providing more control over interactions with the intracellular environment. Accordingly, this chapter describes how the synthetic procedures and characterization techniques detailed in Chapter 2 were utilized to develop novel histone-mimetic nanoscaffolds with the potential to enhance non-viral nucleic acid delivery under physiological conditions. The text, tables, equations, and figures in this chapter are adapted and reprinted with permission from Munsell, E.V.; Fang, B.; and Sullivan, M.O., Histone-mimetic gold nanoparticles as versatile scaffolds for gene transfer and chromatin analysis, Bioconjugate Chemistry. *In Preparation.* (2017).

4.1 Introduction

Nanoparticles have shown enormous promise in applications ranging from catalysis to biology, leading to an explosion of nanotechnology development in the past decade. Nanoparticle methods offer improved imaging potential, versatile

chemistries, and high surface area to volume ratios that enable efficient surface modification for drug delivery applications. For example, gold nanoparticles (AuNPs) possessing a 2 nm core diameter can accommodate ~100 surface ligands incorporating targeting moieties and/or therapeutic materials.[1,2] As discussed in section 1.7.1, AuNPs can initiate cellular entry,[3,4] and possess a promising safety profile based on clinical analyses of bulk gold and evaluations of gold nanostructures.[5] Nanogold spheres (d > 1-2 nm) have shown minimal toxicity, both in culture[6-8] and following either local or systemic administration.[9] AuNPs with controlled dimensions and surface modifications have been intensely studied and widely applied in biomedical trials for biosensor applications,[10-13] drug delivery,[14-16] and bioimaging.[17-19]

AuNPs offer exciting potential in gene transfer applications due to their unique electronic and surface properties. For example, several studies have capitalized on the chemical versatility and high surface area in AuNPs to create polycationic gold nanoparticles with significantly enhanced binding stability in association with nucleic acids.[20-25] Additionally, nanogold has been widely used to image gold nanocarriers during *in vivo* and/or intracellular transport, leading to new insights in nanocarrier delivery mechanisms.[26-29] AuNPs are a useful platform for surface modification with peptides and other ligands for a variety of biomedical applications.[30,31] For example, amino acid modified AuNPs have been employed to direct the cytosolic delivery of siRNA[32-34] and proteins.[35,36] Additionally, surface functionalization with various targeting ligands have been employed to direct AuNP localization to specific cells (e.g. cancer cells)[37-40] and even specific organelles. Functionalization with nuclear localization sequences (NLSs) has been shown to enhance AuNP nuclear delivery,[41,42]

while changing ligand surface density has been shown to alter AuNP intracellular distribution.[43]

Previous investigations in our lab (see section 1.5) examined the effects of incorporating the histone H3 tail NLS into polyethylenimine (PEI) gene delivery systems. The H3 NLS plays an essential role in the nuclear translocation and accumulation of the native H3/H4 protein dimer complex.[44,45] Additionally, the H3 NLS has been shown to play an important role in activating chromosomal DNA for transcription through its interactions with histone acetyltransferase (HAT) complexes,[46-48] as shown in Figure 4.1. In nanocarriers, the H3 NLS functioned to significantly enhance transfection efficiency over standard polymeric transfection reagents[49] by altering cellular uptake and intracellular trafficking, and by harnessing native nuclear import machinery during mitosis.[50-52]

Building off of these fundamental insights, we hypothesized that combining H3 tail motifs with polycationic AuNPs would function to mimic the native H3 presentation on the nucleosome, creating nanostructures with the capacity to stably bind as well as controllably deliver plasmid DNA (pDNA). We posited that this biomimetic presentation of the H3 tail motif would better recapitulate native interactions with histone effectors (Figure 4.1), thus directing nuclear delivery and transcriptional activation. In addition, the well-established methods for AuNP surface functionalization would facilitate manipulation of peptide displays, enabling tunable pDNA association and controlled recruitment of nuclear effectors involved in transcription. Thus, extracellular stability and intracellular transcription could be simultaneously optimized.

AuNPs with a variety of core dimensions are typically synthesized by chemical reduction methods.[53-56] AuNPs with low dispersity and small (~2 nm) core dimensions can be readily prepared by the well-established Brust-Schiffrin method involving hydrogen tetrachloroaurate ($HAuCl_4$) reduction with sodium borohydride ($NaBH_4$) in the presence of 1-pentanethiol (C5-SH).[53] These monolayer-protected AuNPs provide an ideal scaffold for post-functionalization with various combinations of organic ligands through the Murray place-exchange reaction.[57] More importantly, ligand composition on the AuNP surface can be tailored by simply manipulating the ratio of incoming ligand to thiolated surface ligand.

Herein, we utilized monolayer-protected AuNPs as scaffolds to display H3 tail peptides in a tunable fashion that would mimic the architecture and dimensions of core histones in the native nucleosome (Figure 4.1). Subsequently, we evaluated whether these histone-mimetic nanoscaffolds would promote efficient histone effector engagement and permit AuNP-pDNA assembly into nucleosome-like structures that could efficiently deliver pDNA. Our data show that H3 tail peptide densities could be varied on monolayer-protected AuNPs over a range of 4-69 ligands, enabling similar or higher peptide densities than those found in the histone octamer. Importantly, these histone-mimetic nanoscaffolds demonstrated significantly improved binding interactions with the H3-specific transcriptional activator HBO1 as compared with AuNPs with similar zeta potentials but without H3 tail peptide modifications. In fact, the H3-AuNPs exhibited a 2-fold higher association with HBO1 following cellular pull-down assays, as compared with the unmodified AuNPs. Furthermore, the nanoscaffolds formed highly stable complexes with pDNA that displayed substantially better stability against heparin displacement than standard polymeric transfection

reagents made with PEI alone. Most notably, the AuNP-pDNA nanoplexes were able to preserve their transfection efficiency in the presence of high concentrations of heparin similar to those found in the extracellular environment, whereas PEI polyplexes exhibited a 9-fold decrease in transfection efficiency in the presence of heparin. Finally, gene delivery was clearly driven by the H3 tail peptides, with ~6-fold enhanced transfection efficiencies as compared with nanoplexes containing unmodified AuNPs. These novel findings represent a significant design advance in gene delivery materials and addresses crucial barriers in pDNA binding stability and biospecific targeting.

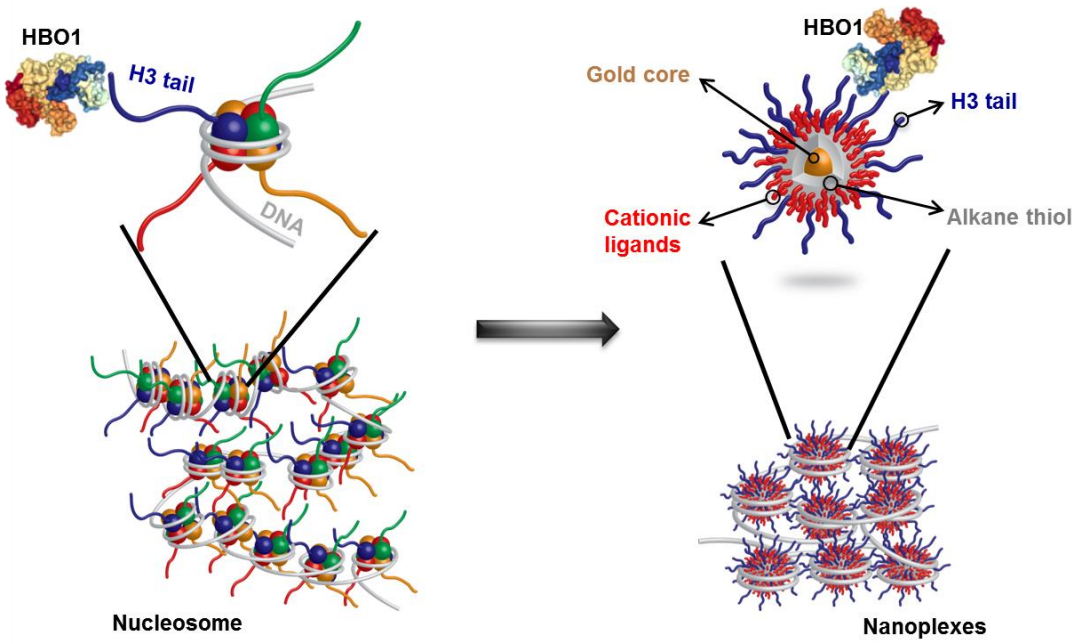

Figure 4.1: Schematic illustration of the bio-inspired design of H3-modified AuNPs that mimic the structure of native histone octamers. The HBO1 transcriptional activator protein interacts with the H3 tail on both the native octamer (left) and the AuNPs (right).

4.2 Results and Discussion

4.2.1 Preparation of the Histone-Mimetic Nanoscaffolds

The histone-mimetic nanoscaffold design was composed of a gold core coated with a layer of thiolated ligands. Construction of the nanoscaffolds began with the synthesis of the gold core via a Brust-Schiffrin procedure. In order to ensure that the Brust-Schiffrin synthesized AuNPs were of the small size required to mimic native nucleosome dimension, both core diameter and dispersity were analyzed by transmission electron microscopy (TEM) as shown in Figure 4.2. Quantitative image analysis (Figure 4.2B) illustrated that the mean core size was ~2.5 nm with a relatively narrow distribution ranging between 1.5 nm and 3.5 nm. Magnified images (Figure 4.2C and D) further confirmed the assembly of the gold core, as indicated by the lattice-like structures of the gold atoms (~2.4 Å lattice spacing), demonstrating the crystallographic planes of face centered cubic gold.[58]

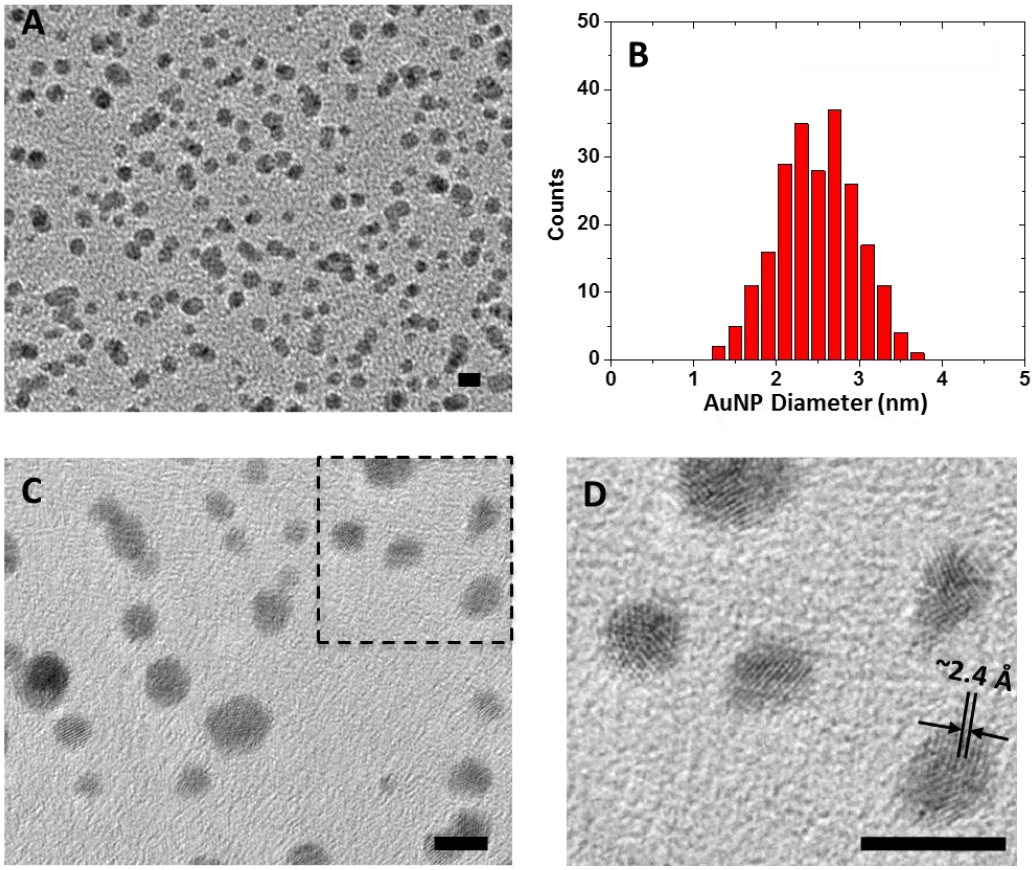

Figure 4.2: TEM images of C5-coated AuNPs and the statistical analysis of AuNP core diameter. (A) Wide view image of the AuNPs; (B) Core diameter statistical analysis of all the AuNPs in (A), average core diameter = 2.5 nm; (C) Magnified image of the AuNPs; (D) High-magnification image of the outlined region in (C) showing the fine lattice structures of the gold cores. Scale bar in all images = 5 nm.

In order to endow the AuNP surface with the appropriate charge for aqueous solubility and pDNA binding capacity, as well as to mimic the native presentation of histone tail sequences on the histone octamer, different species and densities of peptide ligands were installed onto the AuNP surface by a 2-step Murray place exchange process. First, ligands containing a short cationic sequence composed of 5

lysine residues (K5) were exchanged onto the surface of the C5-protected AuNPs (Figure 4.3). The resulting cationic and water-soluble K5-coated AuNPs were then used in a second place exchange with ligands containing the first 1-25 residues of the H3 tail NLS. The final amount of H3 tail displayed on surface of the resulting histone-mimetic nanoscaffolds was tuned by varying the amount of H3 tail ligand present during the second place exchange. Using this 2-step procedure, we generated a small library of cationic AuNPs, ranging from AuNPs with no H3 ligands to AuNPs that were completely covered with the H3 tail.

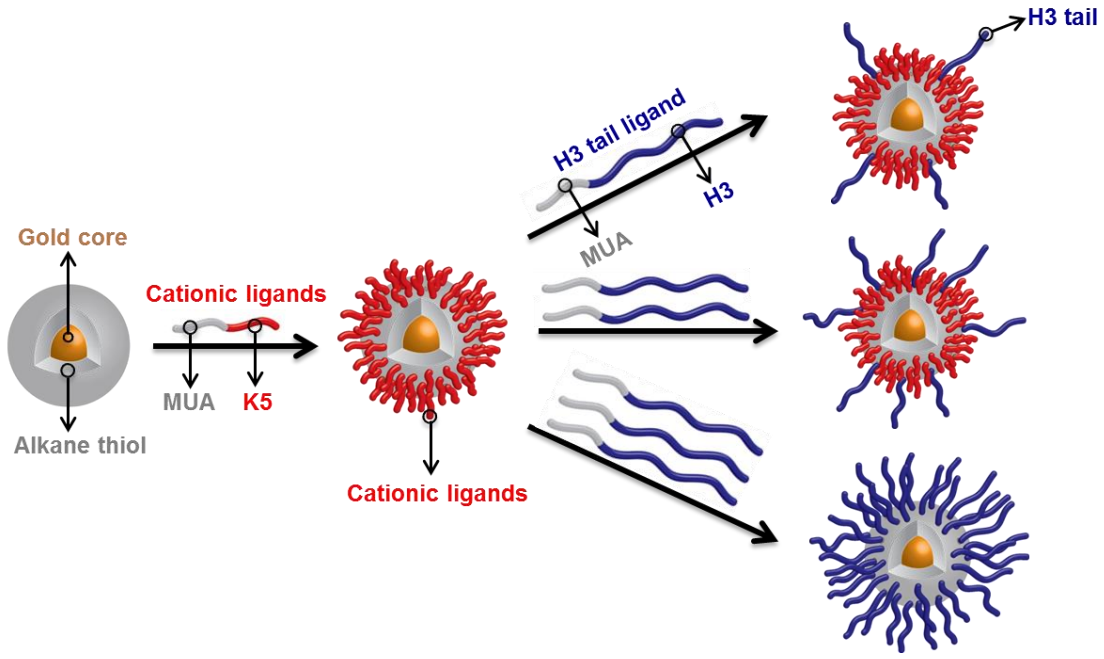

Figure 4.3: Schematic illustration of the 2-step Murray place exchange strategy for ligand installation. Different number densities of H3 tail ligands were controlled by the H3 tail ligand feed. MUA = mercaptoundecanoic acid; K5 = 5-residue polylysine peptide; H3 = H3 tail peptide (residues 1-25).

4.2.2 Synthesis and Characterization of Nanoscaffold Ligands

Synthesis of the K5 and H3 tail peptides was conducted using fluorenylmethyloxycarbonyl (Fmoc) solid-phase peptide synthesis (SPPS). Both peptides were covalently modified with a triphenylmethyl-protected mercaptoundecanoic acid (MUA) alkane chain to help drive the place-exchange reaction and confer stability of the final nanoscaffolds. In the case of the K5-MUA peptide ligand, the MUA was conjugated to the N-terminus following synthesis of the K5 peptide (Figure 4.4). When synthesizing the H3-MUA peptide ligand, a modified synthetic procedure, unique to the work described herein, was employed to ensure that all H3-containing AuNPs mimicked the natural architecture of nucleosomes. Native histone effectors interact with the H3 tail NLS in the N- to C-terminal direction. Thus, it is crucial that the synthesized H3 tail be displayed on the on the gold surface in a similar direction, in order to recapitulate its cellular functionalities. Since standard SPPS proceeds in the opposing C- to N-terminal direction, the MUA conjugate had to be attached at the beginning C-terminus before peptide synthesis proceeded. To accomplish this, a lysine residue possessing a side-chain protecting group fully orthogonal to Fmoc deprotection[59] was incorporated into the synthetic procedure, thus ensuring that the final H3-MUA peptide ligand maintained the correct N to C orientation when place exchanged onto the AuNP surface. Following addition of this orthogonal lysine residue at the C-terminus, the ε-amino protecting group was removed to conjugate the MUA, followed by standard SPPS to generate the H3 tail (Figure 4.5).

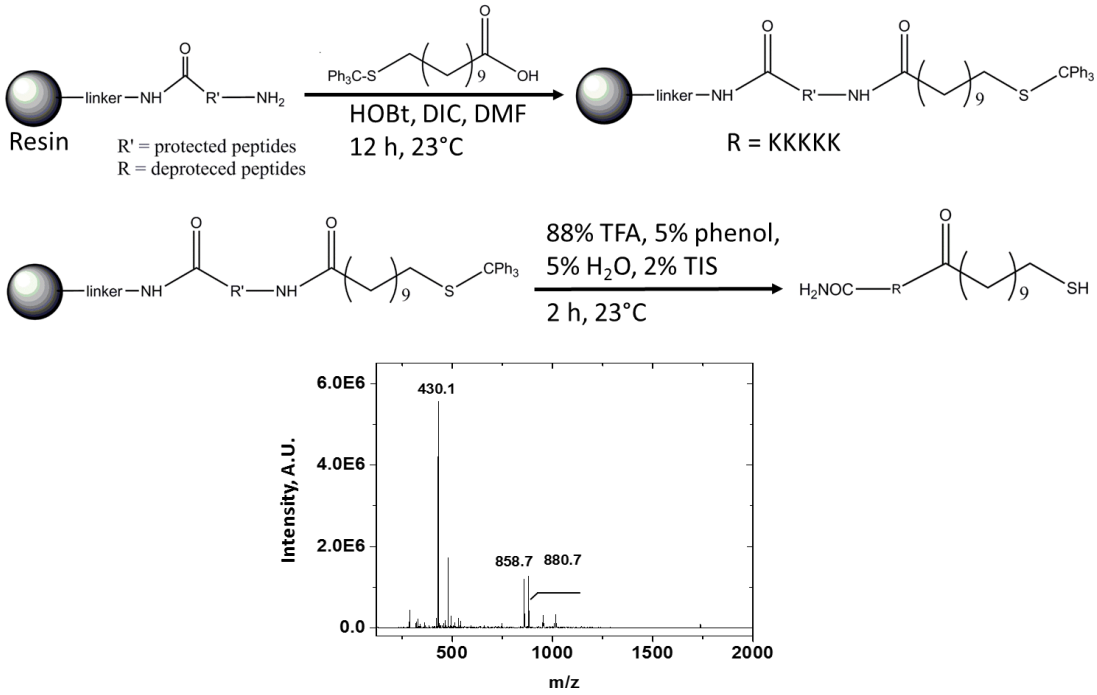

Figure 4.4: Synthetic procedure and electrospray ionization mass spectrometry (ESI MS) characterization of the K5-MUA peptide ligand, which showed major peaks of m/z = 858.7 (+1H), m/z = 880.7 (+1Na) and m/z = 430.1 (+2H). The predicted molecular weight of the K5-MUA peptide ligand was 857.7 Da. K = lysine amino acid; HOBt = hydroxybenzotriazole; DIC = N,N'-diisopropylcarbodiimide; DMF = dimethylformamide; TFA = trifluoroacetic acid; TIS = triisopropylsilane; Ph_3 = triphenylmethyl

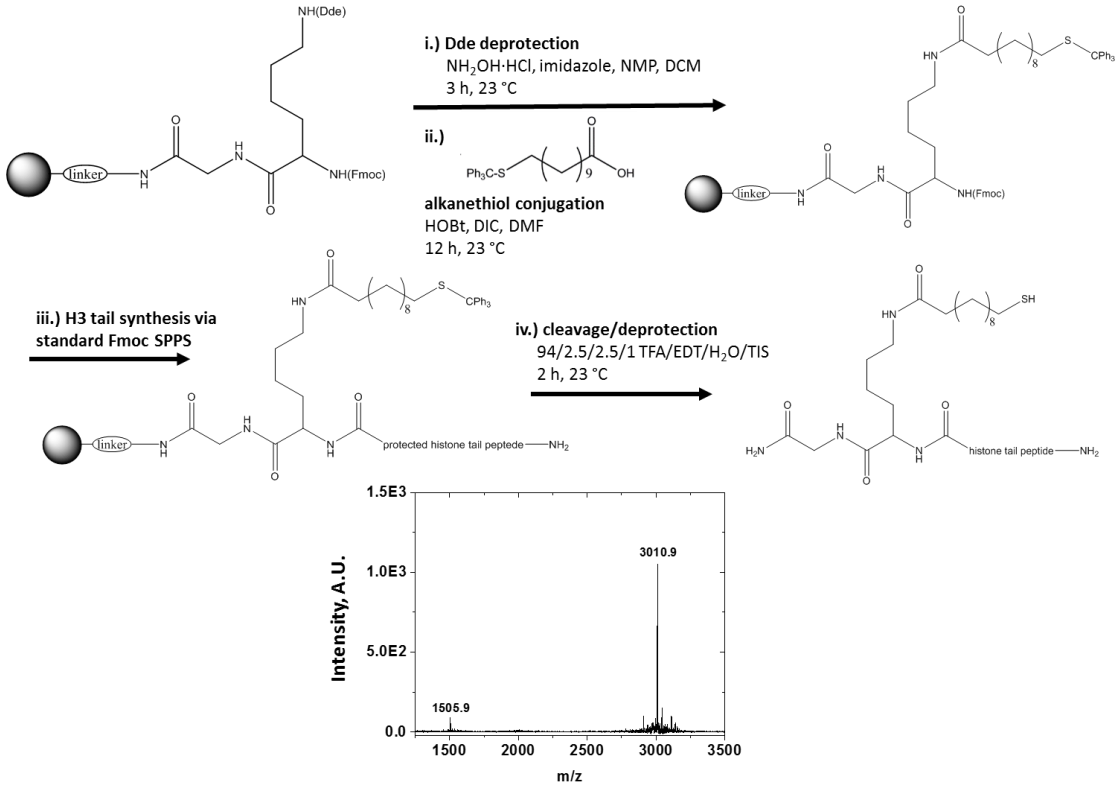

Figure 4.5: Synthetic proceedure and matrix assisted laser desorption/ionization time-of-flight mass spectrometry (MALDI-TOF MS) characterization of the H3-MUA peptide ligand, which showed primary peaks of m/z = 3010.9 (+1H) and m/z = 1505.9 (+2H). The predicted molecular weight of the H3-MUA peptide ligand was 3009.1 Da. Dde = 1-(4,4-dimethyl-2,6-dioxacyclohexylidene)ethyl; NMP = N-methyl-2-pyrrolidone; DCM = dichloromethane; EDT = 1,2-ethanedithiol.

4.2.3 Histone-Mimetic Nanoscaffold Characterization

In order to determine the number of K5-MUA and H3-MUA peptide ligands that had been exchanged onto the nanoscaffold surface, both thermogravimetric analysis (TGA) and carbon-hydrogen-nitrogen-sulfur (CHNS) elemental analysis were employed. The C5-coated AuNP precursors were found to contain ~96 C5 surface ligands based on a weight loss of 16.89 % from TGA (Figure 4.6A), which is in good

agreement with previous studies analyzing the number of cluster ligands on the surface of Brust-Schiffrin synthesized AuNPs.[57,60,61] The amount of K5-MUA ligands present on the AuNP surface following the first place exchange reaction was analyzed by combining results from TGA (Figure 4.6B) and CHNS elemental analysis (Table B.1). TGA established a weight loss of 38.92 % for the K5-coated AuNPs, which is substantially higher than the weight loss from the C5-coated AuNP precursors. A total of 31 K5-MUA ligands were calculated per K5-coated AuNP (see Appendix C).

It is interesting that only ~32 % of the C5 surface ligands were replaced by the incoming K5-MUA peptide ligands, given the fact that a large molar excess of K5-MUA ligands to C5 surface ligands was utilized to ensure a high degree exchange.[57] However, due to the dramatic difference in solubility between the C5-coated AuNPs and the K5-MUA peptide ligands, the place exchange reaction was conducted in a mixture of dichloromethane (DCM) and methanol (MeOH). It is likely that the resulting K5-coated AuNPs precipitated out of the mixed solvent before complete exchange could take place. This explains the relatively low number of K5-MUA ligands found on the surface, in comparison to the precursor C5-coated AuNPs. Despite this, the K5-coated AuNPs were only soluble under aqueous conditions. In addition, due to the relatively low molecular weight of C5-SH, the residual C5 surface ligands only occupied ~13 wt % of the K5-coated AuNP surface, which explains the high solubility of these AuNPs in aqueous media.

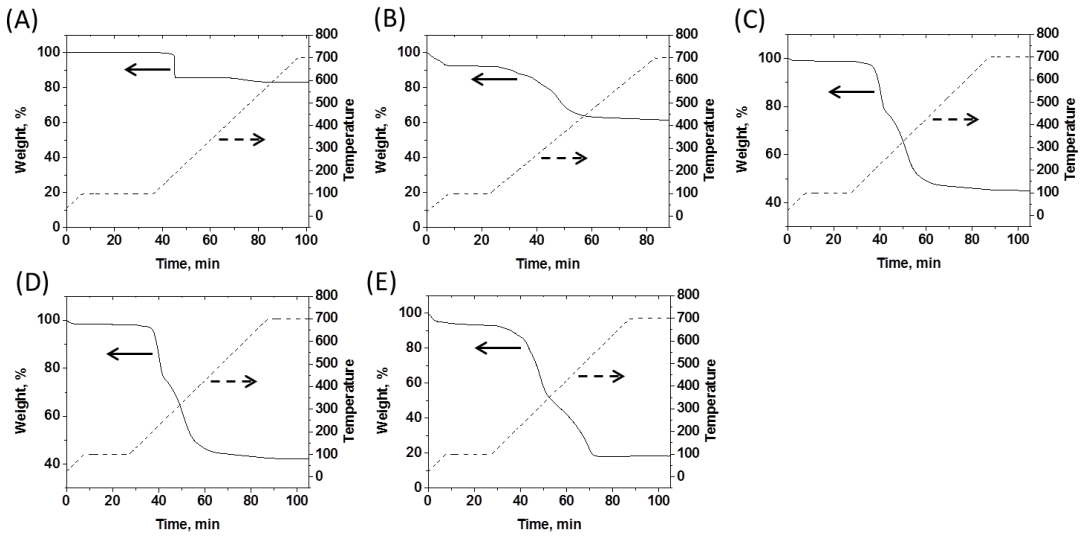

Figure 4.6: TGA of (A) C5-coated AuNPs, (B) K5-coated AuNPs, (C) low-coverage H3 AuNPs, (D) mid-coverage H3 AuNPs, and (E) high-coverage H3 AuNPs. Solid lines = temperature traces; dashed lines = weight percent data.

In the second place exchange reaction, the H3-MUA ligands replaced a fraction of both the K5-MUA ligands and the residual C5 ligands on the AuNP surface. Since the K5-coated AuNPs and H3-MUA peptide ligands were both readily dissolved in water, the amount of place exchange was reasonably controlled by tuning the feed ratio of H3-MUA peptide ligands to AuNP surface ligands. Thus, the final AuNPs took on different amounts of H3-MUA peptide ligand, resulting in nanoparticle preparations characterized as low-coverage H3 AuNPs, mid-coverage H3 AuNPs and high-coverage H3 AuNPs. These final histone-mimetic nanoscaffolds were also subjected to TGA (Figures 4.6C, 4.6D, and 4.6E) and CHNS elemental analysis (Table B.1). TGA yielded 54.1 %, 57.1 % and 81.1 % weight losses for the low-, mid-, and high-coverage H3 AuNPs respectively. These results were combined

with CHNS elemental analysis to estimate the surface ligand compositions in the 3 different H3-containing mixed monolayer AuNPs (see Appendix C). Final ligand composisitons for all the synthesized AuNPs are reported in Table 4.1.

Although the AuNPs possess a small core dimension (~2.5 nm), this size does not accurately reflect their morphology under aqueous conditions. These properties were evaluated by dynamic light scattering (DLS). DLS hydrodynamic radius measurements of both the K5-coated and histone-mimetic AuNPs show a dramatic increase in nanoscaffold dimension compared to the gold core (Table 4.1). The average hydrodynamic radius of the K5-coated AuNPs was 7.8 nm. Hydrodynamic size increased ~5-fold following installation of the much longer H3-MUA peptide ligand, consistent with molecular simulation estimations of K5 peptide versus H3 tail peptide length. As expected, average hydrodynamic radii were similar for the low-, mid-, and high-coverage H3 AuNPs: 37 nm, 38 nm, and 41 nm respectively.

Table 4.1: Ligand compositions and hydrodynamic radii of synthesized AuNPs. The hydrodynamic radii were determined by DLS measurements in water.

Sample	Ligand(s)	Ligand # / AuNP	Hydrodynamic radius (nm)
C5-coated AuNPs	C5	96	--
K5-coated AuNPs	K5	31	7.8 ± 0.3
Low-H3 AuNPs	K5 and H3	48 and 4	37 ± 0.4
Mid-H3 AuNPs	K5 and H3	35 and 10	38 ± 0.2
High-H3 AuNPs	H3	69	41 ± 1.2

4.2.4 Nanoscaffold Association with Histone Effector Complexes

Given our previous studies confirming the enhanced nuclear activities and histone effector binding capacities of H3-based nanocarriers,[46] we asked whether

improved H3 tail display on the surface of AuNPs conferred improved interactions with nuclear protein complexes, specifically the HBO1-HAT complex. The HBO1-HAT complex binds the H3 tail sequence and catalyzes acetylation of downstream lysine residues on the H3 tail[62-64] thereby activating chromosomal DNA for transcription.[65] Pull-down assays were employed to examine the interactions between the nanoscaffolds and HBO1. Nanoscaffolds were incubated with HBO1-enhanced cell lysates purified from human embryonic kidney (HEK) 293T cells, and the resulting interactions with HBO1 were analyzed via Western blotting (Figure 4.7). As expected, AuNPs completely covered by the H3 tail ligand (high-coverage H3 AuNPs; 69 ligands total) successfully pulled down HBO1. To confirm that these interactions were not caused by non-specific interactions, the ability of the K5-coated AuNPs to pull down HBO1 was also evaluated. As shown in Figure 4.7A, the K5-coated AuNPs displayed low levels of HBO1 interaction when incubated with cell lysates at the same overall concentration of positive charge. Densitometry analysis of band intensities (Figure 4.7B) revealed a 2-fold higher association between HBO1 and the histone-mimetic nanoscaffolds compared to the unmodified (K5-coated) AuNPs.

The ability of K5-coated AuNPs to pull down HBO1 indicates that a small non-specific level of interaction exists between the unmodified AuNPs and HBO1, likely due to electrostatics. It is reasonable to expect that some threshold of H3 tail display (i.e. below ~69 H3 tail ligands) on the gold surface exists where specific H3 peptide interaction with HBO1 overcomes non-specific electrostatic interactions. Additionally, it is interesting to note that there appear to be multiple bands detected by the HBO1 primary antibody (Figure 4.7A). This was attributed to different glycosylation tags occurring on the expressed HBO1 protein. The purchased HBO1-

enhanced cell lysate expressed HBO1 with a C-terminal FLAG tag. Probing the same blot with an anti-FLAG primary antibody revealed an identical band pattern (Figure B.1), confirming that all bands represent the HBO1 protein, but with different glycosylation levels.

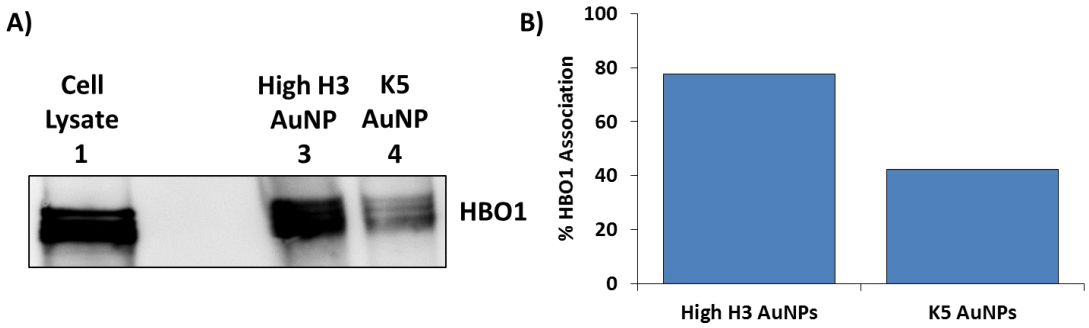

Figure 4.7: HBO1 pull-down assay. (A) Western blot against HBO1 following pull-down from HBO1-enhanced cell lysates using high-coverage H3 and K5-coated AuNPs. Lane 1 contains a sample of lysate proteins that were not incubated with AuNPs. Lanes 3 and 4 contain samples of lysate proteins that associated with the indicated AuNPs during the pull-down. (B) Densitometry analysis of band intensities in (A), representing the amount of HBO1-AuNP association relative to the amount of HBO1 present in the cell lysate control (lane 1).

4.2.5 Characterization and Stabilization of pDNA-AuNP Nanoplexes

To assess the pDNA condensation and packaging effects of the prepared nanoscaffolds, AuNP-pDNA nanoplexes were assembled at a range of N:P ratios in 4-(2-hydroxyethyl)-1-piperazineethanesulfonic acid) (HEPES) buffer (20 mM, pH 6.0). The resulting structures were evaluated by agarose gel electrophoresis with ethidium bromide (EtBr) staining. Nanoplex formation was detected as a reduction in pDNA mobility in the gel, since binding by the intercalating EtBr dye is reduced when pDNA

is sufficiently condensed and unable to migrate through the gel. The electrophoretic assay showed that all AuNPs formed stable nanoplexes with pDNA above an N:P ratio of 1 (Figure 4.8), as indicated by the absence of pDNA mobility and EtBr fluorescence. The observed EtBr fluorescence in the wells at an N:P ratio of 1 was likely caused by incomplete pDNA condensation, resulting in large complexes that could not enter the gel pores. In contrast, pDNA polyplexes formed with the common cationic polymer PEI displayed significantly lower packaging capability, requiring an N:P ratio of at least 4 before full pDNA condensation began. These results indicated that the modified AuNPs enabled enhanced pDNA binding capacity over common polymeric transfection reagents. This was likely due to the improved presentation of cationic ligands on the gold surface. The negatively charged pDNA backbone had better access to primary amines on each ligand, resulting in stronger electrostatic interactions and ultimately tighter complexes than those obtained with PEI, which contains a mixture primary and secondary amine groups.

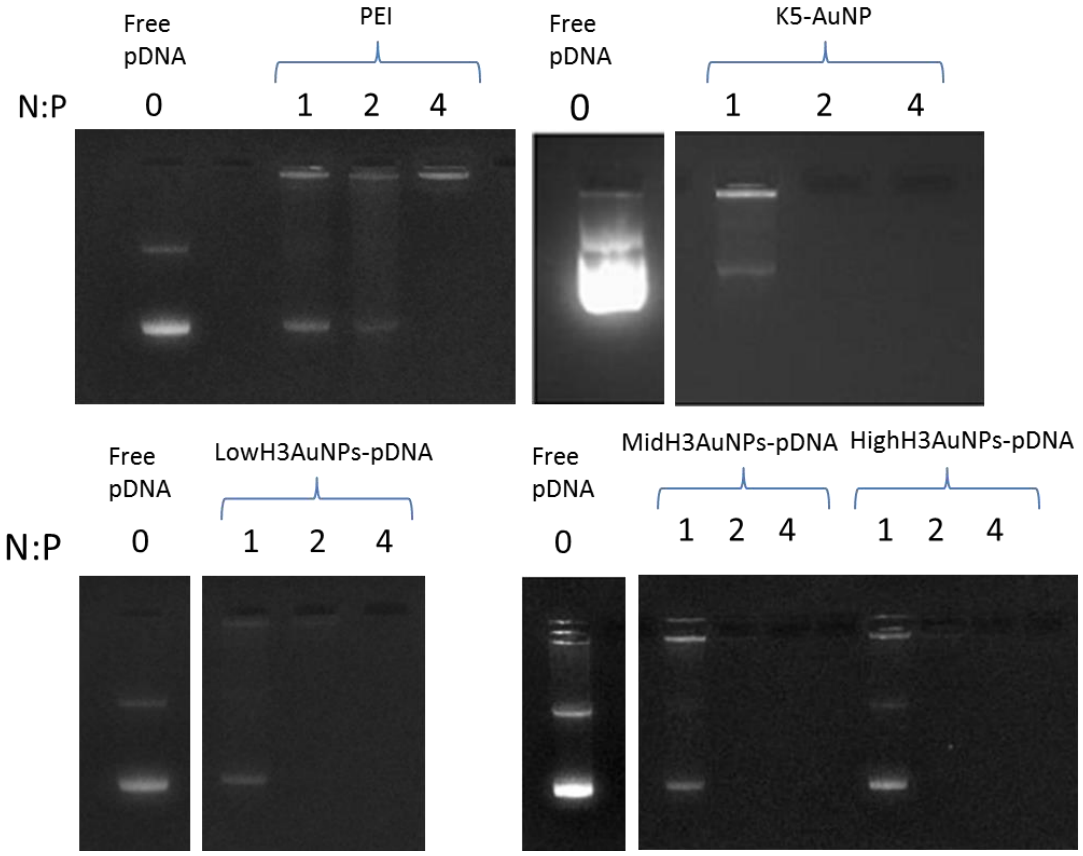

Figure 4.8: Representative agarose gel electrophoresis showing pDNA complexation at various N:P ratios via ethidium bromide staining for each of the indicated nanoplexes and polyplexes. The first lane in all images contains only pDNA.

Complimentary to these agarose gel analyses, the hydrodynamic radii of the assembled nanoplexes were measured to confirm that nanoplex size was within a reasonable range for efficient endocytosis.[66] As shown in Table 4.2, increasing the N:P ratio led to reductions in the overall dimension of the prepared AuNP-pDNA nanoplexes, as the pDNA became more efficiently condensed. A significant decrease in nanoplex hydrodynamic radius was observed as the N:P ratio increased from 1 to 2. The large size and high dispersity of the nanoplexes at an N:P ratio of 1 indicated

incomplete/non-uniform nanoplex assembly. These results were consistent with the agarose gel analyses in Figure 4.8, which showed incomplete pDNA condensation at a N:P ratio of 1 for all prepared nanoplexes. As more AuNPs were incorporated into the assembly process, fully complexed and uniform populations of nanoplexes were observed. The dimensions of the nanoplexes were smaller than the PEI polyplexes at N:P ratios of 1 and 2 (PEI polyplexes do not form at an N:P = 1), which also correspond well with the agarose gel results. Finally, zeta potentials of the formed nanoplexes were all moderately positive (between ~10-15 mV), which indicated that the negatively charged pDNA had incorporated enough AuNPs to reverse its surface charge. Further AuNP addition above an N:P ratio 1 did not significantly contribute to elevating the nanoplex zeta potential.

Table 4.2: Hydrodynamic radii and zeta potentials in pDNA nanoplexes and polyplexes at different N:P ratios. * From Reilly MJ, *et al.*, *Mol Pharm.* 9(5), 1031-40. 2012.[49]

Nano/Polyplex	N:P	Hydrodynamic radius (nm)	Surface Charge (mV)
Low-H3 coated	1	177 ± 106.8	11 ± 2.29
	2	53 ± 0.7	15 ± 3.14
	4	40 ± 0.2	13 ± 3.59
Mid-H3 coated	1	93 ± 44.9	12 ± 2.77
	2	50 ± 0.3	14 ± 4.63
	4	45 ± 0.4	15 ± 2.89
High-H3 coated	1	53 ± 6.7	11 ± 2.23
	2	39 ± 0.4	8 ± 4.11
	4	40 ± 0.2	11 ± 3.12
K5-coated	1	70 ± 6.7	16 ± 3.84
	2	66 ± 0.5	--
	4	57 ± 0.2	--
PEI	1	--	--
	2	108 ± 6.1	-10 ± 5.30*
	4	58 ± 2.5	10 ± 2.32*

Given the capability of the AuNPs to more efficiently bind and condense pDNA at lower N:P ratios, we investigated whether the formed AuNP-pDNA nanoplexes were more resistant to heparin destabilization than polyplexes formed with PEI. Heparin is a common polyanionic glycosaminoglycan (GAG) found in extracellular matrix, and is known to displace nucleic acids from cationic delivery vehicles.[67] Thus enhanced stability against heparin displacement is indicative of nanocarriers that would be more stable under physiological conditions. Nanoplexes and polyplexes were formed at an N:P ratio of 4 and incubated with increasing concentrations of heparin. As shown in Figure 4.9A-D, both K5- and H3-coated AuNP-pDNA nanoplexes were resistant to heparin destabilization until a heparin/pDNA wt/wt ratio of 1.0. Above this wt/wt ratio, the nanoplexes began to

loosen and pDNA began to be displaced, as indicated by the increase in EtBr well fluorescence and the slight amount of pDNA migration down the gel. In contrast, PEI polyplexes (Figure 4.9E) began to destabilize at a heparin/pDNA wt/wt ratio of 0.25. The pDNA was almost completely displaced from PEI polyplexes at a 1.0 wt/wt ratio. These results further demonstrate the ability of both the K5-coated and histone-mimetic nanoscaffolds to form more stable complexes with pDNA that are resistant to destabilization from common extracellular GAGs. The AuNP nanoplexes required 4 times the amount of heparin before the nanoplexes began to loosen and release the pDNA. We hypothesize that by mimicking the natural presentation of cationic moieties on the histone octamer, the modified AuNPs can interact with the anionic pDNA backbone similar to native histone-chromatin interactions in the nucleus, thus providing enhanced stability against native GAG displacement.

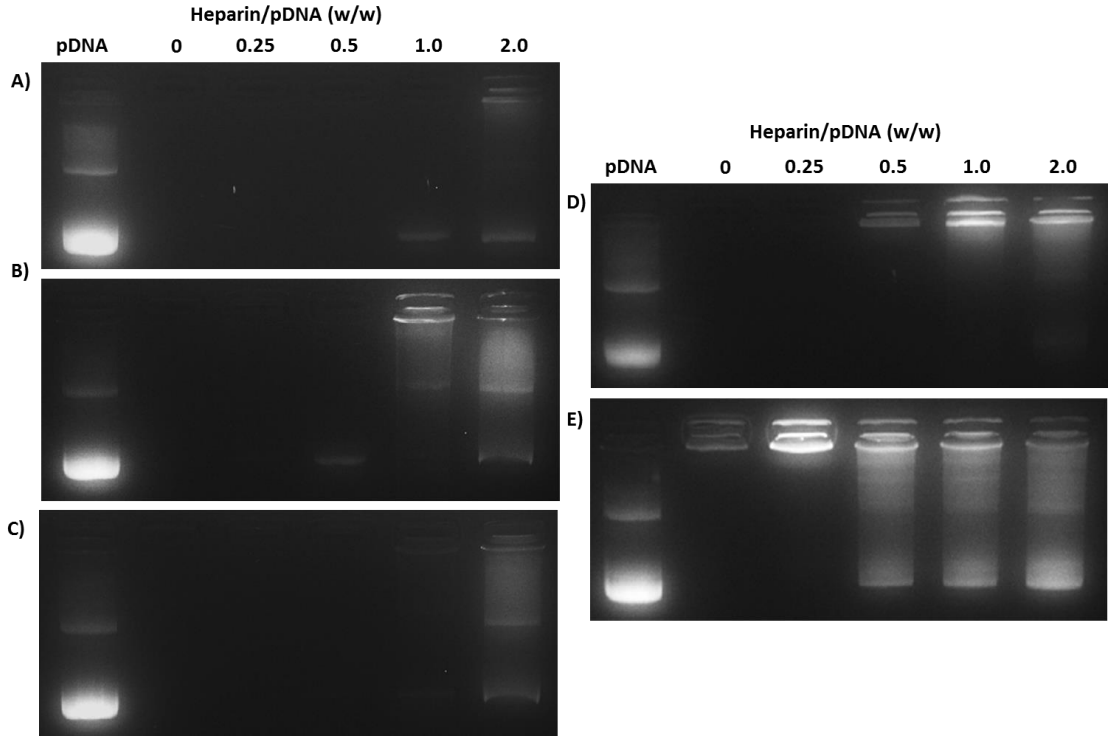

Figure 4.9: Heparin displacement of (A) high-coverage H3 AuNP nanoplexes; (B) mid-coverage H3 AuNP nanoplexes; (C) low-coverage H3 AuNP nanoplexes; (D) K5-coated AuNP nanoplexes; and (E) PEI polyplexes, all at an N:P ratio of 4. The nanoplexes and polyplexes were incubated in the presence of increasing amounts of heparin for 30 min at 37 °C and the incubated samples were subsequently analyzed by agarose gel electrophoresis for pDNA displacement.

4.2.6 Nanoplex Transfection Efficiency

Given the enhanced capacity of both K5-coated and histone-mimetic nanoscaffolds to stably bind and condense pDNA, we next investigated their ability transfect Chinese Hamster Ovary (CHO-K1) cells and improve gene expression. Transfection studies were conducted in serum-free media as well as in the presence of heparin at a concentration of 0.0025 mg/mL to simulate *in vitro* the physiological conditions of the extracellular environment. Based on our previous studies with H3-

targeted nanocarriers,[49] we hypothesized that hybrid nanoplexes formed with a known mediator of cellular uptake, such as PEI, in combination with the modified AuNPs would exhibit both robust stability in the extracellular environment as well as significant cellular accumulation. Furthermore, we hypothesized that histone-mimetic AuNP/PEI hybrid nanoplexes would enable significant improvements in gene expression when compared to K5-coated AuNP/PEI nanoplexes, given the enhanced biological activities of the H3 tail. None of the tested nanoplexes had any significant effects on cellular viability (Figure B.2). The transfection efficiencies of the nanoplexes were analyzed by fluorescence microscopy (Figure 4.10A and B) and flow cytometry (Figure 4.10C and D) following transfection with pDNA encoding for the green fluorescent protein (GFP). Nanoplexes were formed at an overall N:P ratio of 4, with an N:P ratio of 1 contribution from the modified AuNPs and an N:P ratio of 3 contribution from the PEI polymer. Transfections with the K5-AuNP/PEI hybrid nanoplexes produced insignificant levels of GFP-expressing cells (Figure 4.10A). In contrast, hybrid nanoplexes containing the high-coverage H3 AuNPs displayed ~7-fold higher levels of transfection (Figure 4.10A). Additionally, the transfection efficiency of the high-coverage H3 AuNP/PEI nanoplexes was similar to standard PEI polyplexes formulated at the same overall charge ratio (N:P ratio of 4).

Studies have reported[68,69] systemic concentrations of ~0.0016mg/mL for heparin in normal human sera. Localized concentrations of heparin and heparin sulfate in the extracellular space are likely higher, especially in areas of native tissue regeneration, where heparin plays an essential role in facilitating cell motility and growth factor sequestration.[70] Thus, the heparin concentrations used in these studies provide an effective benchmark for evaluating nanoplex transfection efficiency under

physiological conditions. The presence of heparin in the transfection media did not have any significant effects on the overall transfection efficiency of the high-coverage H3-modified AuNP/PEI hybrid nanoplexes (Figure 4.10B and 4.10D). In contrast, heparin incubation completely eliminated the transfection potential of the PEI polyplexes, likely due to polyplex destabilization. These results demonstrate the utility of the histone-mimetic AuNPs in providing the necessary stability against pDNA displacement by native GAG concentrations in the extracellular environment.

The absence of GFP expression following K5-coated AuNP/PEI nanoplex transfection, regardless of heparin concentration, provides evidence of the H3 tail functioning to improve interactions with intracellular trafficking, nuclear import, and transcriptional activation machinery to ultimately enhance gene expression. Transfections with low- and mid-coverage H3 AuNP/PEI hybrid nanoplexes yielded an insignificant number of GFP-expressing cells (Figure B.3), with and without heparin incubation. These results further indicate that there are likely a certain number of H3 tail ligands that must be displayed on the surface of the AuNPs before native histone effectors can be engaged. Overall, these nanoscaffold transfection efficiency evaluations not only demonstrated the utility of the modified AuNPs to stabilize gene delivery complexes from extracellular disassembly, but also showed that tuning ligand surface display could effectively tune interactions with intracellular effectors to enhance overall gene delivery and expression.

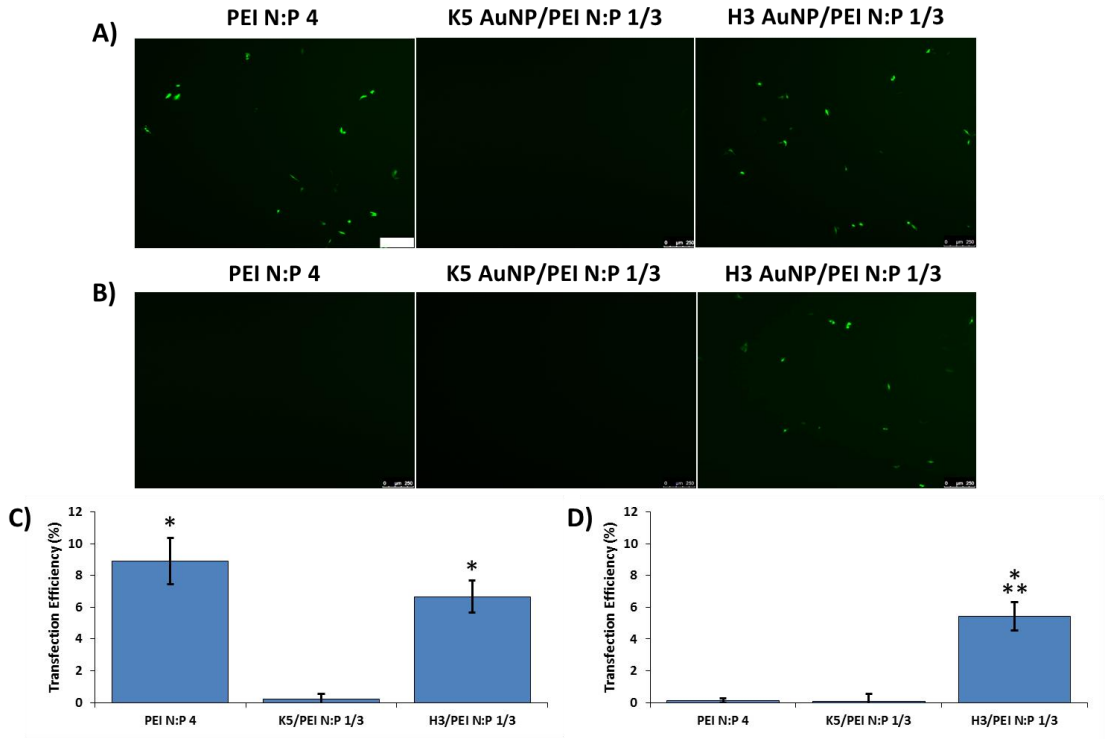

Figure 4.10: CHO-K1 transfection with GFP-encoding pDNA. Representative fluorescence microscopy images of GFP expression 24 h post-transfection with the indicated nanoplexes/polyplexes either (A) without or (B) with heparin (0.0025 mg/mL). Quantification of transfection efficiency (C) without or (D) with heparin using flow cytometry. All results are shown as the mean ± standard deviation of data collected from 3 independent experiments. * Indicates a significant difference from zero ($p < 0.05$). ** Indicates a significant difference from PEI polyplexes. Scale bar = 250 μm.

4.3 Conclusions

In this study, we demonstrated that alkanethiol-coated AuNPs provide ideal scaffolds for the tunable display of histone H3 tail peptides. Utilizing Murray place exchange, a small library of modified AuNPs was created, each displaying different levels of the H3 tail peptide. TGA and elemental analysis were utilized to accurately estimate the number ligands displayed on the surface of each collection of

nanoscaffolds, classified as low-coverage H3 (4 ligands), mid-coverage H3 (10 ligands), and high-coverage H3 (69 ligands) AuNPs. The synthesized AuNPs mimicked the natural dimensions and tail presentation of the native histone octamer. This design approach to harness native gene regulatory processing with chromatin-derived motifs addresses a key need for biospecific targeting that does not rely on pathogenic capsids or proteins to impart activity.

Pull-down assays revealed that the improved display of the H3 tail peptide facilitated interactions with native histone effectors, and that these interactions could be tuned by changing the amount of H3 tail displayed on the AuNP surface. Nanoplex formation studies indicated that the modified AuNPs displayed enhanced pDNA binding and condensation at half the overall charge ratio when compared to common transfection reagents. The resulting pDNA-AuNP nanoplexes were highly stable against heparin displacement, requiring nearly 4-fold higher heparin concentrations before releasing pDNA, as compared to PEI polyplexes. Nanoplexes containing the high-coverage H3 AuNPs resulted in an 8-fold improvement in transfection efficiency when compared to unmodified nanoplexes, suggesting their ability to engage native histone processing pathways. Most notably, the transfection efficiency of these nanoplexes remained unchanged in the presence of physiologically relevant amounts of heparin. In contrast, the heparin levels completely destabilized the PEI polyplexes, eliminating their ability to transfect cells. Collectively, these findings demonstrate the utility of using AuNPs as an effective scaffold for mimicking the natural presentation of histone-tails within a gene delivery vehicle in order to better stabilize the resulting nanoplex from extracellular degradation and better engage native intracellular trafficking and nuclear import machinery for enhanced gene transfer and expression.

4.4 Experimental Section

4.4.1 Materials

Hydrogen tetrachloroaurate tri-hydrate ($HAuCl_4 \bullet 3H_2O$), $NaBH_4$, C5-SH, and 11-bromoundecanoic acid were purchased from Sigma-Aldrich (St. Louis, MO). Triphenylmethyl mercaptan (Ph_3C-SH) and tetraoctylammonium bromide (TOAB) were purchased from Acros Organics (Waltham, MA). Fmoc-protected amino acids, O-Benzotriazole-N,N,N',N'-tetramethyl-uronium-hexafluoro-phosphate (HBTU), HOBt, and DIC were purchased from Novabiochem (Burlington, MA). H-Rink amide ChemMatrix® resin was purchased from PCAS Biomatrix (Quebec, Canada). Primary antibodies against the human HBO1-HAT complex (rabbit monoclonal IgG) and a C-terminal FLAG tag (mouse monoclonal IgG2a) were purchased from Abcam (Cambridge, MA) and Origene (Rockville, MD) respectively. Human HBO1-enhanced cell lysate purified from HEK293T cells was purchased from Origene. All other reagents were purchased from Fisher Scientific (Fairlawn, NJ). The gWIZ-GFP (5757 bp) mammalian expression vector was purchased from Genlantis (San Diego, CA). The plasmid was amplified in NEB 5α electrocompetent *Escherichia coli* purchased from New England Biolabs and purified with a QIAGEN EndoFree Maxi Kit (Valencia, CA), according to the manufacturer's protocols.

4.4.2 Triphenylmethyl-Protected Mercaptoundecanoic acid (MUA) Synthesis

Ph_3C-SH (11.06 g, 40 mmol) was dissolved in 50 mL of an ethanol/toluene (1:1) mixture, and NaOH (3.2 g, 80 mmol) in 50 mL of double deionized water (ddH_2O) was added. The above mixture was added to a stirred ethanol/toluene solution (1:1, 30 mL) of 11-bromoundecanoic acid (5.3 g, 20 mmol). The reaction mixture was stirred at room temperature for 16 h. A 1 M aqueous HCl solution was added dropwise

into the mixture at 0 °C until a pH value between 2 and 3 was reached. The above mixture was washed 3X with a saturated NaCl aqueous solution. The organic layer was separated, dried over anhydrous sodium sulfate and concentrated on a rotary evaporator. The product was purified using flash column chromatography over silica gel with a mixture of DCM:MeOH (98:2, v/v) as the mobile phase. The solvent was removed by vacuum to obtain the final product, triphenylmethyl-protected MUA (yield: 9.0 g, >75 %; nuclear magnetic resonance shown in Figure B.4).

4.4.3 Peptide Ligand Synthesis

The peptides were synthesized using automated Fmoc SPPS on a Tribute™ peptide synthesizer (Protein Technologies Inc., Tucson, AZ). The H3 NLS peptide sequence incorporates residues 1–25 of the N-terminal tail of the H3 protein (ARTKQTARKSTGGKAPRKQLATKAA*KG*-$CONH_2$, where the italicized residues are exogenous residues added as a putative reactive handle). The exogenous glycine at the C-terminus acts as spacer between the resin and the exogenous 1-(4,4-dimethyl-2,6-dioxacyclohexylidene)ethyl (Dde)-protected lysine residue used for MUA conjugation. Following Fmoc-lysine(Dde)-OH attachment, the Dde protecting group was removed by the addition of a weak base, as described previously.[59] Briefly, 1.25 g of hydroxylamine hydrochloride (NH_2OH•HCl) (1.80 mmol) and 0.918 g of imidazole (1.35 mmol) were dissolved in 5 mL of N-methyl-2-pyrrolidone (NMP) via sonication for 3 h. The resulting solution was diluted with 1 mL of DCM, added to the peptide-resin, and stirred for 3 h at room temperature. Following Dde deprotection, the MUA ligand was conjugated to the primary amine on the lysine side chain using HOBt and DIC in DMF while mixing (12 h, 23 ˚C). After MUA conjugation, synthesis of the H3 tail peptide continued under standard SPPS conditions. Cleavage of the H3-MUA

peptide ligand from the resin was performed using a cocktail of 94:1:2.5:2.5 TFA/triisopropylsilane (TIS)/ddH_2O/1,2-ethanedithiol (EDT) for 2 h. Purification of the peptide was performed by reverse-phase high performance liquid chromatography (RP-HPLC) on a Prominence chromatography instrument (Shimadzu, Inc., Columbia, MD) equipped with a Viva C18 (4.2 mm x 50 mm, 5 mm particle diameter) column from Restek (Lancaster, PA). ddH_2O with 0.1 % TFA (Solvent A) and acetonitrile with 0.1 % TFA (Solvent B) were employed as HPLC solvents with a gradient of solvent B from 10 %–35 % over 50 min at a flow rate of 5 mL/min. The eluent absorbance was monitored at 210 nm. The $[M+H]^+$ was determined with matrix assisted laser desorption ionization-time of flight mass spectrometry (MALDI-TOF MS, Bruker Microflex), which showed primary peaks of m/z = 3010.9 (+1H) and m/z = 1505.9 (+2H). Predicted molecular weight of the H3-MUA peptide ligand was 3009.1 Da.

The K5 (KKKKK-$CONH_2$) peptide sequence was also synthesized using SPPS. Following N-terminal Fmoc removal, triphenylmethyl-protected MUA was conjugated to the N-terminus of the K5 peptide using the same conditions described above. Cleavage of the K5-MUA peptide ligand from the resin was performed using a cocktail consisting of 88:5:5:2 TFA/phenol/ddH_2O/TIS (v/v) for 2 h. Purification of the peptide was performed similarly by RP-HPLC with a gradient of 0.1 % TFA in ddH_2O (A) and 0.1 % TFA in acetonitrile (B) as the mobile phase. The gradient was allowed to run from 10 % B to 35 % B over 50 min at a flow rate of 5 mL/min. Peptide elution was monitored by absorbance measurements at 210 nm. The $[M+H]^+$ was determined with electrospray ionization-mass spectrometry (ESI MS) on a Thermo Finnigan LCQ MS (Waltham, MA), which showed major peaks of m/z =

858.7 (+1H), m/z = 880.7 (+1Na) and m/z = 430.1 (+2H). Predicted molecular weight of the K5-MUA peptide ligand was 857.7 Da.

4.4.4 C5-AuNP Synthesis

The standard Brust-Schiffrin two-phase method[53] was used to synthesize C5 monolayer-protected AuNPs. Briefly, 30 mL of 30 mmol/L $HAuCl_4$ aqueous solution was added to 80 mL of 50 mmol/L TOAB toluene solution until all $AuCl_4^-$ was transferred to the organic phase and the aqueous phase turned fully clear. Subsequently, 1.8 mmol of C5-SH was added to the organic phase. Next, 25 mL of an 18 mmol $NaBH_4$ aqueous solution was added rapidly into the reaction mixture. The mixture was stirred for 3 h. The organic phase was collected and concentrated on a rotary evaporator. The concentrated AuNPs were purified by multiple acetone/ethanol washing and precipitation cycles as described previously.[71] The purified AuNPs were dried in a vacuum oven at room temperature. The final dry powder product was sealed under N_2 and stored at –20 °C.

4.4.5 K5/H3-Containing AuNP Preparation

The Murray place exchange reaction[57] was employed in two steps to replace the C5 monolayer with K5-MUA and H3-MUA peptide ligands. Briefly, C5-coated AuNPs (10 mg) were dissolved in 10 mL of DCM and the resulting mixture was purged with N_2; ~40 mg of K5-MUA peptide ligands were dissolved in 5 mL of DCM/MeOH (40:60, v/v) and the resulting solution was also purged with N_2. Solutions of both the C5-coated AuNPs and K5-MUA ligands were mixed, and the resulting solution stirred for 3 days at room temperature. The solvents were rotovapped under reduced pressure at 37 °C, and excessive ligands were removed by

washing 3X with DCM:MeOH (20:1 v/v) as well as dialysis against ddH_2O for 3 days (10 kDa molecular weight cut off). The aqueous suspension of peptide-coated AuNPs was lyophilized to obtain a brownish solid product. H3 ligand-containing AuNPs were prepared by a second place exchange reaction using the K5-coated AuNPs and H3-MUA peptide ligands suspended in ddH_2O for 3 days. 12, 23, or 45 mg of H3-MUA ligands were used to react with 10 mg of K5-AuNPs in a total of 20 mL ddH_2O to make the low-, mid-, and high-H3 coverage AuNPs respectively. Excess ligands were removed by multiple washing and filtering cycles using AmiconUltra centrifugal filters (EMD Millipore, Burlington, MA) with a 10 kDa molecular weight cutoff.

4.4.6 AuNP Characterization

The core dimensions of the AuNPs were measured by bright-field TEM using a JEM-3010 ultrahigh resolution analytical electron microscope at an accelerating voltage of 300 kV. The samples were prepared by pipetting ~5 μL of a 0.5 mg/mL AuNP solution onto carbon-coated copper grids and allowed to stand for 60 s. Excess solution was wicked away from the grid using clean filter paper. All samples were dried for at least 1 h before imaging.

TGA used to evaluate the total weight of organic ligands on the AuNP surface using a Discovery TGA (TA Instrument, New Castle, DE) at a heating rate of 10 °C/min under an N_2 atmosphere. The temperature ramping range was 25 °C to 700 °C, and the ligand weight portion was calculated based on the recorded weight loss using an assumption of spherical gold cores with a density of 19.3 g/cm^3 (Appendix C).

CHNS elemental analyses were performed on AuNPs displaying 2 or more ligands on the surface. Measurements were conducted by Intertek Pharmaceutical Services (Whitehouse, NJ) for the K5-, low-H3, and mid-H3 coated AuNPs. Results

were reported as the wt % of carbon, hydrogen, nitrogen, and sulfur relative to the entire sample analyzed (Table B.1).

The hydrodynamic radii of the AuNPs were analyzed using a Wyatt Mobius DLS Zeta Potential Detector (Wyatt Technology, Santa Barbara, CA) at 20 °C. Hydrodynamic radii were determined by intensity-weighted analysis on sample data from 10 runs of 2 min each. AuNP solutions were prepared at a concentration of 1 mg/mL in ddH_2O for analysis.

4.4.7 HBO1 Pull-Down Assay

Free AuNP solutions at equivalent concentrations of positive charge were prepared in 150 μL of 20 mM HEPES buffer (pH 6.0). 1.5 μL of a 100X Halt Protease solution was added to the AuNP solutions and the mixtures were incubated on ice for 10 min. Next, 6 μL of FLAG-tagged HBO1-enhanced cell lysate was added to each sample. Samples were gently mixed and agitated for 4 h at 4 ˚C. Protein corona-coated AuNPs were collected by ultracentrifugation for 1.5 h at 15,000 RPM.[72] Samples were washed with phosphate buffered saline (PBS) to remove the soft corona and the resulting pellets were resuspended in 30 μL of PBS containing 5 μL Laemmli buffer and 3 μL β-mercaptoethanol. These solutions were boiled for 10 min and the denatured protein solutions were analyzed via sodium dodecyl sulfide-polyacrylamide gel electrophoresis (SDS-PAGE) on a 4 %-40 % acrylamide gel for 35 min at 150 V. Subsequently, the protein was transferred onto a poly(vinylidene fluoride) membrane for 75 min at 18 V. The membrane was blocked in 5 vol % non-fat milk in Tris-HCl buffered saline (50 mM Tris-HCl, pH 7.4, and 150 mM NaCl) containing 0.1 vol % Tween-20 (TBST) at room temperature for 1 h. The membrane was incubated with either anti-HBO1 (diluted 1/3000 in TBST) or anti-FLAG (diluted 1/2000 in TBST) at

4 ˚C overnight. The next day, the membrane was washed and incubated with a goat anti-rabbit or anti-mouse polyclonal IgG antibody conjugated to horseradish peroxidase (diluted 1/5000 in TBST) at room temperature for 1 h. Target proteins were visualized on a FluorChem® FC2 equipped with a Nikon Sigma EXDG camera (Cell Biosciences, Palo Alto, CA) after incubation with the SuperSignal West Dura Chemiluminescent Substrate.

4.4.8 Nanoplex/Polyplex Formation and Characterization

Nanoplexes and polyplexes were formed by self-assembling pDNA with PEI or AuNPs. Briefly, equal volume solutions of pDNA and PEI or AuNPs were prepared in 20 mM HEPES at pH 6.0, and the PEI/AuNP solutions were added drop-wise to the pDNA solutions while vortexing so that the final pDNA concentration was 20 μg/mL. The PEI and AuNP concentrations in the mixtures were varied such that the N:P ratio, defined as the ratio of the number of amines (N) in the polymer/AuNP to the number of phosphates (P) in the plasmid, would be as specified. The nano/polyplex solutions were incubated for 10 min at room temperature to allow self-assembly to occur.

Hybrid AuNP/PEI nanoplexes were prepared in a similar fashion. First, a solution of AuNPs at the indicated N:P ratio was added dropwise to a solution of pDNA while vortexing. The resulting solution was allowed to incubate at room temperature for 10 min. Subsequently, a solution containing the PEI polymer at the indicated N:P ratio was added to the AuNP-pDNA solution while vortexing. Again, complexation was allowed to proceed for 10 min at room temperature.

The hydrodynamic radii and zeta potentials of the nano/polyplexes at multiple N:P ratios were evaluated similarly to the free AuNPs, as described above. Samples were prepared in 20 mM HEPES, pH 6.0 at 20 μg/mL followed by a 2-fold dilution in

HEPES. Hydrodynamic radii and zeta potentials were determined by intensity-weighted analysis on sample data from 10 runs of 2 min each.

The nanoplexes were also analyzed by agarose gel electrophoresis according to standard protocols. Briefly, a 1 % agarose gel containing 0.5 μg of ethidium bromide/mL was formed in 1X tris/borate/ethylenediaminetetraacetic acid (TBE) buffer. 20 μL of each nanoplex solution was added to 5 μL of gel loading buffer and the resulting solutions were added to the gel well. Gels were run for 2 h at 100 V and imaged using a BioRad Gel Doc XR (Hercules, CA).

For heparin stability studies, nanoplexes and polyplexes containing 0.5 μg of pDNA were formed as described above using either the modified AuNPs or PEI and the complexes were subsequently incubated with the indicated heparin solutions (over the reported ranged of heparin/pDNA wt/wt ratios) for 30 min at 37 ˚C. Samples were subsequently analyzed by gel electrophoresis as described above.

4.4.9 Nanoplex Transfection Efficiency and Flow Cytometry

CHO-K1 cells were obtained from the American Type Culture Collection (ATCC, Manassas, VA). The cells were cultured according to ATCC protocols at 37 ˚C and 5 % CO_2 in Dulbecco's modified Eagle's medium (DMEM) supplemented with 10 % fetal bovine serum (FBS) and 1 % penicillin-streptomycin. For transfection, cells were seeded in multiwell plates at a density of 15,000 cells/cm^2. Immediately prior to transfection, the cells were washed in PBS and covered in Opti-MEM. Nanoplex or polyplex solutions containing 1 μg of DNA/cm^2 well surface area were added dropwise to the cells 20 h post-seeding. After a 2 h incubation with the transfection reagents, the cells were washed with PBS and cultured in 1 mL of fully supplemented DMEM for an additional 24 h. When conducting transfection efficiency

studies in the presence of heparin, a solution of heparin in ddH_2O was added to each well to a final concentration of 0.0025 mg/mL and incubated with the rest of the transfection reagents.

Cells were imaged on a Leica 6000 fluorescence microscope (Wetzler, Germany). GFP expression was quantified on a FACS Caliber Flow Cytometer (San Jose, CA). For cytometry analyses, cells were collected after imaging by standard trypsin mediated collection protocols. Cells were resuspended in PBS containing 0.2 vol % bovine serum albumin, filtered through 35 μm nylon mesh to remove aggregates, and stored at 4 ˚C until analysis. Scattering plots were gated for quantification purposes, and a total of 10,000 live cells were analyzed for each sample. Dead cells were excluded from transfection efficiency analyses.

4.4.10 Cell Viability and Live Cell Surface Coverage

Following the transfection protocols described above, both live and dead cells were visualized by fluorescence microscopy following staining with Calcein-AM and propidium iodide. Cells were washed twice with PBS 24 h post-transfection and incubated in Opti-MEM containing 0.1 vol % Calcein-AM and propidium iodide for 50 min at 37 ˚C. The percent of viable cells was quantified by counting the number of live and dead cells using ImageJ analysis software.[73] Live cell surface area coverage was also quantified using ImageJ analysis by counting the total number of live cells and scaling to the surface area of the well. All samples were analyzed relative to untransfected controls

4.4.11 Statistical Analyses

Results for all plots are shown as the mean ± standard deviation of data obtained from at least three independently prepared and analyzed samples. Statistical analyses were performed using a Student's *t*-test or one-way analysis of variance (ANOVA). A value of $p < 0.05$ was considered to be statistically significant.

REFERENCES

1. Love, J. C.; Estroff, L. A.; Kriebel, J. K.; Nuzzo, R. G.; Whitesides, G. M., Self-assembled monolayers of thiolates on metals as a form of nanotechnology. Chemical Reviews 2005, 105 (4), 1103-1169.

2. Hostetler, M. J.; Wingate, J. E.; Zhong, C. J.; Harris, J. E.; Vachet, R. W.; Clark, M. R.; Londono, J. D.; Green, S. J.; Stokes, J. J.; Wignall, G. D.; Glish, G. L.; Porter, M. D.; Evans, N. D.; Murray, R. W., Alkanethiolate gold cluster molecules with core diameters from 1.5 to 5.2 nm: Core and monolayer properties as a function of core size. Langmuir 1998, 14 (1), 17-30.

3. Giljohann, D. A.; Seferos, D. S.; Patel, P. C.; Millstone, J. E.; Rosi, N. L.; Mirkin, C. A., Oligonucleotide loading determines cellular uptake of DNA-modified gold nanoparticles. Nano Letters 2007, 7 (12), 3818-3821.

4. Verma, A.; Uzun, O.; Hu, Y. H.; Hu, Y.; Han, H. S.; Watson, N.; Chen, S. L.; Irvine, D. J.; Stellacci, F., Surface-structure-regulated cell-membrane penetration by monolayer-protected nanoparticles. Nature Materials 2008, 7 (7), 588-595.

5. Thakor, A. S.; Jokerst, J.; Zavaleta, C.; Massoud, T. F.; Gambhir, S. S., Gold Nanoparticles: A Revival in Precious Metal Administration to Patients. Nano Letters 2011, 11 (10), 4029-4036.

6. Thakor, A. S.; Paulmurugan, R.; Kempen, P.; Zavaleta, C.; Sinclair, R.; Massoud, T. F.; Gambhir, S. S., Oxidative Stress Mediates the Effects of Raman-Active Gold Nanoparticles in Human Cells. Small 2011, 7 (1), 126-136.

7. Connor, E. E.; Mwamuka, J.; Gole, A.; Murphy, C. J.; Wyatt, M. D., Gold nanoparticles are taken up by human cells but do not cause acute cytotoxicity. Small 2005, 1 (3), 325-327.

8. Pan, Y.; Neuss, S.; Leifert, A.; Fischler, M.; Wen, F.; Simon, U.; Schmid, G.; Brandau, W.; Jahnen-Dechent, W., Size-dependent cytotoxicity of gold nanoparticles. Small 2007, 3 (11), 1941-1949.

9. Thakor, A. S.; Luong, R.; Paulmurugan, R.; Lin, F. I.; Kempen, P.; Zavaleta, C.; Chu, P.; Massoud, T. F.; Sinclair, R.; Gambhir, S. S., The Fate and Toxicity of Raman-Active Silica-Gold Nanoparticles in Mice. Science Translational Medicine 2011, 3 (79).

10. Hu, J.; Zheng, P. C.; Jiang, J. H.; Shen, G. L.; Yu, R. Q.; Liu, G. K., Sub-attomolar HIV-1 DNA detection using surface-enhanced Raman spectroscopy. Analyst 2010, 135 (5), 1084-1089.

11. Mahmoud, K. A.; Luong, J. H. T., Impedance method for detecting HIV-1 protease and screening for its inhibitors using ferrocene-peptide conjugate/Au nanoparticle/single-walled carbon nanotube modified electrode. Analytical Chemistry 2008, 80 (18), 7056-7062.

12. Georganopoulou, D. G.; Chang, L.; Nam, J. M.; Thaxton, C. S.; Mufson, E. J.; Klein, W. L.; Mirkin, C. A., Nanoparticle-based detection in cerebral spinal fluid of a soluble pathogenic biomarker for Alzheimer's disease. Proceedings of the National Academy of Sciences of the United States of America 2005, 102 (7), 2273-2276.

13. Eum, N. S.; Yeom, S. H.; Kwon, D. H.; Kim, H. R.; Kang, S. W., Enhancement of sensitivity using gold nanorods-Antibody conjugator for detection of E. coli O157:H7. Sensors and Actuators B-Chemical 2010, 143 (2), 784-788.

14. Duncan, B.; Kim, C.; Rotello, V. M., Gold nanoparticle platforms as drug and biomacromolecule delivery systems. Journal of Controlled Release 2010, 148 (1), 122-127.

15. Pissuwan, D.; Niidome, T.; Cortie, M. B., The forthcoming applications of gold nanoparticles in drug and gene delivery systems. Journal of Controlled Release 2011, 149 (1), 65-71.

16. Ghosh, P.; Han, G.; De, M.; Kim, C. K.; Rotello, V. M., Gold nanoparticles in delivery applications. Advanced Drug Delivery Reviews 2008, 60 (11), 1307-1315.

17. Wang, H. F.; Huff, T. B.; Zweifel, D. A.; He, W.; Low, P. S.; Wei, A.; Cheng, J. X., In vitro and in vivo two-photon luminescence imaging of single gold nanorods. Proceedings of the National Academy of Sciences of the United States of America 2005, 102 (44), 15752-15756.

18. Durr, N. J.; Larson, T.; Smith, D. K.; Korgel, B. A.; Sokolov, K.; Ben-Yakar, A., Two-photon luminescence imaging of cancer cells using molecularly targeted gold nanorods. Nano Letters 2007, 7 (4), 941-945.

19. Maiorano, G.; Sabella, S.; Sorce, B.; Brunetti, V.; Malvindi, M. A.; Cingolani, R.; Pompa, P. P., Effects of Cell Culture Media on the Dynamic Formation of Protein-Nanoparticle Complexes and Influence on the Cellular Response. Acs Nano 2010, 4 (12), 7481-7491.

20. Ghosh, P. S.; Kim, C. K.; Han, G.; Forbes, N. S.; Rotello, V. M., Efficient Gene Delivery Vectors by Tuning the Surface Charge Density of Amino Acid-Functionalized Gold Nanoparticles. Acs Nano 2008, 2 (11), 2213-2218.

21. Thomas, M.; Klibanov, A. M., Conjugation to gold nanoparticles enhances polyethylenimine's transfer of plasmid DNA into mammalian cells. Proceedings of the National Academy of Sciences of the United States of America 2003, 100 (16), 9138-9143.

22. Sullivan, M. M. O.; Green, J. J.; Przybycien, T. M., Development of a novel gene delivery scaffold utilizing colloidal gold-polyethylenimine conjugates for DNA condensation. Gene Therapy 2003, 10 (22), 1882-1890.

23. Bonoiu, A. C.; Mahajan, S. D.; Ding, H.; Roy, I.; Yong, K. T.; Kumar, R.; Hu, R.; Bergey, E. J.; Schwartz, S. A.; Prasad, P. N., Nanotechnology approach for drug addiction therapy: Gene silencing using delivery of gold nanorod-siRNA nanoplex in dopaminergic neurons. Proceedings of the National Academy of Sciences of the United States of America 2009, 106 (14), 5546-5550.

24. Ding, Y.; Jiang, Z. W.; Saha, K.; Kim, C. S.; Kim, S. T.; Landis, R. F.; Rotello, V. M., Gold Nanoparticles for Nucleic Acid Delivery. Molecular Therapy 2014, 22 (6), 1075-1083.

25. Lee, J. S.; Green, J. J.; Love, K. T.; Sunshine, J.; Langer, R.; Anderson, D. G., Gold, Poly(beta-amino ester) Nanoparticles for Small Interfering RNA Delivery. Nano Letters 2009, 9 (6), 2402-2406.

26. Mishra, S.; Webster, P.; Davis, M. E., PEGylation significantly affects cellular uptake and intracellular trafficking of non-viral gene delivery particles. European Journal of Cell Biology 2004, 83 (3), 97-111.

27. Boisselier, E.; Astruc, D., Gold nanoparticles in nanomedicine: preparations, imaging, diagnostics, therapies and toxicity. Chemical Society Reviews 2009, 38 (6), 1759-1782.

28. Hahn, M. A.; Singh, A. K.; Sharma, P.; Brown, S. C.; Moudgil, B. M., Nanoparticles as contrast agents for in-vivo bioimaging: current status and future perspectives. Analytical and Bioanalytical Chemistry 2011, 399 (1), 3-27.

29. Chithrani, B. D.; Ghazani, A. A.; Chan, W. C. W., Determining the size and shape dependence of gold nanoparticle uptake into mammalian cells. Nano Letters 2006, 6 (4), 662-668.

30. Rana, S.; Bajaj, A.; Mout, R.; Rotello, V. M., Monolayer coated gold nanoparticles for delivery applications. Advanced Drug Delivery Reviews 2012, 64 (2), 200-216.

31. Giljohann, D. A.; Seferos, D. S.; Daniel, W. L.; Massich, M. D.; Patel, P. C.; Mirkin, C. A., Gold Nanoparticles for Biology and Medicine. Angewandte Chemie-International Edition 2010, 49 (19), 3280-3294.

32. Kim, S. T.; Chompoosor, A.; Yeh, Y. C.; Agasti, S. S.; Solfiell, D. J.; Rotello, V. M., Dendronized Gold Nanoparticles for siRNA Delivery. Small 2012, 8 (21), 3253-3256.

33. Jiang, Y.; Tang, R.; Duncan, B.; Jiang, Z.; Yan, B.; Mout, R.; Rotello, V. M., Direct Cytosolic Delivery of siRNA Using Nanoparticle-Stabilized Nanocapsules. Angewandte Chemie-International Edition 2015, 54 (2), 506-510.

34. Lee, S. K.; Han, M. S.; Asokan, S.; Tung, C. H., Effective Gene Silencing by Multilayered siRNA-Coated Gold Nanoparticles. Small 2011, 7 (3), 364-370.

35. Ghosh, P.; Yang, X. C.; Arvizo, R.; Zhu, Z. J.; Agasti, S. S.; Mo, Z. H.; Rotello, V. M., Intracellular Delivery of a Membrane-Impermeable Enzyme in Active Form Using Functionalized Gold Nanoparticles. Journal of the American Chemical Society 2010, 132 (8), 2642-2645.

36. Mout, R.; Ray, M.; Tonga, G. Y.; Lee, Y. W.; Tay, T.; Sasaki, K.; Rotello, V. M., Direct Cytosolic Delivery of CRISPR/Cas9-Ribonucleoprotein for Efficient Gene Editing. Acs Nano 2017, 11 (3), 2452-2458.

37. Bergen, J. M.; Von Recum, H. A.; Goodman, T. T.; Massey, A. P.; Pun, S. H., Gold nanoparticles as a versatile platform for optimizing physicochemical parameters for targeted drug delivery. Macromolecular Bioscience 2006, 6 (7), 506-516.

38. Dixit, V.; Van den Bossche, J.; Sherman, D. M.; Thompson, D. H.; Andres, R. P., Synthesis and grafting of thioctic acid-PEG-folate conjugates onto Au nanoparticles for selective targeting of folate receptor-positive tumor cells. Bioconjugate Chemistry 2006, 17 (3), 603-609.

39. Prabaharan, M.; Grailer, J. J.; Pilla, S.; Steeber, D. A.; Gong, S. Q., Gold nanoparticles with a monolayer of doxorubicin-conjugated amphiphilic block copolymer for tumor-targeted drug delivery. Biomaterials 2009, 30 (30), 6065-6075.

40. Paciotti, G. F.; Kingston, D. G. I.; Tamarkin, L., Colloidal gold nanoparticles: A novel nanoparticle platform for developing multifunctional tumor-targeted drug delivery vectors. Drug Development Research 2006, 67 (1), 47-54.

41. Tkachenko, A. G.; Xie, H.; Liu, Y. L.; Coleman, D.; Ryan, J.; Glomm, W. R.; Shipton, M. K.; Franzen, S.; Feldheim, D. L., Cellular trajectories of peptide-modified gold particle complexes: Comparison of nuclear localization signals and peptide transduction domains. Bioconjugate Chemistry 2004, 15 (3), 482-490.

42. Tkachenko, A. G.; Xie, H.; Coleman, D.; Glomm, W.; Ryan, J.; Anderson, M. F.; Franzen, S.; Feldheim, D. L., Multifunctional gold nanoparticle-peptide complexes for nuclear targeting. Journal of the American Chemical Society 2003, 125 (16), 4700-4701.

43. Sun, L. L.; Liu, D. J.; Wang, Z. X., Functional gold nanoparticle-peptide complexes as cell-targeting agents. Langmuir 2008, 24 (18), 10293-10297.

44. Mosammaparast, N.; Guo, Y. R.; Shabanowitz, J.; Hunt, D. F.; Pemberton, L. F., Pathways mediating the nuclear import of histones H3 and H4 in yeast. Journal of Biological Chemistry 2002, 277 (1), 862-868.

45. Alvarez, F.; Munoz, F.; Schilcher, P.; Imhof, A.; Almouzni, G.; Loyola, A., Sequential Establishment of Marks on Soluble Histones H3 and H4. Journal of Biological Chemistry 2011, 286 (20), 17714-17721.

46. Larsen, J. D.; Reilly, M. J.; Sullivan, M. O., Using the Epigenetic Code To Promote the Unpackaging and Transcriptional Activation of DNA Polyplexes for Gene Delivery. Molecular Pharmaceutics 2012, 9 (5), 1041-1051.

47. Saksouk, N.; Avvakumov, N.; Champagne, K. S.; Hung, T.; Doyon, Y.; Cayrou, C.; Paquet, E.; Ullah, M.; Landry, A. J.; Cote, V.; Yang, X. J.; Gozani, O.; Kutateladze, T. G.; Cote, J., HBO1 HAT Complexes Target Chromatin throughout Gene Coding Regions via Multiple PHD Finger Interactions with Histone H3 Tail. Molecular Cell 2009, 33 (2), 257-265.

48. Mizuguchi, G.; Tsukiyama, T.; Wisniewski, J.; Wu, C., Role of nucleosome remodeling factor NURF in transcriptional activation of chromatin. Molecular Cell 1997, 1 (1), 141-150.

49. Reilly, M. J.; Larsen, J. D.; Sullivan, M. O., Histone H3 Tail Peptides and Poly(ethylenimine) Have Synergistic Effects for Gene Delivery. Molecular Pharmaceutics 2012, 9 (5), 1031-1040.

50. Reilly, M. J.; Larsen, J. D.; Sullivan, M. O., Polyplexes Traffic through Caveolae to the Golgi and Endoplasmic Reticulum en Route to the Nucleus. Molecular Pharmaceutics 2012, 9 (5), 1280-1290.

51. Ross, N. L.; Munsell, E. V.; Sabanayagam, C.; Sullivan, M. O., Histone-targeted Polyplexes Avoid Endosomal Escape and Enter the Nucleus During Postmitotic Redistribution of ER Membranes. Molecular Therapy-Nucleic Acids 2015, 4.

52. Ross, N. L.; Sullivan, M. O., Importin-4 Regulates Gene Delivery by Enhancing Nuclear Retention and Chromatin Deposition by Polyplexes. Molecular Pharmaceutics 2015, 12 (12), 4488-4497.

53. Brust, M.; Walker, M.; Bethell, D.; Schiffrin, D. J.; Whyman, R., Synthesis of Thiol-Derivatized Gold Nanoparticles in a 2-Phase Liquid-Liquid System. Journal of the Chemical Society-Chemical Communications 1994, (7), 801-802.

54. Turkevich, J.; Stevenson, P. C.; Hillier, J., A Study of the Nucleation and Growth Processes in the Synthesis of Colloidal Gold. Discussions of the Faraday Society 1951, (11), 55.

55. Enustun, B. V.; Turkevich, J., Coagulation of Colloidal Gold. Journal of the American Chemical Society 1963, 85 (21), 3317.

56. Frens, G., Controlled Nucleation for Regulation of Particle-Size in Monodisperse Gold Suspensions. Nature-Physical Science 1973, 241 (105), 20-22.

57. Hostetler, M. J.; Templeton, A. C.; Murray, R. W., Dynamics of place-exchange reactions on monolayer-protected gold cluster molecules. Langmuir 1999, 15 (11), 3782-3789.

58. Gibson, J. D.; Khanal, B. P.; Zubarev, E. R., Paclitaxel-functionalized gold nanoparticles. Journal of the American Chemical Society 2007, 129 (37), 11653-11661.

59. Diaz-Mochon, J. J.; Bialy, L.; Bradley, M., Full orthogonality between Dde and Fmoc: The direct synthesis of PNA-peptide conjugates. Organic Letters 2004, 6 (7), 1127-1129.

60. Green, S. J.; Pietron, J. J.; Stokes, J. J.; Hostetler, M. J.; Vu, H.; Wuelfing, W. P.; Murray, R. W., Three dimensional monolayers: Voltammetry of alkanethiolate-stabilized gold cluster molecules. Langmuir 1998, 14 (19), 5612-5619.

61. Templeton, A. C.; Wuelfing, M. P.; Murray, R. W., Monolayer protected cluster molecules. Accounts of Chemical Research 2000, 33 (1), 27-36.

62. Strahl, B. D.; Allis, C. D., The language of covalent histone modifications. Nature 2000, 403 (6765), 41-45.

63. Strahl, B. D.; Ohba, R.; Cook, R. G.; Allis, C. D., Methylation of histone H3 at lysine 4 is highly conserved and correlates with transcriptionally active nuclei in Tetrahymena. Proceedings of the National Academy of Sciences of the United States of America 1999, 96 (26), 14967-14972.

64. Hung, T.; Binda, O.; Champagne, K. S.; Kuo, A. J.; Johnson, K.; Chang, H. Y.; Simon, M. D.; Kutateladze, T. G.; Gozani, O., ING4 Mediates Crosstalk between Histone H3 K4 Trimethylation and H3 Acetylation to Attenuate Cellular Transformation. Molecular Cell 2009, 33 (2), 248-256.

65. Palacios, A.; Moreno, A.; Oliveira, B. L.; Rivera, T.; Prieto, J.; Garcia, P.; Fernandez-Fernandez, M. R.; Bernado, P.; Palmero, I.; Blanco, F. J., The Dimeric Structure and the Bivalent Recognition of H3K4me3 by the Tumor Suppressor ING4 Suggests a Mechanism for Enhanced Targeting of the HBO1 Complex to Chromatin. Journal of Molecular Biology 2010, 396 (4), 1117-1127.

66. Yue, Y. A.; Jin, F.; Deng, R.; Cai, J. G.; Chen, Y. C.; Lin, M. C. M.; Kung, H. F.; Wu, C., Revisit complexation between DNA and polyethylenimine - Effect of uncomplexed chains free in the solution mixture on gene transfection. Journal of Controlled Release 2011, 155 (1), 67-76.

67. Ruponen, M.; Ronkko, S.; Honkakoski, P.; Pelkonen, J.; Tammi, M.; Urtti, A., Extracellular glycosaminoglycans modify cellular trafficking of lipoplexes and polyplexes. Journal of Biological Chemistry 2001, 276 (36), 33875-33880.

68. Engelberg, H., Plasma Heparing Levels in a Normal Man. Circulation 1961, 23 (4), 578.

69. Warren, C.; Manley, G., Measurment of Heparin-Sulfate in Normal Human Serum by Laser Nephelometry. Clinica Chimica Acta 1984, 137 (3), 355-359.

70. Sarrazin, S.; Lamanna, W. C.; Esko, J. D., Heparan Sulfate Proteoglycans. Cold Spring Harbor Perspectives in Biology 2011, 3 (7).

71. Moyano, D. F.; Duncan, B.; Rotello, V. M., Preparation of 2 nm Gold Nanoparticles for In Vitro and In Vivo Applications. In Nanomaterial Interfaces in Biology: Methods and Protocols, Bergese, P.; HamadSchifferli, K., Eds. Humana Press Inc: Totowa, 2013; Vol. 1025, pp 3-8.

72. Monopoli, M. P.; Pitek, A. S.; Lynch, I.; Dawson, K. A., Formation and Characterization of the Nanoparticle-Protein Corona. In Nanomaterial Interfaces in Biology: Methods and Protocols, Bergese, P.; HamadSchifferli, K., Eds. Humana Press Inc: Totowa, 2013; Vol. 1025, pp 137-155.

73. Schneider, C. A.; Rasband, W. S.; Eliceiri, K. W., NIH Image to ImageJ: 25 years of image analysis. Nature Methods 2012, 9 (7), 671-675.

Chapter 5

CONCLUSIONS AND FUTURE DIRECTIONS

5.1 Dissertation Summary

Overall, the work in this dissertation seeks to address hurdles in designing effective non-viral gene delivery systems by combining well-controlled synthesis and assembly approaches (Chapter 2) with methods to understand and direct cellular delivery (Chapters 3 and 4). This work builds off the fundamental insights gained from recapitulating native histone tail trafficking and nuclear import activities within non-viral nucleic acid nanocarriers. In addition, the insights gained from these investigations highlight the utility of histone-targeted gene transfer for regenerative medicine applications. The novel finding that these nanocarriers access the nucleus during mitosis is further explored in Chapter 3, where histone-targeting was utilized to enhance chondrogenic differentiation in actively proliferating mesenchymal stem cells (MSCs) for bone regenerative applications. Chapter 4 further develops the histone-targeted design strategy, creating a novel library of nanocarriers for improved clinical translatability. By employing the controlled synthetic strategies outlined in Chapter 2, highly tunable histone-mimetic nanoscaffolds were generated demonstrating enhanced stability and gene transfer under physiological conditions. Taken together, this work represents key advancements in both the design and application of histone-targeted gene delivery systems, and provides a versatile platform for directing interactions between synthetic nanocarriers and biological systems that will hopefully improve

human health in the future. The following subsections provide more detailed motivations and synopses of the work presented in Chapters 2-4.

5.1.1 Synthetic Strategies and Characterization Techniques (Chapter 2)

The design of non-viral nucleic acid delivery vehicles requires synthetic approaches that provide excellent control over dispersity, purity, and composition. To address these conditions, well-defined materials synthesis strategies were employed to generate novel nanocarriers suitable for gene delivery applications. Gold nanoparticle (AuNP) synthesis using a 2-phase Brust-Schiffrin approach was selected as the best strategy to produce small (~2 nm) sized AuNPs with low dispersity, confirmed with transmission electron microscopy (TEM). Synthesized in this fashion, these AuNPs served as ideal scaffolds for post-functionalization with multiple thiolated ligands to ultimately generate the final nucleic acid nanocarrier. The ligands themselves were synthesized using Fmoc solid-phase peptide synthesis (SPPS). This technique offered exceptional control over the composition of the final peptide ligands, as verified by matrix-assisted laser desorption/ionization time-of-flight (MALDI-TOF) mass spectrometry. In addition, the solid phase approach in combination with reverse-phase high performance liquid chromatography (RP-HPLC), afforded high ligand yields and purities as opposed to common solution chemistry approaches. The Murray place exchange reaction provided the best control for adsorbing the synthesized ligands onto the surface of the AuNPs, ultimately creating the final monodisperse and pure nucleic acid nanocarriers with well-defined surface chemistries. These surface chemistries were effectively characterized through a combination of thermogravimetric and CHNS elemental analyses.

5.1.2 Histone-Targeted Gene Transfer of Bone Morphogenetic Protein-2 (BMP-2) Enhances Mesenchymal Stem Cell (MSC) Chondrogenic Differentiation (Chapter 3)

Native tissue regeneration following traumatic injury involves a complex series of signaling cascades that direct the differentiation of MSCs. In native bone healing for example, these signals are regulated by the expression of growth factors within the fracture site. The controlled expression of the factors has highlighted the role gene therapy may play in augmenting the bone healing response. However, non-viral nanocarriers typically lack the required efficacy needed to enhance growth factor expression to initiate native bone repair cascades. The enhanced nuclear localization and retention properties during mitosis have highlighted the role histone-targeting may play in enhancing nuclear delivery of non-viral nanocarriers in the actively dividing cells present during bone reformation. Using H3-targeted gene transfer, a 4-fold enhancement in osteogenic BMP-2 growth factor was achieved in comparison to untargeted nanocarriers. A unique finding was that the expression of BMP-2 gradually increased over the course of 4 days, followed by a gradual decrease, consistent with expression profiles of BMP-2 during native fracture healing. The enhanced BMP-2 expression following a single H3-targeted transfection led to more robust levels of chondrogenic differentiation in MSCs, an essential first step in the bone regenerative process, over the course of 1-3 weeks. Significant enhancements in cartilage-specific gene and protein expression were achieved over transfections with untargeted nanocarriers. Most notably, the levels of chondrogenesis achieved using H3-targeted gene transfer exceeded the levels produced following treatment with an equivalent amount of recombinant BMP-2 protein. In fact, repeated topical application of 100-fold excess BMP-2 protein was required before similar levels of chondrogenesis were observed. The improvements in differentiation achieved using

H3-targeted gene transfer were in part regulated by enhanced activation of essential transcription factors required to initiate and progress the formation of mature chondrocytes. Taken together, these investigations highlight the unique potential in applying histone-targeted gene transfer for the advancement of regenerative medicine.

5.1.3 Histone-Mimetic Gold Nanoparticles (AuNPs) as Versatile Scaffolds for Gene Transfer and Chromatin Analysis (Chapter 4)

The design of nucleic acid nanocarriers that can effectively navigate the intracellular milieu and deliver the cargo to the therapeutic site of action continues to represent a significant challenge in field of non-viral gene therapy. In addition, nanocarriers must satisfy the seemingly contradictory demands of stably binding the nucleic acid, protecting it from extracellular degradation, and controllably releasing it at the intracellular target. The unique insights gained from our previous investigations have highlighted the role histone-targeting may play in harnessing native trafficking and nuclear import pathways to direct the delivery and controllable release of DNA-encapsulating nanocarriers. To that end, the synthetic strategies outlined in Chapter 2 were employed to create novel histone-mimetic nanoscaffolds that functioned to provide control over these interactions with native cellular processes to ultimately enhance gene transfer. AuNPs were demonstrated to be effective scaffolds for both improving and controlling the display of the histone H3 tail nuclear localization sequence (NLS) within a non-viral gene nanocarrier. A small library of histone-mimetic nanoscaffolds were efficiently synthesized and characterized, each displaying varying amounts of the H3 NLS. Interactions between the nanocarriers and native histone effectors involved in transcriptional activation could be selectively tuned by changing the amount of H3 tail displayed on the surface of the nanoscaffolds. These

nanoscaffolds were able to effectively bind and condense plasmid DNA (pDNA) more efficiently than standard polymeric delivery systems at the same overall charge ratio. Importantly, the formed nanoplexes exhibited 4-fold enhancements in stability against pDNA displacement by common polyanions (heparin) found in the extracellular space. Overall transfection efficiency directly correlated to the amount of H3 NLS displayed on the surface of the nanoscaffold, with high H3-coated AuNPs displaying 7-fold enhancements in transfection efficiency when compared to low H3-coated AuNPs and AuNPs without any H3 tail displayed on the surface. Most notably, no significant changes in overall transfection efficiency were observed with H3-coated AuNP nanoplexes in the presence of physiologically relevant amounts of heparin. In contrast, nanocarriers formed with standard polymeric transfection reagents completely destabilized in the presence of heparin, resulting in insignificant levels of transfection. Thus, this work demonstrates the utility of employing a tailorable histone-mimetic nanocarrier design strategy to stably bind and condense pDNA for extracellular protection, and to control native interactions with intracellular space to ultimately enhance gene transfer and therapeutic efficacy.

5.2 Recommendations for Future Work

5.2.1 Direct Extensions of Current Work

The main thrust that directly builds off of the pioneering work described in previous chapters, relates to translating histone-targeted gene transfer formulations into *in vivo* mouse models of bone tissue regeneration. Formulations can be applied as simple subcutaneous injections aimed at measuring nanocarrier stability, cell invasion, gene expression, and subdermal deposit calcification. More complex fracture healing

models can also be explored; applying formulations to large segmental bone defects in mice and monitoring fracture healing/bone reformation. These studies are currently underway in collaboration with Dr. Theresa A. Freeman and her laboratory at Jefferson University.

5.2.1.1 Preliminary *in vivo* Transfection Using Histone Targeting

Previous studies performed by Dr. Nikki L. Ross and Dr. Morgan Urello focused on examining the transfection efficiency of H3-targeted nanocarriers in mouse subdermal deposits. These subcutaneous injection experiments provide access to a wide range of cell types (including native MSCs) which are relevant to bone repair. In these experiments both H3-targeted and untargeted PEI nanocarriers were formed as described in this dissertation and elsewhere.[1-3] For proper *in vivo* application, both large and concentrated doses of nanocarriers are required to maintain efficacy.[4] In addition, application of the nanocarriers needs to be localized (e.g. within the fracture site), in order to reduce off-targeting effects. Thus following formation, nanocarriers were lyophilized in the presence of sucrose (20 mmol/L) to preserve nanocarrier structure and activity.[5] Following lyophilization, the freeze-dried nanocarriers were re-suspended in Matrigel solution, prior to subcutaneous injection. Matrigel serves as an effective extracellular matrix (ECM) mimetic scaffold[6] to ensure localized nanocarrier injection and to promote natural cellular invasion for nanocarrier uptake.

In these experiments, each mouse received four separate 300 μl Matrigel injections: (1) containing H3-targeted nanocarriers (200 μg Luc pDNA dose), (2) nanocarrier free Matrigel with luciferin, (3) nanocarrier free Matrigel without luciferin, and (4) Matrigel/luciferase mixture. Luciferase expression was monitored daily following a small intraperitoneal luciferin injection over a period of ~1 week.

Results demonstrated efficient nanocarrier-mediated transfection with the luciferase gene from Matrigel in subdermal mouse depots (Figure 5.1). These preliminary data suggest that Matrigel will provide robust osteogenic gene transfer using both H3-targeted nanocarriers as well as histone-mimetic nanoscaffolds.

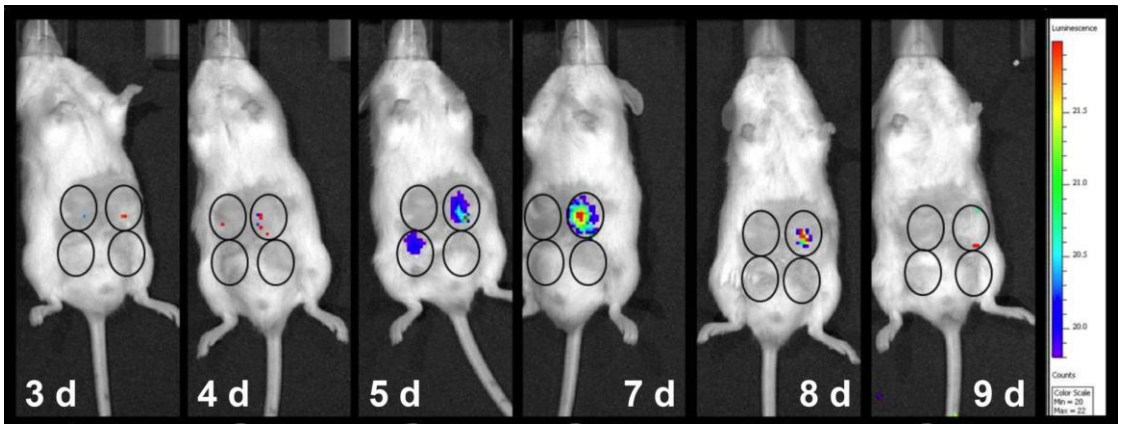

Figure 5.1: H3-targeted nanocarrier transfection (upper right) of host cells in subdermal depots, at 200 μg pDNA per mL of Matrigel. Nanocarrier free Matrigel depots with and without luciferin injection (upper left and lower right respectively), and Matrigel/luciferase depots with luciferin injection (lower left). Red indicates highest luminescence. Figure adapted with permission from NL Ross, Improving non-viral gene delivery with histone-targeted polyplexes: uptake, trafficking, and nuclear deposition, *University of Delaware Thesis*, Published by ProQuest LLC (2016)[7], Copyright 2016, Rights reserved by Nikki Lea Ross.

5.2.1.2 Evaluating *in vivo* Bone Formation Using Mouse Models

The Freeman lab has extensive experience with testing and evaluating endochondral bone reforming models *in vivo*. Simple subcutaneous injection experiments designed similarly to those described in the previous section can be used to deliver localized subdermal Matrigel depots of nanocarriers containing osteogenic growth factor genes such as bone morphogenetic protein-2 (BMP-2). Endochondral

ossification can be effectively monitored within these ectopic masses over the course of 1-2 weeks (Figure 5.2). Early assessment of cartilage formation can be assessed by Alcian blue staining of tissue sections following removal of the masses. Tartrate-Resistant Alkaline Phosphatase (TRAP) enzyme histochemistry can be used to track the appearance of osteoclasts prior to cartilage remodeling. In addition, mature bone formation at later times can be confirmed using μCT analyses and Alizarin red staining to detect calcification within the harvested ectopic masses.

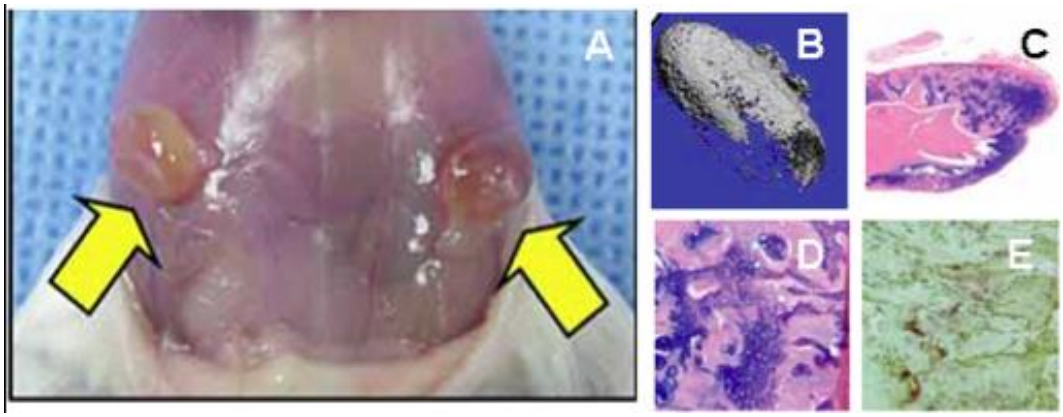

Figure 5.2: Mouse model of endochondral ossification following (A) subdermally injected ectopic masses (arrows) on the abdomen (skin removed). (B) μCT analysis of a mass removed after 10 days. Alcian blue and eosin staining of a mass tissue section after (C) 7 days and (D) 9 days indicating chondrogenesis and bone present. (E) TRAP enzyme histochemistry shows purple staining of mature osteoclasts. Images adapted and modified with permission from K Shimono, TN Morrison, W Tung, RA Chandraratna, et. al., Inhibition of ectopic bone formation by a selective retinoic acid receptor α-agonist: a new therapy for heterotopic ossification?, *J Orthop Res,* 28(2) 271-7 (2010),[8] Copyright 2009, Rights reserved by Wiley Periodicals, Inc.

The primary purpose of these experiments will be to quantify the dose of nanocarriers that maximizes ectopic bone formation within these depots, and evaluate the ability of histone-targeted gene transfer to enable dose reductions versus untargeted approaches. Given the encouraging *in vitro* work described in Chapter 3, it is likely that H3-targeted gene transfer will enable significantly higher levels of endochondral ossification within subdermally injected ectopic masses, compared to untargeted nanocarriers. Additionally, it will be of interest to directly compare the amount of bone formation achieved using the histone-mimetic nanoscaffolds described in Chapter 4 to the levels achieved using the soft materials approach with H3-targeted nanocarriers. The improved ligand display conferred by the nanoscaffolds will likely function to enhance cellular interactions for improved pDNA delivery, expression, and ultimately bone formation. Furthermore, the enhanced tailorability of the nanoscaffolds make them amenable to other surface modifications that may alter pDNA binding (detailed in section 5.2.2.1), cellular interactions (detailed in section 5.2.2.2), and scaffold stability (detailed in section 5.2.2.3), leading to further improvements in bone formation.

The subcutaneous injection experiments described above will provide insight into assessing more complex *in vivo* models of bone regeneration. The Freeman lab has extensive experience with animal defect and fracture models as well as the μCT and histological analyses required to perform these experiments.[9, 10] In these analyses a critical-sized defect (incapable of healing on its own) is created in the animal, typically the rib or the tibia.[11] ECM scaffold solutions containing the nanocarriers will be locally injected into the defect site, and the defect sealed with glue to prevent leakage. Both qualitative and quantitative assessments of healing progression, bone

morphology, and protein expression can be measured over the course of 1-3 weeks. By this method, the ability of histone-targeted gene transfer to augment fracture healing in native models of bone regeneration can be truly assessed and compared directly with untargeted gene transfer methods as well as treatments with recombinant growth factor protein.

5.2.2 Modifications to the Histone-Mimetic Nanoscaffolds

The synthetic strategies outlined in Chapter 2 and employed in Chapter 4 represent an effective method for producing tunable nanocarriers for enhanced gene transfer applications. However, the versatility of these histone-mimetic nanoscaffolds expands beyond the small library that was synthesized and discussed in this dissertation. Additional motifs may be added to the surface via additional place exchange reactions, enhancing their complexity. Conversely, completely different structures may be built starting from the pentanethiol-coated AuNPs. In the context of gene delivery, modifications to the AuNP surface may focus on three key areas: (1) tuning nucleic acid binding, (2) tuning biological interactions, and (3) tuning nanoscaffold stability. These modifications and their possible effects on nucleic acid delivery are further discussed in the following sections.

5.2.2.1 Tuning Nucleic Acid Binding: Altering Cationic Charge Density

An important aspect of effective non-viral gene delivery lies in the ability to control nucleic acid binding versus release.[12, 13] Effective nanocarriers must satisfy contradictory demands: (1) stably bind and protect the nucleic acid from degradation outside the cell, and (2) effectively release the nucleic acid cargo at the therapeutic site of action within the cell. The synthesized histone-mimetic nanoscaffolds discussed in

this dissertation contain a high cationic charge density, given the number of primary amine groups present in the ligands used (5 from the K5 peptide ligand, 9 from the H3 tail peptide ligand). This high positive charge density is likely playing an important role in stabilizing the final nanocarriers, as discussed in Chapter 4. However, it is possible that the stable pDNA condensation may also be preventing full release of the pDNA once it reaches the nucleus, contributing to the low levels of transfection efficiency overall. One way to evaluate these effects would be to dilute the positive charge present on the nanoscaffold surface. This can be accomplished in a variety of ways. The most effective would be to synthesize new ligands with reduced charge density. Shorter lysine chains or chains that contain both charged (e.g. lysine, arginine) and uncharged (e.g. serine, threonine) residues may function to lower the strength of electrostatic interactions between the pDNA and histone-mimetic nanoscaffolds to ultimately achieve better pDNA release in the nucleus for improved expression. In addition, the versatility of SPPS[14, 15] (as discussed in Chapter 2) provides an ideal platform for synthesizing a variety of modified peptide ligands with reduced cationic charge density.

5.2.2.2 Tuning Cellular Interactions: Altering Ligand Display Chemistries

The investigations discussed in Chapter 4 focused on the synthesis of histone-mimetic nanoscaffolds displaying varying amounts of the H3 tail NLS. The amount of H3 tail on the AuNP surface was shown to effectively tune the amount of interaction with the native histone effector HBO1 histone acetyltransferase (HAT). However, in order to truly mimic native histone architecture, it is of interest to introduce additional histone tail ligands onto the AuNP surface. The histone H2A and H2B tail sequences play important roles in the higher order packaging of chromosomal DNA and do not

play direct roles in transcriptional activation. In contrast, the histone H4 tail sequence functions cooperatively with the H3 tail to control chromatin activation and nuclear retention. In nature, the histone H3 and H4 proteins are synthesized as an active dimer during S phase for chromatin assembly during replication. Ultimately, interactions between H3 and H4 tails and importins help mediate nuclear import and affect chromatin deposition of the H3-H4 dimer. In addition, the H4 tail plays a particularly key role in nuclear retention. Thus, the combined display of H3 and H4 tail ligands on the surface of histone-mimetic nanoscaffolds will likely function to enhance nanocarrier nuclear delivery during mitosis. Furthermore, the enhanced nuclear retention properties of the H4 tail may retain nanocarrier nuclear localization during mitosis, resulting in longer sustained expression of the delivered pDNA.

The H4 peptide ligand can be easily synthesized via the methods described in this dissertation, and introduced to the AuNP surface via the Murray place exchange reaction. H4 can be exchanged onto the surface following H3 exchange, or during H3 exchange, at various molar ratios to produce a larger library of histone-mimetic nanoscaffolds with various H3:H4 ratios (e.g. H3 only, 75:25, 50:50, 25:75, H4 only). It will be of great interest to investigate how the mixtures of H3/H4 tail display on the surface influence interactions with intracellular trafficking and nuclear import machinery to effect nanocarrier delivery and DNA expression.

5.2.2.3 Tuning Nanoscaffold Stability: Modifying the Alkanethiol Chains

Ensuring AuNP stability under physiological conditions is essential to their successful application *in vivo*. It is well documented that the physiochemical properties of the AuNP surface directly determine interactions with physiological systems.[16, 17] Following administration, a layer of proteins absorb to the AuNP surface

forming a protein corona.[18-20] The surface chemistry of the AuNPs largely dictates the thickness, decoration, and identity of the protein corona.[21] These ultimately influence AuNP interactions with the cargo to be delivered as well as interactions with target cells.[22-24] Although the studies presented in this dissertation focus on circumventing issues with protein corona formation by using a localized delivery approach, the histone-mimetic nanocarriers will undoubtedly interact with proteins in the extracellular space in some manner. Thus it is important to ensure that the NPs themselves will remain stable against aggregation/degradation when exposed to the *in vivo* environment.

Recent work by Dr. Vincent M. Rotello's group at the University of Massachusetts, Amherst has focused on improving AuNP stability via the addition of oligo(ethylene glycol) units to the alkanethiol monolayer.[25] Appending a tetraethylene glycol (TEG) repeat to the end of the stabilizing alkanethiol chain was shown to improve solubility, biocompatibility, and prevent non-specific interactions with biomolecules.[26] Most notably, the TEG group was shown to help expose the terminal functional groups on the AuNP surface, allowing for more stable and reversible interactions with proteins (Figure 5.3).[27] The Rotello group has since utilized these TEG-functionalized AuNPs in a wide variety of protein delivery[28, 29] and diagnostic applications.[25, 30, 31]

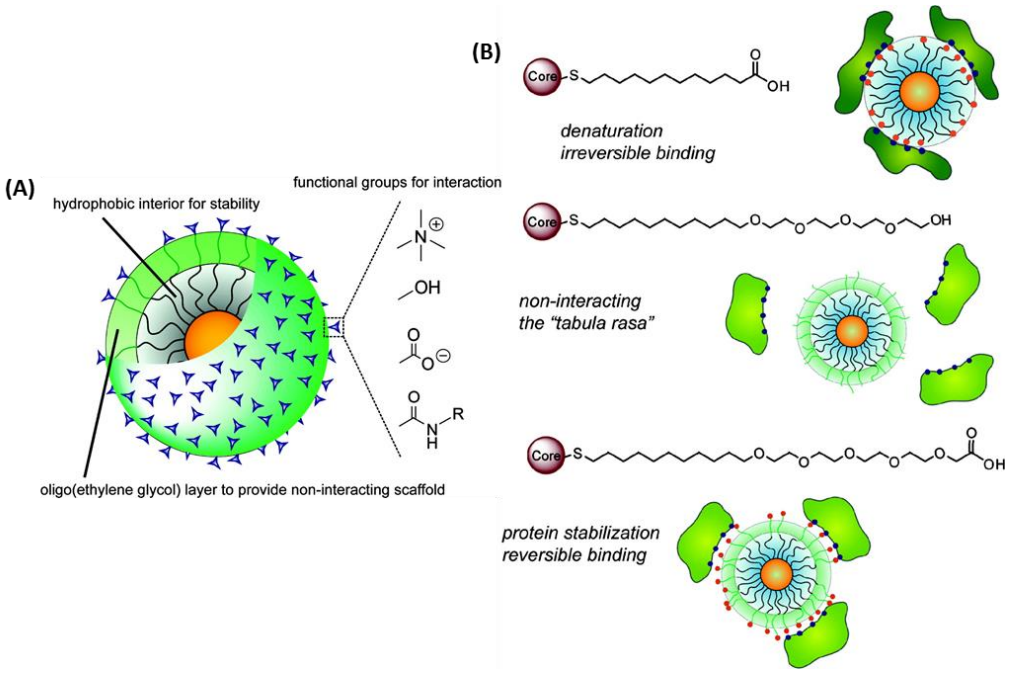

Figure 5.3: (A) AuNP monolayer design featuring stability and a controlled presentation of functionality. (B) Effect of the monolayer on AuNP-protein interactions. Simple alkanethiol-based monolayers result in protein degradation. TEG-functionalized particles are non-interacting, while carboxyl-terminated TEG layers provide reversible protein binding and stability against degradation. Figures adapted and reproduced with permission from DF Moyano and VM Rotello, Nano meets biology: structure and function at the nanoparticle interface, *Langmuir* 27(17) 10376-85 (2011).[25] Copyright 2011, Rights reserved by the American Chemical Society.

It would be interesting to examine the changes in nanocarrier stability that occur following incorporation of a TEG functionality into the histone-mimetic nanoscaffolds. The TEG group may function to alter/stabilize interactions with the pDNA, similar to native proteins (Figure 5.3). Whether these altered interactions serve to enhance or hinder pDNA delivery/expression will have to be tested *in vitro*. However, the addition of the TEG group to the histone-mimetic nanoscaffolds will

likely serve to enhance biocompatibility and also provide enhanced stability against opsonization, making these nanocarriers more amenable to *in vivo* applications in regenerative medicine.

5.2.3 Improving Understanding of Cellular Mechanisms

Another extension of the work described in Chapter 4 will be to monitor the intracellular trafficking and nuclear import of the histone-mimetic nanocarriers following endocytosis. Similar studies to those previously performed in the group,[3, 32, 33] can be employed to understand how trafficking and nuclear delivery of these nanocarriers are regulated. It will also be of interest to monitor how these interactions change depending on different modifications made to the AuNP surface (section 5.2.2). In addition, the enhanced optical, electronic, and chemical properties of the gold core provide the unique opportunity to employ higher resolution imaging techniques, such as electron microscopy (EM).[34] These techniques can be utilized to identify key trafficking and release steps to gain better insight into the role of the nanocarrier in mediating delivery. This may open a wide range of opportunities for exploiting specific cellular pathways to gain access to particular areas within the intracellular space in order to deliver different types of therapeutic cargoes.

The enhanced imaging properties of the AuNPs highlight the potential of utilizing these histone-mimetic nanoscaffolds as intracellular diagnostic probes. One possible application would be to further examine how histone-targeted nanocarriers interact with chromatin post-mitosis. Previous work by Dr. Nikki L. Ross demonstrated that histone-targeting influenced chromatin interaction/deposition,[33] which likely functioned to enhance nuclear retention of H3-targeted nanocarriers. It would be of interest to further explore how histone-targeted nanocarriers and

chromatin interact with one another using high resolution EM imaging, and what role these interactions play in enhancing nuclear retention. Furthermore, a better understanding of nanocarrier unpackaging could be gained. Possessing these fundamental insights will ultimately help guide future nanocarrier design parameters aimed at controlling and optimizing chromatin interactions for sustained transcriptional activation.

5.2.4 Controlling Growth Factor Expression Profiles with Histone-Targeted Gene Transfer

Native regeneration and growth following traumatic injury often requires the coordinated expression of specific growth factors to reform fully mature tissue. For example, during bone repair osteogenic factors (e.g. transforming growth factors, BMPs), angiogenic factors (e.g. vascular endothelial growth factor, fibroblast growth factor), and inflammatory growth factors (e.g. factor-α, interferon-γ) are all expressed during specific phases of the bone healing process.[35-37] Simultaneous (Figure 5.4) and sequential delivery of growth factors over controlled timeframes have been shown to significantly improve bone tissue regeneration in animal models of critical-sized bone defects.[35, 38]

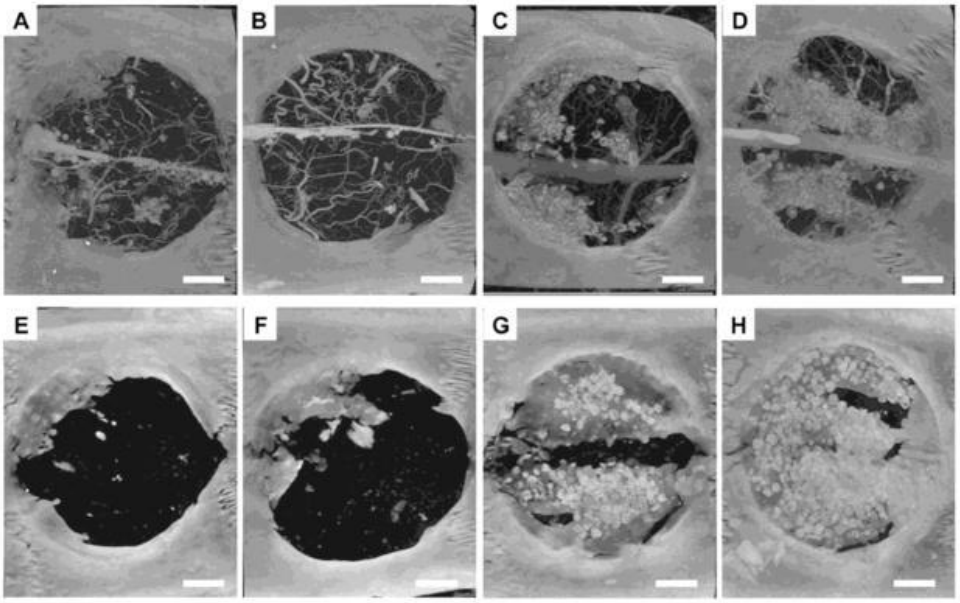

Figure 5.4: Micro-computed tomography images of bone regeneration in a rat calvarial critical size defect at 4 (top row) and 12 (bottom row) weeks with no growth factor delivery (panels A and E), VEGF delivery only (panels B and F), BMP-2 delivery only (panels C and G) and VEGF/BMP-2 dual delivery (panels D and H). Bone formation with dual delivery is higher at 4 weeks and comparable at 12 weeks to BMP-2 delivery alone. Scale bar represents 200 μm. Figure reproduced with permission from TN Vo, FK Kasper, and AG Mikos, Strategies for controlled delivery of growth factors and cells for bone regeneration, *Adv Drug Deliv Revs*, 64(12), 1292-309, (2012)[35]. Copyright 2012, Rights reserved by Elsevier B.V.

An interesting finding from the work presented in Chapter 3 was that following a single H3-targeted transfection, BMP-2 expression gradually increased and decreased over the course of 1 week, reaching a maximum at day 4 post-transfection. It was hypothesized that a combination of nanocarrier nuclear retention due to histone-targeting and growth factor sequestration by collagen type I functioned to promote gradual and sustained BMP-2 expression. Combining this effect with the need for controlled spatiotemporal expression of growth factors during tissue repair highlights

a unique opportunity to explore the effect of substrate type in promoting growth factor capture following histone-targeted gene transfer. For example, histone-targeted nanocarriers containing two (or more) growth factor genes could be formulated in ECM-mimetic scaffolds designed to promote sequestration of certain growth factor proteins over others. Through concentrated efforts to control gene retention in the nucleus via histone-targeted nanocarrier design, the timing of expression of multiple growth factor proteins could be systematically controlled within a localized area from a single scaffold. These investigations will provide unique insight into how both non-viral nanocarrier and scaffold design can be combined to promote native growth factor expression profiles for improved tissue repair.

5.2.5 Summary of Recommended Future Directions

There are four main categories for future work: direct extensions of the current work, modifications to the AuNP surface chemistries, improving understanding of cellular mechanisms, and controlling growth factor expression profiles. Initially, I recommend continuing to evaluate histone-targeted nanocarriers *in vivo* in order for primary hurdles associated with delivery under physiological to be identified early and subsequently addressed. In particular, I suggest focusing on *in vivo* evaluations of the histone-mimetic nanoscaffolds discussed in Chapter 4. Preliminary *in vivo* results discussed in section 5.2.1.1 indicate that Matrigel formulations should be ideal for bone regenerative applications. However, issues with stability and/or cellular uptake may arise, meaning that modifications to the AuNP surface chemistries may have to be made before progress can continue *in vivo*. In parallel with *in vivo* studies, changes made to the AuNP surface chemistries, can also be evaluated *in vitro* as described in section 5.2.3. These *in vitro* evaluations may partially inform the work performed *in*

vivo, providing a better understanding of how the histone-mimetic nanoscaffolds are interacting with the cellular environment. Overall, the complex nature of animal models makes it difficult to determine which types of surface chemistries will provide the most effective delivery and the best bone healing response. However, the ideas described in this chapter provide an initial starting point for effectively addressing key challenges that may be encountered as the delivery systems advance through pre-clinical evaluations.

5.3 Final Perspectives

The field of gene therapy has continued to grow exponentially since its first inception as a possible treatment strategy for genetic defects in 1972.[39] For example, in the time it took to write this dissertation, yet another form of gene therapy achieved FDA approval,[40] bringing the total number of commercial gene therapies in the United States to two. Yescarta, developed by Kite Pharma, was approved in October 2017 to treat non-Hodgkin's lymphoma in adults who have not responded to chemotherapy. Although this may be an exaggerated example, gene therapy undoubtedly stands poised to revolutionize the way we treat and ultimately cure human disease.

Despite these landmark achievements, there still remains an immense gap between the number of clinically approved gene therapy treatments and those that typically fail in both pre-clinical and clinical trials. Understanding the natural cellular mechanisms involved in cellular trafficking, endosome escape, and nuclear import is crucial to achieving effective gene delivery. Additionally, more quantitative assessments of endosome escape and nuclear delivery need to be established in order to develop improved delivery techniques. The advances achieved in this dissertation: designing multifunctional formulations that possess both tailorability and the capacity

to interact favorably with the numerous biological signals encountered during the delivery process, are essential to enhancing nanocarrier design. Combining multifunctional biomimetic carrier design strategies with natural mechanistic insight will help elucidate the complex journey taken by engineered nanocarriers en route to their active site within the cell, greatly enhancing both the therapeutic efficacy and clinical translatability of non-viral nucleic acid delivery.

REFERENCES

1. Larsen, J. D.; Reilly, M. J.; Sullivan, M. O., Using the Epigenetic Code To Promote the Unpackaging and Transcriptional Activation of DNA Polyplexes for Gene Delivery. Molecular Pharmaceutics 2012, 9 (5), 1041-1051.

2. Reilly, M. J.; Larsen, J. D.; Sullivan, M. O., Histone H3 tail peptides and poly(ethylenimine) have synergistic effects for gene delivery. Mol Pharm 2012, 9 (5), 1031-40.

3. Ross, N. L.; Sullivan, M. O., Histone-Targeted Polyplexes Avoid Endosomal Escape and Enter the Nucleus During Post-Mitotic Redistribution of ER Membranes. Molecular Therapy 2015, 23, S195-S195.

4. Bhattarai, N.; Gunn, J.; Zhang, M. Q., Chitosan-based hydrogels for controlled, localized drug delivery. Advanced Drug Delivery Reviews 2010, 62 (1), 83-99.

5. Lei, Y. G.; Huang, S. X.; Sharif-Kashani, P.; Chen, Y.; Kavehpour, P.; Segura, T., Incorporation of active DNA/cationic polymer polyplexes into hydrogel scaffolds. Biomaterials 2010, 31 (34), 9106-9116.

6. Kleinman, H. K.; Martin, G. R., Matrigel: Basement membrane matrix with biological activity. Seminars in Cancer Biology 2005, 15 (5), 378-386.

7. Ross, N. L., Improving non-viral gene delivery with histone-targeted polyplexes: uptake, trafficking, and nuclear deposition, University of Delaware Thesis, Published by ProQuest LLC, 2016.

8. Shimono, K.; Morrison, T. N.; Tung, W. E.; Chandraratna, R. A.; Williams, J. A.; Iwamoto, M.; Pacifici, M., Inhibition of Ectopic Bone Formation by a Selective Retinoic Acid Receptor alpha-Agonist: A New Therapy for Heterotopic Ossification? Journal of Orthopaedic Research 2010, 28 (2), 271-277.

9. Adams, C. S.; Antoci, V.; Harrison, G.; Patal, P.; Freeman, T. A.; Shapiro, I. M.; Parvizi, J.; Hickok, N. J.; Radin, S.; Ducheyne, P., Controlled Release of Vancomycin from Thin Sol-Gel Films on Implant Surfaces Successfully Controls Osteomyelitis. Journal of Orthopaedic Research 2009, 27 (6), 701-709.

10. Freeman, T. A.; Patel, P.; Parvizi, J.; Antoci, V.; Shapiro, I. M., Micro-CT Analysis with Multiple Thresholds Allows Detection of Bone Formation and Resorption during Ultrasound-Treated Fracture Healing. Journal of Orthopaedic Research 2009, 27 (5), 673-679.

11. Li, Y.; Chen, S. K.; Li, L.; Qin, L.; Wang, X. L.; Lai, Y. X., Bone defect animal models for testing efficacy of bone substitute biomaterials. Journal of Orthopaedic Translation 2015, 3 (3), 95-104.

12. Burke, P. A.; Pun, S. H.; Reineke, T. M., Advancing Polymeric Delivery Systems Amidst a Nucleic Acid Therapy Renaissance. Acs Macro Letters 2013, 2 (10), 928-934.

13. Ruvinov, E.; Kryukov, O.; Forti, E.; Korin, E.; Goldstein, M.; Cohen, S., Calcium-siRNA nanocomplexes: What reversibility is all about. Journal of Controlled Release 2015, 203, 150-160.

14. Merrifield, R. B., Solid phase peptide synthesis: 1. Synthesis of a tetrapeptide. Journal of the American Chemical Society 1963, 85 (14), 2149-&.

15. Behrendt, R.; White, P.; Offer, J., Advances in Fmoc solid-phase peptide synthesis. Journal of Peptide Science 2016, 22 (1), 4-27.

16. Albanese, A.; Tang, P. S.; Chan, W. C. W., The Effect of Nanoparticle Size, Shape, and Surface Chemistry on Biological Systems. In Annual Review of Biomedical Engineering, Vol 14, Yarmush, M. L., Ed. Annual Reviews: Palo Alto, 2012; Vol. 14, pp 1-16.

17. Saha, K.; Bajaj, A.; Duncan, B.; Rotello, V. M., Beauty is Skin Deep: A Surface Monolayer Perspective on Nanoparticle Interactions with Cells and Biomacromolecules. Small 2011, 7 (14), 1903-1918.

18. Mahmoudi, M.; Lynch, I.; Ejtehadi, M. R.; Monopoli, M. P.; Bombelli, F. B.; Laurent, S., Protein-Nanoparticle Interactions: Opportunities and Challenges. Chemical Reviews 2011, 111 (9), 5610-5637.

19. Hamad-Schifferli, K., Exploiting the novel properties of protein coronas: emerging applications in nanomedicine. Nanomedicine 2015, 10 (10), 1663-1674.

20. Monopoli, M. P.; Aberg, C.; Salvati, A.; Dawson, K. A., Biomolecular coronas provide the biological identity of nanosized materials. Nature Nanotechnology 2012, 7 (12), 779-786.

21. Saha, K.; Rahimi, M.; Yazdani, M.; Kim, S. T.; Moyano, D. F.; Hou, S.; Das, R.; Mout, R.; Rezaee, F.; Mahmoudi, M.; Rotello, V. M., Regulation of Macrophage Recognition through the Interplay of Nanoparticle Surface Functionality and Protein Corona. Acs Nano 2016, 10 (4), 4421-4430.

22. Walkey, C. D.; Olsen, J. B.; Song, F. Y.; Liu, R.; Guo, H. B.; Olsen, D. W. H.; Cohen, Y.; Emili, A.; Chan, W. C. W., Protein Corona Fingerprinting Predicts the Cellular Interaction of Gold and Silver Nanoparticles. Acs Nano 2014, 8 (3), 2439-2455.

23. Cifuentes-Rius, A.; de Puig, H.; Kah, J. C. Y.; Borros, S.; Hamad-Schifferli, K., Optimizing the Properties of the Protein Corona Surrounding Nanoparticles for Tuning Payload Release. Acs Nano 2013, 7 (11), 10066-10074.

24. Kah, J. C. Y.; Grabinski, C.; Untener, E.; Garrett, C.; Chen, J.; Zhu, D.; Hussain, S. M.; Hamad-Schifferli, K., Protein Coronas on Gold Nanorods Passivated with Amphiphilic Ligands Affect Cytotoxicity and Cellular Response to Penicillin/Streptomycin. Acs Nano 2014, 8 (5), 4608-4620.

25. Moyano, D. F.; Rotello, V. M., Nano Meets Biology: Structure and Function at the Nanoparticle Interface. Langmuir 2011, 27 (17), 10376-10385.

26. Ghosh, P.; Yang, X. C.; Arvizo, R.; Zhu, Z. J.; Agasti, S. S.; Mo, Z. H.; Rotello, V. M., Intracellular Delivery of a Membrane-Impermeable Enzyme in Active Form Using Functionalized Gold Nanoparticles. Journal of the American Chemical Society 2010, 132 (8), 2642-2645.

27. Hong, R.; Fischer, N. O.; Verma, A.; Goodman, C. M.; Emrick, T.; Rotello, V. M., Control of protein structure and function through surface recognition by tailored nanoparticle scaffolds. Journal of the American Chemical Society 2004, 126 (3), 739-743.

28. Mout, R.; Ray, M.; Tay, T.; Sasaki, K.; Tonga, G. Y.; Rotello, V. M., General Strategy for Direct Cytosolic Protein Delivery via Protein-Nanoparticle Co-engineering. Acs Nano 2017, 11 (6), 6416-6421.

29. Tang, R.; Wang, M.; Ray, M.; Jiang, Y.; Jiang, Z. W.; Xu, Q. B.; Rotello, V. M., Active Targeting of the Nucleus Using Nonpeptidic Boronate Tags. Journal of the American Chemical Society 2017, 139 (25), 8547-8551.

30. Jiang, Y.; Huo, S. D.; Mizuhara, T.; Das, R.; Lee, Y. W.; Hou, S.; Moyano, D. F.; Duncan, B.; Liang, X. J.; Rotello, V. M., The Interplay of Size and Surface Functionality on the Cellular Uptake of Sub-10 nm Gold Nanoparticles. Acs Nano 2015, 9 (10), 9986-9993.

31. Elci, S. G.; Tonga, G. Y.; Kim, B.; Kim, C. S.; Jiang, Y.; Saha, K.; Moyano, D. F.; Marsico, A. L. M.; Rotello, V. M.; Vachet, R. W., Dual-Mode Mass Spectrometric Imaging for Determination of in Vivo Stability of Nanoparticle Monolayers. Acs Nano 2017, 11 (7), 7424-7430.

32. Reilly, M. J.; Larsen, J. D.; Sullivan, M. O., Polyplexes Traffic through Caveolae to the Golgi and Endoplasmic Reticulum en Route to the Nucleus. Molecular Pharmaceutics 2012, 9 (5), 1280-1290.

33. Ross, N. L.; Sullivan, M. O., Importin-4 Regulates Gene Delivery by Enhancing Nuclear Retention and Chromatin Deposition by Polyplexes. Molecular Pharmaceutics 2015, 12 (12), 4488-4497.

34. Mishra, S.; Webster, P.; Davis, M. E., PEGylation significantly affects cellular uptake and intracellular trafficking of non-viral gene delivery particles. European Journal of Cell Biology 2004, 83 (3), 97-111.

35. Vo, T. N.; Kasper, F. K.; Mikos, A. G., Strategies for controlled delivery of growth factors and cells for bone regeneration. Advanced Drug Delivery Reviews 2012, 64 (12), 1292-1309.

36. Marsell, R.; Einhorn, T. A., The biology of fracture healing. Injury-International Journal of the Care of the Injured 2011, 42 (6), 551-555.

37. Einhorn, T. A., The cell and molecular biology of fracture healing. Clinical Orthopaedics and Related Research 1998, (355), S7-S21.

38. Patel, Z. S.; Young, S.; Tabata, Y.; Jansen, J. A.; Wong, M. E. K.; Mikos, A. G., Dual delivery of an angiogenic and an osteogenic growth factor for bone regeneration in a critical size defect model. Bone 2008, 43 (5), 931-940.

39. Friedmann, T.; Roblin, R., Gene therapy for human genetic disease. Science 1972, 175 (4025), 949-+.

40. Grody, D., FDA Approves Second Gene-Altering Treatment for Cancer, New York Times, New York. October 18, 2017.

Appendix A

SUPPORTING INFORMATION FOR CHAPTER 3

Sequence Name	Nucleotide Sequence (5' to 3')
COL IIA Forward	GCCAGGATGCCCGAAAATTAG
COL IIA Reverse	CGTCATACCCTCCAGCCATC
Acan Forward	CGTTGCAGACCAGGAGCAAT
Acan Reverse	CTCTCCGGTGGCAAAGAAGT
MMP 13 Forward	GACAAGCAGTTCCAAAGGCTAC
MMP 13 Reverse	GGATGCTTAGGGTTGGGGTC
COL X Forward	CCCAGCACCAGAATCTATCTGA
COL X Reverse	GCTTCCCCGTGGCTGATATT
β-actin Forward	CTGTCGAGTCGCGTCCA
β-actin Reverse	TCATCCATGGCGAACTGGTG

Figure A.1: Forward and reverse primer sets specific to Collagen IIA (COL IIA), Aggrecan (Acan), Matrix-metalloproteinase (MMP 13), Collagen X (COL X), and beta-actin (β-actin) for RT-qPCR analysis of mRNA expression levels. Primers were designed using Primer-BLAST (NCBI-NIH, Bethesda MD).

Appendix B

SUPPORTING INFORMATION FOR CHAPTER 4

Table B.1: CHNS elemental analysis of AuNPs. Numbers represent the wt % of carbon (C), hydrogen (H), nitrogen (N), and sulfur (S) relative to the total sample weight. The balance (unreported percentage) of each material analyzed was the gold (Au) core.

Sample	Ligand Composition	C/H/N/S (wt %)
C5-coated AuNPs	C5	8.93/1.19/0.01/4.41
K5-coated AuNPs	K5	27.72/3.76/7.03/3.40
Low H3-coated AuNPs	K5 and H3	30.18/4.48/8.47/2.32
Mid H3-coated AuNPs	K5 and H3	31.94/4.58/9.38/2.26
High H3-coated AuNPs	H3	34.52/5.16/10.81/2.07

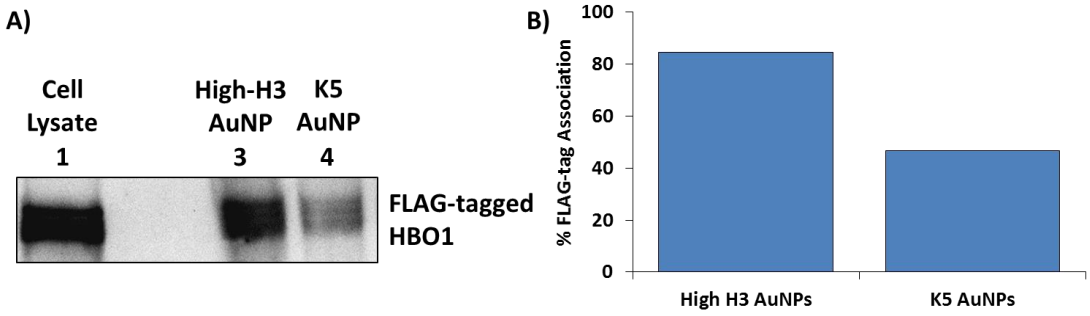

Figure B.1: HBO1 pull-down assay. Western blot against the HBO1 FLAG tag following pull-down of high-coverage H3 and K5-coated AuNPs after incubation with the cell lysate. Lane 1 contains a sample of lysate proteins that were not incubated with AuNPs. Lanes 3 and 4 contain samples of lysate proteins that associated with the indicated AuNPs during the pull-down. (B) Densitometry analysis of band intensities in (A), representing the amount of HBO1 association with AuNPs relative to the amount of HBO1 present in the cell lysate control (lane 1).

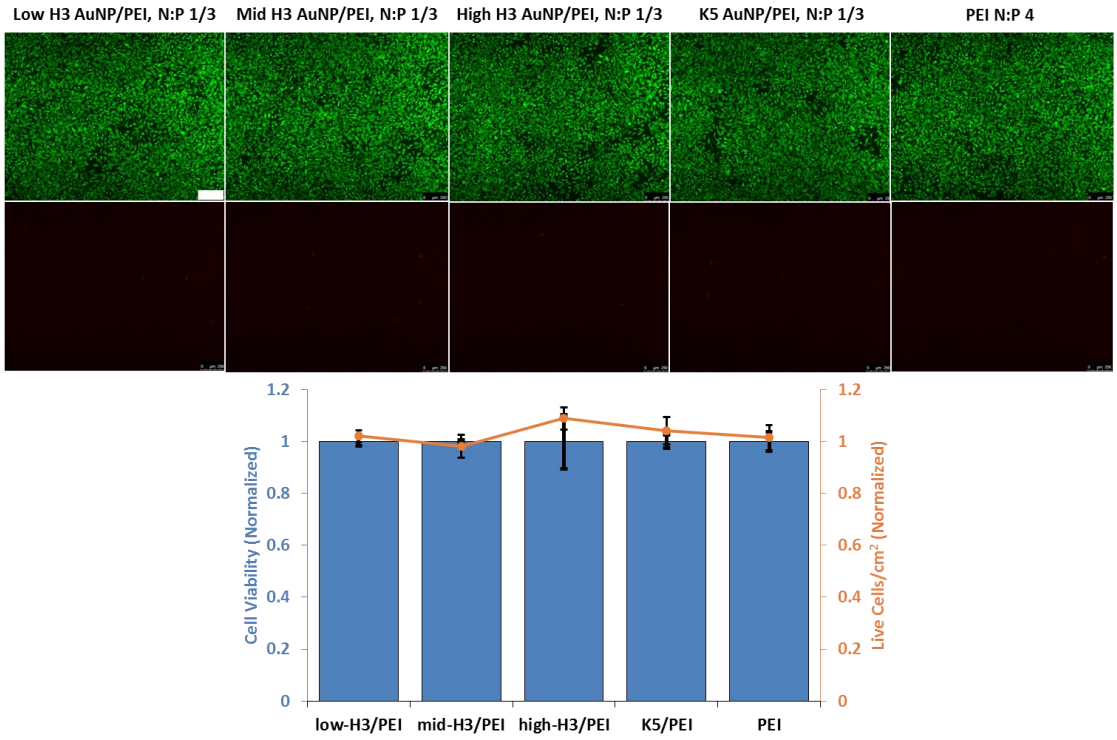

Figure B.2: CHO-K1 cellular viability and live cell surface coverage analyses 24 h post-transfection. (A) Representative fluorescence microscopy images of live cells stained with Calcein AM (green) and dead cells stained with propidium iodide (red) following transfection with the indicated nanoplexes or polyplexes. (B) Quantification of cellular vability (blue bars) and live cell surface coverage (orange line) from the fluorescence microscopy images in (A) calculated by ImageJ analysis. Cellular viability and the number of live cells/cm^2 were normalized to the untransfected controls. All results are shown as the mean ± standard deviation of data collected from at least five images of 3 independent experiments. Scale bar = 250 μm.

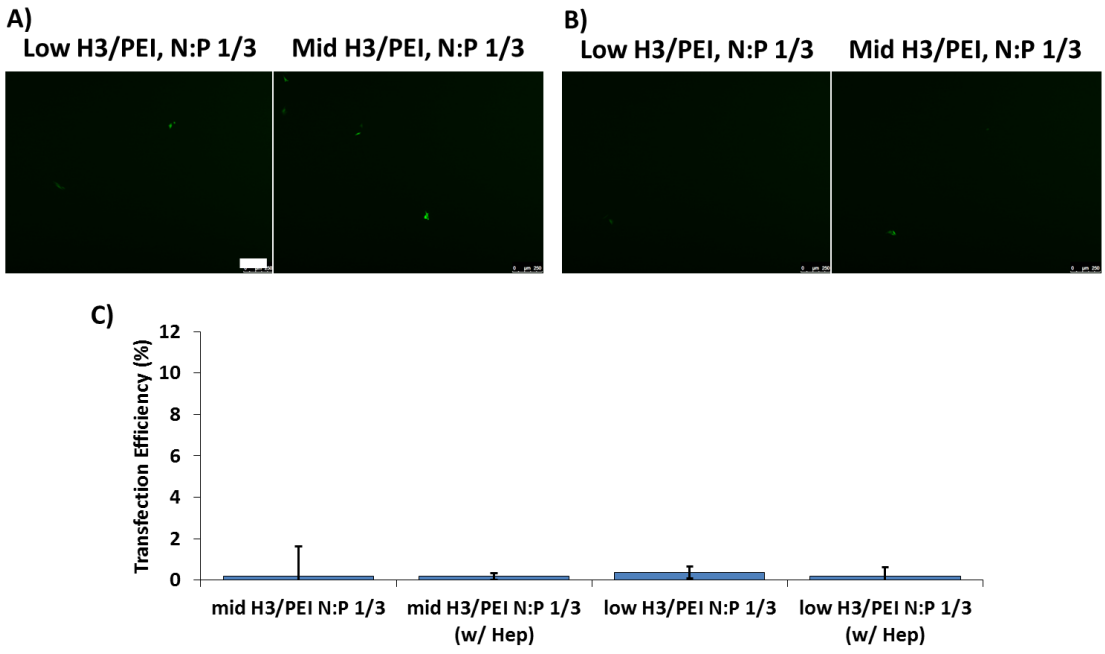

Figure B.3: CHO-K1 transfection efficiency of low- and mid-coverage H3 AuNP/PEI nanoplexes. Representative fluorescence microscopy images of GFP expression 24 h post-transfection with the indicated nanoplexes either (A) without or (B) with heparin (0.0025 mg/mL). Quantification of transfection efficiency (C) using flow cytometry. All results are shown as the mean ± standard deviation of data collected from three independent experiments. Scale bar = 250 μm.

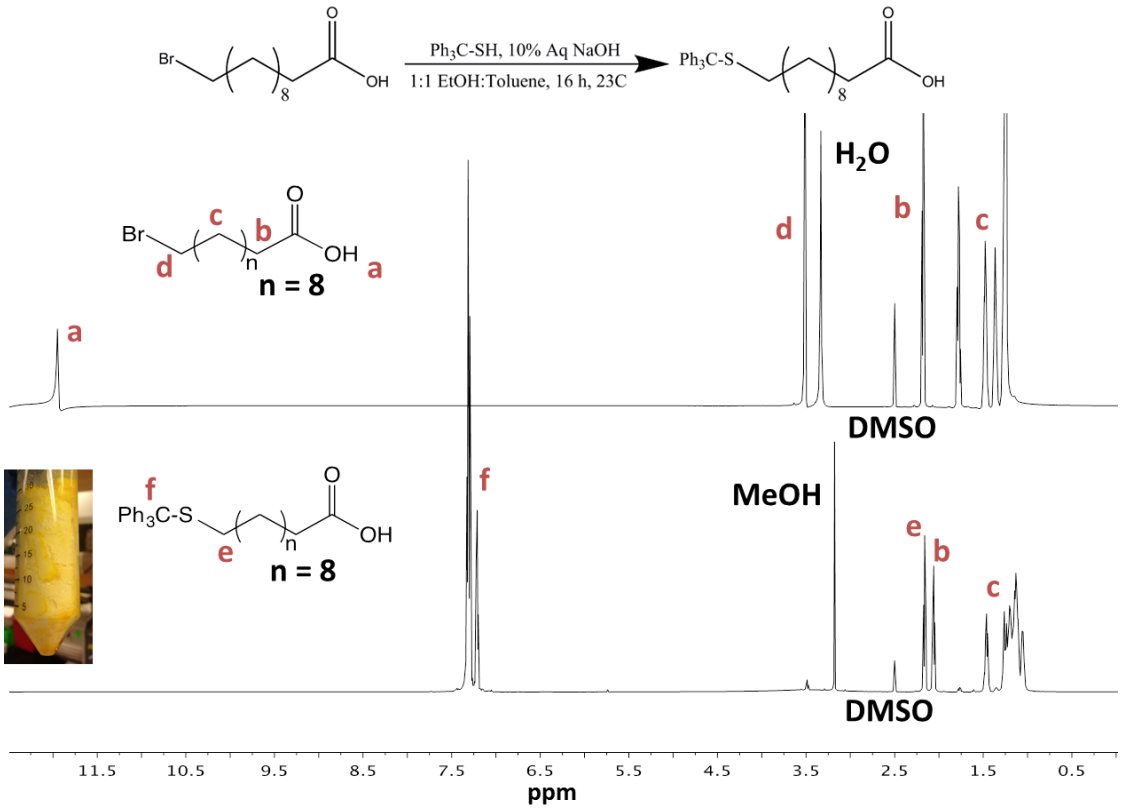

Figure B.4: ^{1}H nuclear magnetic resonance spectra of 11-bromoundecanoic acid and the purified trityl-protected mercaptoundecanoic acid, synthesized under the conditions shown in the schematic. The appearance of peaks associated with the benzene rings on the trityl protecting group and the disappearance peaks from the H atoms adjacent to the bromine indicate successful synthesis and purification.

Appendix C

CALCULATIONS TO ASSESS AuNP SURFACE LIGAND COMPOSITION

In order to accurately characterize the number of ligands displayed on the surface of each synthesized AuNP, both thermogravimetric analysis (TGA) and CHNS elemental were employed, either separately or combined. TGA results yield a total wt % loss as the sample of AuNPs is gradually heated. The wt % loss in this case corresponds to the ligands burning off of the AuNP surface, leaving the solid gold core behind (See Chapters 2 and 4). The same principle applies during CHNS elemental analysis: a sample of AuNPs is rapidly heated and the ligands on the surface undergo combustion, leaving the gold core behind. Various traps capture and analyze the amount of carbon (C), hydrogen (H), nitrogen (N), and sulfur (S) present in the combusted ligands. The CHNS results are reported as percentages of total sample weight (See Chapters 2 and 4).

In all of the following calculations, a spherical assumption was utilized to determine the volume of the gold core (r = ~1.25 nm). The total weight of the gold core was determined using this volume calculation and the density of gold (19.3 g/cm^3). The following sections detail how the number of surface ligands was determined for each of the synthesized AuNPs described in this dissertation.

C.1 C5-Coated AuNPs

The AuNPs synthesized using the Brust-Schiffrin reaction procedure in this dissertation only contain one ligand on the surface, a pentanethiol (C5). Thus, only

one characterization technique is needed to determine the number of C5 ligands on the surface of each AuNP. For these calculations, the results from TGA were utilized to determine the total weight of C5 ligands on the surface of each AuNP. From TGA (Figure 4.6):

$$\frac{W_{ligand(s)}}{W_{ligand(s)} + W_{AuNP\ core}} = 16.89\ \% \quad (1)$$

Calculating $W_{AuNP\ core}$:

$$V_{AuNP} = \left(\frac{4}{3}\right)\pi r^3 = 4.19\ nm^3 = 4.19e^{-21}\ cm^3 \quad (2)$$

$$W_{AuNP\ core} = 19.3\ \frac{g}{cm^3} * V_{AuNP} = 80.87e^{-21} g \quad (3)$$

Plugging (3) into (1) and solving:

$$W_{ligand(s)} = \frac{.1689 * W_{AuNP\ core}}{.8311} = 16.43e^{-21} g \quad (4)$$

Knowing the molecular weight (MW) of C5 (103.21 g/mol) and Avogadro's number (N_A = 6.022x10^{23} molecules/mol), the number of C5 ligands per AuNP can be calculated:

$$N_{ligand(s)} = \left(\frac{W_{ligand(s)}}{MW_{ligand(s)}}\right) * N_A = 96\ C5\ ligands \quad (5)$$

The calculated number of C5 ligands on the surface of the Brust-Schiffrin synthesized AuNPs (96 ligands total) is in good agreement with the number of cluster ligands estimated by studies conducted by Murray and co-workers (108 ligands per AuNP cluster).[1, 3, 4]

To ensure that only C5 ligands coated the surface of the Brust-Schiffrin synthesized AuNPs, CHNS analysis was also performed (Table B.1). The absence of nitrogen (0.01%) indicates that no other organic ligands (i.e. peptides) coat the surface. Additionally the molar ratio of carbon to sulfur can be determined using the

C/S percent ratio from the elemental analysis and the MW of carbon (12.01 g/mol) and sulfur (32.07 g/mol):

$$\frac{C}{S} = \frac{\frac{8.93}{12.01}}{\frac{4.41}{32.07}} = 5.41 \approx \frac{5\ moles\ C}{mole\ S} \tag{6}$$

These results indicate that each ligand contains 5 carbon atoms, further confirming that only C5 ligands coat the surface of the Brust-Schiffrin synthesized AuNPs.

C.2 K5-Coated AuNPs

Following Murray place exchange with the K5-MUA ligands, the resulting AuNPs contained two ligands on the surface, C5 and K5-MUA. In order to accurately determine the number of K5-MUA ligands on the surface of each AuNP, both TGA and CHNS elemental analysis had to be combined. First, from TGA (Figure 4.6):

$$\frac{W_{ligand(s)}}{W_{ligand(s)} + W_{AuNP\ core}} = 38.92\ \% \tag{7}$$

Combine (3) with (7) to yield:

$$W_{ligand(s)} = \frac{.3892 * W_{AuNP\ core}}{.6108} = 51.53e^{-21} g \tag{8}$$

$W_{ligand(s)}$ contains contributions from both C5 and K5-MUA (MW = 856.6 g/mol) ligands. This is represented by the following equation:

$$W_{ligand(s)} = 51.53e^{-21}\ g = \frac{((MW_{C5} * N_{C5}) + (MW_{K5-MUA} * N_{K5-MUA}))}{N_A} \tag{9}$$

Where N_{C5} and $N_{K5\text{-}MUA}$ represent the number of C5 and K5-MUA ligands on the surface of the AuNPs respectively. Solving for these two unknowns requires an additional equation which can be derived from the different ratios of elements reported from the CHNS elemental analysis (Table B.1). An ideal ratio is the N/S ratio since only the K5-MUA peptide ligand contains nitrogen atoms (MW = 14.01 g/mol). From Table B.1:

$$\frac{N}{S} = \frac{\frac{7.03}{14.01}}{\frac{3.40}{32.07}} = 4.72\ \frac{moles\ N}{moles\ S} \quad (10)$$

This ratio can be expressed in terms of ligand number, knowing that each K5-MUA peptide ligand contains 11 nitrogen atoms (5 ε-amines, 5 α-amines, and 1 N-terminus):

$$\frac{N}{S} = \frac{11 * N_{K5-MUA}}{N_{C5} + N_{K5-MUA}} = 4.72 \quad (11)$$

By solving for N_{C5} in (11) and substituting into (9) the number of K5-MUA ligands displayed on the surface of the K5-coated AuNPs was determined to be 31.22 ~ 31 K5-MUA peptide ligands per AuNP.

C.3 Low- and Mid-Coverage H3 AuNPs

For both the low- and mid-coverage H3 AuNPs, it is assumed that there are 3 separate ligands displayed on the surface of the AuNPs: C5, K5-MUA, and H3-MUA. In order to assess ligand surface coverage an additional elemental ratio from CHNS analysis must be included in the calculations. By combining the results from TGA and these two elemental ratios, a system of equations can be solved to determine the number ligands displayed on the AuNP surface. Calculations for both the low- and mid-coverage AuNPs are analogous and thus only the calculations for the mid-coverage AuNPs will be discussed in detail below. The molar ratios of H/S and N/S (MW of hydrogen = 1.01 g/mol) from elemental analysis were combined with TGA to determine ligand compositions. First, the number of carbon, hydrogen, nitrogen, and sulfur atoms was determined for the three respective ligands:

$$C5\ ligands\ \rightarrow C = 5; H = 11; N = 0; S = 1 \quad (12)$$

$$K5MUA\ ligands\ \rightarrow C = 41; H = 82; N = 11; S = 1 \quad (13)$$

$$H3MUA\ ligands\ \rightarrow C = 129; H = 236; N = 45; S = 1 \quad (14)$$

From TGA (Figure 4.6):

$$\frac{W_{ligand(s)}}{W_{ligand(s)} + W_{AuNP\ core}} = 57.10\ \% \tag{15}$$

Combining (3) with (15):

$$W_{ligand(s)} = \frac{.571 * W_{AuNP\ core}}{.429} = 10.76e^{-20} g \tag{16}$$

$W_{ligand(s)}$ contains contributions from C5, K5-MUA, and H3-MUA (MW = 3009 g/mol) ligands. This is represented by the following equation:

$$W_{ligand(s)} = 10.76e^{-20}\ g = \frac{((MW_{C5} * N_{C5}) + (MW_{K5} * N_{K5}) + (MW_{H3} * N_{H3})}{N_A} \tag{17}$$

Where N_{C5}, N_{K5}, and N_{H3} represent the number of C5, K5-MUA, and H3-MUA ligands on the surface of the AuNPs respectively. The ratio of H/S and N/S can be represented in terms of ligand number as follows:

$$\frac{H}{S} = \frac{\frac{4.58}{1.01}}{\frac{2.26}{32.07}} = 64.35\ \frac{moles\ H}{moles\ S} = \frac{[(11 * N_{C5}) + (82 * N_{K5}) + (236 * N_{H3})]}{N_{C5} + N_{K5} + N_{H3}} \tag{18}$$

$$\frac{N}{S} = \frac{\frac{9.38}{14.01}}{\frac{2.26}{32.07}} = 9.50\ \frac{moles\ N}{moles\ S} = \frac{[(11 * N_{K5}) + (45 * N_{H3})]}{N_{C5} + N_{K5} + N_{H3}} \tag{19}$$

By solving (17), (18), and (19) as a system of equations, the number of H3-MUA and K5-MUA peptide ligands on the mid-coverage H3 AuNPs was determined to be 9.97 ~ 10 and 35.46 ~ 35 respectively. By similar analyses, the number of H3-MUA and K5-MUA peptide ligands on the low-coverage H3 AuNPs was determined to be 4 and 48 respectively.

C.4 High-Coverage H3 AuNPs

For the high-coverage H3 AuNPs, a large excess of H3-MUA peptide ligands were introduced to the place exchange reaction mixture with the K5-coated AuNPs. Based on numerous results reported in literature,[1, 2, 5-7] this excess should function to replace the majority of ligands on the AuNP surface with H3-MUA. Thus, once again

the AuNP surface coverage may be approximated using TGA alone. While there may still be a small fraction K5-MUA and/or C5 ligands present on the surface following this place exchange, their contribution to overall ligand surface weight will be low given the fact the H3-MUA is 29-fold and 4-fold heavier than the C5 and K5-MUA peptide ligands respectively. From Figure 4.6:

$$\frac{W_{ligand(s)}}{W_{ligand(s)} + W_{AuNP\ core}} = 81.10\ \% \tag{20}$$

Combining (20) with (3) to yield:

$$W_{ligand(s)} = \frac{.811 * W_{AuNP\ core}}{.189} = 34.7e^{-20}g \tag{21}$$

Solving for $N_{H3\text{-}MUA}$ similar to (5):

$$N_{H3-MUA} = \left(\frac{W_{ligand(s)}}{MW_{H3-MUA}}\right) * N_A = 69\ H3\ ligands \tag{22}$$

REFERENCES

1. Hostetler, M. J.; Templeton, A. C.; Murray, R. W., Dynamics of place-exchange reactions on monolayer-protected gold cluster molecules. Langmuir 1999, 15 (11), 3782-3789.

2. Ghosh, P. S.; Kim, C. K.; Han, G.; Forbes, N. S.; Rotello, V. M., Efficient Gene Delivery Vectors by Tuning the Surface Charge Density of Amino Acid-Functionalized Gold Nanoparticles. Acs Nano 2008, 2 (11), 2213-2218.

3. Templeton, A. C.; Wuelfing, M. P.; Murray, R. W., Monolayer protected cluster molecules. Accounts of Chemical Research 2000, 33 (1), 27-36.

4. Green, S. J.; Pietron, J. J.; Stokes, J. J.; Hostetler, M. J.; Vu, H.; Wuelfing, W. P.; Murray, R. W., Three dimensional monolayers: Voltammetry of alkanethiolate-stabilized gold cluster molecules. Langmuir 1998, 14 (19), 5612-5619.

5. Ghosh, P.; Yang, X. C.; Arvizo, R.; Zhu, Z. J.; Agasti, S. S.; Mo, Z. H.; Rotello, V. M., Intracellular Delivery of a Membrane-Impermeable Enzyme in Active Form Using Functionalized Gold Nanoparticles. Journal of the American Chemical Society 2010, 132 (8), 2642-2645.

6. Rana, S.; Bajaj, A.; Mout, R.; Rotello, V. M., Monolayer coated gold nanoparticles for delivery applications. Advanced Drug Delivery Reviews 2012, 64 (2), 200-216.

7. Sandhu, K. K.; McIntosh, C. M.; Simard, J. M.; Smith, S. W.; Rotello, V. M., Gold nanoparticle-mediated Transfection of mammalian cells. Bioconjugate Chemistry 2002, 13 (1), 3-6.

Appendix D

TEXT AND FIGURE REPRINT PERMISSIONS

Current pharmaceutical design

Order detail ID: 70752820
Order License Id: 4217910775109
ISSN: 1381-6128
Publication Type: Journal
Volume:
Issue:
Start page:
Publisher: BENTHAM SCIENCE PUBLISHERS LTD.

Permission Status: Granted
Permission type: Republish or display content
Type of use: Thesis/Dissertation

Hide details

Requestor type	Author of requested content
Format	Electronic
Portion	chapter/article
The requesting person/organization	Erik
Title or numeric reference of the portion(s)	article, figure 1, figure 4
Title of the article or chapter the portion is from	Journey to the Center of the Cell: Current Nanocarrier Design Strategies Targeting Biopharmaceuticals to the Cytoplasm and Nucleus
Editor of portion(s)	n/a
Author of portion(s)	Erik Munsell
Volume of serial or monograph	n/a
Issue, if republishing an article from a serial	9
Page range of portion	
Publication date of portion	2016
Rights for	Main product
Duration of use	Current edition and up to 5 years
Creation of copies for the disabled	no
With minor editing privileges	no
For distribution to	United States
In the following language(s)	Original language of publication
With incidental promotional use	no
Lifetime unit quantity of new product	Up to 499
Title	Histone-targeted nucleic acid delivery for tissue regenerative applications
Instructor name	n/a
Institution name	n/a
Expected presentation date	Nov 2017

Note: This item will be invoiced or charged separately through CCC's **RightsLink** service. More info **$ 0.00**

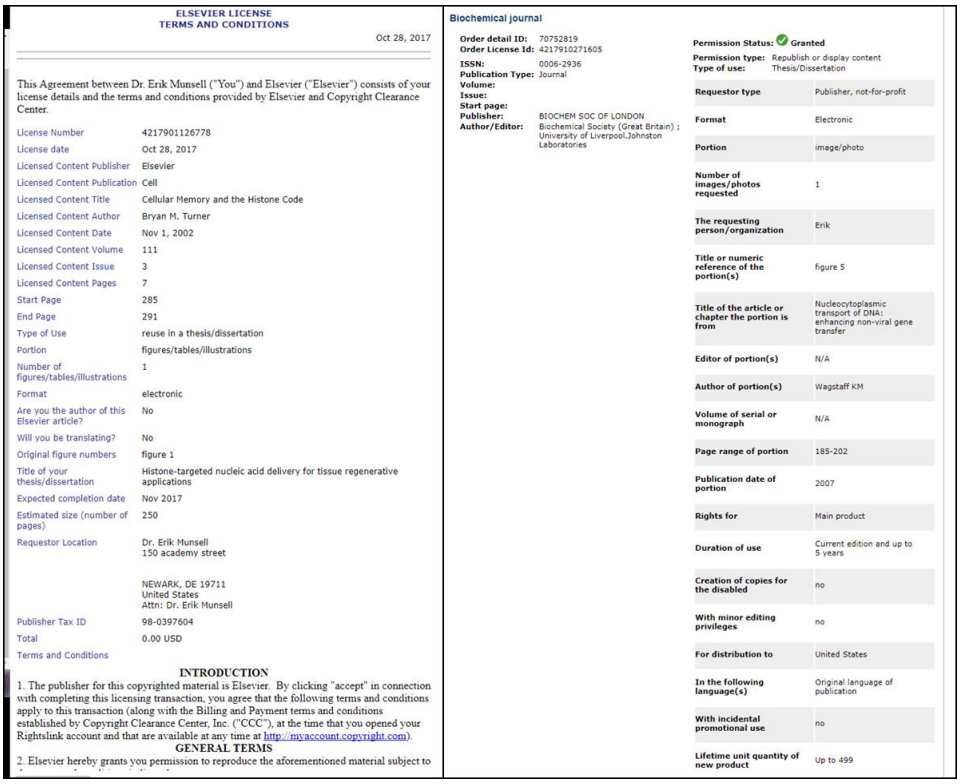

ELSEVIER LICENSE
TERMS AND CONDITIONS

Oct 28, 2017

This Agreement between Dr. Erik Munsell ("You") and Elsevier ("Elsevier") consists of your license details and the terms and conditions provided by Elsevier and Copyright Clearance Center.

License Number	4217901126778
License date	Oct 28, 2017
Licensed Content Publisher	Elsevier
Licensed Content Publication	Cell
Licensed Content Title	Cellular Memory and the Histone Code
Licensed Content Author	Bryan M. Turner
Licensed Content Date	Nov 1, 2002
Licensed Content Volume	111
Licensed Content Issue	3
Licensed Content Pages	7
Start Page	285
End Page	291
Type of Use	reuse in a thesis/dissertation
Portion	figures/tables/illustrations
Number of figures/tables/illustrations	1
Format	electronic
Are you the author of this Elsevier article?	No
Will you be translating?	No
Original figure numbers	figure 1
Title of your thesis/dissertation	Histone-targeted nucleic acid delivery for tissue regenerative applications
Expected completion date	Nov 2017
Estimated size (number of pages)	250
Requestor Location	Dr. Erik Munsell 150 academy street NEWARK, DE 19711 United States Attn: Dr. Erik Munsell
Publisher Tax ID	98-0397604
Total	0.00 USD
Terms and Conditions	

INTRODUCTION

1. The publisher for this copyrighted material is Elsevier. By clicking "accept" in connection with completing this licensing transaction, you agree that the following terms and conditions apply to this transaction (along with the Billing and Payment terms and conditions established by Copyright Clearance Center, Inc. ("CCC"), at the time that you opened your Rightslink account and that are available at any time at http://myaccount.copyright.com).

GENERAL TERMS

2. Elsevier hereby grants you permission to reproduce the aforementioned material subject to

Biochemical journal

Order detail ID:	70752819
Order License Id:	4217910271605
ISSN:	0006-2936
Publication Type:	Journal
Volume:	
Issue:	
Start page:	
Publisher:	BIOCHEM SOC OF LONDON
Author/Editor:	Biochemical Society (Great Britain) ; University of Liverpool.Johnston Laboratories

Permission Status: Granted
Permission type: Republish or display content
Type of use: Thesis/Dissertation

Requestor type	Publisher, not-for-profit
Format	Electronic
Portion	image/photo
Number of images/photos requested	1
The requesting person/organization	Erik
Title or numeric reference of the portion(s)	figure 5
Title of the article or chapter the portion is from	Nucleocytoplasmic transport of DNA: enhancing non-viral gene transfer
Editor of portion(s)	N/A
Author of portion(s)	Wagstaff KM
Volume of serial or monograph	N/A
Page range of portion	185-202
Publication date of portion	2007
Rights for	Main product
Duration of use	Current edition and up to 5 years
Creation of copies for the disabled	no
With minor editing privileges	no
For distribution to	United States
In the following language(s)	Original language of publication
With incidental promotional use	no
Lifetime unit quantity of new product	Up to 499

Copyright Clearance Center RightsLink®

Home | Account Info | Help

ACS Publications
Most Trusted. Most Cited. Most Read.

Logged in as:
Erik Munsell
LOGOUT

Title: Histone H3 Tail Peptides and Poly(ethylenimine) Have Synergistic Effects for Gene Delivery
Author: Meghan J. Reilly, John D. Larsen, Millicent O. Sullivan
Publication: Molecular Pharmaceutics
Publisher: American Chemical Society
Date: May 1, 2012
Copyright © 2012, American Chemical Society

PERMISSION/LICENSE IS GRANTED FOR YOUR ORDER AT NO CHARGE

This type of permission/license, instead of the standard Terms & Conditions, is sent to you because no fee is being charged for your order. Please note the following:

- Permission is granted for your request in both print and electronic formats, and translations.
- If figures and/or tables were requested, they may be adapted or used in part.
- Please print this page for your records and send a copy of it to your publisher/graduate school.
- Appropriate credit for the requested material should be given as follows: "Reprinted (adapted) with permission from (COMPLETE REFERENCE CITATION). Copyright (YEAR) American Chemical Society." Insert appropriate information in place of the capitalized words.
- One-time permission is granted only for the use specified in your request. No additional uses are granted (such as derivative works or other editions). For any other uses, please submit a new request.

If credit is given to another source for the material you requested, permission must be obtained from that source.

BACK | CLOSE WINDOW

Copyright © 2017 Copyright Clearance Center, Inc. All Rights Reserved. Privacy statement. Terms and Conditions.
Comments? We would like to hear from you. E-mail us at customercare@copyright.com

Copyright Clearance Center RightsLink®

Home | Account Info | Help

ACS Publications Most Trusted. Most Cited. Most Read.

Logged in as:
Erik Munsell
LOGOUT

Title: Importin-4 Regulates Gene Delivery by Enhancing Nuclear Retention and Chromatin Deposition by Polyplexes
Author: Nikki L. Ross, Millicent O. Sullivan
Publication: Molecular Pharmaceutics
Publisher: American Chemical Society
Date: Dec 1, 2015
Copyright © 2015, American Chemical Society

PERMISSION/LICENSE IS GRANTED FOR YOUR ORDER AT NO CHARGE

This type of permission/license, instead of the standard Terms & Conditions, is sent to you because no fee is being charged for your order. Please note the following:

- Permission is granted for your request in both print and electronic formats, and translations.
- If figures and/or tables were requested, they may be adapted or used in part.
- Please print this page for your records and send a copy of it to your publisher/graduate school.
- Appropriate credit for the requested material should be given as follows: "Reprinted (adapted) with permission from (COMPLETE REFERENCE CITATION). Copyright (YEAR) American Chemical Society." Insert appropriate information in place of the capitalized words.
- One-time permission is granted only for the use specified in your request. No additional uses are granted (such as derivative works or other editions). For any other uses, please submit a new request.

BACK | CLOSE WINDOW

Copyright © 2017 Copyright Clearance Center, Inc. All Rights Reserved. Privacy statement. Terms and Conditions.
Comments? We would like to hear from you. E-mail us at customercare@copyright.com

Copyright Clearance Center RightsLink®

Home | Account Info | Help

Title: Monolayer coated gold nanoparticles for delivery applications
Author: Subinoy Rana,Avinash Bajaj,Rubul Mout,Vincent M. Rotello
Publication: Advanced Drug Delivery Reviews
Publisher: Elsevier
Date: February 2012

Copyright © 2011 Elsevier B.V. All rights reserved.

Logged in as:
Erik Munsell
LOGOUT

Order Completed

Thank you for your order.

This Agreement between Dr. Erik Munsell ("You") and Elsevier ("Elsevier") consists of your license details and the terms and conditions provided by Elsevier and Copyright Clearance Center.

Your confirmation email will contain your order number for future reference.

printable details

License Number	4217920960486
License date	Oct 28, 2017
Licensed Content Publisher	Elsevier
Licensed Content Publication	Advanced Drug Delivery Reviews
Licensed Content Title	Monolayer coated gold nanoparticles for delivery applications
Licensed Content Author	Subinoy Rana,Avinash Bajaj,Rubul Mout,Vincent M. Rotello
Licensed Content Date	Feb 1, 2012
Licensed Content Volume	64
Licensed Content Issue	2
Licensed Content Pages	17
Type of Use	reuse in a thesis/dissertation
Portion	figures/tables/illustrations
Number of figures/tables/illustrations	1
Format	electronic
Are you the author of this Elsevier article?	No
Will you be translating?	No
Original figure numbers	Figure 1, 2
Title of your thesis/dissertation	Histone-targeted nucleic acid delivery for tissue regenerative applications
Expected completion date	Nov 2017
Estimated size (number of pages)	250
Requestor Location	Dr. Erik Munsell 150 academy street NEWARK, DE 19711 United States Attn: Dr. Erik Munsell
Publisher Tax ID	98-0397604
Total	0.00 USD

ORDER MORE | CLOSE WINDOW

Copyright © 2017 Copyright Clearance Center, Inc. All Rights Reserved. Privacy statement. Terms and Conditions.
Comments? We would like to hear from you. E-mail us at customercare@copyright.com

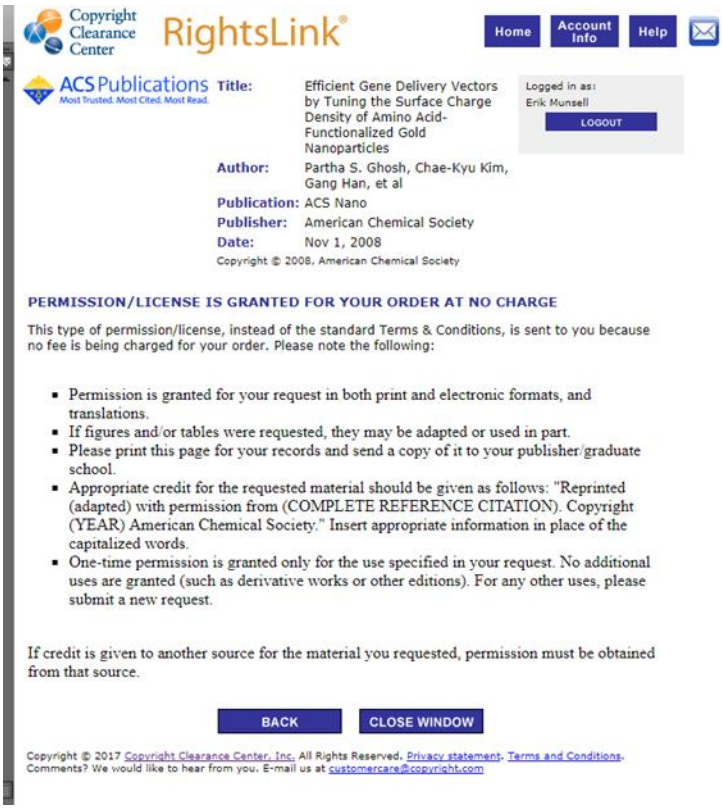

Copyright Clearance Center RightsLink®

Home | Account Info | Help

ACS Publications
Most Trusted. Most Cited. Most Read.

Title: Efficient Gene Delivery Vectors by Tuning the Surface Charge Density of Amino Acid-Functionalized Gold Nanoparticles

Author: Partha S. Ghosh, Chae-Kyu Kim, Gang Han, et al

Publication: ACS Nano

Publisher: American Chemical Society

Date: Nov 1, 2008

Copyright © 2008, American Chemical Society

Logged in as:
Erik Munsell
LOGOUT

PERMISSION/LICENSE IS GRANTED FOR YOUR ORDER AT NO CHARGE

This type of permission/license, instead of the standard Terms & Conditions, is sent to you because no fee is being charged for your order. Please note the following:

- Permission is granted for your request in both print and electronic formats, and translations.
- If figures and/or tables were requested, they may be adapted or used in part.
- Please print this page for your records and send a copy of it to your publisher/graduate school.
- Appropriate credit for the requested material should be given as follows: "Reprinted (adapted) with permission from (COMPLETE REFERENCE CITATION). Copyright (YEAR) American Chemical Society." Insert appropriate information in place of the capitalized words.
- One-time permission is granted only for the use specified in your request. No additional uses are granted (such as derivative works or other editions). For any other uses, please submit a new request.

If credit is given to another source for the material you requested, permission must be obtained from that source.

BACK | CLOSE WINDOW

Copyright © 2017 Copyright Clearance Center, Inc. All Rights Reserved. Privacy statement. Terms and Conditions.
Comments? We would like to hear from you. E-mail us at customercare@copyright.com

Copyright Clearance Center RightsLink®

Home | Account Info | Help

ACS Publications
Most Trusted. Most Cited. Most Read.

Title: On the Mechanism of Metal Nanoparticle Synthesis in the Brust–Schiffrin Method
Author: Siva Rama Krishna Perala, Sanjeev Kumar
Publication: Langmuir
Publisher: American Chemical Society
Date: Aug 1, 2013
Copyright © 2013, American Chemical Society

Logged in as:
Erik Munsell
LOGOUT

PERMISSION/LICENSE IS GRANTED FOR YOUR ORDER AT NO CHARGE

This type of permission/license, instead of the standard Terms & Conditions, is sent to you because no fee is being charged for your order. Please note the following:

- Permission is granted for your request in both print and electronic formats, and translations.
- If figures and/or tables were requested, they may be adapted or used in part.
- Please print this page for your records and send a copy of it to your publisher/graduate school.
- Appropriate credit for the requested material should be given as follows: "Reprinted (adapted) with permission from (COMPLETE REFERENCE CITATION). Copyright (YEAR) American Chemical Society." Insert appropriate information in place of the capitalized words.
- One-time permission is granted only for the use specified in your request. No additional uses are granted (such as derivative works or other editions). For any other uses, please submit a new request.

If credit is given to another source for the material you requested, permission must be obtained from that source.

BACK | CLOSE WINDOW

Copyright © 2017 Copyright Clearance Center, Inc. All Rights Reserved. Privacy statement. Terms and Conditions.
Comments? We would like to hear from you. E-mail us at customercare@copyright.com

Copyright Clearance Center RightsLink®

Home | Account Info | Help

ELSEVIER

Chapter: Chapter 7 Applications of Electron Microscopy in Heterogeneous Catalysis
Book: Catalysis by Materials with Well-Defined Structures
Author: Yuyuan Lin,James A. McCarthy,Kenneth R. Poeppelmeier,Laurence D. Marks
Publisher: Elsevier
Date: 2015

Copyright © 2015 Elsevier Inc. All rights reserved.

Logged in as:
Erik Munsell
LOGOUT

Permission Request Submitted

Your request is now under review.
You will be notified of the decision via email.
Please print this request for your records.

printable details

Order Number	501327854
Order Date	Oct 28, 2017
Licensed Content Publisher	Elsevier
Licensed Content Publication	Elsevier Books
Licensed Content Title	Catalysis by Materials with Well-Defined Structures
Licensed Content Author	Yuyuan Lin,James A. McCarthy,Kenneth R. Poeppelmeier,Laurence D. Marks
Licensed Content Date	2015
Licensed Content Volume	n/a
Licensed Content Issue	n/a
Licensed Content Pages	46
Type of Use	reuse in a thesis/dissertation
Portion	figures/tables/illustrations
Number of figures/tables/illustrations	1
Format	electronic
Are you the author of this Elsevier chapter?	No
Will you be translating?	No
Original figure numbers	figure 1
Title of your thesis/dissertation	Histone-targeted nucleic acid delivery for tissue regenerative applications
Expected completion date	Nov 2017
Estimated size (number of pages)	250
Requestor Location	Dr. Erik Munsell 150 academy street NEWARK, DE 19711 United States Attn: Dr. Erik Munsell
Publisher Tax ID	98-0397604
Total	Not Available

Copyright Clearance Center RightsLink®

Home | Account Info | Help

Title: Inhibition of ectopic bone formation by a selective retinoic acid receptor α-agonist: A new therapy for heterotopic ossification?

Author: Kengo Shimono,Tiffany N. Morrison,Wei-en Tung,Roshantha A. Chandraratna,Julie A. Williams,Masahiro Iwamoto,Maurizio Pacifici

Publication: Journal of Orthopaedic Research

Publisher: John Wiley and Sons

Date: Sep 1, 2009

Copyright © 2009 Orthopaedic Research Society

Logged in as:
Erik Munsell
LOGOUT

Order Completed

Thank you for your order.

This Agreement between Dr. Erik Munsell ("You") and John Wiley and Sons ("John Wiley and Sons") consists of your license details and the terms and conditions provided by John Wiley and Sons and Copyright Clearance Center.

Your confirmation email will contain your order number for future reference.

printable details

License Number	4217930904419
License date	Oct 28, 2017
Licensed Content Publisher	John Wiley and Sons
Licensed Content Publication	Journal of Orthopaedic Research
Licensed Content Title	Inhibition of ectopic bone formation by a selective retinoic acid receptor α-agonist: A new therapy for heterotopic ossification?
Licensed Content Author	Kengo Shimono,Tiffany N. Morrison,Wei-en Tung,Roshantha A. Chandraratna,Julie A. Williams,Masahiro Iwamoto,Maurizio Pacifici
Licensed Content Date	Sep 1, 2009
Licensed Content Pages	7
Type of use	Dissertation/Thesis
Requestor type	University/Academic
Format	Electronic
Portion	Figure/table
Number of figures/tables	2
Original Wiley figure/table number(s)	figure 2, figure 4
Will you be translating?	No
Title of your thesis / dissertation	Histone-targeted nucleic acid delivery for tissue regenerative applications
Expected completion date	Nov 2017
Expected size (number of pages)	250
Requestor Location	Dr. Erik Munsell

Copyright Clearance Center RightsLink®

Home | Account Info | Help

ACS Publications
Most Trusted. Most Cited. Most Read.

Logged in as:
Erik Munsell
LOGOUT

Title: Nano Meets Biology: Structure and Function at the Nanoparticle Interface
Author: Daniel F. Moyano, Vincent M. Rotello
Publication: Langmuir
Publisher: American Chemical Society
Date: Sep 1, 2011
Copyright © 2011, American Chemical Society

PERMISSION/LICENSE IS GRANTED FOR YOUR ORDER AT NO CHARGE

This type of permission/license, instead of the standard Terms & Conditions, is sent to you because no fee is being charged for your order. Please note the following:

- Permission is granted for your request in both print and electronic formats, and translations.
- If figures and/or tables were requested, they may be adapted or used in part.
- Please print this page for your records and send a copy of it to your publisher/graduate school.
- Appropriate credit for the requested material should be given as follows: "Reprinted (adapted) with permission from (COMPLETE REFERENCE CITATION). Copyright (YEAR) American Chemical Society." Insert appropriate information in place of the capitalized words.
- One-time permission is granted only for the use specified in your request. No additional uses are granted (such as derivative works or other editions). For any other uses, please submit a new request.

If credit is given to another source for the material you requested, permission must be obtained from that source.

BACK | CLOSE WINDOW

Copyright © 2017 Copyright Clearance Center, Inc. All Rights Reserved. Privacy statement. Terms and Conditions.
Comments? We would like to hear from you. E-mail us at customercare@copyright.com

Copyright Clearance Center RightsLink®

Home | Account Info | Help

Title: Strategies for controlled delivery of growth factors and cells for bone regeneration
Author: Tiffany N. Vo,F. Kurtis Kasper,Antonios G. Mikos
Publication: Advanced Drug Delivery Reviews
Publisher: Elsevier
Date: September 2012

Logged in as: Erik Munsell
LOGOUT

Copyright © 2012 Elsevier B.V. All rights reserved.

Order Completed

Thank you for your order.

This Agreement between Dr. Erik Munsell ("You") and Elsevier ("Elsevier") consists of your license details and the terms and conditions provided by Elsevier and Copyright Clearance Center.

Your confirmation email will contain your order number for future reference.

printable details

License Number	4217931303545
License date	Oct 28, 2017
Licensed Content Publisher	Elsevier
Licensed Content Publication	Advanced Drug Delivery Reviews
Licensed Content Title	Strategies for controlled delivery of growth factors and cells for bone regeneration
Licensed Content Author	Tiffany N. Vo,F. Kurtis Kasper,Antonios G. Mikos
Licensed Content Date	Sep 1, 2012
Licensed Content Volume	64
Licensed Content Issue	12
Licensed Content Pages	18
Type of Use	reuse in a thesis/dissertation
Portion	figures/tables/illustrations
Number of figures/tables/illustrations	1
Format	electronic
Are you the author of this Elsevier article?	No
Will you be translating?	No
Original figure numbers	figure 3
Title of your thesis/dissertation	Histone-targeted nucleic acid delivery for tissue regenerative applications
Expected completion date	Nov 2017
Estimated size (number of pages)	250
Requestor Location	Dr. Erik Munsell 150 academy street NEWARK, DE 19711 United States Attn: Dr. Erik Munsell
Publisher Tax ID	98-0397604
Total	0.00 USD

ORDER MORE | CLOSE WINDOW

Copyright © 2017 Copyright Clearance Center, Inc. All Rights Reserved. Privacy statement. Terms and Conditions.
Comments? We would like to hear from you. E-mail us at customercare@copyright.com

Copyright Clearance Center RightsLink®

Account Info | Help

ELSEVIER

Chapter: Chapter 7 Applications of Electron Microscopy in Heterogeneous Catalysis
Book: Catalysis by Materials with Well-Defined Structures
Author: Yuyuan Lin,James A. McCarthy,Kenneth R. Poeppelmeier,Laurence D. Marks
Publisher: Elsevier
Date: Jan 1, 2015

Logged in as:
Erik Munsell
Account #:
3001211372
LOGOUT

Copyright © 2015 Elsevier Inc. All rights reserved.

Order Completed

Thank you for your order.

This Agreement between Erik Munsell ("You") and Elsevier ("Elsevier") consists of your order details and the terms and conditions provided by Elsevier and Copyright Clearance Center.

License number	Reference confirmation email for license number
License date	Nov. 29 2017
Licensed Content Publisher	Elsevier
Licensed Content Publication	Elsevier Books
Licensed Content Title	Catalysis by Materials with Well-Defined Structures
Licensed Content Author	Yuyuan Lin,James A. McCarthy,Kenneth R. Poeppelmeier,Laurence D. Marks
Licensed Content Date	2015
Licensed Content Volume	n/a
Licensed Content Issue	n/a
Licensed Content Pages	46
Type of Use	reuse in a thesis/dissertation
Portion	figures/tables/illustrations
Number of figures/tables/illustrations	1
Format	electronic
Are you the author of this Elsevier chapter?	No
Will you be translating?	No
Original figure numbers	figure 1
Title of your thesis/dissertation	Histone-targeted nucleic acid delivery for tissue regenerative applications
Expected completion date	Nov 2017
Estimated size (number of pages)	250
Requestor Location	Dr. Erik Munsell 150 academy street NEWARK, DE 19711 United States Attn: Dr. Erik Munsell
Publisher Tax ID	98-0397604
Billing Type	Invoice
Billing address	Dr. Erik Munsell 150 academy street